

**University of Napoli FEDERICO II**

*Faculty of Engineering*

PH.D. PROGRAMME IN MATERIALS AND STRUCTURES

COORDINATOR PROF. D. ACIERNO E G. MENSITIERI

*XXIII CICLO*



*ALBERTO ZINNO*

PH.D THESIS

**Multiscale Approach for the Design of Composite  
Sandwich Elements**

TUTORS: DR. ANDREA PROTA

PROF. DR. CHARLES E BAKIS

## ***ABSTRACT***

In the present work, composite sandwich components, that perfectly match the challenging demands of lightweight and more customized structures, have been characterized and designed as a roof panels of a railway vehicle.

The most critical issue related to the design and assessment of composite sandwich structures are discussed and analyzed in a multiscale procedure.

A multiscale procedure has been developed using knowledge-based procedure for the optimal stiffness design of composite sandwich structures under some classified design rules. Recent developments of multifunctional design tools, integrating structural and functional features, enables a next step toward the exploitation of the composite sandwich benefits in a wide range of applications

In particular new phenolic impregnated composite skins have been characterized and involved in sandwich configuration for load carrying components. The selected composite materials have been analyzed with different core configuration and the use of both numerical and analytical tools have been assessed with particular attentions to various failure mode that can be expected..

However, the use of fiber reinforced composite materials presents a significant challenge with respect to the methods of joining to be used in body fabrication. At this aim the project provides the characterization of potential joining techniques available to the railway industry involving both

composite and aluminum components. Problems related to strength and durability of the joints have been experimentally characterized.

The durability of composites, in addition to being dependent on loading conditions, is strongly dependent on the environmental conditions, in terms of the specific combinations of temperature, relative humidity, exposure to electro-magnetic radiation, to solvents, acid and alkaline conditions and of their (cyclic) evolution during time. Since the degradation process of a composite sandwich structure depends on the environmental conditions, type of skins and core material, and production process, mechanical properties through accelerated ageing tests have been performed in order to predict long-term performances of sandwich composites and to determine the correlation between mechanical damage and aging due to different environmental factors..

In addition to the aforementioned issues, in order to reliably predict the structural safety of composite sandwich structures, understanding the adverse effect of in-service impact events (e.g. impact and penetration damage) has become important in the transportation industry. Both quasi static and dynamic impact have been experimentally analyzed in the present study and the damage mechanism have been related to the type of impact events.

Finally optimization and validation of the designed sandwich structures have been performed by means of finite element simulation.

# **CONTENTS**

University of Napoli FEDERICO II.....	I
ABSTRACT	I
CONTENTS	III
Chapter I	1
INTRODUCTION.....	1
1.1.Historical overview .....	1
1.2.Research purpose.....	2
1.3.Multiscale procedure and research outline .....	5
Chapter II	10
MECHANICAL BEHAVIOR OF SANDWICH MATERIALS .....	10
2.1.Common sandwich materials .....	10
2.2.Fiber reinforced composite skin .....	11
2.2.1.Characteristic and configuration .....	12
2.2.2.Modeling the mechanical behavior of composites.....	14
2.2.3.Elastic behavior of composite lamina .....	15
2.2.4.Strength of composite lamina.....	23
2.2.5.Elastic behavior of composite laminates .....	29

---

2.2.6.Strength of composite laminates .....	33
2.3.Cellular core materials .....	36
2.3.1.Cellular structure .....	37
2.3.2.Response of cellular structures to loading.....	41
2.3.3.The uniaxial in-plane behavior of honeycombs .....	44
2.3.4.The uniaxial behavior of open-cell foams.....	52
2.3.5.The in-plane biaxial behavior of honeycombs .....	56
2.3.6.The multiaxial behavior of foams .....	58
References	61
Chapter III	62
ANALYSIS OF SANDWICH STRUCTURES.....	62
3.1.Ordinary sandwich beam theory .....	62
3.1.1.Flexural stiffness .....	62
3.1.2.Stresses in the sandwich beam .....	65
3.1.3.Shear deformation and stiffness .....	68
3.1.4.Governing equation .....	70
3.1.5.Wide and narrow beams.....	74
3.2.High-order sandwich beam theory .....	75
3.3.Numerical simulation .....	80
3.4.Failure mode	81
3.4.1.Skin failure .....	81
3.4.2.Core failure .....	82
3.4.3.Failure mode map.....	83
3.5.Sandwich structure with composite skins .....	84
References .....	86

---

Chapter IV	88
<i>Design criteria</i>	88
4.1.Introduction to framework activities	88
4.2.Literature review	88
4.3.Design criteria	91
4.3.1.Structural requirements	91
4.3.2.Non-structural requirements	95
4.4.Material selection	97
4.5.Design concept	102
References	104
Chapter V	106
<i>EXPERIMENTAL CHARACTERIZATION AND VALIDATION</i>	106
5.1.Introduction to framework activities	106
5.2.Testing methods	107
5.2.1.Composite laminae tests	107
5.2.2.Sandwich tests	111
5.3.Skin characterization	113
5.4.Sandwich characterization	118
5.5.Analysis of structural behavior	128
5.6.Final remarks	137
References	138
Chapter VI	141
<i>ANALYSIS OF JOINING TECHNIQUES</i>	141
6.1.Introduction to framework activities	141
6.2.Review of joining techniques	142

---

6.2.1. Adhesive bonding.....	143
6.2.2. Mechanical fasteners.....	147
6.3. Adhesively bonded joint tests.....	150
6.3.1. Static tests.....	150
6.4. Mechanically fastened joint tests.....	159
6.5. Final remarks	167
References.....	168
Chapter VII.....	173
<i>DEGRADATION ISSUES: ENVIRONMENTAL CONDITIONING</i> .....	173
7.1. Introduction of framework activity.....	173
7.2. Review of degradation factors.....	173
7.2.1. Thermal degradation.....	174
7.2.2. Hygrothermal degradation.....	176
7.2.3. Photodegradation.....	177
7.2.4. Chemical degradation.....	178
7.3. Thermo-mechanical tests.....	179
7.3.1. Tensile tests.....	179
7.3.2. DMA tests.....	183
7.4. Accelerated ageing tests.....	186
7.4.1. Laminate tests.....	188
7.4.2. Sandwich tests.....	189
7.5. Final remarks	192
References.....	193
Chapter VIII.....	196
<i>DEGRADATION ISSUES: IMPACT ANALYSIS</i> .....	196

---

8.1.Introduction to framework activities .....	196
8.2.Review of impact on sandwich structures.....	196
8.2.1.Contact between a sandwich beam and a cylindrical indenter.....	197
8.2.2.Contact between a sandwich plate and a spherical indenter .....	200
8.2.3.Impact Dynamics.....	200
8.2.4.Impact Damage .....	201
8.2.5.Strain rate effects.....	202
8.2.6.Experimental techniques .....	203
8.3.Quasi-Static tests .....	204
8.3.1.Uniaxial Compressive tests .....	204
8.3.2.Indentation tests .....	204
8.4.Dynamic tests	207
8.4.1.Uniaxial Compressive tests .....	207
8.4.2.Impact tests .....	208
8.5.Final remarks .....	214
References .....	215
Chapter IX .....	217
SUBCOMPONENTOPTIMIZATION AND VALIDATION .....	217
9.1.Introduction to framework activities .....	217
9.2.Literature review .....	217
9.3.Optimization procedure.....	219
9.3.1.Preliminary finite element analysis .....	221
9.3.2.Refined FE model.....	224
9.3.3.Stacking sequence optimization.....	228

9.4.Final Validation.....228

References ..... **Errore. Il segnalibro non è definito.**

CONCLUSION .....233

## **Chapter I**

### **INTRODUCTION**

#### **1.1. Historical overview**

Reviewers of the history of sandwich constructions seems to disagree on who was the first person to publish a description of the advantages of the concept of combining different materials as in a sandwich. It seems like, however, has occurred independently to many engineers at different time. Introduction

The concept behind sandwich constructions is relatively simple and has been exploited in the design of common I-beams. The concept developed from consideration of the most materially efficient method of providing a high-stiffness structure, having as much material stiffness located as far from the neutral axis of bending as possible. Sandwich structure achieves this by bonding high-density, high-strength facesheets (or skins) to either side of a low density core material. This structure is ideally suited to applications requiring high stiffness-to-weight ratios, such as aircraft structures.

However, it was the invention and widespread acceptance of structural adhesives in England and the United State in the 1930's that prepared the way for widespread application of bonded sandwich panels. The Mosquito aircraft, produced in England during the Second World War, is often quoted as the first major applications to incorporate sandwich panels.

Military interests have speeded up the development of sandwich constructions especially in the aircraft and marine industry. Today, in high-performance applications, sandwich structures are extensively used on both primary load carrying area and aerodynamic control surfaces (e.g. flaps, spoilers) to achieve maximum weight savings and provide more efficient features.

New challenges in material and manufacturing fields allow the development of sandwich configurations in a wide range of less spectacular applications such as ground transportation vehicle (e.g. trains, buses) and building constructions.

In particular, research developments on both fiber reinforced composite and cellular materials are currently empathizing the layered and multi-material characteristics of a sandwich structure. The unique properties of honeycomb and foam materials, such as the superior mechanical properties of fiber reinforced composite materials over conventional material, may be specified and combined to produce cost-effective, lightweight components of relatively complex geometries and to offer a large number of optimization alternative (e.g. thermal insulation, acoustic damping, energy absorption from impact and stiffness optimization).

## **1.2. Research purpose**

Transportation industry is currently working to accommodate the conflicting requirements of both environmental legislation, and customer demands for greater performance and more luxury and safety features, by developing a lightweight, and therefore essentially, energy-efficient vehicle. A reduction in structural weight of one large component usually triggers positive synergy effects for other parts of the transportation vehicle. For example, a reduction of the mass of a vehicle body could lead to weight savings in the traction system, suspension, brakes and other subsystems.

In the present work, composite sandwich components, that perfectly match the challenging demands of lightweight and more customized structures, have

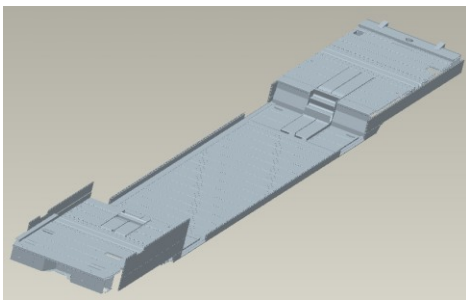
been characterized and designed as a roof panels of a railway vehicle (Fig. 1.2). The activity, herein presented, has been developed within Innovation Project PIA N.C01/0486/P between the Firema Transporti spa and the Department of Structural Engineering of the University of Napoli Federico II [-].



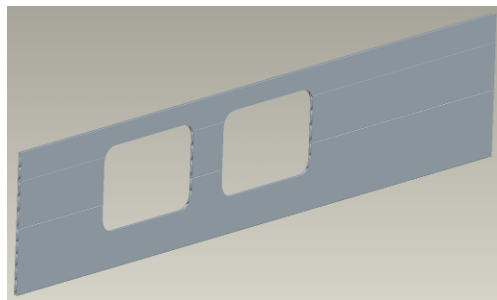
**Figure 1.1.** The train investigated into the study.

The Firema railway vehicle body actually consists by four different extruded aluminum modules (underframe; side body; front body; roof) as shown in Fig. 1.2. Extruded aluminum components are routinely employed in the body structures of railway vehicle in substitution of conventional steel monocoque components.

**Underframe**



**Side body**



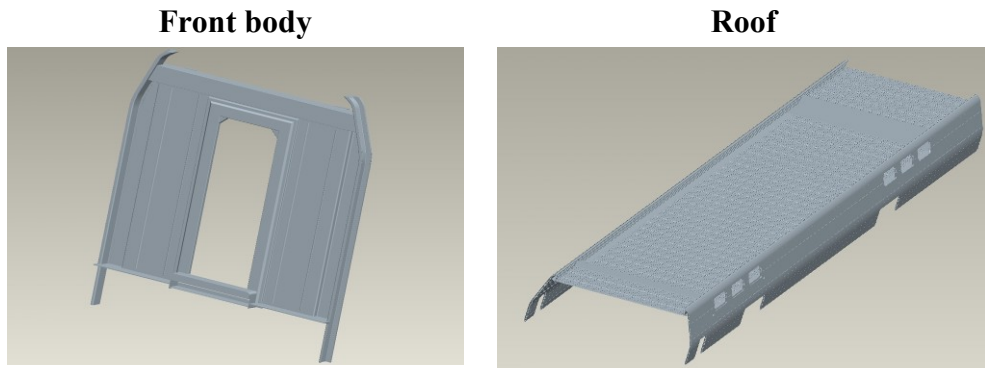


**Figure 1.2.** Extruded aluminum modules of the Firema train.

The roof modulus, object of the present work, is composed by two longitudinal roof side rails transversally connected by roof panels. Both the roof components are made of extruded aluminum structures and are joined through welding techniques (Fig. 1.3).

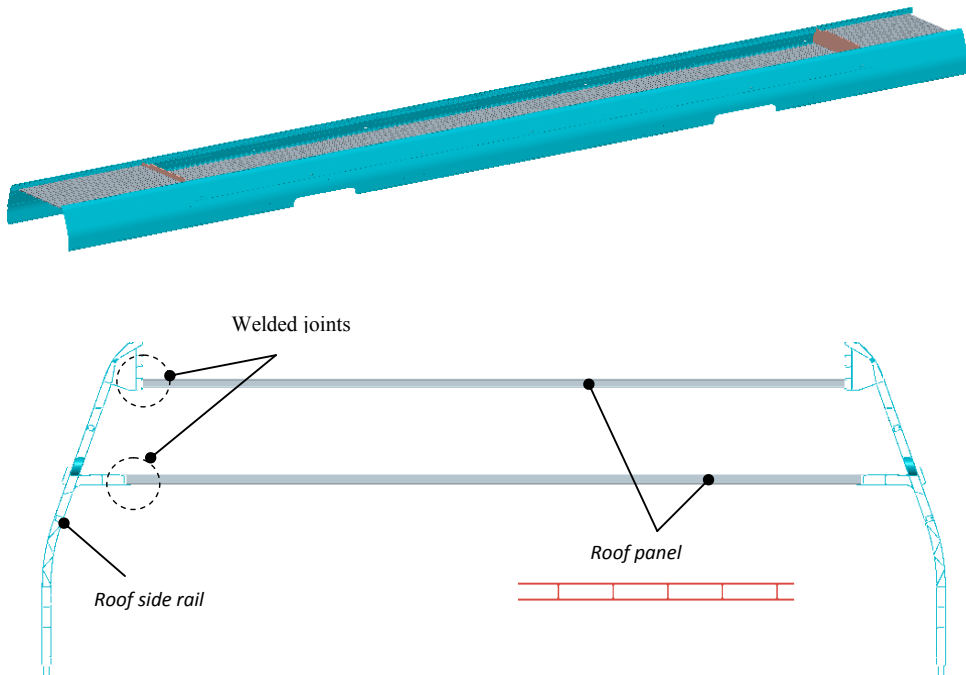


**Figure 1.3.** Extruded Aluminum roof structures of investigated train.

The main innovations introduced by the project is the use of phenolic impregnated sandwich structures, expressly manufactured for the transportation industry, to substitute the aluminum roof panels.

However, the use of fiber reinforced composite materials presents a significant challenge with respect to the methods of joining to be used in body fabrication. At this aim the project provides the characterization of potential joining techniques available to the railway industry involving both composite and aluminum components..

In the present work, the most critical issue related to the design and assessment of composite sandwich structures are discussed and analyzed in a multiscale procedure.

### **1.3. Multiscale procedure and research outline**

It is well known that the characterization of the strength and stiffness of composite structures is complicated by the very large number of variables involved. The situation is, of course, considerably worse with regards to the behavior of composite sandwich structures since, in addition to the material variables, parameters related to the peculiar morphology of a sandwich configuration shall be take into account. The assessment of the global behavior and local stress fields of sandwich structures depends on the material properties of the constituents (skins, core, and adhesive if involved), geometric dimensions, and type of loading. Analysis of this behavior, obtained by means of both analytical and numerical tools, is difficult because the intrinsic complexity of the multilayered configurations and the complex interaction of failure modes.

*Chapter II* and *III* give an accurate review on the mechanical behavior, in terms of the mechanisms of deformation and failure, of sandwich material and sandwich structures respectively.

The development of multifunctional design tools, integrating structural and functional features, enables a next step toward the exploitation of the

composite sandwich benefits. The proposed flow chart (Fig. 1.4) has been developed using knowledge-based procedure for the optimal stiffness design of composite sandwich structures under some classified design rules

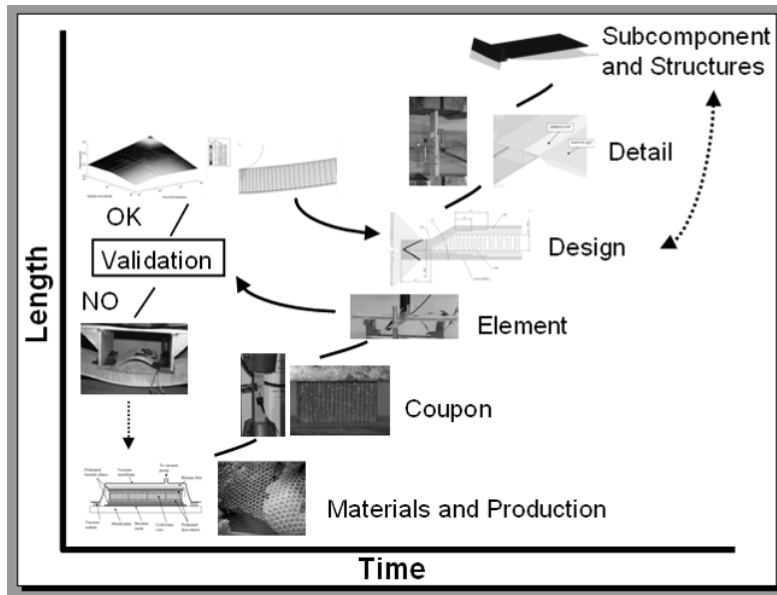


**Figure 1.4: Multiscale procedure for the design and optimization of sandwich structures.**

It starts from the choice of sandwich materials and manufacturing processes as functions of structural requirements, cost and quality considerations and technological flexibility.

The properties of both cellular solids and fiber reinforced composite display a wide range of characteristics depending on the choice of material and specific configuration. The selection of both a specific honeycomb or foam core and fiber reinforced composite skin for a particular engineering application is guided by models which describe their mechanical behavior in terms of the mechanisms of deformation and failure.

The advancements of the transportation industry from mass production to mass customization is based on the need for more customized vehicle to be produced, providing many variants, with the use of fewer resources and materials, in the shortest time possible. The selection of the skin and core materials in engineering design is primarily influenced by structural and

functional requirements, whereas increased complexity in the structural assembly, requires a holistic perspective of the main manufacturing attributes that need to be considered when manufacturing decisions are taken.

**Chapter IV** provides a description of the rail vehicle design criteria and the characteristics of the selected materials and manufacturing process.

The analysis of composites sandwich structures requires both experimental independent characterization of material properties and experimental verification of the analysis and the manufacturing process. The propose flow chart underlines that experimental characterization can be do on several scales with the following major objectives: (a) characterization of basic material properties for use as input in structural design and analysis; (b) investigation and verification of both analytical/numerical prediction and the curing procedure with particular emphasis on the failure modes; (c) experimental stress and failure analysis involving special geometrical, loading, and environmental conditions (e.g. fatigue, impact loading, hygrothermal aging, joints).

**Chapter V** addresses the experimental characterization of selected materials and sandwich configurations. Both analytical and numerical tools are compared with experimental evidences to validate the curing process and material combinations. A preliminary design phase is also involved in the present step to define the better material combination.

A further step is, therefore, required to identify a new combination of thickness which simultaneously satisfies the strength/stiffness and minimum weight requirements.

At this point can start the second, more sophisticated phase of the procedure, usually more demanding in terms of time, due to the need of a careful evaluation of the structure strength after considering the local effects.

In the present case, based on the selected applications, the following three problems are analyzed: (a) the joints between the new composite sandwich roof and the vehicle structures; (b) the durability in term of environmental conditionings; (c) the in service impact events.

Degradation and failure of transportation structures frequently initiate at the joint; therefore, adequacy of joint design exerts strong influence on safety, durability and reliability. The joints are responsible for the majority of vehicle fatigue cracking issues, so the fatigue life of joints both in metallic or composite applications is a topic of primary importance in the structural design. In addition, the use of composite structures presents a significant challenge respect to the traditional techniques of joining to be used in vehicle assembly. Joining of composite structures can be achieved through the use of mechanical, adhesive bonded or hybrid (mechanical/bonded) joints instead of welding joints that are common used in steel and aluminum metal body vehicle.

*Chapter VI* addresses the experimental characterization of joint techniques for the selected materials. It allows to compare the relative benefit and limitation of each technique and to derive the allowable design properties to be use in the assessment procedure.

The durability of composites, in addition to being dependent on loading conditions, is strongly dependent on the environmental conditions, in terms of the specific combinations of temperature, relative humidity, exposure to electro-magnetic radiation, to solvents, acid and alkaline conditions and of their (cyclic) evolution during time. These effects are, in general, peculiar to the polymeric matrix as well as the polymer-fiber interaction and are linked to a wide variety of phenomena that can ultimately lead, for example, to swelling or even to the dissolution of the polymeric matrix.

Since the degradation process of a composite sandwich structure depends on the environmental conditions, type of skins and core material, and production process, it is therefore necessary to evaluate the mechanical properties through accelerated ageing tests in order to predict long-term performances of sandwich composites and to determine the correlation between mechanical damage and aging due to different environmental factors..

In addition to the aforementioned issues, in order to reliably predict the structural safety of composite sandwich structures, understanding the adverse effect of in-service impact events (e.g. impact and penetration damage) has

become important in the transportation industry. In composite structures, impacts create internal damage that often cannot be detected by visual inspection. This internal damage can cause severe reductions in strength and can grow under load. Therefore the effects of foreign objects impacts on composite structures must be understood, and proper measures should be taken in the design process to account for these expected events.

Since the analytical models of these aspects are largely empirical in nature, the procedure is predominately based on experimentally obtained data. *Chapters VII and VIII* reports the experimental activity involved in the case of study. They provide the experimental correlation between mechanical properties and aging due to different environmental factors, and the characterization of quasi static and dynamic response of the selected sandwich materials and structures respectively.

Grow up on the scale, final optimization and assessment of structural integrity can be carried out.

The optimization can be achieved by changing the values of certain design variables in order to minimize the objective function while at the same time satisfying certain behavioral constraints. The optimization procedures are extensively automated whereby iterative finite element solutions are executed under the control of a software suite containing information on the optimization parameters, objective functions and constraints.

The final assessment may be evaluated by means of finite element simulation; and/or few benchmark tests and/or nondestructive testing.

The activity involved in the present step are presented in *Chapter VIII*. Due to the size of the problem, the optimization of the sandwich parameters and the finale assessment have been carried out on a panel by panel basis in order to avoid a large number of design variables at a given time.

## **Chapter II**

# ***MECHANICAL BEHAVIOR OF SANDWICH MATERIALS***

### **2.1. Common sandwich materials**

It is quite difficult to define, and probably does not exist, the best combination of constituents of a sandwich structure because the choice of materials depends not only on strength and stiffness requirements but also on process and cost considerations. In addition, other interesting properties of the constituents can have influence on the design choices, like for instance fire and environment resistance, thermal and acoustic insulation, vibration damping, buoyancy and damage tolerance.

Almost any structural material which is available in the form of thin sheet may be used to form the skins of a sandwich panels. In any efficient sandwich the skins are principally in direct tension and compression. Common materials for the sandwich skins are fiber-composite or wood laminates and thin aluminum sheets. In particular fiber-reinforced composite materials and laminates have been analyzed as sandwich skins due to their superior mechanical properties over conventional materials (high strength and stiffness to weight ratios). Composites are primarily specified because they can be used to produce cost-effective, lightweight components of relatively complex geometries that can be easily molded from composite

structures to perform the aerodynamic profile demanded by modern high performance applications.

A core material is required to perform two essential tasks: it must keep the skins the correct distance apart and it must not allow one face to slide over the other. In other words it must be rigid and strong in direct tension and compression (perpendicular to the faces) and in shear (in the planes perpendicular to the faces).

Cellular structures, with a wide range of materials and properties, have been used extensively to maximize the bending stiffness per unit density and as energy absorbers or cushions to resist external loads. Materials with a cellular structure are widespread they include natural materials such as wood and cork as well as man-made honeycombs and foams. Their cellular structure gives rise to unique properties which can be exploited in engineering design. The selection of a specific honeycomb or foam for a particular engineering application is guided by models which describe their mechanical behavior in terms of the cell geometry and the mechanisms of deformation and failure.

In the following paragraphs models for the mechanical behavior of fiber reinforced and cellular materials are described, The following model will be used as indispensable background to select the optimum design of packaging and of light-weight structural sandwich panels.

## **2.2. Fiber reinforced composite skin**

A structural composite is a material system consisting of two or more phases on a macroscopic scale, whose mechanical performance and properties are designed to be superior to those of the constituent materials acting independently. One of the phases is usually discontinuous, stiffer, and stronger and is called the reinforcement, whereas the less stiff and weaker phase is continuous and is called the matrix. Sometimes, because of chemical interactions or other processing effects, an additional distinct phase called an interphase exists between the reinforcement and the matrix.

The properties of a composite material depend on the properties of the constituents, their geometry, and the distribution of the phases. One of the most important parameters is the volume (or weight) fraction of reinforcement or fiber volume ratio, while the distribution of the reinforcement determines the homogeneity or uniformity of the material system.

Among many different types of reinforcements, continuous-fiber composites are the most efficient from the point of view of stiffness and strength.

The phases of the composite system play different roles, which depend on the type and application of the materials. In the case of high-performance structural composites, the continuous fiber reinforcement is the backbone of the material, which determines its stiffness and strength in the fiber direction. The matrix phase provides protection for the sensitive fibers, bonding, support, and local stress transfer from one fiber to another. The interphase, although small in dimension, can play an important role in controlling the failure mechanisms, failure propagation, fracture toughness and the overall stress-strain behavior to failure of the material.

### **2.2.1. Characteristic and configuration**

The continuous fibers are not always used as straight yarns, but they are often used in the form of woven fabrics or textiles. An orthogonal woven fabric consists of two set of interlaced yarns: the longitudinal direction of the fabric is called wrap and the transverse direction weft or fill. The various types or styles of fabric are characterized by the repeat pattern of the interlaced regions. In the plain weave, for example, each yarn is interlaced over every other yarn in the other direction, that is the smallest number of yarns involved in the repeat pattern in any direction is two; in the twill fabric, each yarn is interlaced over every third yarn in the other direction; in satin weaves each yarn is interlaced over every fourth, fifth, and so on, yarn in the other direction. In addition to the fiber yarn type and weave style, the behavior of fabric reinforcement in a composite is characterized by the fabric crimp, which is a measure of the yarn waviness. The crimp fraction decreases and

the drapeability of the fabric increases moving from plain to twill and multiharness satin weaves. Although woven fabrics are usually two-dimensional and have wrap and fill yarns normal to each other, it is possible to obtain fabrics with different yarn orientations and three dimensional weaves. In addition to woven fabrics, other possible forms of reinforcement include knitted, braided, and nonwoven mats.

A lamina, or ply, is a plane (or curved) layer of unidirectional fibers or woven fabric in a matrix. The lamina is an orthotropic material with principal material axes in the direction of the fibers (longitudinal), normal to the fibers in the plane of the lamina (in-plane-transverse), and normal to the plane of the lamina (Fig. 2.1a). These principal axes are designed as 1, 2 and 3, respectively. In the case of a woven fabric composite, the wrap and the fill directions are the in-plane 1 and 2 principal direction, respectively (Fig. 2.1b).

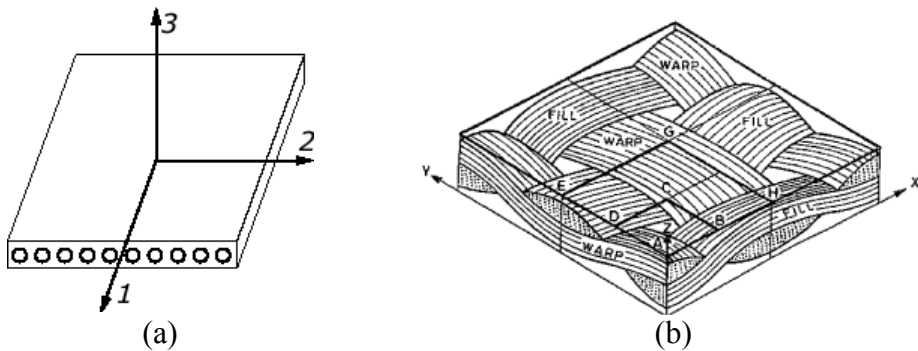


**Figure 2.1. Lamina and principal coordinate axes: (a) unidirectional reinforcement; (b) woven fabric reinforcement.**

A laminate is made up of two or more unidirectional laminae or plies stacked together at various orientations (Fig. 1.2).

The laminae (or ply, or layers) can be of various thickness and consist of different materials. Since the orientation of the principal material axes varies from ply to ply, it is more convenient to analyze laminates using a common fixed system or coordinates  $(x, y, z)$  as shown. The orientation of a given ply is given by the angle between the reference  $x$ -axis and the major principal material axis (fiber orientation or wrap direction) of the ply, measured in a counterclockwise direction on the  $x$ - $y$  plane.

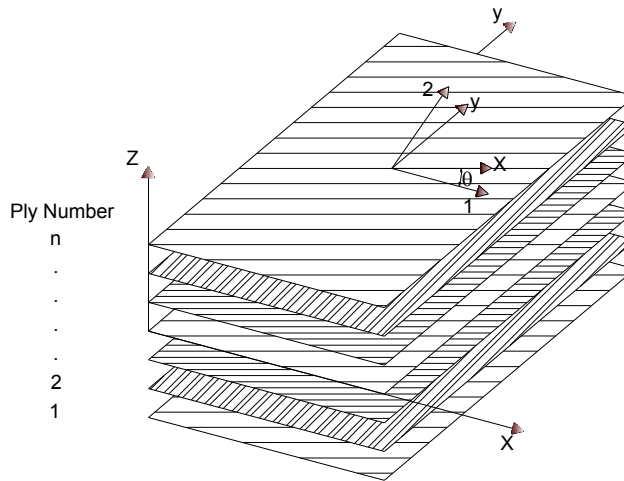


**Figure 2.2. Multidirectional laminate and reference coordinate system.**

Composite laminates are designed in a manner indicating the number, type, orientation, and stacking sequence of the plies. The configuration of the laminate indicating its ply composition is called *layup*; the configuration indicating, in addition to the ply composition, the exact location or sequence of the various piles, is called the *stacking sequence*.

### 2.2.2. Modeling the mechanical behavior of composites

Composite materials can be viewed and analyzed at different levels and on different scales, depending on the particular characteristics and behavior under consideration (Fig. 2.3).

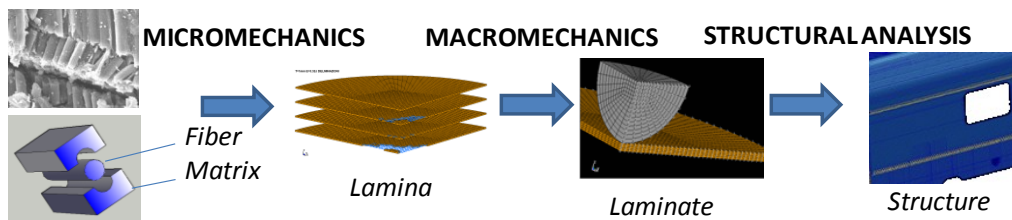


**Figure 2.3. Level of observation and types of analysis for composite materials.**

At the constituent level the scale of observation is on the order of the fiber diameter, particle size, or matrix interstices between reinforcement. *Micromechanics* is the study of the interactions of the constituents on the microscopic level. It deals with the state of deformation and stress in the

constituents and local failures, such as fiber failure (tensile, buckling, splitting), matrix failure (tensile, compressive, shear), and interface/interphase failure (debonding). Micromechanics is particularly important in the study of properties such as failure mechanisms and strength, fracture toughness, and fatigue life, which are strongly influenced by local characteristics that cannot be integrated or averaged. Micromechanics also allows for the prediction of average behavior at the lamina level as a function of constituent properties and local conditions.

At the lamina level it is usually the material homogeneous, albeit anisotropic, and use average properties in the analysis. This type of analysis is called *macromechanics* and considers the lamina as a quasi-homogeneous anisotropic material with its own average stresses and overall lamina strengths without reference to any particular local failure mechanisms. This approach, which assumes material continuity, can be applied in the study of the overall elastic, viscoelastic, or hygrothermal behavior of composite laminates and structures.

At the laminate level the macromechanical analysis is applied in the form of lamination theory dealing with overall behavior as a function of lamina properties and stacking sequence. Finally, at component or structural level, methods such as finite element analysis coupled with lamination theory may predict the overall behavior of the structures as well as the state of stress in each lamina.

### **2.2.3. Elastic behavior of composite lamina**

If the stress and strain at a generic location of fiber reinforced composite may be represented by the components of the tensor of stress  $\underline{\sigma}$  (Fig. 2.4) and strain  $\underline{\epsilon}$ , the mechanical behavior of a homogeneous, elastic, and anisotropic solid may be defined by 21 independent elastic constants as follows:

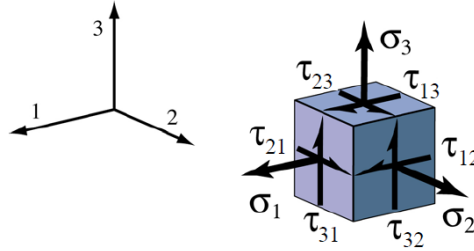


Figure 2.4. Representation of stresses for an infinitesimal element.

$$\underline{\sigma} = [C]\underline{\varepsilon} \Leftrightarrow \begin{Bmatrix} \sigma_1 \\ \sigma_2 \\ \sigma_3 \\ \tau_{23} \\ \tau_{31} \\ \tau_{12} \end{Bmatrix} = \begin{bmatrix} C_{11} & C_{12} & C_{13} & C_{14} & C_{15} & C_{16} \\ C_{12} & C_{22} & C_{23} & C_{24} & C_{25} & C_{26} \\ C_{13} & C_{23} & C_{33} & C_{34} & C_{35} & C_{36} \\ C_{14} & C_{24} & C_{34} & C_{44} & C_{45} & C_{46} \\ C_{15} & C_{25} & C_{35} & C_{45} & C_{55} & C_{56} \\ C_{16} & C_{26} & C_{36} & C_{46} & C_{56} & C_{66} \end{bmatrix} \begin{Bmatrix} \varepsilon_1 \\ \varepsilon_2 \\ \varepsilon_3 \\ \gamma_{23} \\ \gamma_{13} \\ \gamma_{12} \end{Bmatrix} \quad (2.1)$$

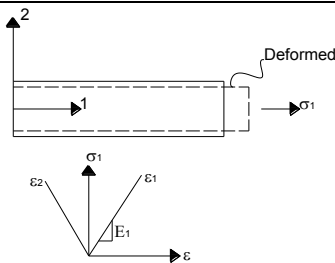
where  $[C]$  is the stiffness matrix. The complete characterization of the stiffness matrix would require the evaluation of the 21 constants by means of combinations of tensile and shear tests. The number of tests to be performed can significantly be reduced if the material has some degree of symmetry, a circumstance that occurs in a majority of fiber-composite materials having engineering interest.

In the case of an orthotropic material the stress-strain relations in general have the same form expressed above. However the number of independent elastic constants is reduced to nine. An orthotropic material is called transversely isotropic when one of its principal planes is a plane of isotropy, that is, at every point there is a plane on which the mechanical properties are the same in all directions. Many unidirectional composites may be considered transversely isotropic; in this case, the independent elastic constants reduce from 21 to only 5 and the stiffness matrix becomes:

$$\begin{Bmatrix} \sigma_1 \\ \sigma_2 \\ \sigma_3 \\ \tau_{23} \\ \tau_{31} \\ \tau_{12} \end{Bmatrix} = \begin{bmatrix} C_{11} & C_{12} & C_{13} & 0 & 0 & 0 \\ C_{12} & C_{22} & C_{23} & 0 & 0 & 0 \\ C_{13} & C_{23} & C_{33} & 0 & 0 & 0 \\ 0 & 0 & 0 & C_{44} & 0 & 0 \\ 0 & 0 & 0 & 0 & C_{55} & 0 \\ 0 & 0 & 0 & 0 & 0 & C_{66} \end{bmatrix} \begin{Bmatrix} \varepsilon_1 \\ \varepsilon_2 \\ \varepsilon_3 \\ \gamma_{23} \\ \gamma_{13} \\ \gamma_{12} \end{Bmatrix} \quad (2.2)$$

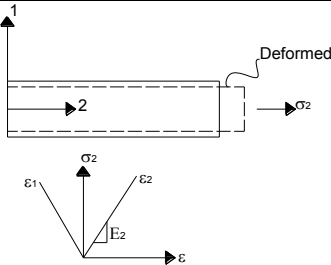
The stress-strain relations acquire more physical meaning when expressed in terms of the familiar engineering constants: moduli and Poisson's ratios. Relations between mathematical and engineering constants are obtained by conducting imaginary elementary experiments (Fig. 2.5).

**TEST 1:** Apply stress in 1-dir.



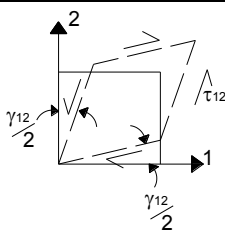
$\sigma_1$  = applied stress  
 $\varepsilon_1$  = axial strain  
 $\varepsilon_2$  = transversal strain  
 $-\varepsilon_2/\varepsilon_1 = \nu_{12}$  major Poisson's ratio  
 $\sigma_1/\varepsilon_1 = E_1$  Longitudinal Young's Modulus

**TEST 2:** Apply stress in 2-dir.



$\sigma_2$  = applied stress  
 $\varepsilon_2$  = axial strain  
 $\varepsilon_1$  = transversal strain  
 $-\varepsilon_1/\varepsilon_2 = \nu_{21}$  major Poisson's ratio  
 $\sigma_2/\varepsilon_2 = E_2$  Longitudinal Young's Modulus

**TEST 3:** Apply shear stress in 1-2 plane



$\tau_{12}$  = applied stress  
 $\gamma_{12}$  = total angle change (rad)  
 $\tau_{12}/\gamma_{12} = G_{12}$  in plane shear modulus

Figure 2.5. Elementary experiments for obtaining relations between mathematical and engineering constants.

The compliance matrix  $[S]$ , defined as the matrix inverse of the stiffness matrix  $[C]$ , can be expressed as a function of the engineering constants as follows:

$$[S] = \begin{bmatrix} 1/E_1 & -\nu_{21}/E_2 & -\nu_{31}/E_3 & 0 & 0 & 0 \\ -\nu_{12}/E_1 & 1/E_2 & -\nu_{32}/E_3 & 0 & 0 & 0 \\ -\nu_{13}/E_1 & -\nu_{23}/E_2 & 1/E_3 & 0 & 0 & 0 \\ 0 & 0 & 0 & 1/G_{23} & 0 & 0 \\ 0 & 0 & 0 & 0 & 1/G_{13} & 0 \\ 0 & 0 & 0 & 0 & 0 & 1/G_{12} \end{bmatrix} \quad (2.3)$$

In most structural application, composite materials are used in the form of thin laminates loaded in the plane of the laminate. Thus, composite laminae (and laminates) can be considered to be under a condition of plane stress, with all stress components in the out of plane direction being zero. The orthotropic stress strain relations are reduced to:

$$\begin{Bmatrix} \sigma_1 \\ \sigma_2 \\ \tau_{12} \end{Bmatrix} = \begin{bmatrix} Q_{11} & Q_{12} & 0 \\ Q_{12} & Q_{22} & 0 \\ 0 & 0 & Q_{66} \end{bmatrix} \begin{Bmatrix} \varepsilon_1 \\ \varepsilon_2 \\ \gamma_{12} \end{Bmatrix} \quad (2.4)$$

$$\begin{Bmatrix} \varepsilon_1 \\ \varepsilon_2 \\ \gamma_{12} \end{Bmatrix} = \begin{bmatrix} S_{11} & S_{12} & 0 \\ S_{12} & S_{22} & 0 \\ 0 & 0 & S_{66} \end{bmatrix} \begin{Bmatrix} \sigma_1 \\ \sigma_2 \\ \tau_{12} \end{Bmatrix} \quad (2.5)$$

The relations above can be expressed in terms of engineering constants:

$$\begin{Bmatrix} \sigma_1 \\ \sigma_2 \\ \tau_{12} \end{Bmatrix} = \begin{bmatrix} \frac{E_1}{1-\nu_{12}\nu_{21}} & \frac{\nu_{21}E_1}{1-\nu_{12}\nu_{21}} & 0 \\ \frac{\nu_{21}E_1}{1-\nu_{12}\nu_{21}} & \frac{E_2}{1-\nu_{12}\nu_{21}} & 0 \\ 0 & 0 & G_{12} \end{bmatrix} \begin{Bmatrix} \varepsilon_1 \\ \varepsilon_2 \\ \gamma_{12} \end{Bmatrix} \quad (2.6)$$

$$\begin{Bmatrix} \varepsilon_1 \\ \varepsilon_2 \\ \gamma_{12} \end{Bmatrix} = \begin{bmatrix} \frac{1}{E_1} & -\frac{\nu_{12}}{E_1} & 0 \\ -\frac{\nu_{12}}{E_1} & \frac{1}{E_2} & 0 \\ 0 & 0 & \frac{1}{G_{12}} \end{bmatrix} \begin{Bmatrix} \sigma_1 \\ \sigma_2 \\ \tau_{12} \end{Bmatrix} \quad (2.7)$$

Noting that:

$$Q_{12} = Q_{21} = \frac{\nu_{21}E_1}{1-\nu_{12}\nu_{21}} = \frac{\nu_{12}E_2}{1-\nu_{12}\nu_{21}}; S_{12} = S_{21} = -\frac{\nu_{12}}{E_1} = -\frac{\nu_{21}}{E_2} \quad (2.8)$$

Thus, as far as in the in-plane stress-strain relations are concerned, a single orthotropic lamina can be fully characterized by four engineering independent constants: Young's moduli  $E_1$ ,  $E_2$ ; shear modulus  $G_{12}$ ; Poisson's ratio  $\nu_{12}$ .

Normally, the lamina principal axes (1, 2) do not coincide with the loading or reference axes ( $x$ ,  $y$ ) (Fig. 2.6).

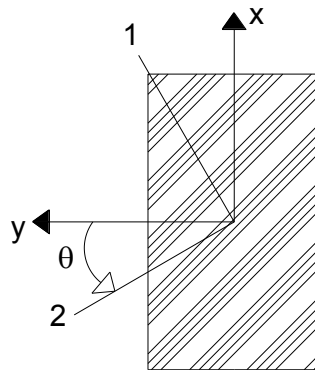


Figure 2.6. Illustration of loading and material axes.

The stress and strain components referred to the principal material axes (1, 2), can be expressed in terms of these referred to the loading axes (x, y) by the following relations:

$$\begin{Bmatrix} \sigma_x \\ \sigma_y \\ \tau_{xy} \end{Bmatrix} = [T]^{-1} \begin{Bmatrix} \sigma_1 \\ \sigma_2 \\ \tau_{12} \end{Bmatrix}; \begin{Bmatrix} \varepsilon_x \\ \varepsilon_y \\ \gamma_{xy}/2 \end{Bmatrix} = [T]^{-1} \begin{Bmatrix} \varepsilon_1 \\ \varepsilon_{12} \\ \gamma_{12}/2 \end{Bmatrix} \quad (2.9)$$

where  $[T]$  is the transformation matrix

$$[T] = \begin{bmatrix} \cos^2 \theta & \sin^2 \theta & 2 \cos \theta \sin \theta \\ \sin^2 \theta & \cos^2 \theta & -2 \cos \theta \sin \theta \\ -\cos \theta \sin \theta & \cos \theta \sin \theta & \cos^2 \theta - \sin^2 \theta \end{bmatrix} \quad (2.10)$$

The transformed stress-strain and strain-stress relations take the forms respectively:

#### Stress-strain

$$\begin{aligned} \begin{Bmatrix} \sigma_x \\ \sigma_y \\ \tau_{xy} \end{Bmatrix} &= [T]^{-1} \begin{Bmatrix} \sigma_1 \\ \sigma_2 \\ \tau_{12} \end{Bmatrix} = [T]^{-1} \begin{bmatrix} Q_{11} & Q_{12} & 0 \\ Q_{12} & Q_{22} & 0 \\ 0 & 0 & Q_{66} \end{bmatrix} \begin{Bmatrix} \varepsilon_1 \\ \varepsilon_2 \\ \gamma_{12} \end{Bmatrix} = \\ &= [T]^{-1} \begin{bmatrix} Q_{11} & Q_{12} & 0 \\ Q_{12} & Q_{22} & 0 \\ 0 & 0 & 2Q_{66} \end{bmatrix} \begin{Bmatrix} \varepsilon_1 \\ \varepsilon_2 \\ \gamma_{12}/2 \end{Bmatrix} = \\ &= [T]^{-1} \begin{bmatrix} Q_{11} & Q_{12} & 0 \\ Q_{12} & Q_{22} & 0 \\ 0 & 0 & 2Q_{66} \end{bmatrix} [T] \begin{Bmatrix} \varepsilon_x \\ \varepsilon_y \\ \gamma_{xy}/2 \end{Bmatrix} \end{aligned} \quad (2.11)$$

Where

$$[Q]_{xy} = [T]^{-1} [Q]_{12} [T]^T \Rightarrow \quad (2.12)$$

$$\begin{aligned} \begin{Bmatrix} \sigma_x \\ \sigma_y \\ \tau_{xy} \end{Bmatrix} &= [T]^{-1} \begin{bmatrix} Q_{11} & Q_{12} & 0 \\ Q_{12} & Q_{22} & 0 \\ 0 & 0 & 2Q_{66} \end{bmatrix} [T] \begin{Bmatrix} \varepsilon_x \\ \varepsilon_y \\ \gamma_{xy}/2 \end{Bmatrix} = \\ &= \begin{bmatrix} Q_{xx} & Q_{xy} & 2Q_{xs} \\ Q_{yx} & Q_{yy} & 2Q_{ys} \\ Q_{sx} & Q_{sy} & 2Q_{ss} \end{bmatrix} \begin{Bmatrix} \varepsilon_x \\ \varepsilon_y \\ \gamma_{xy}/2 \end{Bmatrix} \end{aligned}$$

### Strain-stress

$$\begin{aligned} \begin{Bmatrix} \varepsilon_x \\ \varepsilon_y \\ \gamma_{xy}/2 \end{Bmatrix} &= [T]^{-1} \begin{Bmatrix} \varepsilon_1 \\ \varepsilon_{12} \\ \gamma_{12}/2 \end{Bmatrix} = [T]^{-1} \begin{bmatrix} S_{11} & S_{12} & 0 \\ S_{12} & S_{22} & 0 \\ 0 & 0 & S_{66}/2 \end{bmatrix} \begin{Bmatrix} \sigma_1 \\ \sigma_2 \\ \tau_{12} \end{Bmatrix} = \\ &= [T]^{-1} \begin{bmatrix} S_{11} & S_{12} & 0 \\ S_{12} & S_{22} & 0 \\ 0 & 0 & S_{66}/2 \end{bmatrix} [T] \begin{Bmatrix} \sigma_x \\ \sigma_y \\ \tau_{xy} \end{Bmatrix} \end{aligned} \quad (2.13)$$

Where

$$\begin{aligned} [S]_{xy} &= [T]^{-1} [S]_{12} [T]^T \Rightarrow \\ \begin{Bmatrix} \varepsilon_x \\ \varepsilon_y \\ \gamma_{xy}/2 \end{Bmatrix} &= [T]^{-1} \begin{bmatrix} S_{11} & S_{12} & 0 \\ S_{12} & S_{22} & 0 \\ 0 & 0 & S_{66}/2 \end{bmatrix} [T] \begin{Bmatrix} \sigma_x \\ \sigma_y \\ \tau_{xy} \end{Bmatrix} = \\ &= \begin{bmatrix} S_{xx} & S_{xy} & S_{xs} \\ S_{yx} & S_{yy} & S_{ys} \\ S_{sx}/2 & S_{sy}/2 & S_{ss}/2 \end{bmatrix} \begin{Bmatrix} \sigma_x \\ \sigma_y \\ \tau_{xy} \end{Bmatrix} \end{aligned} \quad (2.14)$$

The strain-stress relations referred to the loading axes can be expressed in terms of engineering constants as following

$$\begin{Bmatrix} \varepsilon_x \\ \varepsilon_y \\ \gamma_s \end{Bmatrix} = \begin{bmatrix} \frac{1}{E_x} & -\frac{\nu_{yx}}{E_y} & \frac{\eta_{sx}}{G_{xy}} \\ -\frac{\nu_{xy}}{E_x} & \frac{1}{E_y} & \frac{\eta_{sy}}{G_{xy}} \\ \frac{\eta_{xs}}{E_x} & \frac{\eta_{ys}}{E_y} & \frac{1}{G_{xy}} \end{bmatrix} \begin{Bmatrix} \sigma_x \\ \sigma_y \\ \tau_{xy} \end{Bmatrix} \quad (2.15)$$

where  $\eta_{sx}$  and  $\eta_{sy}$  are the shear coupling coefficients, that can be calculated as the ratios of the normal strains to the shear strains for the applied pure shear loading.

A computational procedure for calculation of transformed elastic constants is illustrated by the suggested flowchart (Fig. 2.7). It is assumed that the input consists of the basic engineering constants referred to the principal material axes of the lamina and obtained from characterization tests. Then, reduced principal compliance  $[S]_{12}$  and stiffness  $[Q]_{12}$  matrix can be calculated. The transformation relations are used to calculate the transformed lamina compliance  $[S]_{xy}$  and stiffness  $[Q]_{xy}$ . Finally the transformed engineering constants are evaluated using the relations between engineering constants and compliances.

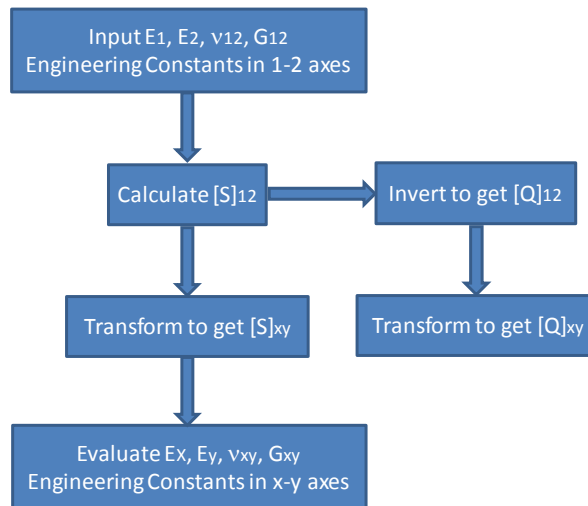


**Figure 2.7. Flow chart for determination of transformed elastic constants of composite lamina.**

#### 2.2.4. Strength of composite lamina

From the macromechanical point of view, the strength of lamina is an anisotropic property, that is, it varies with orientation. A lamina may be characterized by a number of basic strength parameters referred to its principal material direction in a manner analogous to the stiffness parameters defined before. In particular, for in-plane loading, a lamina may be characterized by five strength parameters: longitudinal tensile and compressive strengths  $F_{1t}$  and  $F_{1c}$ ; the transverse tensile and compressive strengths  $F_{2t}$  and  $F_{2c}$ ; the in-plane shear strength  $F_{66}$ . Four additional lamina strength parameters, which are relevant in three-dimensional analysis, are the out of plane or interlaminar tensile  $F_{3t}$ , compressive  $F_{3c}$ , and shear strengths  $F_{23}$  and  $F_{13}$ . At the same way, for in-plane loading, a lamina may be characterized by five strain parameters: ultimate longitudinal/transverse tensile/compressive strain  $\varepsilon^u_{1t}$ ,  $\varepsilon^u_{1c}$ ,  $\varepsilon^u_{2t}$ ,  $\varepsilon^u_{2c}$ ; ultimate in-plane shear strain  $\gamma^u_{12}$ .

Macromechanical failure theories for composites have been proposed by extending and adapting isotropic failure theories to account for the anisotropy in stiffness and strength of the composite. Lamina failure theories can be classified in the following three groups: (i) *limit or noninteractive theories*, in which specific failure modes are predicted by comparing individual lamina stresses or strains with corresponding strengths or ultimate strains – maximum stress and maximum strain criterion; (ii) *interactive theories* (e.g. the Tsai-Hill and Tsai-Wu criterion), in which all stresses components are included in one expression. Overall failure is predicted without reference to particular failure modes; (iii) *partially interactive or failure-mode-based theories* (e.g., the Hashin-Rotem and Puck theories), where separate criteria are given for fiber and interfiber (matrix or interface) failures.

The above theories are based on the assumptions of homogeneity and linear stress-strain behavior to failure.

According to *maximum stress theory*, failure occurs when at least one stress component along one of the principal material axes exceeds the

corresponding strength in that direction. So the failure condition is expressed in the form of the following subcriteria:

$$\sigma_1 = \begin{cases} F_{1t} \Leftrightarrow \sigma_1 > 0 \\ -F_{1c} \Leftrightarrow \sigma_1 < 0 \end{cases}; \sigma_2 = \begin{cases} F_{2t} \Leftrightarrow \sigma_2 > 0 \\ -F_{2c} \Leftrightarrow \sigma_2 < 0 \end{cases}; |\tau_{12}| = F_{66} \quad (2.16)$$

According to the *maximum strain theory*, failure occurs when at least one of the strain components along the principal material axes exceeds the corresponding ultimate strain in that direction. It is expressed in the form of the following subcriteria:

$$\varepsilon_1 = \begin{cases} \varepsilon_{1t}^u \Leftrightarrow \varepsilon_1 > 0 \\ -\varepsilon_{1c}^u \Leftrightarrow \varepsilon_1 < 0 \end{cases}; \sigma_2 = \begin{cases} \varepsilon_{2t}^u \Leftrightarrow \varepsilon_2 > 0 \\ -\varepsilon_{2c}^u \Leftrightarrow \varepsilon_2 < 0 \end{cases}; |\gamma_{12}| = \gamma_{12}^u \quad (2.17)$$

The maximum stress theory is more applicable for the brittle modes of failure of material, closer to transverse and longitudinal tension, and does not take into account any stress interaction under a general biaxial state of stress. Whereas the maximum strain theory allows for some interaction of stress components due to Poisson's ratio effects.

The deviatoric or distortional energy has been proposed by many investigators (e.g. von Mises, Hencky, Nadai) in various forms as failure criterion for isotropic ductile metals. Hill [] modified this criterion for the case of ductile metals with anisotropy and proposed the following form:

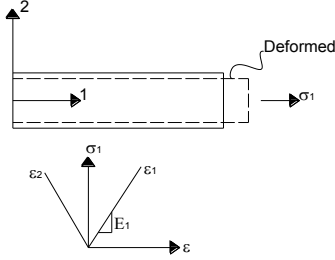
$$A\sigma_1^2 + B\sigma_2^2 + C\sigma_1\sigma_2 + D\tau_{12}^2 = 1 \quad (2.18)$$

where  $A, B, C$ , and  $D$  are material parameters characteristic of the current state of anisotropy. Azzi and Tsai [] adapted this criterion to orthotropic composite materials: the Hill parameters can be related to the basic strength parameters of the lamina by conducting real or imaginary elementary experiments as previously (Fig.2.8).

Substituting the values of the parameters into the Hill equation, it is obtained the *Tsai-Hill criterion* for a two-dimensional state of stress:

$$\frac{\sigma_1^2}{F_1^2} + \frac{\sigma_2^2}{F_2^2} - \frac{\sigma_1\sigma_2}{F_1^2} + \frac{\tau_{12}^2}{F_{66}^2} = 1 \quad (2.19)$$

**TEST 1:** Apply stress in 1-dir.



$$A\sigma_1^2 + B\sigma_2^2 + C\sigma_1\sigma_2 + D\tau_{12}^2 = 1 \Rightarrow A\sigma_1^2 = 1$$

$$\text{For } \sigma_1 > 0 \Rightarrow \sigma_1 = F_{1t} \Rightarrow A = 1/F_{1t}^2$$

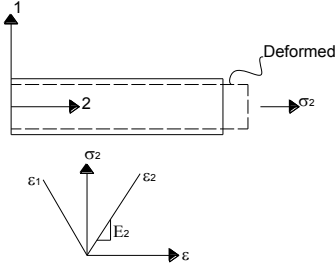
$$\text{For } \sigma_1 < 0 \Rightarrow \sigma_1 = F_{1c} \Rightarrow A = 1/F_{1c}^2$$

$\sigma_1$  = applied stress

$F_{1t}$  = Max tensile  $\sigma_1$

$F_{1c}$  = Max compressive  $\sigma_1$

**TEST 2:** Apply stress in 2-dir.



$$A\sigma_1^2 + B\sigma_2^2 + C\sigma_1\sigma_2 + D\tau_{12}^2 = 1 \Rightarrow B\sigma_2^2 = 1$$

$$\text{For } \sigma_2 > 0 \Rightarrow \sigma_2 = F_{2t} \Rightarrow B = 1/F_{2t}^2$$

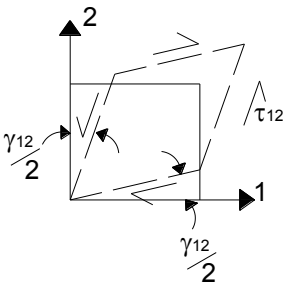
$$\text{For } \sigma_2 < 0 \Rightarrow \sigma_2 = F_{2c} \Rightarrow B = 1/F_{2c}^2$$

$\sigma_2$  = applied stress

$F_{2t}$  = Max tensile  $\sigma_2$

$F_{2c}$  = Max compressive  $\sigma_2$

**TEST 3:** Apply shear stress in 1-2 plane



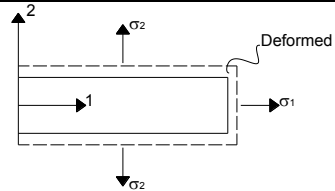
$$A\sigma_1^2 + B\sigma_2^2 + C\sigma_1\sigma_2 + D\tau_{12}^2 = 1 \Rightarrow D\tau_{12}^2 = 1$$

$$\Rightarrow \tau_{12} = F_{66} \Rightarrow D = 1/F_{66}^2$$

$\tau_{12}$  = applied stress

$F_{66}$  = max  $\tau_{12}$

**TEST 4:** Apply Biaxial 1-2 plane



$$\sigma_1 = \sigma_2 \neq 0 \Rightarrow \tau_{12} = 0$$

Failure is governed by  $\sigma_2$

$$\text{For } \sigma_1 = \sigma_2 > 0 \Rightarrow C = -1/F_{1t}^2$$

$$\text{For } \sigma_1 = \sigma_2 < 0 \Rightarrow C = -1/F_{1c}^2$$

Figure 2.8. Elementary experiments for obtaining relations between Hill parameters and the basic strength parameters.

The Tsai-Hill failure theory is expressed in terms of single criterion instead of the multiple subcriteria required in the maximum stress and maximum strain theories. The Tsai-Hill theory, moreover, allows for considerable interaction among the stress components. One disadvantage, however, is that it does not distinguish directly between tensile and compressive strengths.

Tsai and Wu proposed a modified tensor polynomial theory by assuming the existence of a failure surface in the stress space. In contracted notation it takes the form:

$$\sum_{i=1,2,\dots,6} f_i \sigma_i + \sum_{i=1,2,\dots,6} \sum_{j=1,2,\dots,6} f_{ij} \sigma_i \sigma_j = 1 \quad (2.20)$$

Assuming transverse isotropy with 3-2 plane as the plane of isotropy, in a two-dimensional state of stress ( $\sigma_1, \sigma_2, \sigma_6$ ) the *Tsai-Wu criterion* is reduced to the following form:

$$f_1 \sigma_1 + f_2 \sigma_2 + f_{11} \sigma_1^2 + f_{22} \sigma_2^2 + 2f_{12} \sigma_1 \sigma_2 + f_{66} \tau_{12}^2 = 1 \quad (2.21)$$

The coefficients of the general quadratic criterion can be related to the basic strength parameters of the lamina by applying elementary loading to the lamina (Fig. 2.9).

The safety factor  $S_f$  for a given two-dimensional state of stress is a multiplier that is applied to all stress components to produce a critical of failure state as defined by the selected failure criterion. Introducing the safety factor, the Tsai-Wu criterion has the form:

$$\left( f_1 \sigma_1 + f_2 \sigma_2 \right) S_f + \left( f_{11} \sigma_1^2 + f_{22} \sigma_2^2 + 2f_{12} \sigma_1 \sigma_2 + f_{66} \tau_{12}^2 \right) S_f^2 = 1 \quad (2.22)$$

or

$$BS_f + AS_f^2 = 1 \quad (2.23)$$

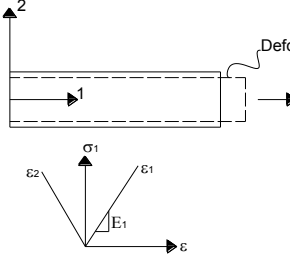
Where

$$A = f_{11} \sigma_1^2 + f_{22} \sigma_2^2 + 2f_{12} \sigma_1 \sigma_2 + f_{66} \tau_{12}^2; B = f_1 \sigma_1 + f_2 \sigma_2 \quad (2.24)$$

Thus, the problem of determining the safety factor is reduced to that of solving the above quadratic equation. The roots are:

$$S_{fa} = \frac{-B + \sqrt{B^2 + 4A}}{2A}; S_{fb} = \left| \frac{-B - \sqrt{B^2 + 4A}}{2A} \right| \quad (2.25)$$

**TEST 1:** Apply stress in 1-dir.

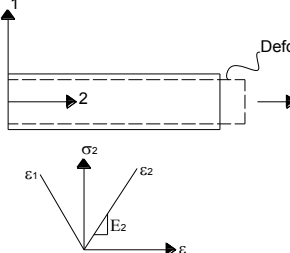


$$f_1\sigma_1 + f_2\sigma_2 + f_{11}\sigma_1^2 + f_{22}\sigma_2^2 + 2f_{12}\sigma_1\sigma_2 + f_{66}\tau_{12}^2 = 1$$

$$\begin{cases} \text{For } \sigma_1 > 0 \Rightarrow f_1F_{1t} + f_{11}F_{1t}^2 = 1 \\ \text{For } \sigma_1 < 0 \Rightarrow -f_1F_{1c} + f_{11}F_{1c}^2 = 1 \end{cases} \Rightarrow \begin{cases} f_1 = \frac{1}{F_{1t}} - \frac{1}{F_{1c}} \\ f_{11} = \frac{1}{F_{1t}F_{1c}} \end{cases}$$

$\sigma_1$ =applied stress  
 $F_{1t}$ =Max tensile  $\sigma_1$   
 $F_{1c}$ =Max compressive  $\sigma_1$

**TEST 2:** Apply stress in 2-dir.

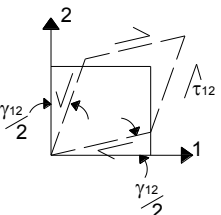


$$f_1\sigma_1 + f_2\sigma_2 + f_{11}\sigma_1^2 + f_{22}\sigma_2^2 + 2f_{12}\sigma_1\sigma_2 + f_{66}\tau_{12}^2 = 1$$

$$\begin{cases} \text{For } \sigma_2 > 0 \Rightarrow f_2F_{2t} + f_{22}F_{2t}^2 = 1 \\ \text{For } \sigma_2 < 0 \Rightarrow -f_2F_{2c} + f_{22}F_{2c}^2 = 1 \end{cases} \Rightarrow \begin{cases} f_{21} = \frac{1}{F_{2t}} - \frac{1}{F_{2c}} \\ f_{22} = \frac{1}{F_{2t}F_{2c}} \end{cases}$$

$\sigma_2$ =applied stress  
 $F_{2t}$ =Max tensile  $\sigma_2$   
 $F_{2c}$ =Max compressive  $\sigma_2$

**TEST 3:** Apply shear stress in 1-2 plane

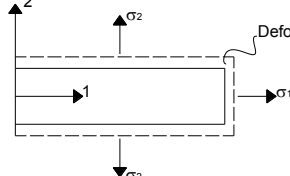


$$f_1\sigma_1 + f_2\sigma_2 + f_{11}\sigma_1^2 + f_{22}\sigma_2^2 + 2f_{12}\sigma_1\sigma_2 + f_{66}\tau_{12}^2 = 1$$

$$\Rightarrow \tau_{12} = F_{66} \Rightarrow f_{66} = 1/F_{66}^2$$

$\tau_{12}$ =applied stress  
 $F_{66}$ =max  $\tau_{12}$

**TEST 4:** Apply Biaxial 1-2 plane



$$f_{12} \cong -\frac{1}{2} \sqrt{f_{11}f_{22}}$$

Figure 2.9. Elementary experiments for obtaining relations between Tsai-Wu parameters and the basic strength parameters.

The Tsai-Wu failure criterion in two dimension has several considerable features: (i) like Tsai-Hill criterion, it is expressed in term of a single criterion, instead of six subcriteria required in the maximum stress and maximum strain theories; (ii) the stress interaction terms can be treated as independent material properties determined by appropriate experiments, unlike the Tsai-Hill theory where the interaction terms are fixed as functions of the other terms; (iii) the theory, through its linear terms, account for the differences between tensile and compressive strength.

The failure criterion is operationally simple and readily amenable to computational procedure. The suggested flowchart is illustrated in (Fig. 1.9). It consists of the following step: (1) enter the given stress components referred to the  $x$ - $y$  coordinate system; (2) calculate the stress components referred to the principal material direction using transformation relations; (3) enter the basic lamina strength for the material; (4) compute the Tsai-Wu coefficients; (5) Compute coefficients of the quadratic expression; (6) obtain the safety factors for actual and reversed (in sign) state of stress; (7) obtain transformed strength components.

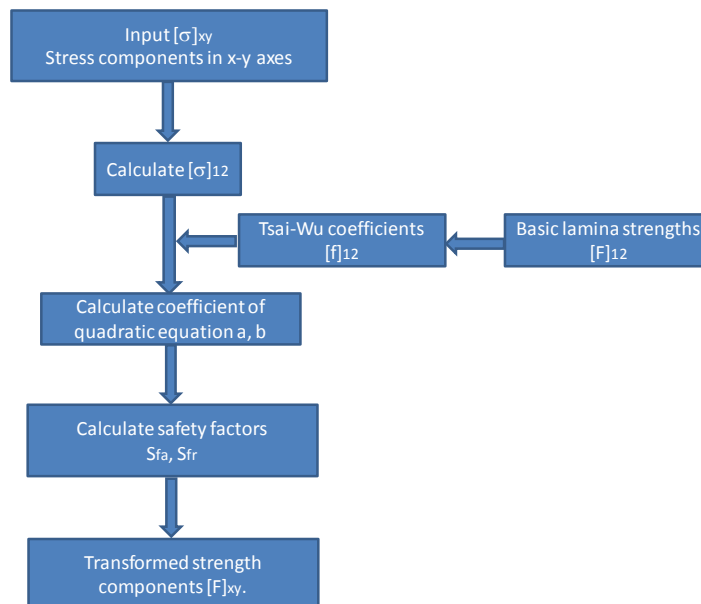


**Figure 2.10. Flowchart for computation of safety factors and transformed lamina strengths based on Tsai-Wu criterion**

### 2.2.5. Elastic behavior of composite laminates

Classical lamination theory predicts the behavior of the laminate as function of properties and stacking sequence of the individual layers. It is based on the following assumptions:

- ✓ Each layer (lamina) of the laminate is quasi-homogenous and orthotropic;
- ✓ The laminate and its layers are in the state of plane stress;
- ✓ All displacements are small compared with the thickness of the laminate;
- ✓ Displacements are continuous throughout the laminate;
- ✓ In-plane displacements vary linearly through the thickness of the laminate;
- ✓ Transverse shear strains and transverse normal strain are zero;
- ✓ Strain-displacement and stress-strain relations are linear.

Figure 2.11 shows a section of the laminate normal to the  $y$ -axis before and after deformation. The  $x$ - $x$  plane is equidistant from the top and bottom surface of the laminate: *midplane* or *reference plane*.

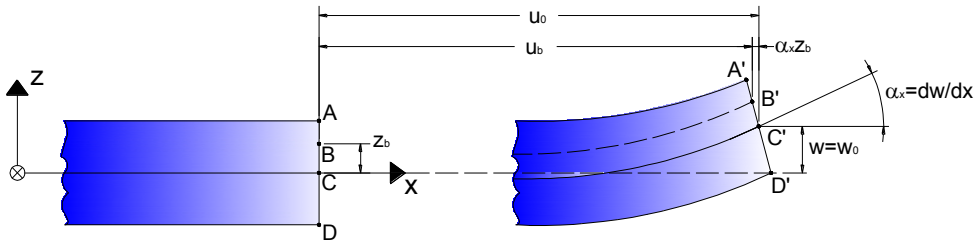


**Figure 2.11. Laminates section before and after deformation.**

It is possible relate the strains at any point in the laminate to the reference plane strains  $[\varepsilon^0]_{xy}$  and the laminate curvatures  $[\kappa]_{xy}$  as follows:

$$\begin{Bmatrix} \varepsilon_x \\ \varepsilon_y \\ \gamma_{xy} \end{Bmatrix}_B = \begin{Bmatrix} \varepsilon_x^0 \\ \varepsilon_y^0 \\ \gamma_{xy}^0 \end{Bmatrix} + z_B \begin{Bmatrix} \kappa_x \\ \kappa_y \\ \kappa_{xy} \end{Bmatrix} \quad (2.26)$$

Consider an individual layer  $B$  in a multidirectional laminate whose midplane is at distance  $z_B$  from the laminate reference plane, the stresses for this layer referred to  $x$ - $y$  axes are:

$$\begin{Bmatrix} \sigma_x \\ \sigma_y \\ \tau_{xy} \end{Bmatrix} = \begin{bmatrix} Q_{xx} & Q_{xy} & Q_{xs} \\ & Q_{yy} & Q_{ys} \\ & & Q_{ss} \end{bmatrix}_B \left\{ \begin{Bmatrix} \varepsilon_x^0 \\ \varepsilon_y^0 \\ \gamma_{xy}^0 \end{Bmatrix} + z_B \begin{Bmatrix} \kappa_x \\ \kappa_y \\ \kappa_{xy} \end{Bmatrix} \right\} \quad (2.27)$$

Figure 2.12 shows the linear strain variation and discontinuous stress variation in multidirectional laminate.

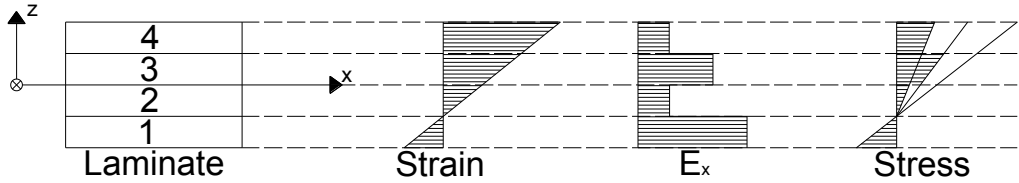


Figure 2.12. Illustration of linear strain variation and discontinuous stress variation in multidirectional laminate.

The stresses acting on a layer of a laminate can be replaced by resultant forces and moments, thus in the case of a multidirectional laminate the total force and moment resultants can be obtained by summing the effects for all layers. For the  $n$ -ply laminate, the force and moment resultants can be expressed as:

$$\begin{Bmatrix} N_x \\ N_y \\ N_{xy} \end{Bmatrix} = \int_{-1/2}^{1/2} \begin{Bmatrix} \sigma_x \\ \sigma_y \\ \tau_{xy} \end{Bmatrix} dz = \sum_{k=1}^n \int_{z_{k-1}}^{z_k} \begin{Bmatrix} \sigma_x \\ \sigma_y \\ \tau_{xy} \end{Bmatrix}_k dz \quad (2.28)$$

$$\begin{Bmatrix} M_x \\ M_y \\ M_{xy} \end{Bmatrix} = \int_{-1/2}^{1/2} \begin{Bmatrix} \sigma_x \\ \sigma_y \\ \tau_{xy} \end{Bmatrix} z dz = \sum_{k=1}^n \int_{z_{k-1}}^{z_k} \begin{Bmatrix} \sigma_x \\ \sigma_y \\ \tau_{xy} \end{Bmatrix}_k z dz$$

Using the previous  $[\sigma]_{xy}$  expression, the force and moment resultants can be expressed as:

$$\begin{Bmatrix} N_x \\ N_y \\ N_{xy} \end{Bmatrix} = \sum_{k=1}^n \left[ \begin{bmatrix} Q_{xx} & Q_{xy} & Q_{xs} \\ & Q_{yy} & Q_{ys} \\ & & Q_{ss} \end{bmatrix}_k \left\{ \int_{z_{k-1}}^{z_k} \begin{Bmatrix} \varepsilon_x^0 \\ \varepsilon_y^0 \\ \gamma_{xy}^0 \end{Bmatrix} dz + \int_{z_{k-1}}^{z_k} \begin{Bmatrix} \kappa_x \\ \kappa_y \\ \kappa_{xy} \end{Bmatrix} z dz \right\} \right] \quad (2.29)$$

$$\begin{Bmatrix} M_x \\ M_y \\ M_{xy} \end{Bmatrix} = \sum_{k=1}^n \begin{bmatrix} Q_{xx} & Q_{xy} & Q_{xs} \\ & Q_{yy} & Q_{ys} \\ & & Q_{ss} \end{bmatrix}_k \left\{ \int_{z_{k-1}}^{z_k} \begin{Bmatrix} \varepsilon_x^0 \\ \varepsilon_y^0 \\ \gamma_{xy}^0 \end{Bmatrix} z dz + \int_{z_{k-1}}^{z_k} \begin{Bmatrix} \kappa_x \\ \kappa_y \\ \kappa_{xy} \end{Bmatrix} z^2 dz \right\}$$

Since the reference plane strain and the curvature are not function of  $z$  and are the same for all plies, they can be factored outside the integration system and the summation sign.

Evaluate the integral and let:

$$\begin{aligned} A_{ij} &= \sum_{k=1}^n (Q_{ij}^{xy})_k (z_k - z_{k-1}) \\ B_{ij} &= \sum_{k=1}^n \frac{1}{2} (Q_{ij}^{xy})_k (z_k^2 - z_{k-1}^2) \\ C_{ij} &= \sum_{k=1}^n \frac{1}{3} (Q_{ij}^{xy})_k (z_k^3 - z_{k-1}^3) \end{aligned} \quad (2.30)$$

the force and moment resultants can be expressed as:

$$\begin{Bmatrix} N_x \\ N_y \\ N_{xy} \end{Bmatrix} = \begin{bmatrix} A_{11} & A_{12} & A_{16} \\ & A_{22} & A_{21} \\ & & A_{66} \end{bmatrix} \begin{Bmatrix} \varepsilon_x^0 \\ \varepsilon_y^0 \\ \gamma_{xy}^0 \end{Bmatrix} + \begin{bmatrix} B_{11} & B_{12} & B_{16} \\ & B_{22} & B_{21} \\ & & B_{66} \end{bmatrix} \begin{Bmatrix} \kappa_x \\ \kappa_y \\ \kappa_{xy} \end{Bmatrix} \quad (2.31)$$

$$\begin{Bmatrix} M_x \\ M_y \\ M_{xy} \end{Bmatrix} = \begin{bmatrix} B_{11} & B_{12} & B_{16} \\ & B_{22} & B_{21} \\ & & B_{66} \end{bmatrix} \begin{Bmatrix} \varepsilon_x^0 \\ \varepsilon_y^0 \\ \gamma_{xy}^0 \end{Bmatrix} + \begin{bmatrix} D_{11} & D_{12} & D_{16} \\ & D_{22} & D_{21} \\ & & D_{66} \end{bmatrix} \begin{Bmatrix} \kappa_x \\ \kappa_y \\ \kappa_{xy} \end{Bmatrix}$$

The expression above can be combined into one general expression relating in-plane forces and moments to reference plane strains and curvatures:

$$\begin{Bmatrix} N \\ M \end{Bmatrix} = \begin{bmatrix} A & B \\ B & D \end{bmatrix} \begin{Bmatrix} \varepsilon^0 \\ \kappa \end{Bmatrix} \quad (2.32)$$

The matrices  $[A]$ ,  $[B]$ , and  $[D]$  are three laminate stiffness matrices, which are functions of geometry, material properties, and stacking sequence of individual plies. In particular:

- ✓  $[A]$  is membrane stiffness relating matrix in-plane loads to in plane strains;
- ✓  $[B]$  is coupling stiffness matrix relating in-plane loads to curvatures and moments in-plane strains. If the  $B_{ij}$  term is  $\neq 0$ : (i) in-plane forces produce flexural and twisting deformation in addition to in-plane deformation; (ii) moments produces extensional and shear deformation of the middle surface in addition to flexural and twisting deformation;
- ✓  $[D]$  is bending stiffness matrix relating moments to curvatures.

Inverting the load-deformation relations, the strains and curvatures can be expressed as function of applied loads and moments:

$$\begin{Bmatrix} \varepsilon^0 \\ \kappa \end{Bmatrix} = \begin{bmatrix} A & B \\ B & D \end{bmatrix}^{-1} \begin{Bmatrix} N \\ M \end{Bmatrix} = \begin{bmatrix} a & b \\ c & d \end{bmatrix} \begin{Bmatrix} N \\ M \end{Bmatrix} \quad (2.33)$$

From the general strain-load relations of a laminates, expressions for engineering constants can be obtained using the normal definitions of engineering properties in term of average in-plane stresses and strains.

The suggested flowchart is illustrated in Fig. 2.13. It consists of the following step: (1) enter the engineering properties of the composite layer referred to the principal material axes; (2) calculate the layer stiffness matrix  $[Q]_{12}$  referred to the principal material direction using transformation relations; (3) enter the principal material axes orientation of each layer; (4) calculate the transformed stiffness matrix  $[Q]_{xy}$  of each layer referred to laminate coordinate system  $(x, y)$ ; (5) Enter the through-the-thickness coordinates of each layer surface; (6) calculate the laminate stiffness matrices  $[A]$ ,  $[B]$ , and  $[D]$ ; (7) calculated the compliance matrix  $[a]$  by inversion of the 6x6 stiffness matrix; (8) enter the total laminate thickness; (9) calculated the laminate engineering properties referred to laminate coordinate system  $(x, y)$ .

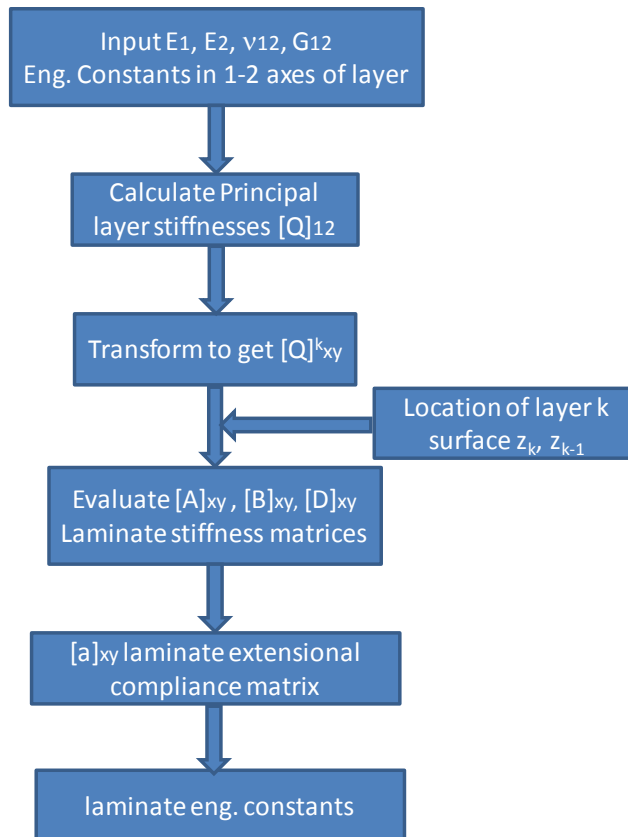


Figure 2.13. Flowchart for computation of engineering elastic properties of laminates

### 2.2.6. Strength of composite laminates

Failure analysis of a laminate is much more complex than that of a single lamina. The stresses in the individual laminae are fundamental and control failure initiation and progression in the laminate. Failure of a lamina does not necessarily imply total failure of the laminate, but is only the beginning of an interactive failure process.

Failure in a laminate may be caused by failure of individual laminae or plies within the laminate (*intralaminar - First ply and Ultimate laminate - failure*) or by separation of continuous laminae or layers (*interlaminar failure*). Failure of a laminate may be defined as the initial failure of the ultimate failure, depending on the degree of conservatism applied.

*First ply failure FPF* criterion assumes a laminated can be considered failed when the first layer (o group of layer) fails. This is determined by conducting a stress analysis of the laminate under the giving loading conditions, determining the state of stress in each individual layer, and assessing the strength of each layer by applying a selected failure criterion. The FPF approach is conservative, but it can be used with low safety factor as general practice in design of primary structures.

A flowchart for computation of safety factors and strength components of a general multidirectional laminate based on the Tsai-Wu failure criterion and on FPF approach. is shown in Fig.. 2.14.



**Figure 2.14. Flowchart for stress and failure analysis of laminates involving first ply failure and Tsai-Wu criterion**

The suggested flowchart consists of the following step: (1) enter the engineering properties of the composite layer referred to the principal material axes; (2) calculate the layer stiffness matrix  $[Q]_{12}$  referred to the principal material direction using transformation relations; (3) enter the principal material axes orientation of each layer; (4) calculate the transformed stiffness matrix  $[Q]_{xy}$  of each layer referred to laminate coordinate system  $(x, y)$ ; (5) Enter the through-the-thickness coordinates of each layer surface; (6) calculate the laminate stiffness matrices  $[A]$ ,  $[B]$ , and  $[D]$ ; (7) calculated the laminate compliance matrices  $[a]$ ,  $[b]$ ,  $[c]$ , and  $[d]$  by inversion of the 6x6 stiffness matrix; (8) enter the mechanical loading, forces and moments; (9) calculated the reference plane strains and curvatures; (10) enter the through-the-thickness coordinate of the point of interest in the layer; (11) calculated the layer strains referred to laminate reference axes  $(x, y)$ ; (12) calculate the layer strains referred to the principal material axes  $(1, 2)$ ; (13) calculate the layer stresses referred to the principal material axes  $(1, 2)$ ; (14) enter the lamina strengths and calculated Tsai-Wu coefficients; (15) calculate the layer safety factors; (16a) determine the laminate safety factors as minimum values between safety factors of all layers; (16b) determining laminate strength components.

*Ultimate laminate failure ULF* criterion assumes a laminated can be considered failed when the maximum load level is reached entailing, in addition to a lamina failure theory, a progressive damage scheme. Following each ply failure, the influence and contribution of the damaged ply on the remaining plies must be evaluated until final laminate failure according to the adopted progressive damaged scheme. The progressive damaged can be easily integrated in the previous flowchart scheme in a iterative procedure. It allows to replace the damaged lamina with one having reduction properties (introduction of stiffness reduction factors  $r$ ) so that the strengths of the previously failed laminae assume to be fictitiously very high to avoid repeated failure indication in the same plies.

*Interlaminar failure* consisting of separation of contiguous layers. This is common form of failure at free edges or in regions of geometric or loading discontinuities. Prediction of this type of failure requires a three-dimensional

stress and failure analysis including interlaminar strength and toughness properties of laminate.

### 2.3. Cellular core materials

Materials with a cellular structure are common in nature: they include wood, sponge, cancellous bone and cork. Such natural cellular materials have been used by man for over 5000 years; wooden artefacts at least that old have been found in the Pyramids of Egypt, and cork has been used for stoppers in bottles and for the soles of shoes since Roman times. More recently, man has made his own cellular materials in the form of either *honeycombs*, with parallel prismatic cells, or *foams* with polyhedral cells. Techniques now exist for making both honeycombs and foams from almost any material: polymers, metallic, ceramic and glasses. Honeycombs can be made in several ways. Usually flat sheers are glued together in strips along the portion to be bonded and then expanded, but they can also be made by gluing sheets which have been pressed into half-hexagonal profile together or by casting or by extrusion. Foams are made using different techniques for different types of solid. Polymers are foamed by introducing a gas into the liquid monomer or hot polymer with a blowing agent, allowing the bubbles to grow and stabilize, and then solidifying the foam by cross-linking or cooling [1]. Metallic foams are made by mixing organic beads (e.g. carbon) into a metal melt in an inert atmosphere; when the metal has cooled and solidified, the carbon is burnt off, leaving a cellular matrix. Ceramic foams are made by infiltrating an open-cell polymer foam with a fine slurry of ceramic (in water or some other fluid); when the aggregate is fired, the slurry bonds to give an image of the original foam, which, of course, burns off.

The unique properties of honeycombs and foams, arising from their cellular structures, can be exploited in engineering design. The small cell size and low volume fraction of solids in closed-cell foams make them excellent thermal insulators for applications ranging from coffee cups to building panels. Because of their low compressive strength and high deformation

capacity, they are outstanding energy absorption; this property is exploited in packaging and protective padding of all sorts. Their low density, furthermore, makes them ideal core materials for light-weight structural sandwich panels used in modern aerospace components and sporting equipment.

### 2.3.1. Cellular structure

The properties of cellular solids can vary widely, depending on the choice of the solid from which they are made, the volume fraction of the solid and geometry of the cells. The selection of a specific honeycombs or foams for a particular engineering application is guided by models which describe their mechanical behavior in terms of the cell geometry and the mechanisms of deformation and failure.

Cellular materials are made up of an interconnected network of struts and plates. A honeycomb (Fig. 2.15a) is an array of parallel prismatic cells giving a two-dimensional cellular structure. Most honeycomb materials have cells which are hexagonal and we shall focus our attention on them, but triangular and rectangular cells are possible, too. A foam (Fig. 2.15b) is made up of polyhedral cells, giving a three-dimensional structure. A further distinction can be made between *open-cell foams*, in which struts form the edges of the cells, and *closed-cell foams*, in which a solid membrane covers the cell faces. The single most important structural characteristic of a cellular solid is its relative density  $\rho^*/\rho_s$  (the density  $\rho^*$  of the foam core divided by the density  $\rho_s$  of the solid from which is made); it is equivalent to the volume fraction of solids. If the solid is entirely in the cell edges, the foam is open celled while, if it is distributed between the edges and the faces, it is closed celled. The relative contributions of the faces and the edges to the properties of the foam depend on the amount of solid in each; the volume of solid in the cell edges relative to the total volume of solid in the cell edges relative to the total volume of solids is defined as  $\phi$ . In many closed-cell foams made from a liquid phase, surface tension forces tend to draw liquid away from the faces and into the edges during the foaming process, increasing  $\phi$  to the point that a closed-cell foam behaves like an open-cell foam.

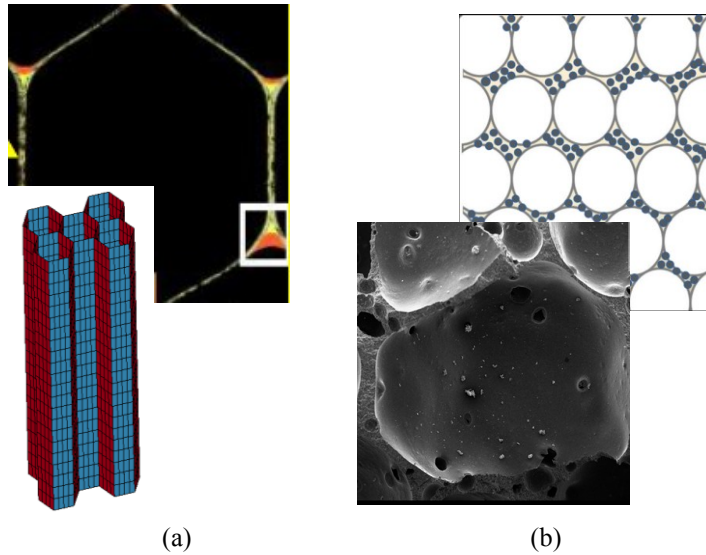


**Figure 2.15. Structure of cellular materials: (a) hexagonal honeycomb; (b) polyurethane foam**

Both honeycombs and foams can be anisotropic; that is, their properties depend on the direction in which they are measured. Anisotropy arises either from the inherent anisotropy in the cell shape. The shape of orthotropic cells (for which a rotation of  $180^\circ$  about a set of three orthogonal axes leaves the structure unchanged) can be described by three mean intercept lengths,  $L_1$ ,  $L_2$  and  $L_3$ , corresponding to the major, intermediate and minor lengths along the three axes of symmetry. Cell shapes is then characterized by the shape anisotropy ratio:

$$R_{ij} = \frac{L_i}{L_j} \quad (2.34)$$

An orthotropic material is characterized by two shape anisotropy ratios while an axisymmetric material is characterized by a single ratio.

Two additional parameters are required for the complete characterization of honeycombs and foams: the edge connectivity  $Z_c$  and the face connectivity  $Z_f$ . The first parameter is the number of edges that meet a vertex; for hexagonal honeycombs it is three and for most foams it is four. The second parameter is the number of faces that meet at an edge in a foam; it is generally three.

Characterization charts are useful for listing the structural features of honeycombs and foams; examples are given in Tables 2.1.

**Table 2.1. Characterization chart for cellular materials**

Characterization chart for honeycombs	Characterization chart for foams
Material	Material
Density $\rho^*$	Density $\rho^*$
Edge connectivity $Z_e$	Open or closed cells
Mean number $\bar{z}$ of edges per cell	Edge connectivity $Z_e$
Cell shape and angles	Face connectivity $Z_f$
Symmetry of structure	Mean number $\bar{z}$ of edges per face
Largest principal cell dimension $L_1$	Mean number $\bar{f}$ of faces per cell
Smallest principal cell dimension $L_2$	Cell shape
Shape anisotropy ratio $R=L_1/L_2$	Symmetry of structure
Standard deviation of cell size	Cell edge thickness $t_e$
Cell wall thickness $t$	Cell face thickness $t_f$
Relative density $\rho^*/\rho_s$	Fraction $\phi$ of material in cell edges
Other specific features	Largest principal cell dimension $L_1$
	Smallest principal cell dimension $L_3$
	Intermediate principal cell dimension $L_2$
	Shape anisotropy ratio $R_{12}=L_1/L_2$ and $L_{12}=L_1/L_2$
	Standard deviation of cell size
	Cell wall thickness $t$
	Relative density $\rho^*/\rho_s$
	Other specific features

Unit cells are often used in modelling cell shape in foams. The non-prismatic polyhedra which pack to fill space are the rhombic dodecahedra, with 12 diamond-shaped faces, and the tetrakaidecahedra, with six square and eight hexagonal faces [3-7]. Other polyhedra which do not pack to fill space have been suggested at various times for the unit cells of foams; they include the tetrahedron (four faces), the icosahedron (20 faces) and the pentagonal dodecahedron (12 regular pentagonal faces) [8-12].

The topology of cells is a field which has fascinated physicists, biologists and metallurgists for centuries. Three simple results can be extracted which help in the characterization of honeycombs and foams: Euler's law, the Aboav-Weaire law and Lewis's rule.

Euler's law relates the number  $V$  of vertices, the number  $E$  of edges, the number  $F$  of faces and the number  $C$  of cells in a large aggregate of cells; it is [13-14]:

$$\begin{aligned}
 F - E + V &= 1 && \text{(two dimensions)} \\
 -C + F - E + V &= 1 && \text{(three dimensions)}
 \end{aligned}
 \tag{2.35}$$

If the number of edges meeting at a vertex (the edge connectivity) is three, it can be shown that for any two-dimensional array of cells the average number of edges per face is six and for an isolated cell in a three-dimensional array of cells, the average number  $\tilde{r}$  of edges per face is [2]:

$$\tilde{r} = \left( \frac{2}{f} \right)
 \tag{2.36}$$

where  $f$  is the number of faces in the cell. An important consequence follows: most cells in foams have faces with five edges, no matter what the shapes of the cells are on average dodecahedra ( $f=12$ ), the average number of edges per face is five exactly. However, if they are tetrakaidecahedra ( $f=14$ ) or icosahedra ( $f=20$ ), the average is 5.14 and 5.4 respectively. So frequent sightings of pentagonal faces in foams do not mean that cells are pentagonal dodecahedra as is often claimed.

In a two-dimensional three-connected net of irregular cells, the average number of edges per cell is, from Euler's law, six. This implies that a five-sided cell can only be introduced into the array if, somewhere, a seven-sided cell is created also; a four-sided cell requires either one eight-sided cell or two seven-sided cells; and so on. It is generally true that a cell with more sides than average has neighbours which, taken together, have less sides than average. This correlation was noted by Aboav [15, 16] in Smith's [5, 17] pictures of soap honeycombs. The observation is described for honeycombs by the Aboav-Weaire law [15] given in formal derivation by Weaire [18]:

$$\tilde{r} = \frac{2}{n}
 \tag{2.37}$$

where  $n$  is the number of edges of the candidate cell and  $\tilde{r}$  is the average number of edges of its  $n$  neighbours. It is possible speculate that a similar result holds in three dimensions, such that:

$$\tilde{r} = \frac{2}{J}
 \tag{2.38}$$

where  $f$  is the number of faces on a cell and  $\bar{f}$  the average number of faces of its neighbours. Calculations by Fortes [19] show this to be a reasonable approximation when  $f=14$ . Rivier [20] gives a more formal description of an alternative three-dimensional generalization.

Observations of two dimensional arrays of cells have produced another remarkable result, Lewis's rule [20-21], which states that area of a two-dimensional cell in the array varies linearly with its number of edges or:

$$\frac{A(n)}{A(\bar{f})} = \frac{n - n_0}{\bar{f} - f_0} \quad (2.39)$$

where  $A(n)$  is the area of the cell with  $n$  sides,  $A(\bar{f})$  is that of the cell with the average number  $\bar{f}$  of sides and  $n_0$  is a constant that Lewis finds equal to two. Rivier and Lessowsky [23] have developed a formal proof for Lewis's rule and Rivier [24] has generalized it to three dimensions:

$$\frac{V(f)}{V(\bar{f})} = \frac{f - f_0}{\bar{f} - f_0} \quad (2.40)$$

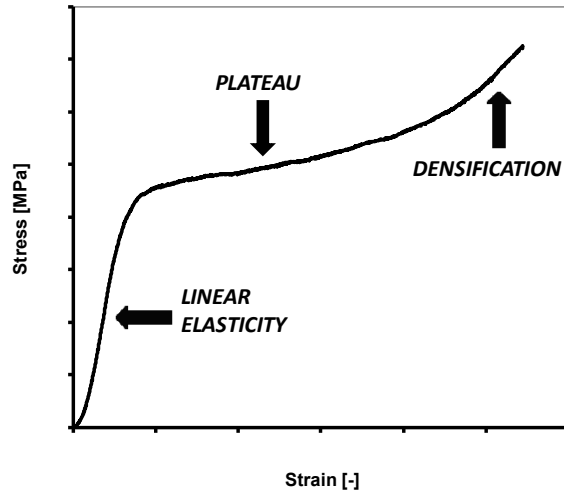
where  $V(f)$  is the volume of a polyhedral cell with  $f$  faces,  $V(\bar{f})$  is that for a cell with the average number  $\bar{f}$  of faces and  $f_0$  is a constant about equal to 3.

Taken together, Euler's law, the Aboav-Weaire law and Lewis's rule quantify some of the more common observations of cell topology. In a two-dimensional array of cells, the average number of edges per cell is six while in a three-dimensional array the average number of edges per face depends on the number of faces per cell; it is often close to five, giving pentagonal faces. Cells with a large number of edges (in two-dimensions) or faces (in three dimensions) tend to be surrounded by cells with fewer edges or faces. The area (in two-dimensions) or volume (in three-dimensions) of a cell increases linearly with its number of edges or faces.

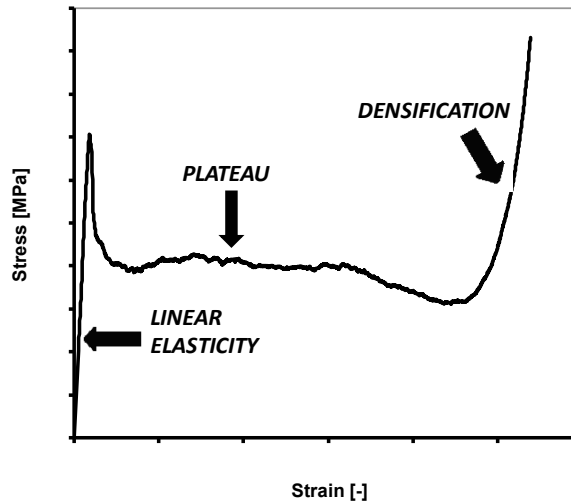
### 2.3.2. Response of cellular structures to loading

Uniaxial compressive and tensile stress-strain curves for honeycomb and foams are shown in Fig. 2.16. The compressive curves for both honeycombs and foams made from different cell wall materials all have the same shape

characterized by three distinct regimes: initial linear elasticity, a stress plateau and a final regime of steeply rising stress corresponding to densification.



(a)



(b)

Figure 2.16. Compressive stress-strain curves: (a) hexagonal honeycomb; (b) polyurethane foam.

Observation on honeycombs and foams loaded at low strain rates indicate that each regime is related to a particular deformation mechanism: linear

elastic behaviour to bending of the cell walls; the stress plateau to elastic buckling, plastic yielding or brittle fracture, depending on the nature of the cell wall material; densification to meeting of opposing cell walls once the cells have completely collapsed.

The tensile behaviour is slightly different. The linear elastic regime is again to bending in the cell walls, but the stress plateau disappears for elastomeric honeycombs and foams do not buckle in tension and brittle honeycombs and foams rupture instead of crushing progressively.

The tensile stress plateau of honeycombs and foams which yield plastically is truncated by cell alignment in tension, at lower strains than densification occurs in compression.

Closed-cell foams have additional deformation mechanisms arising from the stretching of the membranes covering the faces of the cells. The relative amount of bending *vs.* stretching depends on the distribution of solid between the cell edges and faces. In many closed-cell foams, surface tension forces draw material into the cell edges during the foaming process; when this is the case,  $\phi$  is closed to unity and the foam behaves like an open-celled foam.

The fluid within the cells can also contribute to the mechanical response of a cellular solid. If the cells are open, there is the viscous resistance of the fluid to flow through the cells; this effect can be significant if the strain rates are high (of the order of  $10^{-3} \text{ s}^{-1}$ ) or if the fluid is highly viscous. If the cells are closed and the foams is compressed, the cell volume progressively decreases, increasing the fluid pressure within the cell. The contribution to the linear elastic behaviour is negligible. However, the effect gives rise to a sloping stress plateau in elastomeric foams which are able to undergo large deformations (and changes in cell volume) without rupture of the membrane covering the cell faces.

For simplicity, the behaviour of honeycombs and open-cell foams are modelled here at low strain rates, neglecting fluid effects. If the volume fraction of solid in the cell faces is small, closed-cell foams behave like open-cell foams. A more refined analysis, describing the behaviour of true closed-

cell foams and the effects of the cell fluid have been given by Gibson and Ashby [2].

The mechanisms of deformation in both honeycombs and foams are identical; the only difference is geometrical. Honeycombs, with their regular geometry, are easily analyzed. Foams are more difficult, but they, too, can be understood by using dimensional arguments to extend the analysis for honeycombs.

### 2.3.3. The uniaxial in-plane behavior of honeycombs

Honeycombs, with their regular geometry, are relatively straightforward to analyze. A unit cell of a honeycomb made up of an array of hexagonal cells is shown in Table 2.2, deformed cell (a). The cells have two vertical members of length  $h$  and four inclined members of length  $l$ ; the angle of inclination to the horizontal is  $\theta$ . For regular hexagonal cells, which are isotropic in the plane of the hexagons, the ratio  $h/l=1$  and  $\theta =30$ . The cell walls are of uniform thickness  $t$  and of depth  $b$  and have a moment of inertia  $I$  of  $bt^3/12$ . The cell wall material has a density  $\rho_s$ , Young's modulus  $E_s$ , a yield strength  $\sigma_{ys}$  and a modulus of rupture  $\sigma_{fl}$ . The density  $\rho^*$  of the honeycomb divided by the density  $\rho_s$  of the solid, gives the relative density  $\rho^*/\rho_s$  in the first row, last column, of the table; it should be noted that the relative density is largely by cell wall bending [25-30]. Some axial and shear deformations occur, too, but if  $t/l$  is small (less than about 1/4) they are negligible. Four elastic moduli are required to describe the in-plane linear elastic response. Here we calculate  $E_1^*$ ,  $\nu_{12}^*$ ,  $E_2^*$ ,  $\nu_{21}^*$  and  $G_{12}^*$ ; it should be noted that the reciprocal relation holds ( $E_1^* \nu_{21}^* = E_2^* \nu_{12}^*$ ) so that only four of these five moduli are independent. We define Poisson's ratio to be the negative ratio of strain in the  $j$  direction to that in the  $i$  direction for loading in the  $i$  direction ( $\nu_{ij} = -\epsilon_j/\epsilon_i$ ). The analysis is summarized in Table 2.2.

Consider first Young's modulus for loading in the  $x_1$  direction (Table 2.2, deformed cell (b)). Under a stress  $\sigma_1$  the inclined members bend, deflecting by an amount  $\delta$  which is related to the end load  $P$  acting on the member by:

$$\delta = \frac{Pl^3 \sin \theta}{12E_s I} \quad (2.41)$$

The stress  $\sigma_l$  in the  $x_l$  direction is related to the end load  $P$  by:

$$\sigma_l = \frac{P}{b(h + l \sin \theta)} \quad (2.42)$$

and the strain  $\varepsilon_l$  in the  $x_l$  direction is related to the bending deflection  $\delta$  by:

$$\varepsilon_l = \frac{\delta \sin \theta}{l \cos \theta} \quad (2.43)$$

Combining these expressions gives Young's modulus in the  $x_l$  direction:

$$\frac{E_l^*}{E_s} = \left(\frac{t}{l}\right)^3 \frac{\cos^3 \theta}{(h/l + \sin \theta) \sin^2 \theta} \quad (2.44)$$

or for regular hexagons ( $h/l=1$ ;  $\theta=30^\circ$ ).

$$\frac{E_l^*}{E_s} = \frac{4}{\sqrt{3}} \left(\frac{t}{l}\right)^3 \quad (2.45)$$

Poisson's ratio for loading in the  $x_l$  direction is found by taking the ratio

$$\nu_{12}^* = -\frac{\varepsilon_2}{\varepsilon_1} = \frac{\cos^2 \theta}{(h/l + \sin \theta) \sin \theta} \quad (2.46)$$

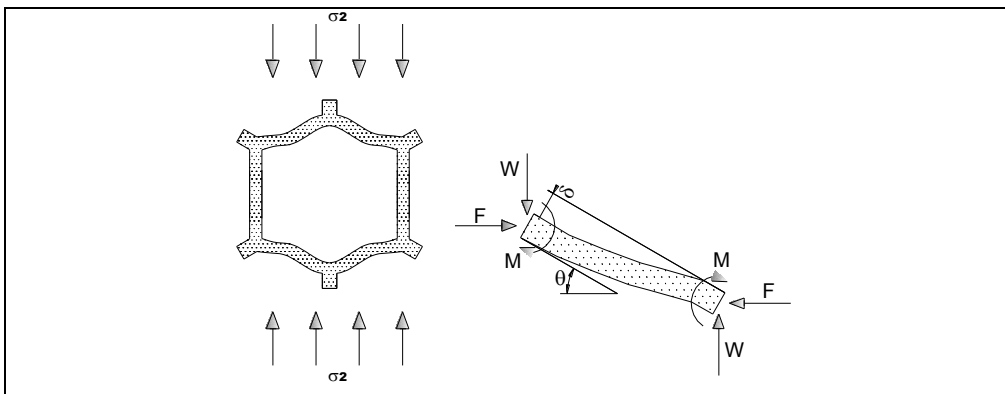
Where

$$\varepsilon_2 = \frac{\delta \cos \theta}{h + l \sin \theta} \quad (2.47)$$

Young's modulus and Poisson's ratio for loading in the  $x_2$  direction and the in-plane shear modulus  $G_{12}^*$  are found in a similar way; the equations for the analysis are given in Table 2.2, deformed cells (c) and (d). Both Young's modulus and the shear modulus depend on the ratio  $t/l$ , on Young's modulus  $E_s$  of the cell wall and on a factor related to the cell geometry ( $h/l$  and  $\theta$ ). Poisson's ratio is independent of  $t/l$  and  $E_s$  and is solely a function of cell geometry; it is interesting to note that it can have negative values for  $\theta < 0^\circ$ , implying that an axial extension causes lateral expansion.

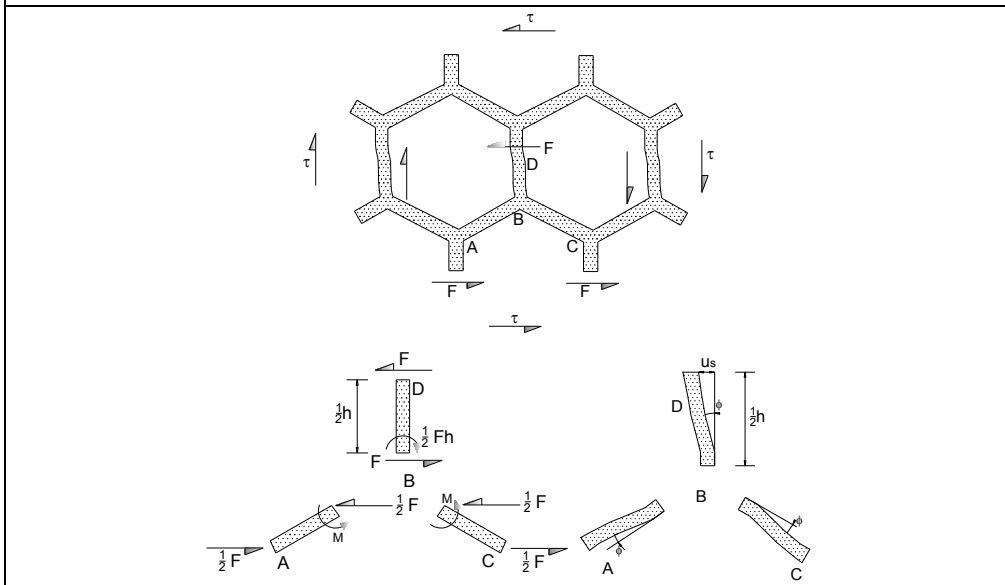
Table 2.2. In-plane elastic moduli of honeycombs.

<b>(a) Deformed cell</b>		
<i>Analysis</i>	<i>Honeycomb Property</i>	<i>Value for h/l=1 and theta=30°</i>
Solid cell wall properties: Density $\rho_s$ Young's modulus $E_s$ Yield strength $\sigma_{ys}$ Modulus of ropture $\sigma_{ft}$	$\frac{\rho^*}{\rho_s} = \frac{t}{l} \frac{h/l + 2}{2 \cos \theta (h/l + \sin \theta)}$ $I = \frac{bt^3}{12}$	$\frac{\rho^*}{\rho_s} = \frac{2}{\sqrt{3}} \frac{t}{l}$
<b>(b) Deformed cell</b>		
<i>Analysis</i>	<i>Honeycomb Property</i>	<i>Value for h/l=1 and theta=30°</i>
$\sigma_1 = \frac{P}{b(h + l \sin \theta)}$ $\varepsilon_1 = \frac{\delta \sin \theta}{l \cos \theta}$ $\varepsilon_2 = \frac{\delta \cos \theta}{h + l \sin \theta}$ $\delta = \frac{Pl^3 \sin \theta}{12E_s I}$ $C = 0$	$\frac{E_1^*}{E_s} = \left(\frac{t}{l}\right)^3 \frac{\cos^3 \theta}{(h/l + \sin \theta) \sin^2 \theta}$ $\nu_{12}^* = \frac{\cos^2 \theta}{(h/l + \sin \theta) \sin \theta}$	$\frac{E_1^*}{E_s} = \frac{4}{\sqrt{3}} \left(\frac{t}{l}\right)^3$ $\nu_{12}^* = 1$
<b>(c) Deformed cell</b>		



Analysis	Honeycomb Property	Value for $h/l=1$ and $\theta=30^\circ$
$\sigma_2 = \frac{W}{bl \cos \theta}$ $\varepsilon_2 = \frac{\delta \cos \theta}{(h+l \sin \theta)}$ $\varepsilon_1 = \frac{\delta \sin \theta}{l \cos \theta}$ $\delta = \frac{Wl^3 \cos \theta}{12E_s I}$	$\frac{E_2^*}{E_s} = \left(\frac{t}{l}\right)^3 \frac{h/l + \sin \theta}{\cos^3 \theta}$ $\nu_{12}^* = \frac{(h/l + \sin \theta) \sin \theta}{\cos^2 \theta}$	$\frac{E_1^*}{E_s} = \frac{4}{\sqrt{3}} \left(\frac{t}{l}\right)^3$ $\nu_{12}^* = 1$

(d) Deformed cell



Analysis	Honeycomb Property	Value for $h/l=1$ and $\theta=30^\circ$
----------	--------------------	---

$\tau = \frac{F}{2bl \cos \theta}$ $\gamma = \frac{2U}{(h + l \sin \theta)}$ $U = \frac{1}{2} \phi h + \frac{F(h/2)^3}{3E_s I}$ $\phi = \frac{Fhl}{24E_s I}$	$\frac{G_{12}^*}{E_s} = \left(\frac{t}{l}\right)^3 \frac{(h/l + \sin \theta)}{(h/l)^2 (1 + 2h/l) \cos \theta}$	$\frac{G_{12}^*}{E_s} = \frac{1}{\sqrt{3}} \left(\frac{t}{l}\right)^3$
--	--	--

The compressive collapse stresses and the tensile fracture toughness are modelled in Table 2.3. Elastic collapse of the cells when loaded in the  $x_2$  direction is caused by elastic buckling. The vertical members of length  $h$  buckle at the Euler load and the elastic collapse stress  $\sigma_{el}^*$  is the Euler load divided by  $2bl \cos \theta$ . The end constraint factor  $n$  in the Euler equation is related to the flexural rigidity of the adjacent inclined members of length  $l$ . It has been calculated by Gibson et al. [28]; typical values are given in the table.

Plastic collapse occurs when plastic hinges form in the cell walls. A lower bound for the plastic collapse stress is found by equating the maximum moment  $M_{max}$  in the beam to the moment  $M_p$  required to form a plastic hinge. Noting also that  $M_p = 1/4 \sigma_{ys} b t^2$ , the equation for the plastic collapse stress  $(\sigma_{pl}^*)_1$  for loading in the  $x_1$  direction can be found. An upper bound argument equating the external work done by the force  $P$  acting on the member with the internal work

done during a plastic rotation of  $\phi$  at the hinges gives the same result, implying that the solution is exact. The results of analogous analyses for loading in the  $x_2$  direction and for the in-plane plastic shear strength of the honeycomb are listed in the table.

The compressive crushing strength  $(\sigma_{cr}^*)_1$  is calculated in a similar way, with the moment  $M_f$  to fracture the cell wall replacing the plastic moment  $M_p$ . The results are listed in Table 2.3, deformed cell (c).

The tensile fracture toughness is calculated as follows (Table 2.3, deformed cell (d)). The local stress a distance  $r$  ahead of the crack tip is

$$\sigma_{loc} = \frac{\sigma_1 (\pi c)^{1/2}}{(2\pi r)^{1/2}} \quad (2.48)$$

For loading in the  $x_1$  direction the first unbroken cell wall ahead of the crack tip is at  $r = (h + l \sin \theta)/2$  (assuming the crack tip to be in the middle of the cell). The force on this cell wall is

$$P = \sigma_1 (h + l \sin \theta) b \quad (2.49)$$

This force exerts a bending moment  $M$  proportional to  $P$ , on the wall:

$$M_1 \propto Pl \sin \theta \quad (2.50)$$

When this moment equals the fracture moment  $M_f = (\sigma_{fs} b t^2 / 6)$ , the crack advances. Combining the results and assuming that the constant of proportionality is unity, we find the tensile

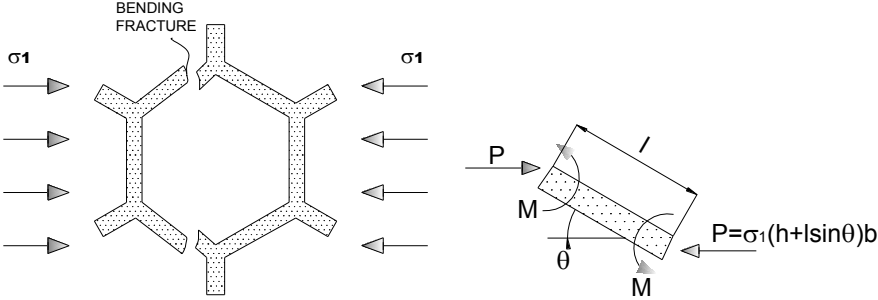
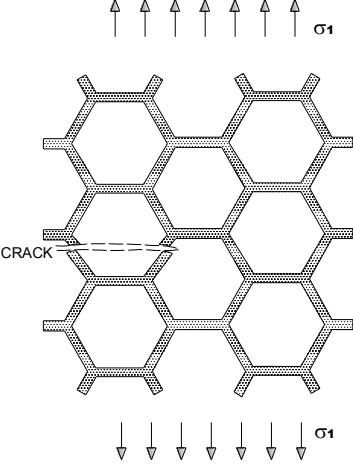
$$\frac{(\sigma_f^*)_1}{\sigma_{fs}} \approx \frac{1}{6(h/l + \sin \theta)^{1/2}} \left(\frac{l}{c}\right)^{1/2} \left(\frac{t}{l}\right)^2 \quad (2.51)$$

A similar calculation gives the tensile fracture strength in the  $x_2$  direction. The fracture toughnesses  $(K_{Ic}^*)_1$  and  $(K_{Ic}^*)_2$  are simply  $(\sigma_f^*)_1 (\pi c)^{1/2}$  and  $(\sigma_f^*)_2 (\pi c)^{1/2}$ .

Three parameters control the in-plane properties of honeycombs: the ratio of  $t/l$ , the relevant cell wall property and the cell geometry (i.e.  $h/l$  and  $\theta$ ). By selecting appropriate values for these three parameters, the engineer can design a honeycomb with the desired properties.

Table 2.3. In-plane strength of honeycombs.

<b>(a) Deformed cell</b>		
<i>Analysis</i>	<i>Honeycomb Property</i>	<i>Value for h/l=1 and theta=30°</i>
$P_{cr} = \frac{(n\pi)^2 E_s I}{h^2}$ $(\sigma_{el}^*)_2 = \frac{P_{cr}}{2bl \cos \theta}$	$(\sigma_{el}^*)_2 = \frac{(n\pi)^2 t^3 l}{24 lh^2 \cos \theta}$	$(\sigma_{el}^*)_2 = 0.22 \left(\frac{t}{l}\right)^3 E_s$
<b>(b) Deformed cell</b>		
<i>Analysis</i>	<i>Honeycomb Property</i>	<i>Value for h/l=1 and theta=30°</i>
$\sigma_1 = \frac{P}{b(h+l \sin \theta)}$ $M_{\max} = \frac{Pl \sin \theta}{2}$ $M_p = \frac{\sigma_{ys} b t^2}{4}$	$\frac{(\sigma_{pl}^*)_1}{\sigma_{ys}} = \left(\frac{t}{l}\right)^2 \frac{1}{2(h/l + \sin \theta) \sin \theta}$ $\frac{(\sigma_{pl}^*)_2}{\sigma_{ys}} = \left(\frac{t}{l}\right)^2 \frac{1}{2 \cos^2 \theta}$	$\frac{(\sigma_{pl}^*)_1}{\sigma_{ys}} = \frac{2}{3} \left(\frac{t}{l}\right)^2$ $\frac{(\sigma_{pl}^*)_2}{\sigma_{ys}} = \frac{2}{3} \left(\frac{t}{l}\right)^2$

$M_f = \frac{\sigma_{fs} b t^2}{6}$	$\frac{(\tau_{pl}^*)_{12}}{\sigma_{ys}} = \left(\frac{t}{l}\right)^2 \frac{1}{(4h/l)\cos\theta}$	$\frac{(\tau_{pl}^*)_{12}}{\sigma_{ys}} = \frac{1}{2\sqrt{3}} \left(\frac{t}{l}\right)^2$
<p><b>(c) Deformed cell</b></p>		
		
<p><i>Analysis</i></p>	<p><i>Honeycomb Property</i></p>	<p><i>Value for h/l=1 and theta=30°</i></p>
	$\frac{(\sigma_{cr}^*)_1}{\sigma_{fs}} = \left(\frac{t}{l}\right)^2 \frac{1}{3(h/l + \sin\theta)\sin\theta}$ $\frac{(\sigma_{cr}^*)_2}{\sigma_{fs}} = \left(\frac{t}{l}\right)^2 \frac{1}{3\cos^2\theta}$	$\frac{(\sigma_{cr}^*)_1}{\sigma_{fs}} = \frac{4}{9} \left(\frac{t}{l}\right)^2$ $\frac{(\sigma_{cr}^*)_2}{\sigma_{fs}} = \frac{4}{9} \left(\frac{t}{l}\right)^2$
<p><b>(d) Deformed cell</b></p>		
		
<p><i>Analysis</i></p>	<p><i>Honeycomb Property</i></p>	<p><i>Value for h/l=1 and theta=30°</i></p>

$\sigma_1 = \frac{P}{b(h+l \sin \theta)}$ $\sigma_{loc} = \frac{\sigma_1 (\pi c)^{1/2}}{(2\pi r)^{1/2}}$ $r = \frac{(h+l \sin \theta)}{2}$ $M_1 \propto Pl \sin \theta \propto \frac{\sigma_{fs} b t^2}{6}$	$\frac{(\sigma_f^*)_1}{\sigma_{fs}} = \left(\frac{t}{l}\right)^2 \frac{1}{6(h/l + \sin \theta)^{1/2}} \left(\frac{l}{c}\right)^{1/2}$ $\frac{(\sigma_f^*)_2}{\sigma_{fs}} = \left(\frac{t}{l}\right)^2 \frac{1}{3\sqrt{2} \cos^{3/2} \theta} \left(\frac{l}{c}\right)^{1/2}$	$\frac{(\sigma_f^*)_1}{\sigma_{fs}} = 0.3 \left(\frac{t}{l}\right)^2 \left(\frac{l}{c}\right)^{1/2}$ $\frac{(\sigma_f^*)_2}{\sigma_{fs}} = 0.3 \left(\frac{t}{l}\right)^2 \left(\frac{l}{c}\right)^{1/2}$
---	--	---

### 2.3.4. The uniaxial behavior of open-cell foams

Because foams deform by the same mechanisms as honeycombs, their properties, too, depend on their relative density, cell wall properties and cell geometry. However, the geometry of foams is much more complex than that of honeycombs, making exact analyses difficult. Instead can be used dimensional arguments which describe the dependence of foam properties on  $t/l$  and on the cell wall properties but do not give any indication of the dependence on the cell geometry; for this an experiment is required.

The results of such a dimensional analysis depend only on the mechanism of deformation analyzed; they are insensitive to the specific cell geometry chosen. For this reason a simple cubic cell geometry is chosen; a typical cubic cell is shown in Table 2.4, deformed cell (a). Adjoining members meet at the midpoints of the cell walls; it is this feature which allows the bending of the cell walls to be modelled, in contrast with initial models of the linear elastic behavior of foams which analyzed only axial cell wall deformations [31-33]. Each edge of the cube has length  $l$  and is of square cross-section  $t^2$ . The relative density  $\rho^*/\rho_s$  of the cells is proportional to the square  $(t/l)^2$  of the thickness-to-length ratio. The moment of inertia of the wall is proportional to  $t^4$ . The cell wall material has a density  $\rho_s$ , Young's modulus  $E_s$ , a yield strength  $\sigma_{ys}$  and a modulus of rupture  $\sigma_{fs}$ .

To illustrate the method and the form of the results, we analyze isotropic open-cell foams loaded at low strain rates such that fluid effects can be neglected. Similar methods can be used for closed-cell foams and for fluid

effects; they have been described by Gibson and Ashby [2]. Anisotropy is discussed at the end of the section. Consider first the linear elastic behavior of a foam (Table 2.4, deformed cell (b)). A load  $P$  bends the cell walls which deflect by  $\delta$ , proportional to  $Pl^3/EI$ . The overall stress and strain on the foam are proportional to  $P/l^2$  and  $\delta/l$  respectively, leading to

$$\frac{E^*}{E_s} \alpha \left( \frac{t}{l} \right)^4 = C_1 \left( \frac{\rho^*}{\rho_s} \right)^2 \quad (2.52)$$

Table 2.4. Elastic moduli and strength of foam.

TABLE 5 Elastic moduli and strength of foams

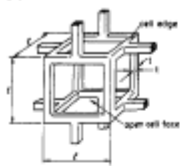
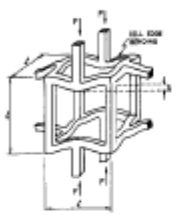
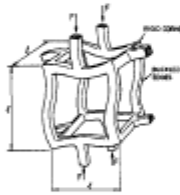
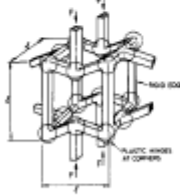
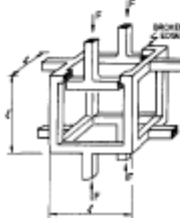
Deformed cell	Analysis	Foam property
(a) 	Solid cell wall properties: Density $\rho_s$ Young's modulus $E_s$ Yield strength $\sigma_y$ Modulus of rupture $\sigma_b$	$\frac{\rho^*}{\rho_s} \propto \left(\frac{t}{l}\right)^2$ $f \propto t^4$
(b) 	$\sigma \propto \frac{P}{l^2}$ $\epsilon \propto \frac{\delta}{l}$ $\delta \propto \frac{Pl^3}{E_s t}$	$\frac{E^*}{E_s} = C_1 \left(\frac{\rho^*}{\rho_s}\right)^2$ $= \left(\frac{\rho^*}{\rho_s}\right)^2$ $\frac{G^*}{E_s} = C_2 \left(\frac{\rho^*}{\rho_s}\right)^2$ $= \frac{3}{8} \left(\frac{\rho^*}{\rho_s}\right)^2$ $\nu^* = C_3 = \frac{1}{2}$
(c) 	$\sigma_y^* \propto \frac{P_y}{l^2}$ $P_y \propto \frac{E_s t^3}{l}$	$\frac{\sigma_y^*}{E_s} = C_4 \left(\frac{\rho^*}{\rho_s}\right)^{3/2}$ $= 0.05 \left(\frac{\rho^*}{\rho_s}\right)^{3/2}$
(d) 	$\sigma_y^* \propto \frac{P^*}{l^2}$ $P^* \propto \frac{M_y}{l}$ $M_y \propto \sigma_y t^3$	$\frac{\sigma_y^*}{E_s} = C_5 \left(\frac{\rho^*}{\rho_s}\right)^{3/2}$ $= 0.3 \left(\frac{\rho^*}{\rho_s}\right)^{3/2}$
(e) 	$\sigma_y^* \propto \frac{P}{l^2}$ $P^* \propto \frac{M_y}{l}$ $M_y \propto \sigma_y t^3$	$\frac{\sigma_y^*}{E_s} = C_6 \left(\frac{\rho^*}{\rho_s}\right)^{3/2}$ $= 0.65 \left(\frac{\rho^*}{\rho_s}\right)^{3/2}$

TABLE 5 (continued)

Deformed cell	Analysis	Foam property
(f)		
	$\sigma_{loc} \propto \frac{\sigma_1(\pi a)^{1/2}}{(2\pi l)^{1/2}}$ $\propto \frac{M_f}{l^3}$ $M_f \propto \sigma_c t^3$ $K_{Ic}^* \propto \sigma_1(\pi a)^{1/2}$	$\frac{K_{Ic}^*}{\sigma_c} = C_1(\pi l)^{1/2} \left( \frac{\sigma_c^*}{\rho_s} \right)^{1/2}$ $= 0.65(\pi l)^{1/2} \left( \frac{\sigma_c^*}{\rho_s} \right)^{1/2}$

The analysis for the shear modulus gives the same result with a different constant of proportionality. Poisson's ratio is the ratio of two strains; because of this it is independent of the relative density and Young's modulus of the cell wall and depends only on the cell geometry. Like honeycombs, it is possible to make foams with negative Poisson's ratios by inverting the cell angle [35].

Elastic collapse is caused by the elastic buckling of the cell walls once the Euler load  $P_{cr} \propto EI/l^2$  is reached (Table 5, deformed cell (c)). Plastic collapse is caused by the formation of plastic hinges in the cells walls at a load  $P \propto M_p/l$  (Table 2.4, deformed cell (d)). Brittle crushing is caused by the bending fracture of the cell walls at a load  $P \propto M_f/l$  (Table 2.4, deformed cell (e)). Noting that in each case the stress  $\sigma$  on the foam is proportional to  $P/l^2$  gives the elastic collapse stress  $\sigma_{el}^*$ , the plastic collapse stress  $\sigma_{pl}^*$  and the brittle crushing stress  $\sigma_{cr}^*$ .

The tensile fracture toughness for a foam can be calculated by considering the local stress field ahead of the crack tip [45] (Table 2.4, deformed cell (f)). The local stress on the member immediately ahead of the crack tip is

$$\sigma_{loc} \propto \frac{\sigma_1(\pi a)^{1/2}}{(2\pi l)^{1/2}} \propto \frac{M_f}{l^3} \quad (2.53)$$

and the fracture moment  $M_f$  is given, as before, by  $\sigma_{fs}t^3$ . Combining these expressions, and noting that  $K_{Ic} = \sigma_1(\pi a)^{1/2}$  gives the fracture toughness of the foam.

In general, the simple model based on dimensional arguments gives a good description of the uniaxial behavior of isotropic foams. In particular, the dependence of each property on the relative density is well predicted. The uncertainty in the model arises in the estimating the cell wall properties. Part of the difficulty arises from the fact that the moduli of polymers (from which most foams are made) vary with the frequency of the cross-links joining the polymer chains, so that for one type of polymer a range of moduli are possible, and part arises from the foaming process itself which can alter the structure and properties of the cell wall polymer. In practice, errors in estimating the cell wall properties are combined into the proportionality constant relating to the cell geometry in the model.

### **2.3.5. The in-plane biaxial behavior of honeycombs**

The linear elastic behavior of a honeycomb under a uniaxial load is well described by considering the bending of the cell walls, neglecting axial deformations. However, under an in-plane biaxial load some combination of  $\sigma_1$  and  $\sigma_2$  can always be found for which the bending moments in the cell walls cancel, eliminating bending deflections; the only remaining deformation is then axial extension or compression and it can no longer be neglected. For instance, a honeycomb made up of regular hexagonal cells subjected to an equal biaxial tensile stress deforms solely by axial extension of the cell walls; the bending moments and deformations in the cell walls are completely eliminated.

The mechanism of deformation in a honeycomb depends on the stress state to which it is subjected. As a result, axial as well as bending deformations and stresses must be considered in analyzing the response of honeycombs to biaxial stresses. The linear elastic response of honeycombs under biaxial loading is obtained by adding the axial and bending deformations. In particular, the result for regular hexagonal honeycombs is

$$\begin{aligned}\varepsilon_1 &= \frac{1}{(4/\sqrt{3})E_s(t/l)^3}(\sigma_1 - \sigma_2) + \frac{1}{(4/\sqrt{3})E_s(t/l)^3}(3\sigma_1 + \sigma_2) \\ \varepsilon_2 &= \frac{1}{(4/\sqrt{3})E_s(t/l)^3}(\sigma_2 - \sigma_1) + \frac{1}{(4/\sqrt{3})E_s(t/l)^3}(\sigma_1 + 3\sigma_2)\end{aligned}\quad (2.54)$$

The first term, describing the contribution of bending to the strain, depends on the shear stress  $\sigma_1 - \sigma_2$ . It reduces to the previous result  $\varepsilon = \sigma/E^*$  for uniaxial loading. The second term, accounting for axial deformations, depends on  $3\sigma_1 + \sigma_2$  or  $\sigma_1 + 3\sigma_2$ .

The elastic collapse stress is more difficult to analyze. Under a biaxial stress state, the mode of buckling changes, making the calculation of the end constraint factor in the Euler buckling equation difficult. Timoshenko and Gere [59] give a solution for the case of a single square frame subjected to biaxial loading. The results can be approximated to within 10% as a linear interaction between the loads in the two directions.

As a first approximation, can be assumed that the elastic buckling of hexagonal gridworks can be described by

$$\sigma_1 + \sigma_2 = -\frac{n\pi^2 E_s (t^3/lh^2)}{24 \cos \theta} \quad (2.55)$$

with  $n$  given by Table 2.3, deformed cell (a), as before. The plastic collapse stress can be calculated by equating the maximum moment in the honeycomb members to the plastic moment. The maximum moment from the biaxial stress is calculated in the same way as that from a uniaxial stress. The plastic moment is modified by the axial stress  $\sigma_a$  in the member to

$$M_p = \frac{\sigma_{ys} b t^2}{4} \left\{ 1 - \left( \frac{\sigma_a}{\sigma_{ys}} \right)^2 \right\} \quad (2.56)$$

This neglects the beam-column interaction but is an acceptable approximation since at one extreme the member is in almost pure bending with little axial load (and  $M_p = \sigma_{ys} b t^2 / 4$ ) while at the other the member sees pure axial load with no bending (and yield occurs when  $\sigma_a = \sigma_{ys}$ ). The result for the plastic yield surface for a honeycomb with regular hexagonal cells is

$$\pm \left( \frac{\sigma_1}{\sigma_{ys}} - \frac{\sigma_2}{\sigma_{ys}} \right) = \frac{2}{3} \left( \frac{t}{l} \right)^2 \left[ 1 - \left\{ \frac{\sqrt{3^3} (\sigma_1/\sigma_{ys} + (1/3)\sigma_2/\sigma_{ys})}{4t/l} \right\}^2 \right] \quad (2.57)$$

or, in terms of the uniaxial plastic collapse stress  $\sigma_{pl}^* = 2/3 \sigma_{ys} (t/l)^2$ ,

$$\pm \left( \frac{\sigma_1}{\sigma_{pl}^*} - \frac{\sigma_2}{\sigma_{pl}^*} \right) = 1 - \left\{ \frac{\sqrt{3} \left( \frac{\sigma_1}{\sigma_{pl}^*} + \frac{1}{3} \frac{\sigma_2}{\sigma_{pl}^*} \right) t}{l} \right\}^2 \quad (2.58)$$

The strength of the honeycomb in biaxial tension is about eight times the uniaxial tensile strength, reflecting the change from bending to axial deformation of the members.

Brittle failure under a biaxial load is calculated in a similar way. The maximum bending stress in a member is

$$\sigma_{\max} = \frac{6M}{bt^2} \quad (2.59)$$

Crushing of the cell walls occurs when this bending stress plus the axial stress in the wall equals the modulus of rupture  $\sigma_{fs}$  of the cell wall material itself. The brittle failure surface for a regular hexagonal honeycomb is given by

$$\pm \left( \frac{\sigma_1}{\sigma_{fs}} - \frac{\sigma_2}{\sigma_{fs}} \right) = \frac{4}{9} \left( \frac{t}{l} \right)^2 \left\{ 1 - \frac{\sqrt{3^3}}{4(t/l)} \left( \frac{\sigma_1}{\sigma_{fs}} + \frac{1}{3} \frac{\sigma_2}{\sigma_{fs}} \right) \right\} \quad (2.60)$$

or, in terms of the uniaxial crushing strength  $\sigma_{cr}^* = 4/9 \sigma_{fs} (t/l)^2$

$$\pm \left( \frac{\sigma_1}{\sigma_{cr}^*} - \frac{\sigma_2}{\sigma_{cr}^*} \right) = 1 - \frac{1}{\sqrt{3}} \left( \frac{\sigma_1}{\sigma_{cr}^*} + \frac{1}{3} \frac{\sigma_2}{\sigma_{cr}^*} \right) \frac{t}{l} \quad (2.61)$$

### 2.3.6. The multiaxial behavior of foams

The contribution of axial deformation to the behavior of foams under triaxial stress parallels that of honeycombs. The linear elastic moduli must be modified to account for axial deformations under multiaxial stresses. The bending deflection is proportional to the moment acting in the cell wall or to the deviatoric stress  $\sigma_d$

$$\delta_b \propto \frac{Ml^2}{E_s I} \propto \frac{\sigma_d l^5}{E_s t^4} \quad (2.62)$$

while the axial deformation is proportional to the mean stress  $\sigma_m$

$$\delta_a \propto \frac{Pl}{E_s A} \propto \frac{\sigma_m l^3}{E_s t^2} \quad (2.63)$$

The strain in the cell wall is proportional to the total deflection divided by the cell length  $l$ .

Young's modulus, for loading under a uniaxial stress, is then (taking the constants of proportionality to be roughly equal)

$$E^* = \frac{E_s (\rho^* / \rho_s)^2}{1 + \rho^* / \rho_s} \quad (2.64)$$

while the bulk modulus for loading under a hydrostatic stress with  $\sigma_1 = \sigma_2 = \sigma_3 = \sigma$  ( $\sigma_m = \sigma$ ,  $\sigma_d = 0$ ) is

$$K^* = E_s \frac{\rho^*}{\rho_s} \quad (2.65)$$

The elastic buckling failure surface for foams is, like that for honeycombs, difficult to calculate. Part of the difficulty arises from possible changes in the buckling mode under multiaxial stress, and part lies in the difficulty in calculating the change in the rotational stiffness of the vertices of the cells. As a first approximation, Ashby and coworkers [60, 61] assume that there is no change in buckling mode and calculate the change in the rotational stiffness of a single tetrahedral vertex under a compressive hydrostatic pressure  $p$ . From this they find that buckling occurs under a hydrostatic pressure equal to 0.82 of the uniaxial elastic collapse stress  $\sigma_{el}^*$ .

The plastic yield surface is calculated by an extension of the method used for honeycombs. The plastic moment required for the formation of plastic hinges in the cell wall is

$$M_p = \frac{1}{4} \sigma_{ys} t^3 \left\{ 1 - \left( \frac{\sigma_a}{\sigma_{ys}} \right)^2 \right\} \quad (2.66)$$

The average axial stress in the cell wall is proportional to the mean stress divided by  $(t/l)^2$  and the mean stress is  $(\sigma_1 + \sigma_2 + \sigma_3)/3$ . The average bending moment is proportional to the deviatoric stress  $\sigma_d$  times the cube of the edge length:

$$M \propto \sigma_d l^3 \propto l^3 \left[ \frac{1}{2} \left\{ (\sigma_1 - \sigma_2)^2 + (\sigma_2 - \sigma_3)^2 + (\sigma_3 - \sigma_1)^2 \right\} \right]^{1/2} \quad (2.67)$$

Combining these expressions and noting the limits  $\sigma_d = \sigma_{pl}^*$  when  $\sigma_m = 0$  and  $\sigma_m = 1/3 \sigma_{ys} (\rho^*/\rho_s)$  when  $\sigma_d = 0$  gives the yield criterion for an isotropic foam under multiaxial stress:

$$\frac{\sigma_d}{0.3 \sigma_{ys} (\rho^*/\rho_s)^{3/2}} + \left( \frac{3 \sigma_m}{\sigma_{ys} (\rho^*/\rho_s)} \right)^2 = 1 \quad (2.68)$$

or, in terms of the uniaxial plastic collapse stress  $\sigma_{pl}^*$ ,

$$\frac{\sigma_d}{\sigma_{pl}^*} + 0.81 \left( \frac{\sigma_m}{\sigma_{pl}^*} \right)^2 \left( \frac{\rho^*}{\rho_s} \right) = 1 \quad (2.69)$$

The brittle failure surface, too, can be found by an extension of this method. Crushing occurs when the sum of the maximum bending stress and the axial stress equals the modulus of rupture of the cell wall, or when

$$\frac{6M}{t^2} + \sigma_a = \sigma_{fs} \quad (2.70)$$

The moment and axial stress are related to the deviatoric and mean stresses as before. Taking the limits  $\sigma_d = \sigma_{cr}^*$  when  $\sigma_m = 0$  and  $\sigma_m = 1/3 \sigma_{fs} (\rho^*/\rho_s)$  when  $\sigma_d = 0$  gives the brittle failure criterion

$$\frac{\sigma_d}{0.20 \sigma_{fs} (\rho^*/\rho_s)^{3/2}} + \frac{3 \sigma_m}{\sigma_{fs} (\rho^*/\rho_s)} = 1 \quad (2.71)$$

or, in terms of the uniaxial crushing strength  $\sigma_{cr}^*$ ,

$$\frac{\sigma_d}{\sigma_{cr}^*} + 0.60 \frac{\sigma_m}{\sigma_{cr}^*} \left( \frac{\rho^*}{\rho_s} \right)^{1/2} = 1 \quad (2.72)$$

The method outlined here can be extended to anisotropic foams by assuming that the failure surface has the same form as that for the isotropic

case but is rotated such that the intercepts on the three stress axes correspond to the (anisotropic) uniaxial strengths.

## References

- Daniel I.M. and Ishai O., *Engineering Mechanics of Composite Materials*, Oxford University Press, 2006.
- L.J. Gibson, M.F. Ashby, *Cellular solids: structure and properties*, Pergamon Press, 1988.
- J. Zhang, M.F. Ashby, “The out-of-plane properties of honeycombs”, *International Journal of Mechanical Science*, 34(5), 475-489, 1992.

## **Chapter III**

# ***ANALYSIS OF SANDWICH STRUCTURES***

### **3.1. Ordinary sandwich beam theory**

The peculiar morphology of a sandwich panel—the layered and multimaterial structure—requires special attention during the design phase. Reliable stiffness and strength predictions can be made only by using suitable, accurate methodologies accounting for the intrinsic structural complexity and the several failure modes that a panel can experience. The theoretical analysis of sandwich panels is summarized by Allen [1] and more recently by Zenkert [2] and Vinson [3], including a systematic design strategy for stiffness and strength.

In this section the fundamentals of sandwich beam theory will be derived. It is virtually the same as engineering beam theory with the exception that now one must account for transverse shear deformations. This is what is usually called Timoshenko beam theory. Another novelty is that different loads will be carried by different parts of the structure.

#### **3.1.1. Flexural stiffness**

Recall the basic problem of a straight beam subjected to a constant bending moment giving the beam a curvature  $\kappa_x$  (inverse of radius of curvature  $R_x$ ) according to Fig.3.1. This theory is based on these assumptions: the beam bends in a cylindrical manner with no curvature in  $yz$ -plane; cross-sections

which are plane and perpendicular to the longitudinal axis of the beam remain so when the bending takes place. For simplicity, all beams are assumed to have unit width, i.e., loads, stiffness etc. will be given per unit width.

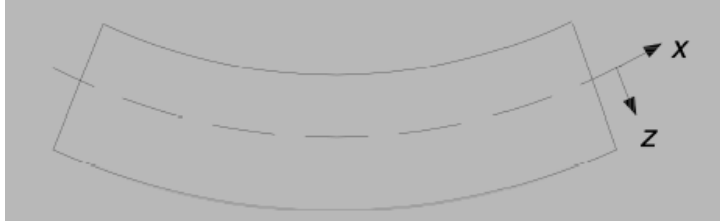


**Figure 3.1 A beam subjected to a bending moment..**

The strain in a fiber situated a distance  $z$  from the neutral axis is now:

$$\varepsilon_x = \kappa_x z \quad (3.1)$$

i.e., linearly varying with  $z$ . The applied bending moment needed to cause the curvature  $\kappa_x$  is then:

$$M_x = \int \sigma_x z dz = \int \frac{Ez^2}{R_x} dz = \kappa_x \int Ez^2 dz = \frac{EI}{R_x}, \text{ where } EI = \int Ez^2 dz = D \quad (3.2)$$

$EI$  is the flexural rigidity which normally is the product of the elastic modulus  $E$  and the moment of inertia  $I$ . From now on,  $EI$  will be designated  $D$  for the following reason; if Young's modulus  $E$  varies along the  $z$ -coordinate then it cannot be removed outside the above integral. Hence, the definition of the moment of inertia  $I$  is lost. Therefore, for a general cross section, eq.(3.2) must be used as given and the flexural rigidity  $D$  will be the only property well defined. The general expression for the bending strain will then be:

$$\varepsilon_x = \frac{M_x z}{D} \quad (3.3)$$

Hence, the strain still varies linearly with  $z$  over the cross-section.

Now that the basic equations are established, one may commence calculating the cross-sectional properties and stresses in a sandwich beam. First, define the coordinate system and positive directions for the loads as in Fig.3.2.

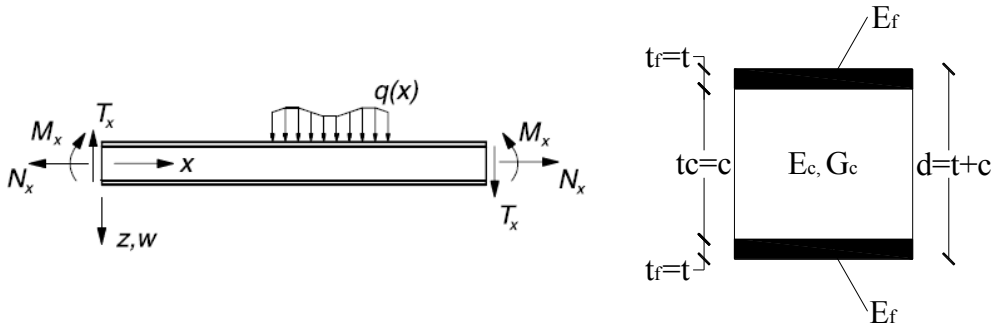


**Figure 3.2** A beam subjected to a bending moment..

In order not to complicate the analysis at this stage, assume a symmetrical lay-up of the sandwich: the faces have the same thickness  $t$  with elastic modulus  $E_f$  and are separated by a relatively thick core of thickness  $c$  and elastic modulus  $E_c$ . It is assumed that all three layers are perfectly bonded together.

The *flexural stiffness*  $D$  is then for a cross-section as in Fig. 3.2.

$$D = \int E z^2 dz = \frac{bt^3}{6} + E_f \frac{btd^2}{2} + E_c \frac{bc^3}{12} = 2D_f + D_0 + D_c \quad (3.4)$$

where  $d$  is the distance between the center lines of the upper and lower faces. The first term  $D_f$  corresponds to the flexural rigidity of the faces alone bending about their individual neutral axes, the second  $D_0$  represents the stiffness of the faces associated with bending about the centroidal axis of the entire sandwich and the third term  $D_c$  is the flexural rigidity of the core.

In real sandwich beams, the faces are usually thin compared with the core, i.e.,  $t_f \ll t_c$ , and the first term of eq.(3.4) is therefore quite small and is less than 1 percent of the second if:

the second term is invariably dominant. In fact, the first and the third terms amount to less than 1% of the second term when

$$3 \left( \frac{d}{t} \right)^2 > 100 \text{ or } \frac{d}{t} > 5.77 \quad (3.5)$$

As a result of materials selection, the core usually has a much lower modulus than that of the face, i.e.,  $E_c \ll E_f$ . Hence, the third term in eq.(3.4) is less than 1 percent of the second if

$$6 \frac{E_f}{E_c} \frac{t}{c} \left( \frac{d}{c} \right)^2 \geq 100. \quad (3.6)$$

So, equation (3.4) becomes:

$$D \approx E_f \frac{btd^2}{2} \quad (3.7)$$

### 3.1.2. Stresses in the sandwich beam

Using the strain definition in eq.(3.3), the stresses in the sandwich due to bending are readily found. The face and core stresses are:

$$\begin{aligned} \sigma_f &= \frac{M_x z E_f}{D} \quad \text{for } \frac{c}{2} < |z| < \frac{c}{2} + t \\ \sigma_c &= \frac{M_x z E_c}{D} \approx 0 \quad \text{for } |z| < \frac{c}{2} \end{aligned} \quad (3.8)$$

Hence, the stresses vary linearly within each material constituent, but there is a jump in the stress at the face/core interface.

The direct stress and strain due to an in-plane load is simply:

$$\varepsilon_{x0} = \frac{N_x}{2E_f t + E_f c} = \frac{N_x}{A_x}, \quad \text{and thus } \sigma_f = \varepsilon_{x0} E_f \quad \text{and} \quad \sigma_c = \varepsilon_{x0} E_c \quad (3.9)$$

where  $\varepsilon_{x0}$  is the strain at the neutral axis. The strains and stresses due to bending and in-plane loads can then be superimposed.

In the same manner as outlined above, a more general definition must also be found for the shear stress. Consider an element  $dx$  of a beam (for example of the beam in Fig.3.2) as shown in Fig.3.3. The shear force must balance the change in the direct stress field (the same equation arises by integration of the equilibrium equation)

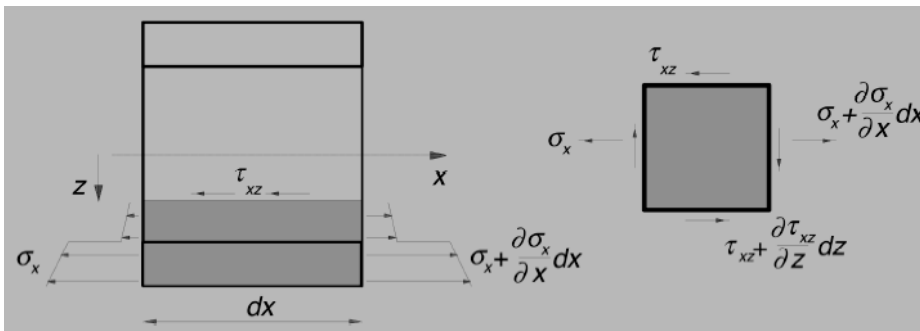


Figure 3.3 Beam section  $dx$  defining equilibrium for a sub-area.

$$\frac{d\sigma_x}{dx} + \frac{d\tau_{xy}}{dz} = 0 \rightarrow \tau_{xy}(z) = \int_z^{(d+t)/2} \frac{d\sigma_x}{dx} dz \quad (3.10)$$

when using the fact that  $\tau_{xz}$  at  $d/2+t$  is zero. Now, using  $dM_x/dx = T_x$  :

$$\tau_{xy}(z) = \frac{T_x}{D} \int_z^{(d+t)/2} E z dz = \frac{T_x B(z)}{D} \quad (3.11)$$

where  $B(z)$  is the first moment of area. The formula reduces for a homogeneous cross-section to the more well-known formula  $T_x J(z)/I$  where  $J$  is the first moment of area by its most usual definition. Now, instead, the integral

$$B(z) = \int_z^{(d+t)/2} E z dz \quad (3.12)$$

is the new, and more general, definition for the first moment of area. In the core material for  $|z| \leq c/2$  the first moment of area is

$$B(z) = \frac{E_f t d}{2} + \frac{E_c}{2} \left( \frac{c}{2} - z \right) \left( \frac{c}{2} + z \right) \quad (3.13)$$

Yielding the shear stress in the core

$$\tau_c(z) = \frac{T_x}{D} \left[ \frac{E_f t d}{2} + \frac{E_c}{2} \left( \frac{c^2}{4} - z^2 \right) \right] \quad (3.14)$$

And similarly in the faces for  $c/2 \leq |z| \leq t+c/2$

$$B(z) = \frac{E_f}{2} \left( \frac{c}{2} + t - z \right) \left( \frac{c}{2} + t + z \right) \Rightarrow \tau_f(z) = \frac{T_x}{D} \frac{E_f}{2} \left( \frac{c^2}{2} + ct + t^2 - z^2 \right) \quad (3.15)$$

The maximum shear stress appears at the neutral axis, i.e., for  $z=0$ .

$$\tau_{c,\max}(z=0) = \frac{T_x}{D} \left( \frac{E_f t d}{2} + \frac{E_c c^2}{8} \right) \quad (3.16)$$

And the shear stress in the face/core interface will be

$$\tau_{c,\max} = \tau_{f,\max} = \tau \left( z = c/2 \right) = \frac{T_x}{D} \left( \frac{E_f t d}{2} \right) \quad (3.17)$$

the shear stress in the outer fiber of the faces is zero, which evidently must be the case for a free surface.

The approximations can now be summarized on stresses equations as: if the core is weak,  $E_c \ll E_f$ , the stresses can be written

$$\begin{aligned} \sigma_c(z) &= 0; & \sigma_f(z) &= \frac{M_x z E_f}{(D_0 + 2D_f)} \\ \tau_c(z) &= \frac{T_x E_f t d}{2(D_0 + 2D_f)} & \tau_f(z) &= \frac{T_x}{2(D_0 + 2D_f)} \frac{E_f}{2} \left( \frac{c^2}{4} + ct + t^2 - z^2 \right) \end{aligned} \quad (3.18)$$

if the core is weak,  $E_c \ll E_f$  and the faces are thin  $t \ll c$ , the eqs. (3.18) reduce to the simplest possible form

$$\sigma_c(z) = 0; \quad \sigma_f(z) = \pm \frac{M_x}{td}; \quad \tau_c(z) = \frac{T_x}{d}; \quad \tau_f(z) = 0 \quad (3.19)$$

This simplifies the modus operandi or the principal load carrying and stress distributions in a structural sandwich construction to: the faces carry bending moments as tensile and compressive stresses and the core carries transverse forces as shear stresses.

The stress distributions for the different degrees of approximation can also be graphically represented by plotting the above equations as functions of  $z$ , as illustrated in Fig.3.4.

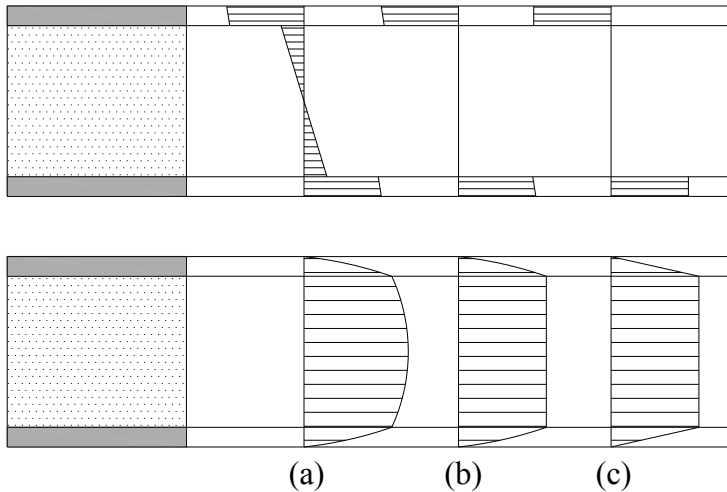


**Figure 3.4 Direct and shear stresses for different levels of approximations: (a) true stresses distribution; (b) effect of weak core; (c) effect of weak core, neglecting the local bending stiffness of the skins;**

### 3.1.3. Shear deformation and stiffness

For sandwich beams it is necessary to account for transverse shear deformations. In classical engineering beam theory these are rightfully neglected as they add only marginally to the total deformation of beams with relatively high shear stiffness, such as beams with homogeneous cross-sections. The only case where transverse shear deformations must be accounted for even for shear stiff beams is if the beams are short, for which engineering beam theory is hardly valid anyway, and two or three dimensional elasticity theory must be used.

For any type of structure, e.g., beams, plates or shells, the deformation always consists of two parts: (i) deformations due to bending moments  $w_b$ ; (ii) deformations due to shear forces  $w_s$ .

Shear deformations are usually neglected in classical analysis of structures with homogeneous cross-sections unless the studied member has a very short span, because the shear part is usually only a small fraction of the bending part. But for short beams or cross-sections with low shear stiffness this deformation component must be included and for sandwich beams the latter is commonly true. For a sandwich with thin faces the two deformation parts may be superimposed as

$$w = w_b + w_s \quad (3.20)$$

When a structural element is subjected to shear forces it will deform, without volume change however, according to Fig.3.5. This deformation can be divided into two different parts, *transverse* (middle) and *in-plane* (far right) shear deformation.

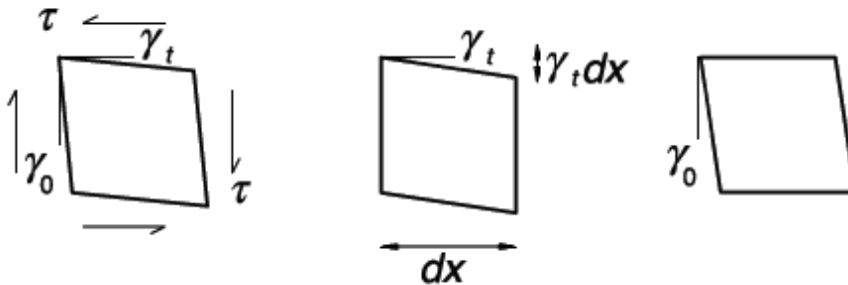
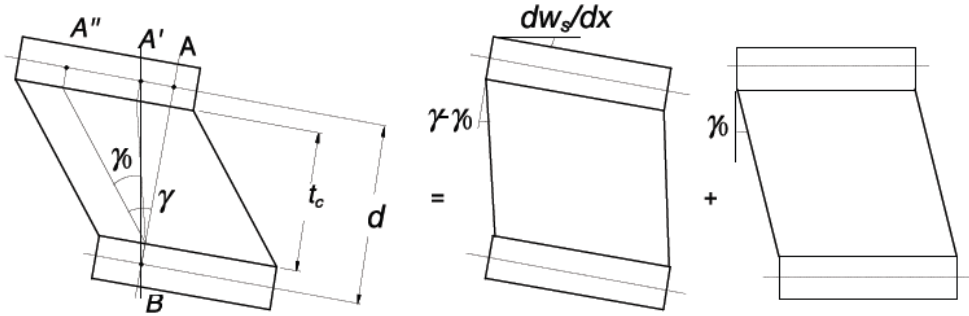


Figure 3.5 Deformation of a structural element subjected to shear forces.

These are again schematically illustrated in Fig.3.6 but drawn with the assumption that the shear deformation only occurs in the core, i.e. with  $G_f = \infty$ , and that this deformation is linear, i.e.,  $E_c \ll E_f$  giving a constant core shear stress ( $\tau_{xz} = T_x/d$ ) and a constant shear strain.



**Figure 3.6** Shear deformation of a sandwich element.

Denote the total shear in the core by  $\gamma$  and the in-plane core shear part by  $\gamma_0$ . By studying Fig. 3.6, the following geometrical relation is found which is valid for a general case where a part of the shear deformation also may occur in the plane of the beam. A straight line A-B prior to deformation has moved due to the shear deformation; first the point A has moved to position A' due to the out-of-plane shear and then another distance, from A' to A'', due to the in-plane shear. Hence, the distance between A and A' can then be written

$$\frac{dw_s}{dx} d = (\gamma - \gamma_0) c \Rightarrow \frac{dw_s}{dx} = \frac{\gamma c}{d} - \frac{\gamma_0 c}{d} = \frac{T_x}{U} - \frac{\gamma_0 c}{d} \rightarrow \frac{d^2 w_s}{dx^2} = \frac{1}{U} \frac{dT_x}{dx} \quad (3.21)$$

since approximately equals  $T_x/Gd$ . By integration can be obtained that

$$w_s = \int_0^x \left( \frac{T_x}{U} - \frac{\gamma_0 c}{d} \right) dx = \frac{M_x}{U} \frac{\gamma_0 c x}{d} + \text{constant} \quad (3.22)$$

or

$$U w_s = M_x + A x + B \text{ constant} \quad (3.23)$$

where  $U$  is the shear stiffness. Solving for  $w_s$  leaves two unknown constants to be found from the boundary conditions. As seen,  $\gamma_0$  or  $A$  corresponds to a rigid body rotation and  $B$  to a rigid body translation, which are both governed by boundary conditions.

The shear stiffness of a cross-section is defined as the relation between some measure of the shear strain and the transverse force,  $\gamma = T_x/U$ . For a homogeneous cross-section the shear stiffness,  $U$ , is often written as:

$$U = \frac{Gh}{k} \quad (3.24)$$

where  $G$  is shear modulus,  $h$  the height and  $k$  a shear factor, which for a rectangular homogeneous cross-section equals 1.2. For a general cross-section, the shear stiffness can be computed more accurately by using an energy balance equation, that is, so that the potential energy of the applied load equals the strain energy of the system. The shear stiffness,  $U$ , is found by calculating the average shear angle of the cross-section,  $\gamma$ . This then becomes

$$\frac{1}{2} T_x \gamma = \frac{1}{2} \int \tau_{xy}(z) \gamma_{xy}(z) dz, \text{ where by definition } \gamma = \frac{T_x}{U} \quad (3.25)$$

Using the approximations for a sandwich with thin faces,  $t \ll c$ , weak core,  $E_c \ll E_f$ , and that the shear modulus of the faces  $G_f$  are large, it is seen that  $\tau_{xz} = T_x/d$ . Eq.(25) then becomes

$$\frac{1}{2} T_x \gamma = \frac{1}{2} \int_{-c/2}^{c/2} \frac{T_x}{d} \frac{T_x}{G_c d} dz = \frac{T_x^2 c}{2G_c d^2} = \frac{T_x^2}{2U} \quad (3.26)$$

so that the shear stiffness is defined by

$$U = \frac{G_c d^2}{c} \quad (3.27)$$

### 3.1.4. Governing equation

Next consider the beam in Fig.3.2 again along with Fig 3.7 defining local coordinate systems for the faces and the core. First define the kinematic assumption, namely that the in-plane and out-of-plane deformations can be written as

$$u(z) = u_0 + z\theta_x \text{ and } w = w_b + w_s \quad (3.28)$$

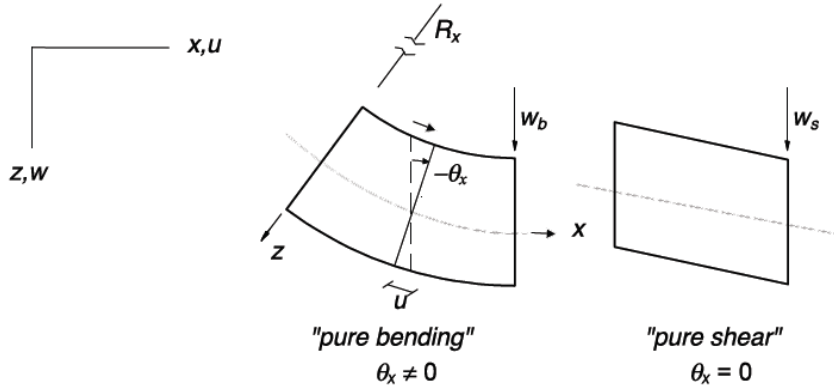


**Figure 3.7** Definition of deflections, rotation, bending and shear of a sandwich cross-section.

where the in-plane deformation  $u$  is thus a linear function in  $z$ , and  $\theta_x$  is the cross-section rotation (defined as a positive rotation about the  $y$ -axis), which only depends on the bending deformation  $w_b$  of the beam (since shear only causes sliding of the cross-section). Thus,

$$\theta_x = -\frac{dw_b}{dx} \quad \text{and} \quad \varepsilon(z) = \frac{du}{dx} = \frac{du_0}{dx} + z \frac{d\theta_x}{dx} = \frac{du_0}{dx} + z \frac{d^2w_b}{dx^2} \quad (3.29)$$

It is important to realize at this stage the difference between engineering beam theory and the present formulation. In engineering beam theory, the shear deformations are zero and this implies that we have a restriction in the kinematics so that  $\theta = -dw/dx$ . This will in some cases have a profound effect on the theory, especially for the development of finite elements for beam problems.

The governing equation for the shear part has already been obtained. For bending, they are the same of the ordinary beam bending theory. Assuming small deflection theory, the radius of curvature can be found in terms of the displacement field by a geometrical study as outlined in Fig. 3.8.

From Fig. 3.8, it is then seen that,  $dx = R_x d\varphi$ , and  $d\varphi - (\theta_x + dx d\theta_x/dx) = -\theta_x$ , so that  $d\varphi = dx d\theta_x/dx$ . This means that

$$\frac{1}{R_x} = \kappa_x = \frac{d\theta_x}{dx} = -\frac{d^2w_b}{dx^2} \quad (3.30)$$

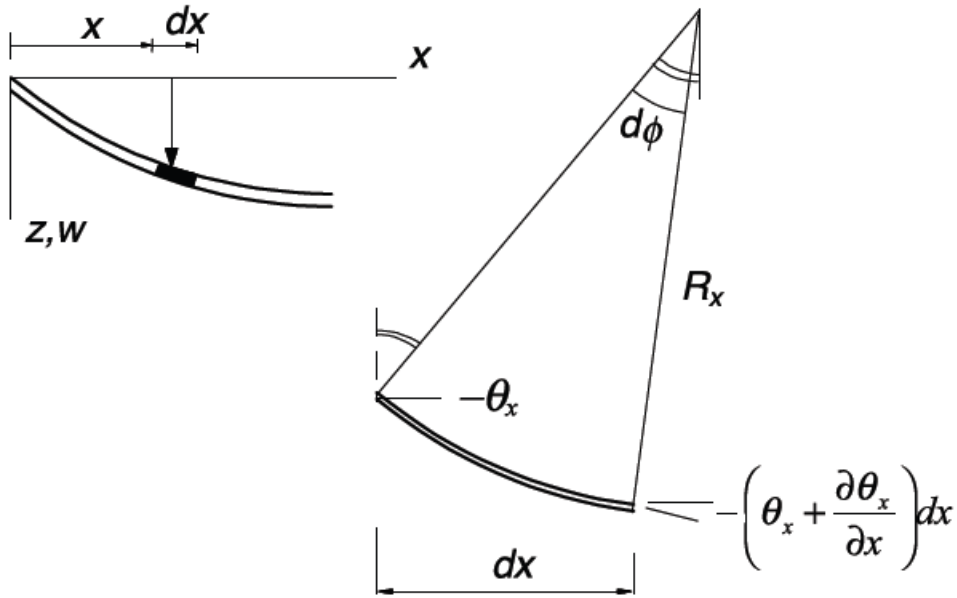


**Figure 3.8** Definition of curvature.

There are now several ways to proceed with the beam theory. It is possible to write the average shear strain as

$$\gamma = \frac{dw}{dx} + \theta_x = \frac{T_x}{U} \quad (3.31)$$

or using partial deflections equivalently as

$$\frac{dw_s}{dx} = \frac{dw}{dx} - \frac{dw_b}{dx} = \frac{T_x}{U} \quad (3.32)$$

The bending moment can now also be written as

$$M_x = \int \sigma_x z dz = \int \frac{Ez^2}{R_x} dz = \frac{d\theta_x}{dx} \int Ez^2 dz = D \frac{d\theta_x}{dx} = -D \frac{d^2 w_b}{dx^2} \quad (3.33)$$

There are several ways to describe the kinematics of a sandwich beam. In the general case, as for plates, one commonly use the displacement  $w$  and the rotation  $\theta$  as variables, and as seen above, all other properties like bending moments, transverse forces, shear strains, etc, can be obtained as function of these variables. This approach is somewhat more straightforward when one shall, for example, derive finite elements, since then the displacement and rotation are equivalent to physical degrees-of-freedom in the finite element formulation. The partial deflection  $w_b$  and  $w_s$  can equivalently use to describe

the same properties. The final governing equations can still be obtained in one single variable  $w$  irrespective of choice of variables. The choice of partial deflections is used here since it provides a more physical interpretation of the modes of deformation of a sandwich beam.

The most straightforward way is by direct integration of the differential equations for the partial deflections. Taking the beam part deflection first and then the shear part, these equations are integrated in general terms to

$$D \frac{d^4 w_b}{dx^4} = q \rightarrow Dw_b = M_x = \iiint \iiint q dx^4 + A_1 \frac{x^3}{6} + A_2 \frac{x^2}{2} + A_3 x + A_4 \quad (3.34)$$

$$U \frac{d^2 w_s}{dx^2} = -q \rightarrow Uw_s = -\iint q dx^2 - A_1 x + A_2$$

where the  $A$ 's are integration constants. The total deflection can thus be written as

$$w(x) = w_b(x) + w_s(x) = \frac{1}{D} \left\{ \iiint \iiint q dx^4 + A_1 \frac{x^3}{6} + A_2 \frac{x^2}{2} + A_3 x + A_4 \right\} + \frac{1}{U} \left\{ \iint q dx^2 - A_1 x + A_2 \right\} \quad (3.35)$$

The four integration constants can be found by the boundary conditions of the problem.

For example, consider a simply supported sandwich beam (Fig. 3.9) of span  $L$ , width  $b$  and central load  $W$ . Assume thin faces,  $t \ll c$ , and weak core,  $E_c \ll E_f$ , and that all other material data are known. The flexural rigidity and the shear stiffness are:

$$D = \frac{E_f t d^2}{2} \quad \text{and} \quad S = \frac{G_c d^2}{c} \quad (3.36)$$

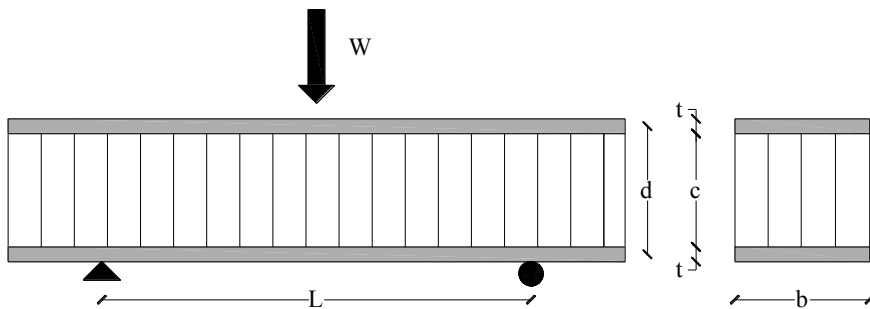


Figure 3.9. Simply supported beam and its cross-section.

The maximum shear force,  $T_x$ , is equal to  $W/2$  and the maximum bending moment at the midspan  $M_{x\max}$  is equal  $WL/4$  and the corresponding maximum stress  $\sigma_f$  in the skins is given by:

$$\sigma_f = \pm \frac{M}{D} E_f \frac{d}{2} = \frac{WL}{4dt} \quad (3.37)$$

whereas the constant core shear stress is given by

$$\tau_c = \frac{W}{2bd} \quad (3.38)$$

The total deflection  $w_{\max}$  at midspan of a sandwich beam loaded in three-point bending is the sum of the deflection due to the bending of the face sheets and the shear of the core:

$$w_{\max} = \frac{WL^3}{48D} + \frac{WL}{4U} \quad (3.39)$$

### 3.1.5. Wide and narrow beams

In the above analysis it is assumed that sandwich beams bend in a cylindrical manner (no curvature in the  $y$ - $z$  plane). If the beam is narrow, in the sense that the width  $b$  is less than the core depth  $c$ , the lateral expansions and contractions of the faces in the  $y$  direction (associated to the membrane stresses in the  $x$  direction) may take place fairly freely without causing unduly large shear strain in the core in the  $y$ - $z$  plane. The faces are therefore mainly in a state of unidirectional stress and the ratio to stress-strain is equal to  $E$ . The same argument does not apply to local bending stresses in the faces; each face is a thin plate in a cylindrical bending and the ratio of stress to strain is strictly  $E/(1-\nu^2)$ . However, these stresses and strains are of secondary importance and it seems reasonable to adopt  $E$  throughout in order to avoid undue complication.

If the beam is wide, in the sense that the width  $b$  is greater than the core depth  $c$ , the lateral expansions and contractions of the faces in the  $y$  direction are severely restricted by the inability of the core to undergo indefinitely large shear deformations in the  $y$ - $z$  plane. In this case it may be more reasonable to assume that the strains in the  $y$  direction are zero. The ratio of stress to strain in the  $x$  direction is therefore  $E/(1-\nu^2)$  for both the membrane stresses and the

local bending stresses, and this value should be used in place of  $E$  in all the above equations.

### 3.2. High-order sandwich beam theory

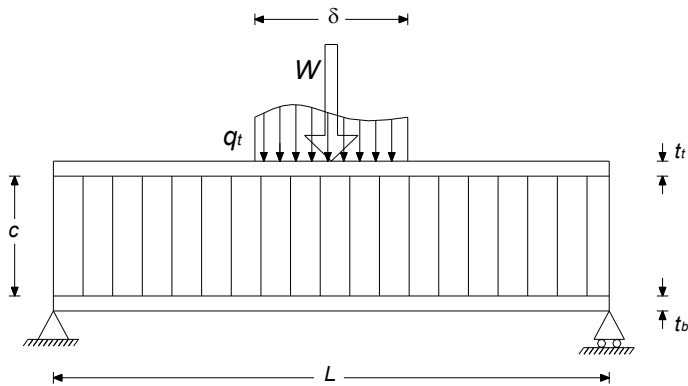
Fundamental analyses of sandwich beams assume that the core is incompressible in the out-of-plane direction. These models further assume that the skins have only bending rigidity while the core has only shear rigidity. This approach is appropriate for sandwich structures with incompressible cores. To model the local effects at the load points for non-metallic honeycomb sandwich panels with low transverse stiffness, deformation of the core in the vicinity of the applied loads must be considered. Accordingly the elastic foundation model has been applied to this problem [3,4]. However foundation models neglect interactions between the top and bottom skins. The non-planar deformed cross-section of the sandwich beams, observed in experiments, suggests a model that allows non-linear variations of in-plane and vertical displacements through the thickness of the core. Frostig and Baruch [5-7] used variational principles to develop a higher-order sandwich panel theory, which includes the transverse flexibility of the core and the displacements that vary nonlinearly through the thickness. This section presents a high-order sandwich beam (HOSBT) approach based on that introduced by Frostig and Baruch [6]. The basic assumptions of the HOSBT approach in [6] are:

- the shear stresses in the core are uniform through the thickness of the core;
- the core vertical displacement variation is a quadratic polynomial in  $z$ , allowing the core to distort and its height to change;
- the core is considered as a 3D elastic isotropic medium, which has significant out-of-plane compressive and shear rigidity, but negligible in-plane normal and shear rigidity.
- the skins are thin, elastic, isotropic plates

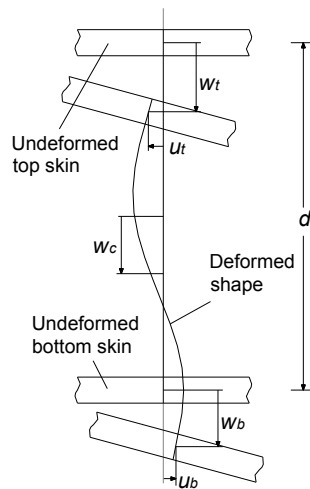
In the present investigation, the 3D problem of [6] is reduced to a 2D problem. A sandwich beam (see Fig. 3.10a) of span  $L$ , unit width and

distributed load on the top skin  $q_t$ , consisting of a core with thickness  $c$ , Young's modulus  $E_c$  and shear modulus  $G_c$  and two skins with the same thickness  $t=t_t=t_b$ , Young's modulus  $E_f$  and Poisson's ratio  $\nu_f$  is considered. The model is 2D because variations in displacements across the width are neglected.

The displacement and stress of the core are expressed in terms of the in-plane deformations the top and bottom skins in the  $x$ -direction  $u_t$  and  $u_b$ , respectively, the corresponding vertical displacements  $w_t$  and  $w_b$  at the mid-plane of the skins, and of the shear stresses  $\tau_x$  in the core. The notation is illustrated in Fig. 3.10b.



(a)



(b)

**Figure 3.10. (a) Sandwich beam configuration; (b) Non-linear displacement of a sandwich beam section.**

The governing equations given by [6], adapted to a two-dimensional model, are:

$$\left\{ \begin{array}{l} A_t \frac{\partial^2 u_t}{\partial x^2} + \tau_x = 0, \\ A_b \frac{\partial^2 u_b}{\partial x^2} - \tau_x = 0, \\ D_t \frac{\partial^4 w_t}{\partial x^4} - \frac{E_c}{c} (w_b - w_t) - \frac{c+t}{2} \frac{\partial \tau_x}{\partial x} = q_t, \\ D_b \frac{\partial^4 w_b}{\partial x^4} - \frac{E_c}{c} (w_b - w_t) - \frac{c+t}{2} \frac{\partial \tau_x}{\partial x} = 0, \\ u_t - u_b - \frac{c+t}{2} \frac{\partial w_t}{\partial x} - \frac{c+t}{2} \frac{\partial w_b}{\partial x} - \frac{c}{G_c} \tau_x - \frac{c^3}{12E_c} \frac{\partial \tau_x}{\partial x} = 0, \end{array} \right. \quad (3.40)$$

where:

$$A_t = A_b = \frac{E_f t}{(1 - \nu_f^2)}, \quad (3.41)$$

$$D_t = D_b = \frac{E_f t^3}{12(1 - \nu_f^2)}; \quad (3.42)$$

are the in-plane and flexural rigidities, respectively, of the skins.

For a simply supported sandwich beam, the solution can be expressed as a Fourier series expressing the variation of the relevant variables in the  $x$ -direction as:

$$u_t(x) = \sum_{m=1}^M C_m^{ut} \cos \frac{m\pi x}{L}; \quad (3.43)$$

$$u_b(x) = \sum_{m=1}^M C_m^{ub} \cos \frac{m\pi x}{L}; \quad (3.44)$$

$$w_t(x) = \sum_{m=1}^M C_m^{wt} \sin \frac{m\pi x}{L}; \quad (3.45)$$

$$w_b(x) = \sum_{m=1}^M C_m^{wb} \sin \frac{m\pi x}{L}; \quad (3.46)$$

$$\tau_x(x) = \sum_{m=1}^M C_m^{\tau x} \cos \frac{m\pi x}{L}; \quad (3.47)$$

where  $m$  is an index for wavelength of the Fourier term and  $M (=3000)$  is the number of terms in the Fourier series. The Fourier coefficients  $C_m^i$  are constants to be determined. It is assumed that the external load is applied only on the top skin. In this way it can be expressed in terms of the Fourier series:

$$q_t(x) = \sum_{m=1}^M C_m^{qt} \sin \frac{m\pi x}{L}; \quad (3.48)$$

where  $C_m^{qt}$  is a constant that depends on the distribution of the external load. To simplify calculations, the indentation line load,  $W$ , is assumed to be applied to the beam uniformly. This assumption is appropriate for sandwich panels typically used in industry, as discussed in detail by Patras and Sutcliffe [10]. So, the Fourier coefficient  $C_m^{qt}$  is given by:

$$C_m^{qt} = \frac{4W}{m\pi\delta} \sin\left(\frac{m\pi}{2}\right) \sin\left(\frac{m\pi\delta}{2L}\right). \quad (3.49)$$

After substituting every term of the Fourier series, Eqs. (11-15), into the governing Eq. (3.40), the problem can be expressed in matrix form as:

$$[H] \cdot [C] = [Q] \quad (3.50)$$

where:

$$[H] = \begin{bmatrix} -A_i \left(\frac{m\pi}{L}\right)^2 & 0 & 0 & 0 & 1 \\ 0 & -A_b \left(\frac{m\pi}{L}\right)^2 & 0 & 0 & -1 \\ 0 & 0 & -D_i \left(\frac{m\pi}{L}\right)^4 + \frac{E_c}{c} & -\frac{E_c}{c} & \frac{c+t}{2} \frac{m\pi}{L} \\ 0 & 0 & -\frac{E_c}{c} & -D_c \left(\frac{m\pi}{L}\right)^4 + \frac{E_c}{c} & \frac{c+t}{2} \frac{m\pi}{L} \\ 1 & -1 & -\frac{c+t}{2} \frac{m\pi}{L} & -\frac{c+t}{2} \frac{m\pi}{L} & \frac{c}{G_c} + \frac{c^3}{12E_c} \left(\frac{m\pi}{L}\right)^2 \end{bmatrix} \quad (3.51)$$

$$C = \begin{bmatrix} C_m^{ut} \\ C_m^{ub} \\ C_m^{wt} \\ C_m^{wb} \\ C_m^{\tau x} \end{bmatrix} \text{ and } Q = \begin{bmatrix} 0 \\ 0 \\ C_m^{qt} \\ 0 \\ 0 \end{bmatrix} \quad (3.52)$$

Solving Eq. (3.50) for  $C$ , the problem can be expressed as:

$$[C] = [Q][H]^{-1} \Rightarrow \begin{bmatrix} C_m^{ut} \\ C_m^{ub} \\ C_m^{wt} \\ C_m^{wb} \\ C_m^{\tau x} \end{bmatrix} = C_m^{qt} \begin{bmatrix} C & & & & \\ \bar{R} & \bar{R} & & & \\ & C & & & \\ \bar{R} & \bar{R} & & & \\ & & R & & \\ \bar{Z} & N & R & R & \\ & & R & & \\ \bar{Z} & N & R & R & \\ & & Q & C & \\ \bar{R} & \bar{R} & & & \end{bmatrix} \quad (3.53)$$

where:

$$\left\{ \begin{array}{l} Q \\ Z \\ N \\ C \\ \Omega_c \\ R \\ R \end{array} \right. \begin{array}{l} \left( \frac{m\pi}{L} \right)^2, \\ \left( \frac{m\pi}{L} \right)^4 + \frac{E_c}{c}, \\ \bar{c}, \\ \frac{m\pi}{L}, \\ \frac{c}{G_c} + \frac{c^3}{12E_c} \left( \frac{m\pi}{L} \right)^2, \\ Z \quad Q \quad Q \quad C \\ N \quad Z \quad Q \quad C \end{array} \quad (3.54)$$

In this way, all the in-plane and out-of-plane displacements and the core shear stresses can be calculated. The in-plane normal stresses in the top skin,

$\sigma_{txx}$ , and out-of-plane normal stresses in the top skin-core interface,  $\sigma_{zz}$ , can be calculated indirectly as:

$$\sigma_{txx} = E_f \frac{\partial u_t}{\partial x}; \quad (3.55)$$

$$\sigma_{zz} = \frac{c}{2} \frac{\partial \tau_x}{\partial x} + \frac{E_c}{c} (w_b - w_t); \quad (3.56)$$

Substituting Eqs. (3.45-3.47) and the above Fourier coefficients into (3.56), the normal stresses in the top skin-core interface are given as:

$$\sigma_{zz} = \sum_{m=1}^M \left( -\frac{c}{2} \frac{m\pi}{L} C_m^{rx} + \frac{E_c}{c} (C_m^{wb} - C_m^{wt}) \right) \sin \frac{m\pi x}{L} = \sum_{m=1}^M C_m^{qt} \left( -\frac{cmx}{2L} \begin{matrix} \text{Q} & \text{C} & \text{N} \\ \text{R} & \text{R} & \text{Z} & \text{N} \end{matrix} \frac{m\pi x}{L} \right) \quad (3.57)$$

Equation (25) shows that the Fourier coefficients for the stress  $\sigma_{zz}$  at the skin-core interface can be separated into two parts: the first part consists of the coefficient  $C_m^{qt}$ , which depends only on the distribution of the load; the second part represents the “transmission coefficient” [10]  $C_m^{\sigma_{zz}}$  that depends on the geometric and materials properties of the sandwich beam and on the semi-wavelength of the  $m^{\text{th}}$  term of the Fourier series.

The equations described in this section can be implemented using commercial program language to calculate the beam response. Moreover the vertical displacement of the core is derived by [8]:

$$w_c(x, z) = -\frac{\partial \tau_x}{\partial x} \frac{-z^2 + cz}{2E_c} + (w_b - w_t) \frac{z}{c} + w_t \quad (3.58)$$

### 3.3. Numerical simulation

Considering the complicated geometry of the real sandwich structures, the more suitable tools for the structural analysis seem to be the finite element codes. A great accuracy in the analysis can be reached even for large, complicated structures due to the huge computational capabilities of the recent computers. The Finite Element modeling of a sandwich structure can be approached using different strategies: (i) the simplest bi-dimensional way, by using layered shell elements and a tri-dimensional model where both skins and honeycomb cells are modelled with shell elements; (ii) model the skins with layered shell elements and the core with isotropic (in the case of foam)

or orthotropic (in the case of honeycomb) solid elements; (iii) use layered solid elements for the skins and solid elements for the core; (iv) a further possible solution for a through-the-thickness analysis is the bidimensional modeling of a panel section with 2D elements under plane strain conditions. As said for the analytical methods, even by using finite element analysis, the greater degree of accuracy obtained for instance by using sophisticated 3D solid models is paid in terms of modeling and solution time as well as in a more complicated evaluation of the results. The correct analysis of the stress fields due to the local effects requires, however, very accurate and refined models. In the attempt to satisfy the accuracy requirements and limit the drawbacks, after a preliminary analysis on a shell element model, a sub-modeling of the critical zones of the structure can be carried out by using 3D solid models. Another option is the combined use of 2D (shell) and 3D (solid) elements in the same FE model. In this case, however, great attention and experience is required for the calibration of the model and for the validation of the coupling procedure between 2D and 3D elements. Despite the modeling strategy adopted, the use of correct input data for the constituent properties is of fundamental importance, considering their great influence on the final results. This note seems to be obvious and trivial but, actually, it is very important indeed due to the frequent lacking of reliable data for composite laminates and honeycomb cores, particularly for the out-of-plane properties.

### **3.4. Failure mode**

#### **3.4.1. Skin failure**

The expressions for the maximum stress in the face sheets derived by sandwich beam theory can be used to predict the beam failure due to the skin failure modes—i.e., face ultimate strength, face wrinkling and intra-cellular buckling (Fig. 3.11). In a symmetric beam, the stress is the same in the compression and tension faces.

For composite faces, the critical face is generally the compressive face. The failure occurs when the axial stress in either of the skins,  $\sigma_f$ , reaches the in-

plane ultimate strength,  $F_c$ .

$$\sigma_f = F_c. \quad (3.59)$$

In the case of wrinkling of the compression face, the wavelength of the buckled face is of the same order as the thickness of the core. This problem may be analyzed as the buckling of a beam (the face sheet) supported transversely by an elastic foundation (the core). With three-point bending, wrinkling of the top skin occurs in the vicinity of the central load. Allen [1] gives the critical compressive stress  $\sigma_{fw}$  that results in wrinkling:

$$\sigma_{fw} = B_1 E_f^{\frac{1}{3}} E_c^{\frac{2}{3}}, \quad (3.60)$$

where:

$$B_1 = 3 \left[ 12(3 - \nu_{cz})^2 (1 + \nu_{cz})^2 \right]^{\frac{1}{3}} \quad (3.61)$$

and  $\nu_{cz}$  and  $E_c$  are respectively the out-of-plane Poisson's ratio and Young's modulus of the core.

A sandwich with a honeycomb core may fail by buckling of the face in a small region where it is unsupported by the walls of the honeycomb. The following expression has been proposed [15] for the in-plane stress  $\sigma_{fi}$  in the skin at which intra-cellular buckling occurs:

$$\sigma_{fi} = \frac{2E_f}{(1 - \nu_f^2)} \left( \frac{t}{R} \right)^2, \quad (3.62)$$

where  $R$  is the cell size of the honeycomb core.

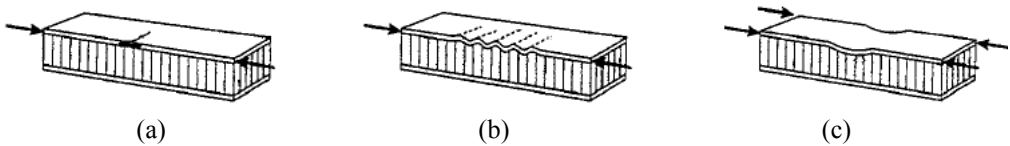


Figure 3.11. Skin failure modes: (a) compressive failure; (b) intra-cell buckling; (c) wrinkling failure.

### 3.4.2. Core failure

Sandwich structures loaded in bending can fail due to core failure. Pertinent modes are shear failure or indentation by local crushing in the vicinity of the loads application.

Shear failure (Fig. 3.12a) occurs when the applied shear stress,  $\tau_c$ , equals the shear strength,  $\tau_{cu}$ , of the core:

$$\tau_c = \tau_{cu}. \quad (3.63)$$

In the case of honeycomb cores, should be considered that the honeycomb core shows two different values of the ultimate shear strength in the two in-plane directions, depending on the direction of the honeycomb ribbon.

Indentation failure (Fig. 3.12b) is predicted when the out-of-plane compressive stress,  $\sigma_z$ , equals the out-of-plane compressive strength,  $\sigma_{cc}$ , of the core. Knowing the length of contact,  $\delta$ , between the central loading bar and the top face sheet, it is assumed that the load is transferred uniformly to the core over this contact length. The out-of-plane compressive stress in the core is assumed to be given by:

$$\sigma_z = \frac{W}{b\delta}. \quad (3.64)$$

To evaluate the core failure mechanism, stiffness and strength properties for honeycomb and foam core are required. As described in the previous chapter the data required for the failure analysis can be derived using the given relations between the properties of the core and its solid material.



Figure 3.12. Core failure modes: (a) shear failure; (b) indentation failure.

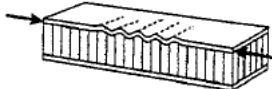
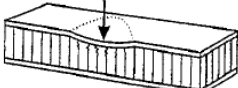
### 3.4.3. Failure mode map

The critical failure mode for a particular beam design can be found using a failure mode map. The map is constructed as follows. Noting that each of the failure equations depends on the beam width  $b$  and the core depth  $c$  in the same way, the transition from one failure mode to another can be expressed in terms of two variables: the ratio  $t/L$  of the face thickness to the beam span and the relative density  $\rho^*/\rho_s$  of the core. By using simple mechanics models based on the review of cellular structures models, the core shear properties

can be expressed as function of the core relative density and solid characteristics, i.e. compressive strength  $\sigma_{sc}$ , elastic  $E_c$  and shear modulus  $G_c$ . Using these two beam design parameters as the axes of the failure mode map, the transitions between one failure mode and another can plot on the map by simply equating pairs of failure equations in turn.

Table 3.1 reports the failure equations in the case of a sandwich beams, with thin skins and weak core, loaded in three point bending. The equations of core failure are expressed as function of  $K_1$ ,  $n$ ,  $K_2$ , and  $m$  constants, which can be evaluated for both honeycomb and foam core on the basis of cellular structure and solid material.

**Table 3.1. Failure equation for three-point bending configuration**

Skin compressive failure		$W_0 = 4dF_c \left( \frac{t}{L} \right)$
Intra-cell buckling		$W_0 = \frac{8dE_f}{1-\nu_f^2} \left( \frac{t}{R} \right)^2 \left( \frac{t}{L} \right)$
Face Wrinkling		$W_0 = 4dB_1E_f^{\frac{1}{3}}E_s^{\frac{2}{3}} \left( \frac{t}{L} \right) \left( \frac{\rho^*}{\rho_s} \right)^{\frac{2}{3}}$
Core shear		$W_0 = 2K_1E_s d \left( \frac{\rho^*}{\rho_s} \right)^n$
Indentation		$W_0 = K_2b\delta\sigma_{sc} \left( \frac{\rho^*}{\rho_s} \right)^m$

### 3.5. Sandwich structure with composite skins

The analysis of the sandwich behavior presented in the previous section is generally developed for isotropic skins. However it can be easily extended in the case of composite skins.

In the case of sandwich beams, all the elastic properties of the skins along the beam direction can be evaluated by using the flow chart reviewed in the Chapter II. In particular, knowing the basic lamina properties, skins layup and stacking sequence, from flow-charts of Figs. 2.13 and 2.14 it is possible estimate the skin engineering elastic properties and strengths respectively along the beam direction.

At the same way, the sandwich construction can be considered as a special type of composite laminates and its analysis can be performed by using classical laminate theory as reviewed in the previous Chapter. However these approach do not provide quickly solution in the case of sandwich beam for which previous described procedure are involved in the following Chapters. Whereas, Classical laminate theory is a powerful tools for the analysis of sandwich plate. In particular the classical laminate theory needs to be modified in order to account the effects of shear deformation that in the case of thicker laminates and laminates with low-stiffness central plies cannot be removed.

In the modified theory, referred to as first-order shear deformation laminated plate theory, the equation 2.28 given in the previous Chapter are modified, and the force and moment resultants can be expressed as:

$$\begin{Bmatrix} N_x \\ N_y \\ N_{xy} \end{Bmatrix} = \begin{bmatrix} A_{xx} & A_{xy} & A_{xs} \\ A_{yx} & A_{yy} & A_{ys} \\ A_{sx} & A_{sy} & A_{ss} \end{bmatrix} \begin{Bmatrix} \varepsilon_x^0 \\ \varepsilon_y^0 \\ \gamma_{xy}^0 \end{Bmatrix} - \begin{bmatrix} B_{xx} & B_{xy} & B_{xs} \\ B_{yx} & B_{yy} & B_{ys} \\ B_{sx} & B_{sy} & B_{ss} \end{bmatrix} \begin{Bmatrix} \frac{\partial \alpha_x}{\partial x} \\ \frac{\partial \alpha_y}{\partial y} \\ \frac{\partial \alpha_x}{\partial x} + \frac{\partial \alpha_y}{\partial y} \end{Bmatrix} \quad (3.65)$$

$$\begin{Bmatrix} N_x \\ N_y \\ N_{xy} \end{Bmatrix} = \begin{bmatrix} B_{xx} & B_{xy} & B_{xs} \\ B_{yx} & B_{yy} & B_{ys} \\ B_{sx} & B_{sy} & B_{ss} \end{bmatrix} \begin{Bmatrix} \varepsilon_x^0 \\ \varepsilon_y^0 \\ \gamma_{xy}^0 \end{Bmatrix} - \begin{bmatrix} D_{xx} & D_{xy} & D_{xs} \\ D_{yx} & D_{yy} & D_{ys} \\ D_{sx} & D_{sy} & D_{ss} \end{bmatrix} \begin{Bmatrix} \frac{\partial \alpha_x}{\partial x} \\ \frac{\partial \alpha_y}{\partial y} \\ \frac{\partial \alpha_x}{\partial x} + \frac{\partial \alpha_y}{\partial y} \end{Bmatrix}$$

$$\begin{Bmatrix} V_q \\ V_r \end{Bmatrix} = \begin{bmatrix} A_{qq} & A_{qr} \\ A_{rq} & A_{rr} \end{bmatrix} \begin{bmatrix} \frac{\partial w}{\partial y} - \alpha_y \\ \frac{\partial w}{\partial x} - \alpha_x \end{bmatrix}$$

where  $\alpha_x$  and  $\alpha_y$  are the rotations of the cross sections normal to the  $x$ - and  $y$ -axes. The laminate stiffness  $A_{ij}$ ,  $B_{ij}$ , and  $D_{ij}$  ( $i, j = x, y, z$ ) are defined as in the previous Chapter, whereas the  $A_{ij}$  ( $i, j = q, r$ ) are defined as

$$A_{ij} = \sum_{k=1}^n C_{ij}^k t_k \quad (3.66)$$

The stiffnesses  $C_{qq}$ ,  $C_{qr}$ , and  $C_{rr}$  are related to the engineering shear moduli  $G_{23}$  and  $G_{13}$ .

The same procedure proposed for the classical laminate theory can be used for the analysis of the composite sandwich plate.

## References

- H.G. Allen, Analysis and design of structural sandwich panels, Pergamon Press, 1969.
- D. Zenkert, An introduction to sandwich construction, Engineering Materials Advisory Services, 1997.
- J.R. Vinson, The behavior of sandwich structures of isotropic and composite materials, Technomic Publishing, 1999.
- E.W. Kuenzi, Sandwich design criteria, Forest products laboratory, 1959.
- T.C. Triantafillou, L.J. Gibson, "Failure mode maps for foam core sandwich beams", Material Science and Engineering, 95, 37-53 (1987).
- Y. Shenhar, Y. Frosting, E. Altus, "Stresses and failure patterns in the bending of sandwich beams with transversely flexible cores and laminates composite skins", Composite Structures, 35, 143-152 (1996).
- Frosting Y., Baruch M. "Bending of sandwich panels with transversely flexible core". AIAA Journal, 28, pp 523-531, 1990.
- Frosting Y., Baruch M. "Localized load effects in high-order bending of sandwich panels with flexible core". Journal of Engineering Mechanics, 122, pp 1069-1076, 1996.

Frosting Y., Baruch M. “High-order theory for sandwich-beam behaviour with transversely flexible core”. *Journal of Engineering Mechanics*, 118, pp 1026-1043, ASCE 1992.

Patras A., Sutcliffe MPF. “Failure mode maps for honeycomb sandwich panels”. *Composite Structures*, 37, 97-108, 1997.

Patras A. and Sutcliffe MPF. “Indentation failure analysis of sandwich beams”. *Composite Structures*, 50, pp 311-318, 2000.

Patras A. and Sutcliffe MPF. “Indentation resistance of sandwich beams”. *Composite Structures*, 46, pp 413-424, 1999.

## **Chapter IV**

### ***Design criteria***

#### **4.1. Introduction to framework activities**

The activities presented in this Chapter were conducted to achieve the first step of the presented procedures within the Firema project. The design criteria and requirement of the railway vehicle are presented and discussed. In addition, based on structural, safety requirements, and literature review the selected materials and manufacturing process, involved in the project, are presented.

#### **4.2. Literature review**

In ground transportation sandwich structures can be found in cars, busses and trains. Since the 80s front cabs of locomotives have been built with sandwich technology because of its high strength and good impact and energy absorption properties. Some examples of this are the XPT locomotives in Australia, the ETR 500 locomotives in Italy, the French TGV and the Swiss locomotive 2000. Two large projects in railway application are Bombardier Transportation's C20 FICA and the Korean Tilting Train Express.

FICA is a "Flat package" concept, i.e. the car body is made up of several modules that are bolted together. Compared to the conventional vehicle body, the FICA system has introduced large scale lightweight sandwich panels into

the load bearing construction. This has increased the aisle space with 30% and reduced the tare weight per passenger by about 8%.

The C20 FICA body structure consists of sandwich panels in the sides, roof and floor. Steel end beams were inserted into the sides as supports. The sandwich elements consist of steel face bonded with an epoxy adhesive to a PMI foam core.

The C20 FICA structure has given, as mentioned, increased interior space, thus increasing passenger comfort and mobility. The reduced weight enables increased passenger loading capacity or lower energy consumption and lower maintenance cost. The sandwich design has also reduced assembly effort and development time because fewer parts are needed to cover all the integrated functions of the sandwich panel, e.g. sound reduction, insulation etc. The system however encountered several problems:

- No set fire standards.
- The sandwich system was not optimal for the floor. The floor required additional mineral wool for the fire barrier which eliminated eventual weight and space savings in the floor.
- Manufacturing had to be strictly controlled.
- Less tolerant to major external damage. Repair and adjustment was as complicated as for the conventional vehicle.

The Korea Railroad Research Institute (KRRRI) designed the Korean tilting train . The carbody of the Korean tilting train has developed using a hybrid design concept combined with a sandwich composite structure for bodyshell and a stainless steel structure for the under frame to match the challenging demands with respect to cost efficient lightweight design or railway carriage structures. The Stainless steel under frame introduces a low centre of gravity thereby increases stability during curves. The steel under frame also provides increased stiffness against global bending. The sandwich structure allowed to reduce the upper car body weight by 39% compared to a stainless steel car body.

Train bodyshell consists of aluminum honeycomb sandwich structures with woven fabric carbon/epoxy face and inner reinforced frames made of mild steel. A preliminary design of the car body was without the supporting inner

frame. However, during verification calculations, the deformation of the body shell during vertical loading was deemed excessive. In order to reinforce the structure the inner frames were inserted into the sides, roof and end structures of the car body

Under the financial support of the Ministry of Construction and Transportation, the Korean researchers are developing a the Korean low floor bus (KLFB) using a hybrid design concept combined with sandwich and laminated composite structures. The sandwich constructions are being considered for primary structures such as bodyshell, roof and floor, while laminated composites are being considered only for the components of relatively high curvatures and complex geometry where is more troublesome to be manufactured using the sandwich panels.

The sandwich panels are classified into two groups. One group is the sandwich panels for application to bodyshell structures that would be composed of the woven glass fabric/epoxy laminate facesheet and balsa or aluminum honeycomb core. The second group is the sandwich panels for application to floor structures that would be consisted of the metal aluminum facesheet and aluminum honeycomb or foaming aluminum core.

More example of sandwich structures in ground transportation industry can be found in: (i) Belingardi et al. [] performed the material characterization of front structure of a high-speed train involving glass fiber composite/foam sandwich structure; (ii) Ning et al. [] designed a mass transit bus side body panel using thermoplastic composite sandwich structures involving E-glass fiber/polypropylene (glass/PP) face sheets and PP honeycomb core as constituents; (iii) Harte et al. [] designed the bodyshell of a light rail vehicle involving composite sandwich panel configuration and steel stiffener frames. The sandwich panel comprises facesheets made from glass fibre reinforced epoxy composite plies with a polyurethane foam core; (iv) Raschbichler [] tested vehicle chassis made with two glass fiber-reinforced polyester or epoxy resin shells and a rigid polyurethane (PU) foam core.

Table 4.1 summarizes the material and manufacturing selected in the major application found in literature.

**Table 4.1. Review of common material and manufacturing employed in ground transportation vehicle.**

Project /Author	Vehicle element	Skin Material	Core Material	Manufacturing
<i>C20 Fica</i>	Side body panels Roof Floor	Steel	PMI foam core	
<i>Korean tilting train</i>	Side body panels Roof	Carbon fabric /epoxy	Aluminum honeycomb core	Autoclave molding
<i>Korean low floor bus</i>	Side body panels Roof  Floor	Glass fabric /epoxy  Metal aluminum	balsa and aluminum honeycomb core  aluminum foaming and honeycomb core	Autoclave molding
<i>Belingardi et al.</i>	Front shield	Glass fabric/epoxy	PVC foam core	
<i>Ning et al.</i>	Side body panels	Glass/PP	PP honeycomb	Vacuum forming
<i>Harte et al.</i>	Side body panels	Glass/epoxy	PU foam core	
<i>Raschbichler et al.</i>	Side body panels Roof	Glass polyester or epoxy	PU foam core	

### 4.3. Design criteria

#### 4.3.1. Structural requirements

The composite sandwich roof have been designed according to the European standard guidelines in order to achieve the structural requirements of railway vehicle bodies EN 12663 [].

Railway vehicle bodies comprises the main load carrying structure above the suspension units. It includes all components which are affixed to this structure which contribute directly to its strength, stiffness and stability.

The design criteria are based on the following classification of railway vehicles. Due to the specific nature of their construction and different design objectives there are two main groups, namely freight vehicles and passenger vehicles including locomotives. The two group are subdivided further into categories according to their structural requirements. In particular the passenger category includes all type of railway vehicle intended for transport passengers, ranging from main line vehicles, suburban and urban transit stock to tramways. Passenger vehicles are divided into five structural design categories into which all vehicle may be allocated.

The investigated train is classified into category P-II (e.g. fixed units) according to European standard. All the value and combination reported in the following section are referred to the selected vehicle category

According to the European standard “The vehicle body shall withstand the maximum loads consistent with their operational requirements and achieve the required service life under normal operating conditions with an adequate probability of survival. The assessment shall be based on the following criteria:

- a) exceptional loading defining the maximum loading which shall be sustained and a full operational condition maintained;
- b) acceptable margin of safety, such that if the exceptional load is exceeded, catastrophic fracture or collapse will not occur;
- c) stiffness, such that the deformation under load and the natural frequencies of the structure meet limits as determined by the operational requirements;
- d) Service or cyclic loads being sustained for the specified life without detriment to the structural safety.”

It means that the composite sandwich roof shall be demonstrated, by calculation and/or testing, that: (i) no permanent deformation or fracture of the structure as a whole, or of any individual element, will occur under the prescribed static design load cases. (ii) adequate flexural and torsional

stiffness will ensure to provide that the sandwich panels remains within its required space envelope and unacceptable dynamic responses are avoided. The required stiffness may be defined in terms of an allowable deformation under a prescribed load or a minimum frequency of vibration. The natural modes of vibration shall be separate sufficiently or otherwise decoupled so as to avoid the occurrence of undesirable responses at any speed, vehicle loading, or suspension condition; (iii) no permanent deformation or fracture of the structure as a whole, or of any individual element, will occur under the prescribed static design load cases. The structures of a railway vehicle are subjected to a very large number of dynamic loads of varying magnitude during their operation life. The effects of these loads are most apparent at critical features in the vehicle body structures such as joints between structural member.

European guidelines provides five different static loading combinations involving both vertical loads and longitudinal forces. Vertical loads are due to the mass of the vehicle body in working order  $m_1$  and the mass of the maximum payload  $m_2$ . The mass in working order  $m_1$  consists of the completely vehicle body with all mounted parts, this includes the full operating reserves of water, sand, fuel, foodstuffs, etc. and the overall weight of staff. The maximum payload  $m_2$  depends on the number of seats for passengers and on the number of passengers per  $m^2$  in the standing areas. These values are fixed by the operator, taking into account any statutory regulations, and give the mass for the payload and the number of passengers which are allowed to be transported in the selected vehicles. For P-II vehicle, the European standard provide the typical weights of 80 kg per passenger with luggage with a typical passenger densities in standing area of 2 to 4 passenger per  $m^2$ . Vertical loads are applied to the underframe (Fig. 4.1a). Longitudinal forces involves compressive  $F_{lc}$  and tensile  $F_{lt}$  forced at buffers and/or coupling area (Figs. 4.1b and 4.1c) due to the traction and braking operation. For P-II vehicle, the European standard provide the following value of longitudinal forces:  $F_{lc}=1500$  kN and  $F_{lt}=1000$  kN.

In order to demonstrate a satisfactory static strength, the European guideline considers as a minimum the superposition of five static load cases as indicate

in Table 4.2. In addition, Table 4.2 gives empirical vertical and acceleration level, suitable for an endurance limit approach, consistent with normal European operations, which shall be adopted to the assessment and to ensure that fatigue design requirements are achieved.

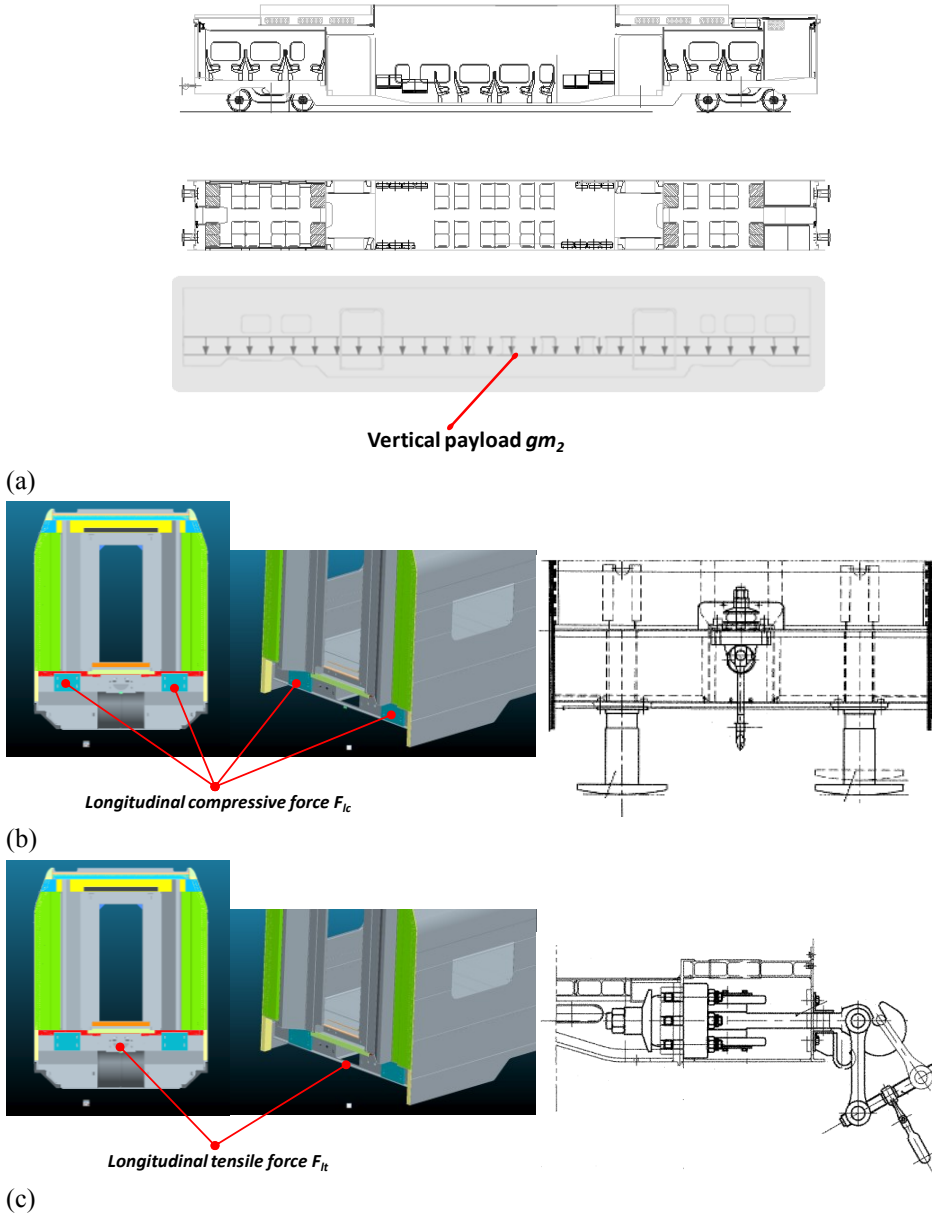


**Figure 4.1. Static load and forces applied to frame bogie structure.**

In addition, design of the composite sandwich roof shall be ensure the

following additional requirements: sustain lifting operation, equipment weights and the weight of two maintenance men.

**Table 4.2. Static and fatigue loading configuration**

<b>Static loading combinations</b>		
1	Maximum vertical load	$1.3g(m_1+m_2)$
2	Vertical load + compressive force	$F_{lc}+g(m_1+m_2)$
3	Dead load + compressive force	$F_{lc}+gm_1$
4	Vertical load + tensile force	$F_{lt}+g(m_1+m_2)$
5	Dead load + tensile force	$F_{lt}+gm_1$
<b>Fatigue loading</b>		
1	Longitudinal acceleration	$\pm 0.15g$
2	Vertical acceleration	$1\pm 0.15g$

The dynamics of the running gear and its interaction with the track can exhibit a natural periodic motion with a frequency of typically a few cycles per second. The magnitude of this motion depends on the quality of the track and the running gear and is usually augmented by worn wheels and rails. Low frequency vibrations of the railway vehicle are known to cause nausea and travel sickness and thus these frequencies should be avoided. For these reasons it is common practice to design vehicles so that they have no natural frequencies in bending below approximately 10 Hz. This solves the motion problems and it also results in a very stiff, and thereby strong, body which can easily fulfill most other strength requirements that are imposed upon it.

In addition to the bending frequency measuring test, vertical deformation and equivalent bending stiffness of the vehicle will be checked. In general, the maximum deflection of the railway vehicle has to be less than 1/1000 of the distance between centers of bogies, because the large deflection of the body structure under the vertical load can lead to large deformation of the cutouts for windows and side entrance doors.

#### **4.3.2. Non-structural requirements**

Over the last years, fire protection has become one of the major topic in the design and construction of railway vehicles. This is due to new international standards and guidelines and past experiences of fire events. Nowadays, the

planning and construction of new railway vehicles always involves more severe requirements and new fire protection measures.

The composite sandwich roof, according to the Italian guidelines UNI CEI 11170-1 [];11170-2 [];11170-3 [] for fire protection of railway, shall provide the objectives of prevent fire, retard its growth and spread, and provide adequate evacuation time for passengers and crew. Based on the type vehicle categories, the selected standards define three different risk levels *LR* related to the evacuation time *t*:

- LR1:  $0 < t \leq 5$  min
- LR2:  $5 < t \leq 15$  min
- LR3:  $15 < t \leq 30$  min

The roof structures shall provide compartmentation of the fire and correspond to the risk level *LR2*. The fire safety requirements and performance criteria for individual materials shall be measured by different small-scale test methods.

The individual test methods measure one or more of four different fire performance phenomena: ignition resistance, flame spread, smoke emission, and fire endurance. Table 4.3 reports the main national standards in each sector of fire safety.

**Table 4.3. National standard in each sector of fire safety**

Country	Flame propagation	Fume toxicity	Smoke generation
<b>Italy</b>	UNI 8456; UNI 8457	-	UNI 9174; UNI 9175
<b>UK</b>	BS 6853	BS 6853 Annex B	BS 6853 Annex D
<b>French</b>	NF F16 101	NF F16 101 6.3	NF F16 101 6.2
<b>Germany</b>	DIN 53438	-	-
<b>US</b>	ASTM E 162	SMP 800C	ASTM E 662

Thus, in order to achieve the fire safety requirements, materials involved in the sandwich roof configuration shall provide minimum performance criteria related to the corresponding risk level per each sector of fire safety. In particular, Italian standards are take into account for the evaluation of the performance of flame propagation and smoke generation, while French standard is considered for the analysis of the fume toxicity requirements since it provide more stringent requirements within European code.

In addition, in the railway field, materials are required for its durability against many kinds of degradation factors of the applied products. The expected service life of the materials used in transportation fields is approximately between 20-30 years—a long period of exposure for polymer materials. Degradation process of polymer materials indicated various changes in the mechanical strength depending on the condition, type of polymer material, production process of polymer material, and additive package. Therefore, an artificial aging test and a reproduction test under practical conditions are important to investigate the degradation factor of the material involved in the new composite sandwich roof.

Generally, damage by aging or weathering—environmental degradation of structural components of vehicle—can be due to a combination of processes. The European guideline EN 50125-1 [13] provides these values for the structural components of a train vehicle (Fig.4.2). The railway vehicle is mainly used in outdoor condition; the practical temperature range of the railway vehicle approximately changed from -20 to 70 °C. Even in the interior product, the temperature range is similar to the outdoor products. In case of periodical inspection, the railway vehicle is placed outdoor all over the day in every season; therefore, the temperature of the interior rises to more than 60 °C in summer and falls to less than -10 °C in winter. In addition, UV, atmospheric oxygen and rain water easily affect the products not only in the outdoor but also in the interior. During the railway service, door is frequently opened and sunlight irradiates the passenger's room. In addition, the passengers bring in the rain water into the passenger's cabin.

#### **4.4. Material selection**

Problems with the fire resistance of organic matrix composites are seen by many as the most significant factor hindering their rapid expansion into a wide range of engineering applications in transport and infrastructure [7]. Resins are in the front line of fire resistance and dominate in terms of fire reaction, so the selection of composite material is primarily focused on the matrix component.

Among the currently available sandwich composite materials, in the present work phenolic resin-impregnated sandwich structure are considered for the structural design of load carrying components of civil transportation vehicles for their inherently fire-retardant properties that evolve low levels of smoke and combustion products in a fire, instead of other types of composites that burn and release large amounts of heat, smoke and toxic fumes that pose a risk to people, especially in the confined space of vehicles, and make it difficult for fire fighters to extinguish the fire.



**Figure 4.2. Degradation factors of long-term environment as suggested by EN 50125-1**

On the downside, however, cured phenolics tend to be brittle, have limited peel strength (a significant drawback for sandwich structures), have traditionally been difficult to process, with potential health hazards for operatives, and are more expensive. Even so, these resins are the most likely to meet stringent mass transit test requirements in Europe, Japan and the USA. The USA, where phenolics are well established in the aerospace and offshore sectors, is in the vanguard of adopting phenolic composites. In particular phenolics are already widely used in aircraft interiors, automotive applications such as engine compartment firewalls, and in components for the offshore industry.

Despite the great interest on phenolic composite structures, most scientific

papers cover the epoxy, polyester and vinylester reinforced resins. Only few publications contain information about mechanics and material characteristics of phenolic composites [25-31].

In fact polyester, epoxy and vinyl ester resins have long been used in boat, plane and other vehicle builders accepting that these will have to be modified to meet fire safety requirements. Resin suppliers have responded with material modifications that include the use of retardant fillers (filled resins) and incorporation of additives into chemical structure in unfilled resins. Popular additives up to now have been halogen compounds, since bromine and chlorine are highly effective in neutralizing the free radicals released when composites burn, and hence in retarding the spread of fire. However, pressure due to health and safety concerns is progressively making the use of halogens non-acceptable.

Some modifications target the spread of flame only. Others, notably for materials destined for trains and vehicles used underground, must prevent the release of smoke also, and still others must limit heat release as well as meeting the flame and smoke requirements.

In the present study glass and carbon fabric (plain weave 8 H satin) in a phenolic resin supplied as pre-impregnates sheets have been investigated as sandwich skin. The selected skins are certificated according to French and Italian standards in regards to fire safety requirements.

Figure 4.3 shows the response of glass/phenolic skins to small flame [ ] or flame to ignite in the presence of radiant heat [34]. The mentioned tests were run on 10 sandwich panels (340 x 104 x 16 mm), positioned in vertical direction and 6 sandwich panels (800 x 155 x 16 mm), positioned without a fireproof roof, respectively. Before the execution of the testing for reaction to fire all specimens were conditioned for at least 24h in air-conditioned chamber at 20°C and 65% of RH. The classification of fire reaction by small flame and heat radiant, according to UNI 9177 [35], was awarded on the basis of the results of the described tests. Based on the test results, the phenolic sandwich panel can be classified as 1 class of fire reaction.

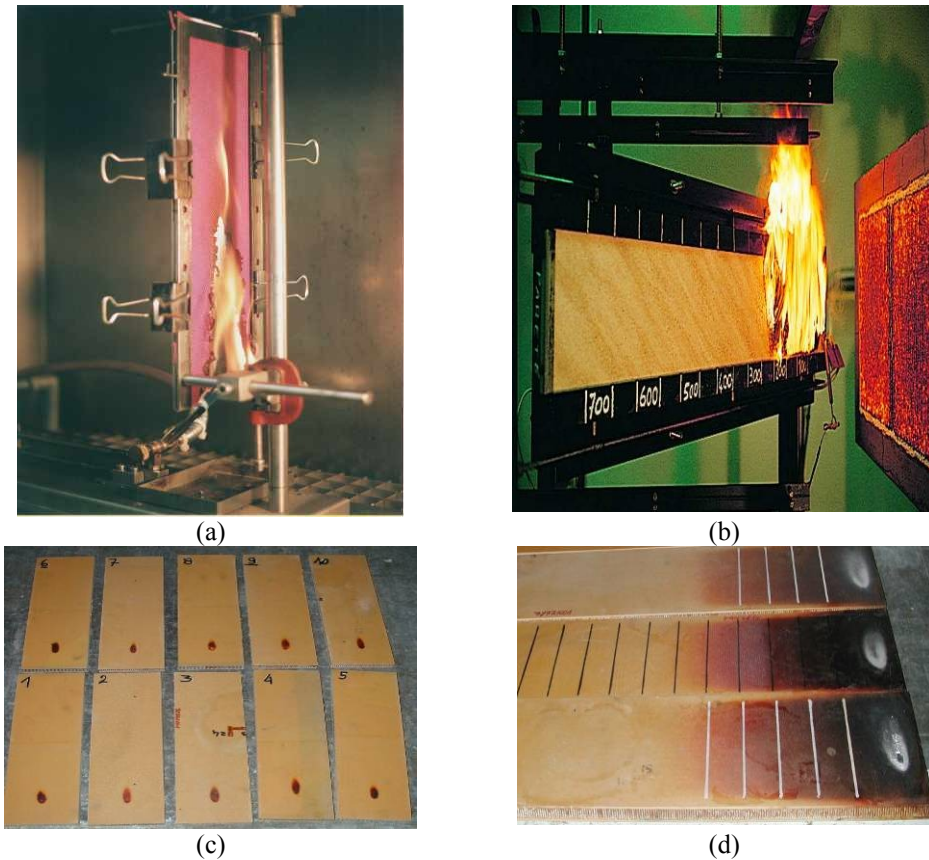


**Figure 4.3.** Fire resistance tests: a) small flame test; b) radiant panel test; c) samples after test by small flame, d) samples after test by radiant panel test.

The phenolic skins have been combined with either a  $130 \text{ kg/m}^3$  high-performance expanded PVC foam or a  $48 \text{ kg/m}^3$  aramid fiber reinforced phenolic (Nomex) honeycomb with a nominal cell size of 3.18 mm or  $49.6 \text{ kg/m}^3$  aluminum honeycomb with a nominal cell size of 4.76 mm, to define sandwich configuration.

In-plane properties of core materials are deduced by the manufacturer's data [19-21] and are showed in Table 4.4, while mechanical properties of the skins have been derived by experimental tests as illustrated in the next Chapter.

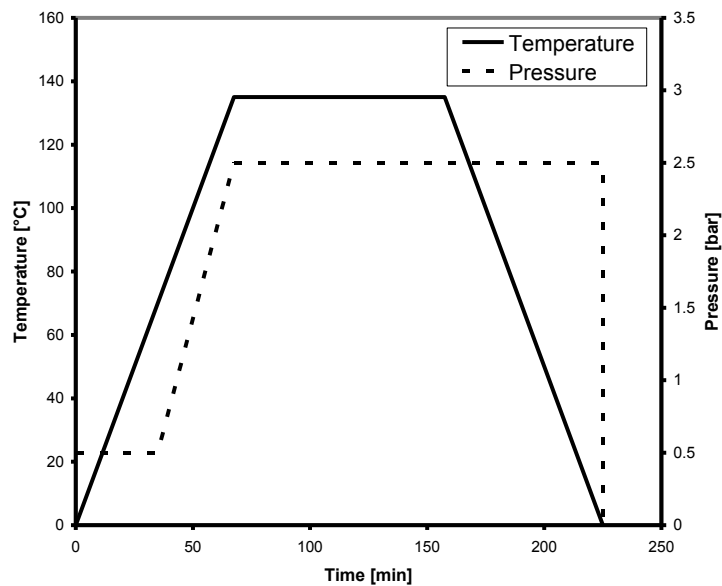
The manufacturing process is one of the most important step in the application of composite materials. Autoclave molding process has been selected to manufacture the sandwich roof. It is a low-volume process and labor intensive and therefore costly. Whereas it allows to meet a product free

of defects (voids, cracks, fiber waviness), uniform in properties, fully cured and reproducible.

**Table 4.4. Mechanical properties of core materials according to manufacturer data.**

	Density Compressive			Shear			
	$\rho$	$\sigma$	E	$\tau$ [MPa]		G [MPa]	
	[Kg/m <sup>3</sup> ]	[MPa]	[MPa]	L Direction	W Direction	L Direction	W Direction
<b>Aluminum Alloy 5052-3/16</b>	49.6	2.31	517.11	1.45	0.86	310.26	151.68
<b>Nomex HRC-10 1/8</b>	48	2.24	137.95	1.21	0.69	44.83	24.14
<b>Klegecell TR 130</b>	130	2.5	86	1.95		50	

The selected basic cure cycle for the composite laminates is shown in Figure 4.4a. It counts a vacuum pressure of 2.5 bar, a ramping temperature up to 135°C at 2°C/min and maintaining this temperature for 90 minutes. The use of prepreg material and autoclave molding process avoid the use of additional adhesive layer between the skin and the core. Figure 4.4b shows the autoclave chamber used for the production in the A-Technology spa manufacturing plant.



(a)



(b)

Figure 4.4.: Manufacturing methods: (a) Curing cycle; (b) Autoclave chamber.

## 4.5. Design concept

From the Korean Tilting Trains experience, it can be known that the lightweight design of large composite sandwich components in a railway vehicle can lead to reduce stiffness rather than strength.

In order to prevent excessive deformation and low frequency of the natural periodic motion during service life, hybrid design concept involving composite sandwich panels and inner aluminum frame has been developed. The aluminum frame can be realized joining transverse aluminum beams to the longitudinal side rails. The roof structure is then completed by 10 composite sandwich panels joined to the aluminum frame (Fig. 4.5). Three different modules (*A*, *B*, and *C*) have been individuated based on geometric and loading characteristics, due to different . In particular the new roof counts eight 2450x2674 mm *A* panels, two 2200x2510 mm panels, and one 2200x912 mm *C* panels. In addition, modules *A* and *B* differs due to different weight of attached equipments.

In the present study, the optimization and assessment procedure have been presented for the composite sandwich panels of *A* module.

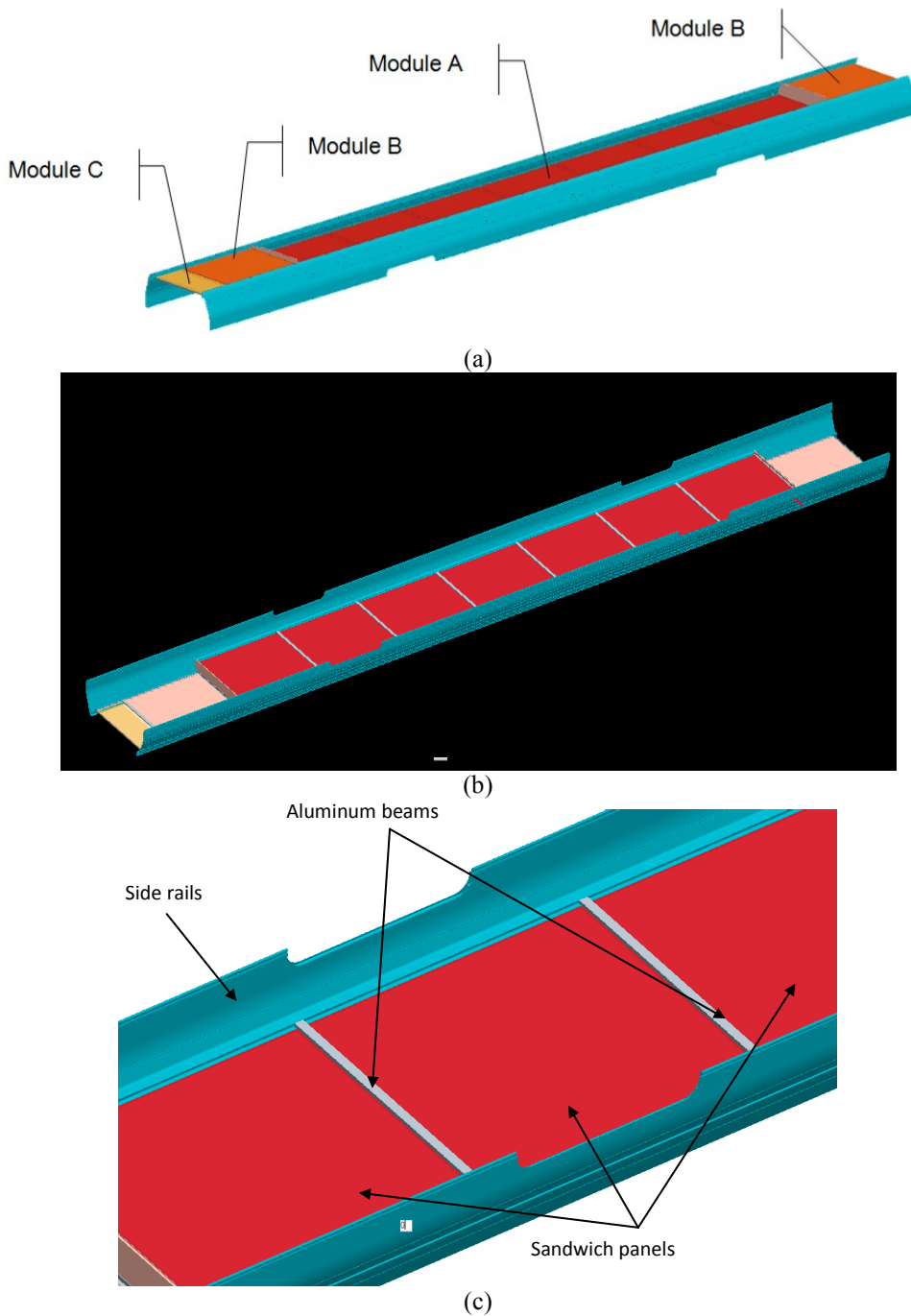


Figure 4.5. New hybrid roof structures: (a) top view; (b) bottom view; (c) detail of A module.

## References

- Hexcel, “Mechanical properties of Hexcel honeycomb materials”.
- DIAB, “Klegecell TR Grade Technical data”.
- Belingardi G., Cavarota M.P., Duella R., “Material characterization of a composite-foam sandwich for the front structure of high speed train”. *Composite Structures*, 61, pp 13-25, 2003.
- Shin K.B., Lee J.Y., Cho S.H., “An experimental study of low-velocity impact responses of sandwich panels for Korean low floor bus”. *Composite Structures*, 84, pp 228-240, 2008.
- Kim J. S., Lee S.J., Shin K.B., “Manufacturing and structural safety evaluation of a composite train carbody”. *Composite Structures*, 78, pp 468-476, 2007.
- Kim J. S., Chung S.K., “A study on the low-velocity impact response of laminates for composite railway bodyshells”. *Composite Structures*, 77, pp 484-492, 2007.
- NAFEMS, Quality system supplement to ISO 9001 relating to Finite element analysis in the design and validation of Engineering products. National Agency for Finite Element Methods and Standards. Issue 1.3, 1993.
- AFNOR NF F16-101, “Matériel roulant ferroviaire - Comportement au feu - Choix des matériaux”, October 1988.
- UNI 9174 (1987), UNI 9174/A1 (1996) “Fire reaction of materials subjected to the action of a flame to ignite in the presence of radiant heat”.
- UNI 9177 (1987) “Reaction to fire. Combustible materials classification.”
- UNI CEI 11170-3, “Railway and Tramway Vehicles - Guidelines for Fire Protection of Railway, Tramway and Guided Path Vehicles - Evaluation of Fire Behaviour of Materials - Limits of Acceptance”, 2005.
- CEI EN 50125-1 “Condizioni ambientali per le apparecchiature nel materiale rotabile”.
- Charalambides MN, Williams JG, “Fracture toughness characterization of phenolic resin and its composite”, *Polymer Composites* (1995), 16, 17-28.
- St Jhon NA, Brown JR, “Flexural and interlaminar shear properties of glass-phenolic composites”, *Composites: Part A* (1998), 29, 936-946.

Branco CM, Ferreira JM, Richardson MOW, Fael P, “Fatigue behaviour of a phenolic matrix composite”, *Int J Fatigue* (1992), 14, 367-376.

Echtermeyer AT, Engh B, Buene L, “Lifetime and Young’s modulus changes of glass/phenolic and glass/polyester composites under fatigue”, *Composites* (1995), 26, 10-16.

Zhou G, “Damage mechanisms in composite laminates impacted by flat-ended impactor”, *Composites Science and Technology* (1995), 54, 267-273.

Gellert EP, Turley DM, “Seawater immersion ageing of glass-fiber reinforced polymer laminates for marine applications”, *Composites: Part A* (1999), 30, 1259-1265.

[31] Heimbs S, Schmeer S, Middendorf P, Maier M, “Strain rate effects in phenolic composites and phenolic-impregnated honeycomb structures”, *Composites Science and Technology* (2007), 67, 2827-2837.

## **Chapter V**

# ***EXPERIMENTAL CHARACTERIZATION AND VALIDATION***

### **5.1. Introduction to framework activities**

The activities presented in this Chapter were conducted to achieve the second and third step of the presented procedures. In particular, the results on experimental characterization of independent material properties and experimental verification of the sandwich analysis and manufacturing process are presented and discussed.

The overall behavior of sandwich structures depends on the material properties of the constituents (skins, core, and adhesive if involved), geometric dimensions, and type of loading. Analysis of this behavior is difficult because of the intrinsic complexity of the multilayered configurations and the complex interaction of failure modes. For these reasons, the present step involves The experimental activity on material properties is primarily focused on the mechanical characterization of the composite skins that requires the determination of a large number of independent data (generally do not provided by manufacture's datasheet). Instead manufacture's datasheet provides an exhaustive characterization of the core properties that can be easily checked by mechanical test on sandwich configurations and by mechanical models reviewed in the first chapter.

Common test procedure on composite materials and sandwich elements have

been reviewed. The presented procedure are intended for both unidirectional or textile composite and core material forms include those with continuous bonding surfaces (e.g. balsa wood and foams) as well as those with discontinuous bonding surfaces (i.e. honeycomb structures). All the presented procedure may be use in the multiscale flow chart.

## **5.2. Testing methods**

### **5.2.1. Composite laminae tests**

Experimental methods for composite materials are more complex than for isotropic materials and require significant modifications. Characterization of composite skin materials can be achieved determining tensile, compressive, shear and through-thickness properties.

*Uniaxial tensile tests* can be conducted on composite laminate to determine the following properties: (i) longitudinal and transverse Young's moduli; (ii) major and minor Poisson's ratios; (iii) longitudinal and transverse tensile strengths; (iiii) longitudinal and transverse ultimate tensile strains. Tensile specimens are straight-sides coupons of constant cross section with adhesively bonded tabs. In order to achieve longitudinal and transverse tensile properties, the composite laminate are obtained stacking all the plies with the principal direction parallel and perpendicular to the load respectively. More details (e.g. geometry, test procedure) are given in ASTM specification D 3039. The specimen are loaded to failure under uniaxial tensile loading. A continuous record of load and deformation is obtained by an appropriate digital data acquisitions system. Axial and transverse strains are obtained by means of a pair of two-gage rosettes mounted on both sides of the specimen.

*Compressive testing* of composite materials is one of the most difficult types of testing because of the tendency for premature failure due to global buckling or end crushing. The test is sensitive to many experimental parameters, such as alignment, specimen geometry, load introduction scheme, and stability. Over the years many test methods have been developed and used incorporating a variety of specimen designs and loading fixtures.

One of the most commonly used test methods today involves specially designed fixture that allows to load the coupon in compression by a shear load acting along special trapezoidal wedge grips. More details on test fixture, specimen geometry and procedure are given in ASTM specification D 3410. The limitation of the described test method is the maximum load that can be transmitted through shear by the tabs, which is controlled by the adhesive shear strength, the interlaminar shear strength of the tab and specimen materials, and the total tabbed area.

ASTM specification D 6641 establishes a procedure for determining the compressive strength and stiffness properties of polymer matrix composite materials using a combined loading compression (CLC) test fixture. The fixture, which subjects the specimen to combined end - and shear - loading, is itself loaded in compression between flat platens in a universal testing machine. The test fixture can be used to test the untabbed, straightsided composite specimen of rectangular cross section.

The ultimate compressive strength of the material, as obtained with these test fixtures and specimens, can be obtained from the maximum load carried before failure. Strain is monitored with strain or displacement transducers so the stress-strain response of the material can be determined, from which the ultimate compressive strain, the compressive modulus of elasticity, Poisson's ratio in compression, and transition strain can be derived.

Another approach to compression testing consists of bonding the composite laminates to a low-stiffness honeycomb or foam core to produce a sandwich specimen. Sandwich specimens can be tested in pure bending under four-point bending configuration in order to subject the top composite facesheet to nearly uniform compression. The specimen geometry should be adjusted to ensure compressive failure in the top facesheet. In fact, if the beam is not long enough, core failure or indentation may occur before composite compressive failure. More details (e.g. geometry, test procedure) are given in ASTM specification D 7249. Strains are measure by means of strain gauges mounted on the composite top facesheet, which stress is determined by assuming uniform deformation in the facesheets and neglecting the bending stress in the core.

Full characterization of composite material in two dimensions requires the determination of lamina properties under *in-plane shear* parallel to the fibers, that is, shear modulus, shear strength, and ultimate shear strain. There are four generally accepted methods for determination of these properties: (1) the  $[\pm 45]_{ns}$  coupon test; (2) the  $10^\circ$  off-axis test; (3) the rail shear test; (4) the torsion test.

The first method utilizes an eight-ply  $[\pm 45]_{2s}$  coupon subjected to an uniaxial tensile stress. A uniaxial tension test of a  $\pm 45^\circ$  laminate is performed in accordance with Test Method D 3039, although with specific restrictions on stacking sequence and thickness. A fully description of test procedure is reported in ASTM standard D3518. Using expressions derived from laminated plate theory, the in-plane shear stress in the material coordinate system is directly calculated from the applied axial load, and the related shear strain is determined from longitudinal and transverse normal strain data measured with two strain gage rosettes. The in plane shear modulus of the unidirectional lamina is obtained from the initial slope of the shear stress-strain curve. The above method tends to overestimate the in-plane shear strength of the constraint imposed on the lamina by the adjacent plies. In estimating this strength the method does not take into account edge effects or the influence of the longitudinal and transverse stress components on the lamina.

The second test method is the  $10^\circ$  off-axis test. The  $10^\circ$  angle is chosen to minimize the effects of longitudinal and transverse stress components on the shear response. The specimen is six-ply coupon with the principal fibers oriented to  $10^\circ$  to the loading axis. A uniaxial tension test is performed in accordance with Test Method D 3039. Using expressions derived from laminated plate theory, the in-plane shear stress in the material coordinate system is directly calculated from the applied axial load, and the related shear strain is determined from longitudinal and transverse normal strain data measured with two strain gage rosettes oriented at  $\pm 45^\circ$  to the principal fiber direction. The in plane shear modulus of the unidirectional lamina is obtained from the initial slope of the shear stress-strain curve.

In both methods above the estimation of shear strength is based on the

implicit assumption of the maximum stress criterion. Different value of shear strength would be obtained if interaction failure, such as Tsai-Hill criterion, is used.

The third method of determining shear properties is the rail shear test, two-rail or three-rail test as described in ASTM standard D4255. In two-rail test, a rectangular composite coupon is gripped along its long edges by two pair of rails that are loaded in a direction nearly parallel to the edges. In three-rail test, a rectangular composite coupon is clamped between three parallel pairs of rails- The loaded is applied to one end of the middle rails and reacted at opposite ends of the two outer pairs of rails. The shear strain is obtained from a single gage placed at the center of the exposed specimen at  $45^\circ$  to the rail axes.. The state of stress near the ends is not pure shear, and the large normal stress concentrations at the ends may results in premature failures.

The fourth method is the torsion method utilizing a solid rod or a hollow tubular specimen subjected to torque. The shear strain can be obtained by measuring the angle twist or the strain at  $\pm 45^\circ$  with strain gages. Although the tube torsion test seems very desirable from the mechanical point of view, tubular specimens are difficult to make and load. The solid rod torsion test is less desirable because of the shear stress gradient across the section.

Since composite sandwich structures involves thin composite laminate facesheet, through-thickness characterization can be achieved by determining only *interlaminar shear* properties. Interlaminar shear strength is a measure of the in situ shear strength of the matrix layer between plies. There is no method available for exact determination of this property. Approximate values of the interlaminar shear strength, or apparent interlaminar shear strength, can be obtained by various tests.

The most commonly used test is the short beam under three-point bending. The beam is machined from a relatively thick laminate with the all plies stacked with principal fibers in the axial direction and is loaded normally to the plies, in the 3-direction according to ASTM standard D 2344. Because of its simplicity, the short-beam shear test is also used as a quality control test of the lamination process and related matrix-dominated properties of the composite. The apparent interlaminar shear strength is obtained from

classical beam theory.

Another test proposed for measurement of interlaminar shear strength is the double-notch shear test described in ASTM specification D3846. The specimen is a laminate with all plies stacked with principal fibers in the axial direction. Two parallel notches or grooves are machined, one on each face of specimen. When this specimen is loaded in uniaxial tension, shear failure results along the midplane of the specimen between the notches.

### 5.2.2. Sandwich tests

Experimental characterization on sandwich construction have been involved in the proposed procedure in order to investigate the structural behavior, the complex interaction of failure modes, the manufacturing process. In addition, tests on sandwich component provide the determination of some material properties.

Common test procedure on sandwich configuration have been reviewed. The following test method can be used to produce data for structural design allowables, material specifications, and research and development applications; it may also be used as a quality control test for bonded sandwich panels.

Flexure tests on flat sandwich construction may be conducted to determine the sandwich flexural stiffness, the core shear strength and shear modulus, or the facings compressive and tensile strengths. In the case of honeycomb core, the shear strength, modulus, and stiffness are function of the direction that the core is oriented relative to the length of the specimen.

The loading fixture for flexural tests consists of either a 3-point or 4-point loading configuration with two support bars that span the specimen width located below the specimen, and one or two loading bars that span the specimen width located on the top of the specimen. Generally the deflection of the specimen in flexure is measured in the center of the support span by a deflectometer LVDT.

Calculations of *sandwich flexural, shear stiffness and shear modulus* can be determined by simultaneous solution of the complete deflection equations under two or more different loading configurations. The complete procedure

is described in the ASTM specification D 7250.

Flexural test involving long beam loading configuration, as described in the previous section, allows to obtaining the *facing properties* of sandwich construction and to obtaining load-deflection data for use in calculating sandwich beam flexural and shear stiffness using ASTM practice D7250.

Flexural test involving short beam loading configuration, as described in ASTM specification C393, allows to obtaining the *core shear strength or core-to-facing shear strength* and to obtaining load-deflection data for use in calculating sandwich beam flexural and shear stiffness using ASTM practice D7250. If the core material has insufficient shear or compressive strength, it is possible that the core may locally crush at or near the loading points, thereby resulting in facing failure due to local stresses. In other cases, facing failure can cause local core crushing. When there is both facing and core failure in the vicinity of one of the loading points it can be difficult to determine the failure sequence in a post-mortem inspection of the specimen as the failed specimens look very similar for both sequences.

Otherwise, the core shear strength and modulus can be obtained using the compressive and/or tensile plate shear test method. The load is applied with two steel plates bonded to the core specimen. Details on specimen geometry and test procedure are described in ASTM standard C273. The shear strength of the core is obtained as function of the ultimate load. The shear modulus is calculated as the slope of the initial straight line portion of the stress-strain curve. High density cores are sometimes difficult to fail in shear by the plate shear method because of the high shear loads introduced to the adhesive bond between the core and steel plates.

In a sandwich panel, core-to-facing bond integrity is necessary to maintain facing stability and permit load transfer between the facings and core. ASTM C297 test method can be used to provide information on the strength and quality of core-to-facing bonds. It can also be used to produce flatwise *tensile strength* data for the core material.

Uniaxial compressive test on sandwich construction, according to ASTM C365, provides a standard method of obtaining the *out-of-plane compressive strength and modulus* for sandwich core properties. Deformation data can be

obtained, and from a complete force versus deformation curve, it is possible to compute the compressive stress at any applied force (such as compressive stress at proportional limit force or compressive strength at the maximum force) and to compute the effective modulus of the core. In order to prevent local crushing at the edges of some honeycomb cores, it is often desirable to stabilize the edges with a suitable material, such as a thin layer of resin or thin facings. Flatwise compressive strength data may be generated using either stabilized specimens (reported as stabilized compression strength) or non-stabilized specimens (reported as bare compression strength). It is customary aerospace industry practice to determine compression modulus only when using stabilized specimens.

ASTM standard C364 covers the compressive properties of structural sandwich construction in a direction parallel to the sandwich facing plane. This test method consists of subjecting a sandwich panel to monotonically increasing compressive force parallel to the plane of its faces. The force is transmitted to the panel through either clamped or bonded end supports. Stress and strength are reported in terms of the nominal cross-sectional area of the two facesheets, rather than total sandwich panel thickness, although alternate stress calculations may be optionally specified. The only acceptable failure modes for edgewise compressive strength of sandwich constructions are those occurring away from the supported ends. The sandwich column, no matter how short, usually is subjected to a buckling type of failure unless the facings are so thick that they themselves are in the short column class. The failure of the facings manifests itself by wrinkling of the facing, in which the core deforms to the wavy shape of the facings; by dimpling of the facings into the honeycomb cells; by bending of the sandwich, resulting in crimping near the ends as a result of shear failure of the core; or by failure in the facing-to-core bond and associated facesheet buckling.

### **5.3. Skin characterization**

In the present section, mechanical characterizations of both selected carbon and glass phenolic skins were developed to define the in-plane properties.

Based on the summary of tests methods, Table 5.1 reports the selected test procedure and configurations, while specimen informations (e.g. geometries, staking sequences) are reported in Table 5.2.

**Table 5.1. Test methods involved in the mechanical characterization of skin materials.**

Test (ASTM Standard)	Loading Configuration	Mechanical Properties	Mechanical Parameters
Tensile test in warp direction (D3039)		Elastic modulus $E_1$ Poisson's ratio $\nu_{12}$ in warp direction	Ultimate tensile stress $F_{1t}$ and strain $\epsilon^u_{1t}$ in warp direction
Tensile test in fill direction (D3039)		Elastic modulus $E_2$ Poisson's ratio $\nu_{21}$ in fill direction	Ultimate tensile stress $F_{2t}$ and strain $\epsilon^u_{2t}$ in fill direction
In plane shear tests by tensile loading (D3518)		In-plane shear modulus $G_{12}$	In-plane ultimate shear stress $F_6$ and strain $\gamma^u_6$
Short-beam tests (D2344)		Interlaminar shear strength $ILSS$	

All laminate tests were run on a 10 kN universal test frame controlled by an electronic control unit which allows monitoring the applied load and the stroke of the top cross head. Strain signals were acquired by a digital data acquisition system. Figure 5.1 depicts the loading configurations considered adopted in the experimental activity.

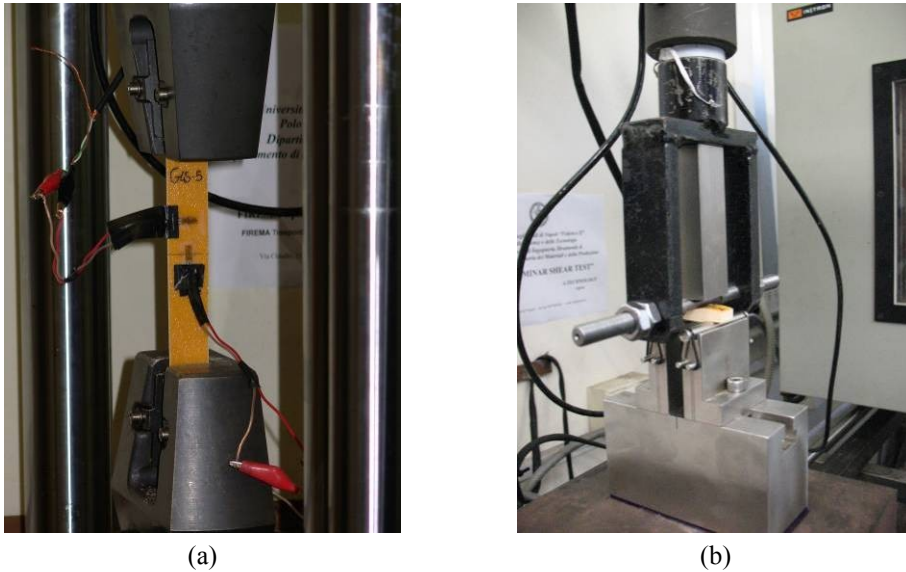


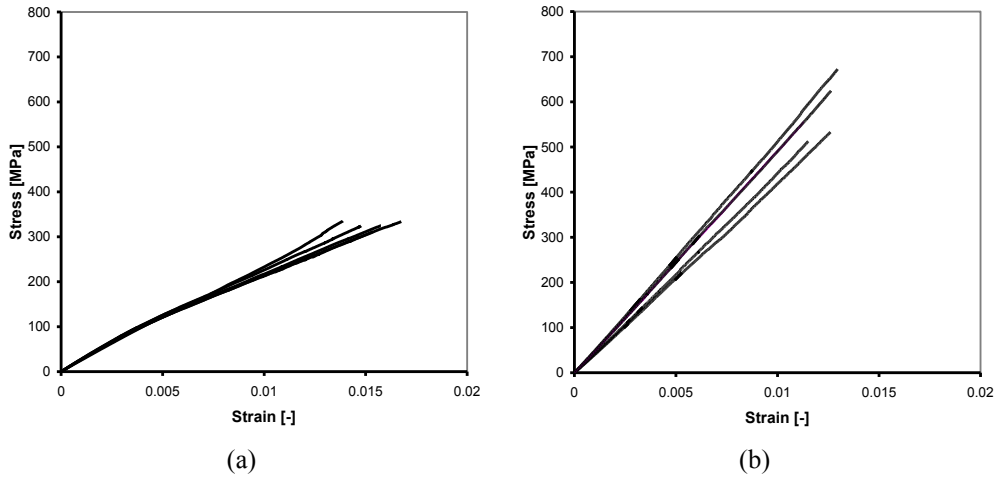
Figure 5.1. Loading configurations involved in the experimental activity on fiber reinforced skins (a) tensile test; (b) short beam test.

Table 5.2. Coupon geometries for laminate tests.

		n.	Lt	Lg	L	w	t	$\theta$
		coupon	[mm]	[mm]	[mm]	[mm]	[mm]	[-]
Tensile    warp direction	Glass fabric	6	60	190	250	15	1	all 0°
	Carbon fabric	5	60	190	250	25	0.8	all 0°
Tensile $\perp$ warp direction	Glass fabric	6	60	190	250	15	1	all 90°
	Carbon fabric	5	60	190	250	25	0.8	all 90°
Shear	Glass fabric	5	60	190	250	25	2	[+45°/-45°] <sub>2s</sub>
	Carbon fabric	5	60	190	250	25	1.6	[+45°/-45°] <sub>2s</sub>
Short-beam	Glass fabric	6	-	-	36	12	6	all 0°
	Carbon fabric	6	-	-	36	13	5	all 0°

Ultimate tensile stress and strain, elastic modulus, and Poisson's ratio have been derived for both warp and fill directions by meaning of two series of tensile tests (one series with the warp fibers parallel to the load and a second

series with warp fibers perpendicular to the load - fill direction -). Figure 5.2 and 5.3 depict the experimental stress-strain behavior of both carbon and glass phenolic laminates for tensile test in warp and fill direction respectively.



**Figure 5.2. Stress-strain curves derived by tensile tests on composite laminate in warp direction: (a) phenolic/E-glass laminate; (b) phenolic/carbon laminate;**

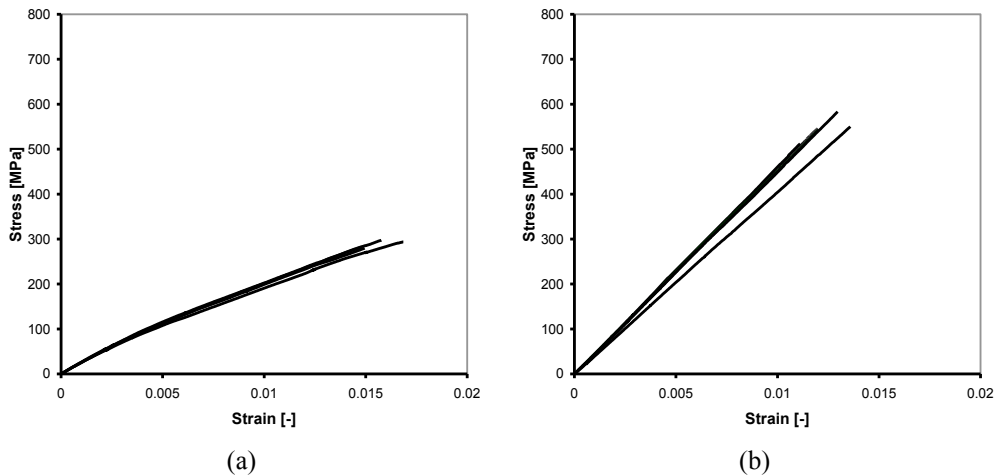


**Figure 5.3. Stress-strain curves derived by tensile tests on composite laminate in fill direction: (a) phenolic/E-glass laminate; (b) phenolic/carbon laminate.**

In-plane shear modulus, ultimate shear stress and strain have been derived by meaning of tensile tests on  $[\pm 45]_{ns}$  coupon. Figure 5.4 shows the experimental stress-strain behavior of both carbon and glass specimens.

For both in plane tensile and shear characterization, tests were conducted at a constant cross head velocity of 2 mm/min and three strain gauges were applied to each coupon, in order to monitor the longitudinal and transverse strain and the possible bending due to misalignment of the specimens.

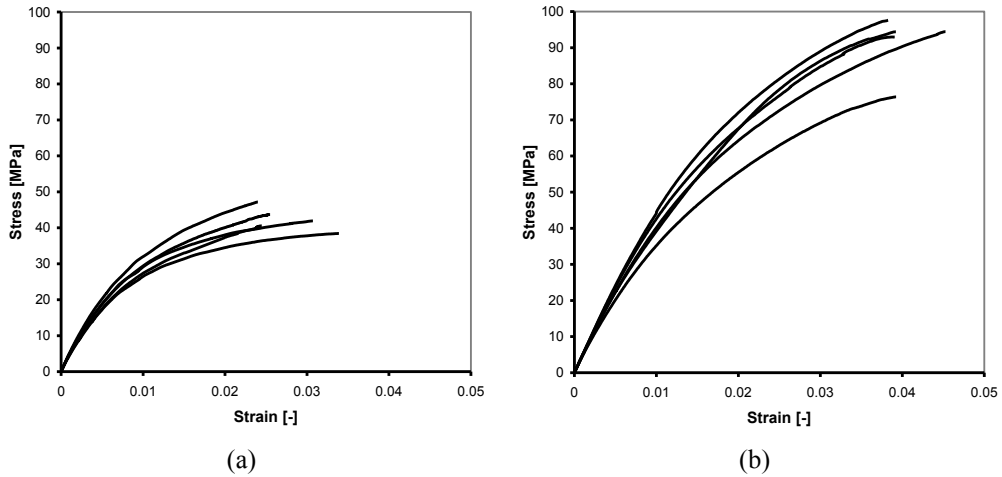


**Figure 5.4: Stress-strain curves derived by in plane shear tests on composite laminate: (a) phenolic/E-glass laminate; (b) phenolic/carbon laminate.**

Interlaminar shear stress have been derived by “short-beam” tests using a three-point bending set-up, with a support span of 24 mm. Tests were conducted at a constant cross head velocity of 1 mm/min. Fig. 5.5 depicts the stress-displacements behavior of both family specimens investigated.

Compressive mechanical parameters of selected composite skin are evaluated as 90% of the tensile values, according to the manufacture’s suggestion. The compressive value have been compared by means of flexural tests on sandwich specimens in accordance with ASTM C393 standard.

Table 5.3 shows all the mechanical properties derived by the described tests.

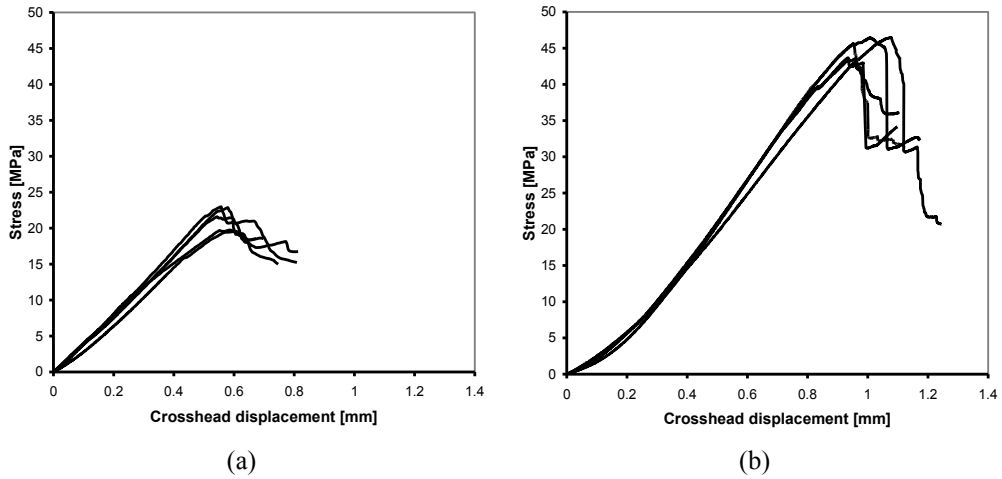


Figure 5.5. Stress-displacement curves derived by Short-beam tests on composite laminate: (a) phenolic/E-glass laminate; (b) phenolic/carbon laminate.

Table 5.3: Mechanical properties of composite skins derived by experimental tests.

	$E_1$	$E_2$	$G_{12}$	$F_{1t}$	$F_{2t}$	$F_6$	ILSS	$\epsilon_{1t}^u$	$\epsilon_{2t}^u$	$\gamma_6^u$	$\nu_{12}$
	[GPa]	[Gpa]	[GPa]	[MPa]	[MPa]	[MPa]	[MPa]	[-]	[-]	[-]	[-]
<b>Glass fabric</b>	25.54	22.97	3.41	325.77	288.21	43.30	21.34	1.53	1.56	2.47	0.15
<b>Carbon fabric</b>	46.65	44.32	4.44	579.59	546.90	91.19	45.09	1.22	1.23	4.12	0.10

## 5.4. Sandwich characterization

In the present section flexural behavior of composite sandwich specimens have been experimentally investigated by means of three-point and/or four point bending tests.

Four-point bending tests (Fig. 5.6) have been preliminary run on sandwich specimens obtained combining phenolic/E-glass sandwich skins with either hexagonal Nomex and aluminum honeycomb cores described in the previous chapter. The selected test fixture provides a support span  $S$  of 420mm and a loading span of 140mm.

The tests were performed on three specimens per each sandwich configurations. More details on specimen characteristics are reported in Table 5.4. All the sandwich specimens, involving honeycomb core, have been assembled with the  $L$  direction of the honeycomb core along the primary

direction. The suffixes L, W, T may be interpreted as “length”, “width”, and “transverse” direction respectively as shown in Fig. 5.7.

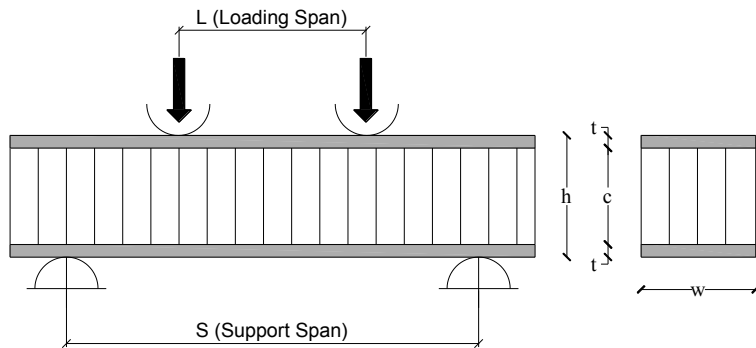


Figure 5.6. Four-point bending set-up for sandwich specimens.

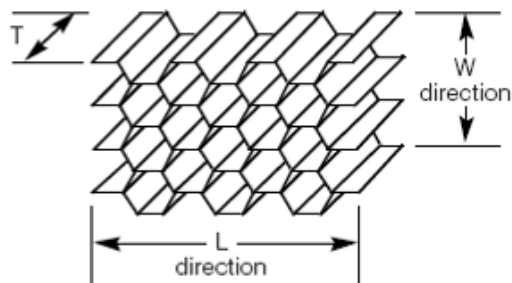


Figure 5.7. Shape geometry of the hexagonal honeycomb core.

Specimen deformations were monitored by four longitudinally-oriented electrical resistance strain gauges—two at the mid-span of the bottom skin and two at the mid-span of the top skin, whereas the displacement of the mid-span was monitored using a LVDT transducer. The tests were conducted in stroke control with a cross-head speed of 6 mm/min. The load was applied by a 25 mm wide flat steel blocks.

**Table 5.4. Four-point bending specimen characteristics.**

Material	Specimen code	Width w [mm]	Skin thickness t [mm]	Skin staking sequence	Core thickness c [mm]
Glass Aluminun	GA_1	100	0.5	[0/90]	21.50
Glass Nomex	GN_2	100	0.5	[0/90]	21.50
Glass Nomex	GN_3	100	1	[0/90]s	21.50
Glass Nomex	GN_4	100	2	[0/90]2s	21.50

In order to compare the results of the different specimen geometries and loading configurations, the flexural response of the selected sandwich panels has been reported in terms of bending moment-curvature curves.

The sandwich curvatures have been calculated by the strain signals of the top and bottom skins at the mid-span. Bending moments at the mid-span have been derived by the value of the applied force and loading configuration.

Figure 5.8 depicts the experimental behavior of *GA\_1* and *GN\_1* sandwich specimens. Each curve is the mean data of the three replicate specimens.

As expected, experimental flexural stiffnesses (slope of the curves) are very similar for both the specimen groups. It underline that core material do not contribute to the flexural stiffness of the sandwich configuration.

At the same way a large difference is observed in term of ultimate load. The low value of ultimate load of *GA\_1* specimens are related to premature failures occurred during the tests.

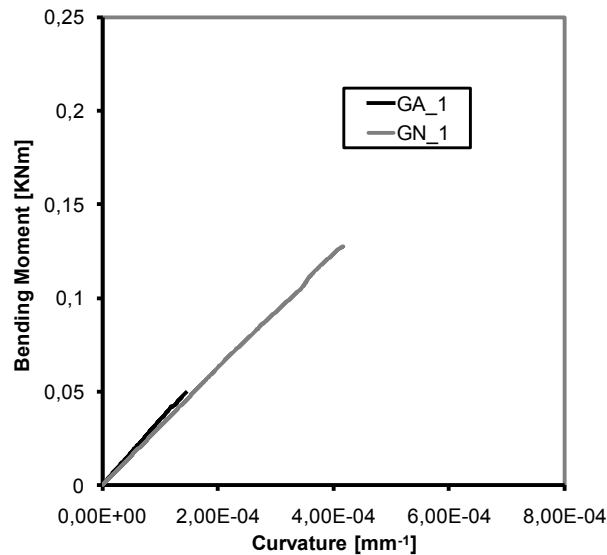


**Figure 5.8.** Comparison between Aluminum and Nomex honeycomb sandwich behaviors.

Typical failure mode in *GA\_1* specimens is the debonding. Debonding failure was observed both in mid span of the specimen (due to the maximum bending moment) and in the supported end of the specimen (due to the maximum shear force). These failure mode are reported in Figs. 5.9a and 5.9b respectively.



**Figure 5.9.** Failure mode of *GA\_1* specimens: (a) mid-span debonding; (b) support edge debonding.

Figure 5.10 depicts bending moment-curvature curves derived by four-point

bending tests on *GN* specimens. Each curve is the mean data of the three replicate specimens. It allows to compare the flexural behavior of the same sandwich configuration when the skin thickness is increased.

Can be observed that variation on the skin thickness not only allows to achieve different flexural stiffness but may also influence the flexural response with regard of failure mode.

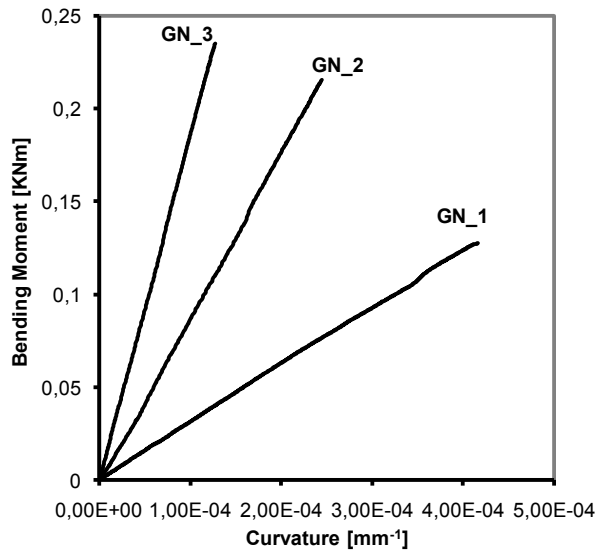


**Figure 5.10.** Bending moment-curvature curves of *GN* specimens subjected to four-point bending tests.

In the present case, top skin compressive failure have been observed for all the three specimens of *GN\_1* configuration (Fig. 5.11a), whereas shear failure have been occurred in both *GN\_2* and *GN\_3* specimens under four-point bending loading as shown in Fig. 5.11b.

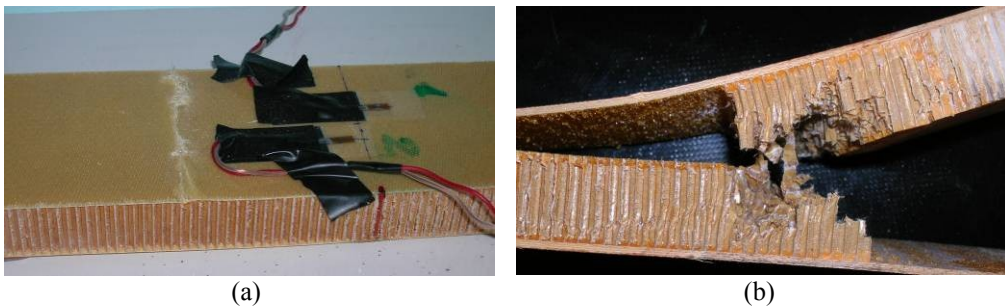


**Figure 5.11:** Failure mode of *GN* specimens: (a) top skin compressive failure of *GN\_1* specimens; (b) core shear failure of *GN\_2* and *GN\_3* specimens.

The results of these preliminary investigation allow to establish that Nomex honeycomb allows to achieve a better compatibility with the phenolic skin than the aluminum honeycomb core. As consequence, only Nomex honeycomb core are involved in the have following experimental activity.

In order to compare the sandwich behavior involving the different core and skins materials described in the previous chapter, three point bending tests (Fig. 5.12) have been run on sandwich specimens obtained combing either glass and carbon phenolic skins with either Nomex honeycomb and foam cores.

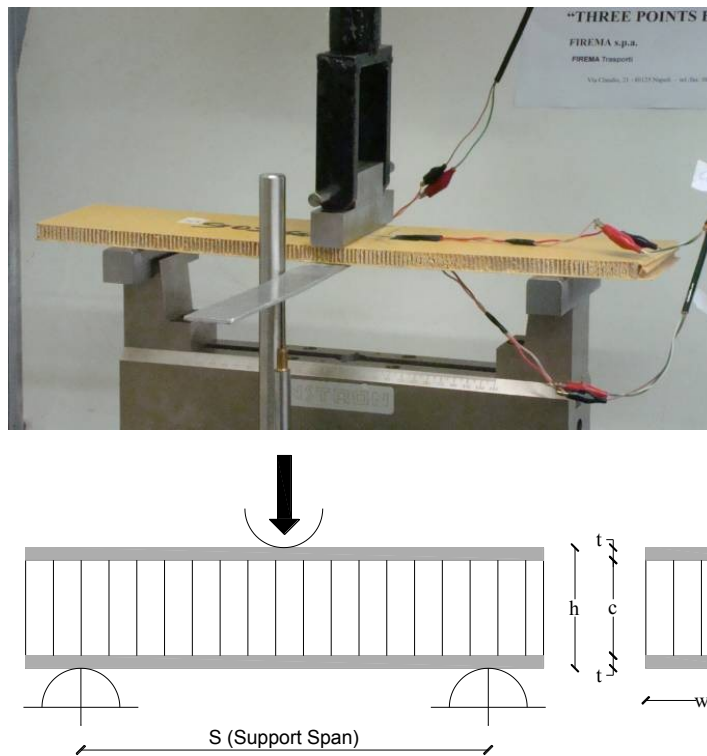


**Figure 5.12. Three-point bending set-up for sandwich specimens.**

The tests were performed on two replicate specimens per each sandwich and loading configurations. More details on specimen characteristics and loading configuration are reported in Table 5.5.

Specimen deformations were monitored by three longitudinally-oriented electrical resistance strain gauges—one at the mid-span of the bottom skin and one at a 25-mm distance from the mid-span on the top and bottom skins,

so that bending curvatures can be calculated by the strain signals of the top and bottom skin at a 25-mm distance from the mid-span. The displacement of the mid-span was monitored using a LVDT transducer. The tests were conducted in stroke control with a cross-head speed of 6 mm/min and the load was applied by a 25 mm wide flat steel block.

**Table 5.5. Four-point bending specimen characteristics.**

Material	Specimen code	Width w [mm]	Skin thickness t [mm]	Skin staking sequence	Core thickness c [mm]	Support Span S [mm]
<b>Glass Nomex</b>	GN_4a	100	1	[0/90] <sub>s</sub>	10.50	325
<b>Glass Nomex</b>	GN_4b	100	1	[0/90] <sub>s</sub>	10.50	265
<b>Glass Nomex</b>	GN_5a	100	2	[0/90] <sub>2s</sub>	10.50	170
<b>Glass Nomex</b>	GN_5b	100	2	[0/90] <sub>2s</sub>	10.50	150
<b>Glass Foam</b>	GF_1a	100	1	[0/90] <sub>s</sub>	10.50	325
<b>Glass Foam</b>	GF_1b	100	1	[0/90] <sub>s</sub>	10.50	265
<b>Carbon Nomex</b>	CN_1a	100	0.4	[0/90]	10.50	325
<b>Carbon Nomex</b>	CN_1b	100	0.4	[0/90]	10.50	265
<b>Carbon Foam</b>	CF_1a	100	0.4	[0/90]	10.50	325
<b>Carbon Foam</b>	CF_1b	100	0.4	[0/90]	10.50	265

Figure 5.13 depicts the mean experimentally bending moment-curvature curves derived by both four-point and three-point bending tests on *GN* specimens. Figure 5.13 allows comparing the flexural stiffness (slope of the curves) of the *GN* sandwich specimens obtained by varying the core and/or skin thicknesses.

As expected, a higher increase in the sandwich stiffness can be obtained by increasing the core thickness (from GN\_4 to GN\_2 / from GN\_5 to GN\_3)

than by increasing the skin thickness (from GN\_4 to GN\_5 / from GN\_2 to GN\_3).

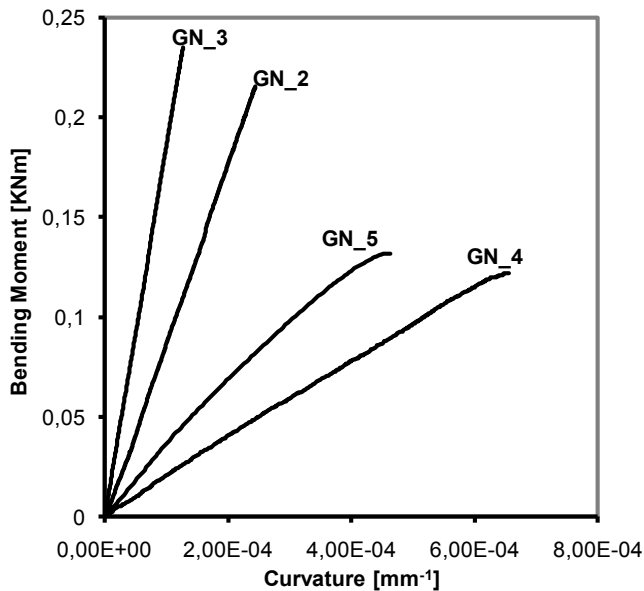


**Figure 5.13. Bending moment-curvature curves of GN specimens failed by core shear.**

All the specimen considered in these comparison failed due to core shear. The difference in the ultimate applied load (and consequently bending moment) are due to the difference in the core thicknesses. According to the ASTM standard C393, the core shear ultimate stress of Nomex honeycomb core can be derived as function of ultimate applied loads and specimen geometry. The experimental ultimate core shear is equal to 0.72 MPa (c.v. 4.07%). The derived value is too close to the 0.69 MPa provided by manufacture's data.

Figure 5.14 depicts the load-displacements response, obtained by mean data of the two replicate specimens, of the four combination of sandwich specimens under three-point bending tests with a support span of 265mm.

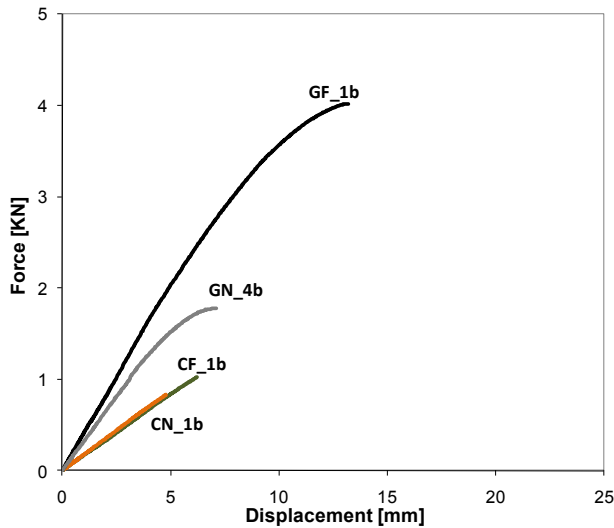
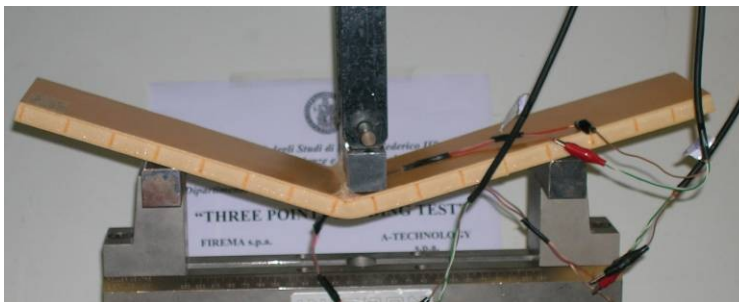


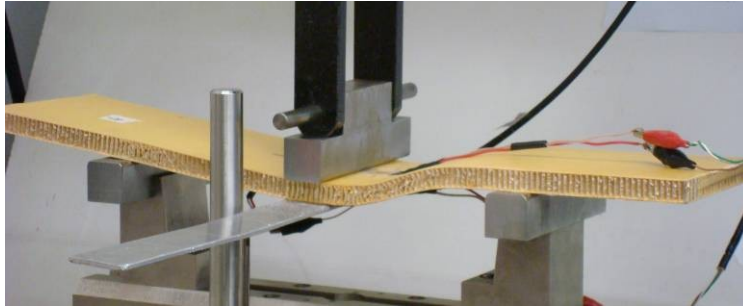
**Figure 5.14.** Load-displacement curves of specimens loaded in three point bending configuration with a support span of 265mm.

The flexural behavior of *GN\_4* and *GF\_1* specimens are very similar for low value of the load - shear deformation of the core can be neglected -, whereas increasing the load, the slope of the curves differs due to different shear modulus of the core materials.

The ultimate applied load achieved by the *GN* and *GF* specimens is conditioned by the failure mode . In particular skin compressive failure (Fig. 5.15a) was observed for *GF* specimens, whereas, as mentioned before, core shear failure (Fig. 5.15b) characterized the *GN* specimens loaded in three-point bending configurations.



(a)



(b)

**Figure 5.15. Failure mode of  $GF_1$  and  $GN_4$  specimens loaded in three-point bending: (a) top skin compressive failure of  $GF_1$  specimens; (b) core shear failure of  $GN_4$  specimens.**

Shear deformation effects do not influence the flexural response of  $CN_1$  and  $CF_1$  specimens, where instability phenomena of compressive top skin determined low valued of ultimate load. In particular, wrinkling failure mode (Fig. 5.16a) was observed in the compressive top skin of the  $CF_1$  specimens, whereas intra-cellular buckling (Fig. 5.16b) failure occurred at the compressive top skin of  $CN_1$  specimens.

Experimental flexural  $D$  and shear  $U$  stiffness of  $GN_4$ ,  $GF_1$ ,  $CF_1$ , and  $CN_1$  sandwich configurations have been derived by comparing the results of each specimen configuration tested with different support span according to ASTM D7250 standard.

Table 5.6 allows to compare the flexural and shear stiffness derived by experimental results and analytical formulation reviewed in the third chapter. Based on the derived sandwich skin properties, transverse shear rigidity and, consequently, core shear modulus have been calculated as a function of given deflections and applied forces from the results of a single loading configuration test in accordance with ASTM standard D7250. The experimental shear modulus of the Nomex honeycomb core is equal to 45.11 MPa (c.v. 6.07%). The derived value is very close to the 44.83 MPa provided by manufacture's data. Whereas the experimental shear modulus of the foam core is equal to 50.75 MPa (c.v. 5.11%). The derived value is very close to the 50 MPa provided by manufacture's data.

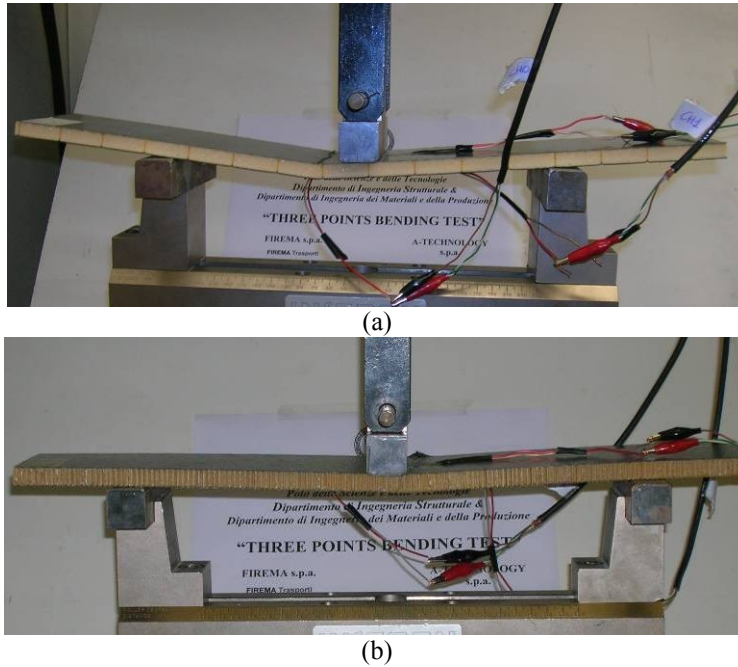


Figure 5.16. Failure mode of *CF\_1* and *CN\_1* specimens loaded in three-point bending: (a) top skin wrinkling instability of *CF\_1* specimens; (b) top skin intra-cellular buckling of *CN\_1* specimens.

Table 5.6: Comparison between experimental and analytical flexural and shear stiffness

Specimen code	Experimental		Analytical	
	D [kNmm <sup>2</sup> ]	U [kNmm]	D [kNmm <sup>2</sup> ]	U [kNmm]
GN_4	189905.37	59.05	183864.96	58.69
GF_1	168578.79	62.55	168862.09	62.98
CN_1	57082.05	51.26	58522.43	51.12
CF_1	53648.66	54.35	53413.84	54.52

## 5.5. Analysis of structural behavior

Closed-form analytical and numerical tools, discussed in the second chapter, have been analyzed in order to capture the experimentally behavior both in term of stiffness and in regard to failure modes. Theoretical analysis have been based on both ordinary bending theory and higher-order sandwich beam

theory (HOSBT). For both approaches, the analysis is elastic, which is appropriate to describe the beam response up to peak load for the possible material combinations.

As discussed in the third Chapter, the ordinary theory have been adopted in order to evaluate the stresses in the core or skins and hence the applied loads corresponding to various failure mechanisms. The failure loads depend on properties of the skin and solid core material, relative density of the core, thickness of both skins and core and beam span and loading details. The maximum stress in the face sheets can be used to predict the beam failure due to the skin failure modes—i.e., face ultimate strength, face wrinkling and intra-cellular buckling. The expressions related to the various skin failure modes are summarized in the second chapter.

Moreover sandwich structures loaded in bending can fail due to core failure. Pertinent modes are shear failure or indentation by local crushing in the vicinity of the loads application. Shear failure occurs when the applied shear stress equals the shear strength of the core. Indentation failure is predicted when the out-of-plane compressive stress equals the out-of-plane compressive strength of the core.

In order to achieve explicit expression of failure load such as reported in Chapter III, the core failure mechanism, stiffness and strength properties for the Nomex honeycomb and foam core are required.

The out-of-plane Poisson's ratio, required for the failure analysis, can be taken, to a first approximation, as that of the solid materials  $\nu_s$ . The out-of-plane Young's modulus of the Nomex honeycomb is given by the rule of mixture expression as described in the second chapter:

$$\frac{E_c}{E_s} = \frac{\rho^*}{\rho_s}, \quad (5.1)$$

where  $\rho_s$  and  $E_s$  are the density and Young's modulus of the solid honeycomb material, respectively. For a honeycomb with regular hexagonal cells, Wierzbicki [] gives the following expression for the ultimate out-of-plane compressive strength:

$$\sigma_{cc} = 3.25\sigma_{sc} \left( \frac{\rho^*}{\rho_s} \right)^{5/3}, \quad (5.2)$$

where  $\sigma_{sc}$  is the compressive strength of the solid from which the core is made. Petras and Sutcliffe [ ] derive the following Expressions for the out-of-plane shear strengths of regular hexagonal honeycomb core:

$$\frac{\tau_{c31}}{E_s} = 1.7 \left( \frac{\rho^*}{\rho_s} \right)^3, \quad (5.3)$$

$$\frac{\tau_{c32}}{E_s} = 2.6 \left( \frac{\rho^*}{\rho_s} \right)^3. \quad (5.4)$$

Based on a analysis of the manufacturer's modulus and strength data, for the selected foam core the following expressions are derived:

$$\frac{E_c}{E_s} = 1.16 \left( \frac{\rho^*}{\rho_s} \right)^{1.28}, \quad (5.5)$$

$$\frac{\sigma_{cc}}{\sigma_{sc}} = 1.10 \left( \frac{\rho^*}{\rho_s} \right)^{1.63}, \quad (5.6)$$

$$\frac{\tau_c}{\sigma_{sc}} = 0.78 \left( \frac{\rho^*}{\rho_s} \right)^{1.28}. \quad (5.7)$$

The actual behavior is then governed by the mode with the minimum failure load that can be reached combining all the described mechanisms. Failure load surfaces and the relative failure mode maps have been drawn, using the Matlab programming language, for the tested sandwich structures (Fig. 5.17-5.20). The failure modes and loads are plotted as a function of core relative density and skin thickness to span ratio, at fixed core thickness to span ratio. When plotting the experimental measurements for each sandwich configuration, it is observed that the experimental failure modes are consistent with the analytical predictions in each case. It is interesting to observe that, for sandwich structures with a Nomex honeycomb, the intracellular buckling mode represents less severe condition than the wrinkling failure when phenolic/glass skins are employed. Whereas the opposite behavior is observed when phenolic/carbon skins are employed. However, the wrinkling surface represents a small area of the failure mode map since

the honeycomb sandwich has a high modulus in the out-of plane direction, thus limiting the wrinkling phenomenon.

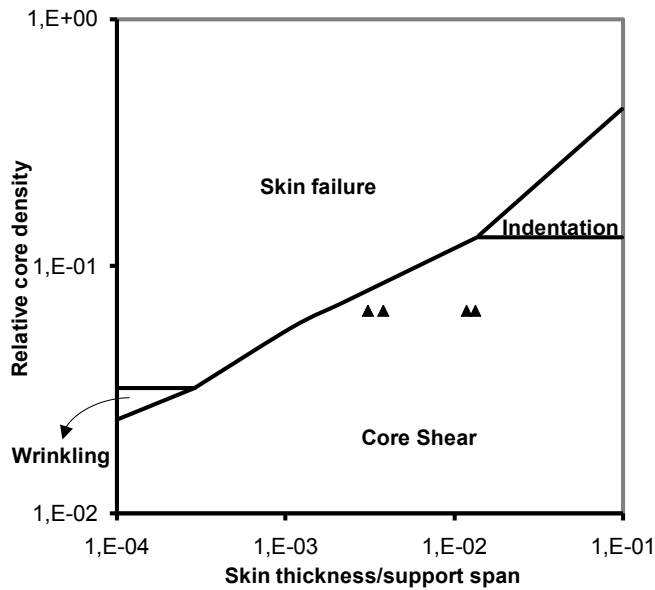
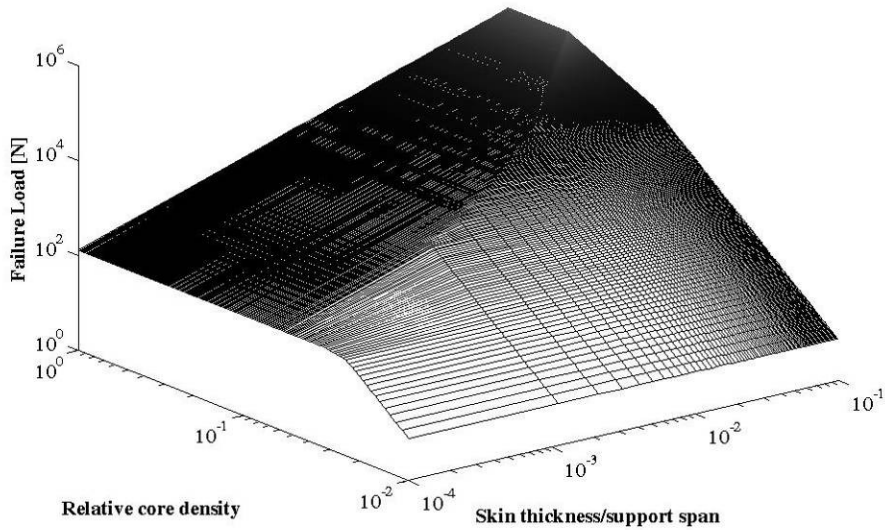


Figure 5.17. Failure mode map of *GN* sandwich specimens under three point bending tests. The ▲ symbols identify experimental measurements.

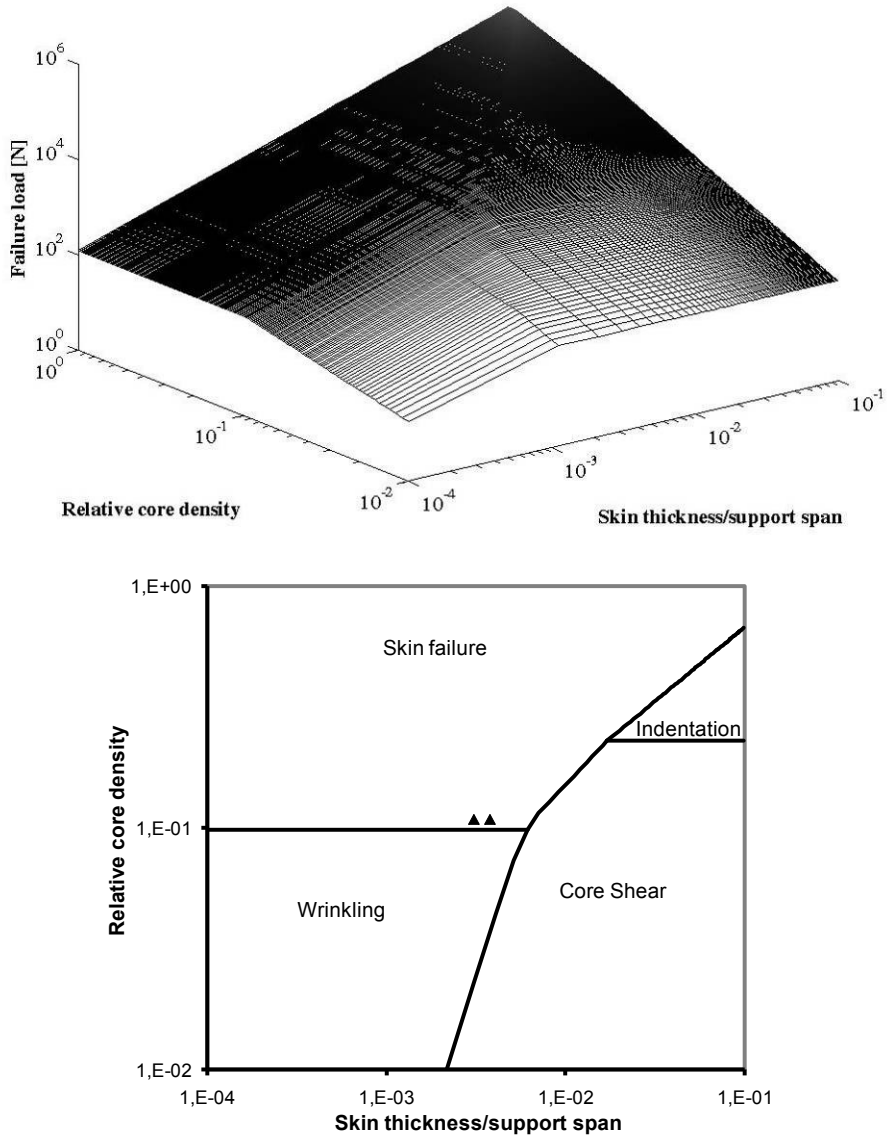


Figure 5.18. Failure mode map of *GF* sandwich specimens under three point bending tests. The ▲ symbols identify experimental measurements.

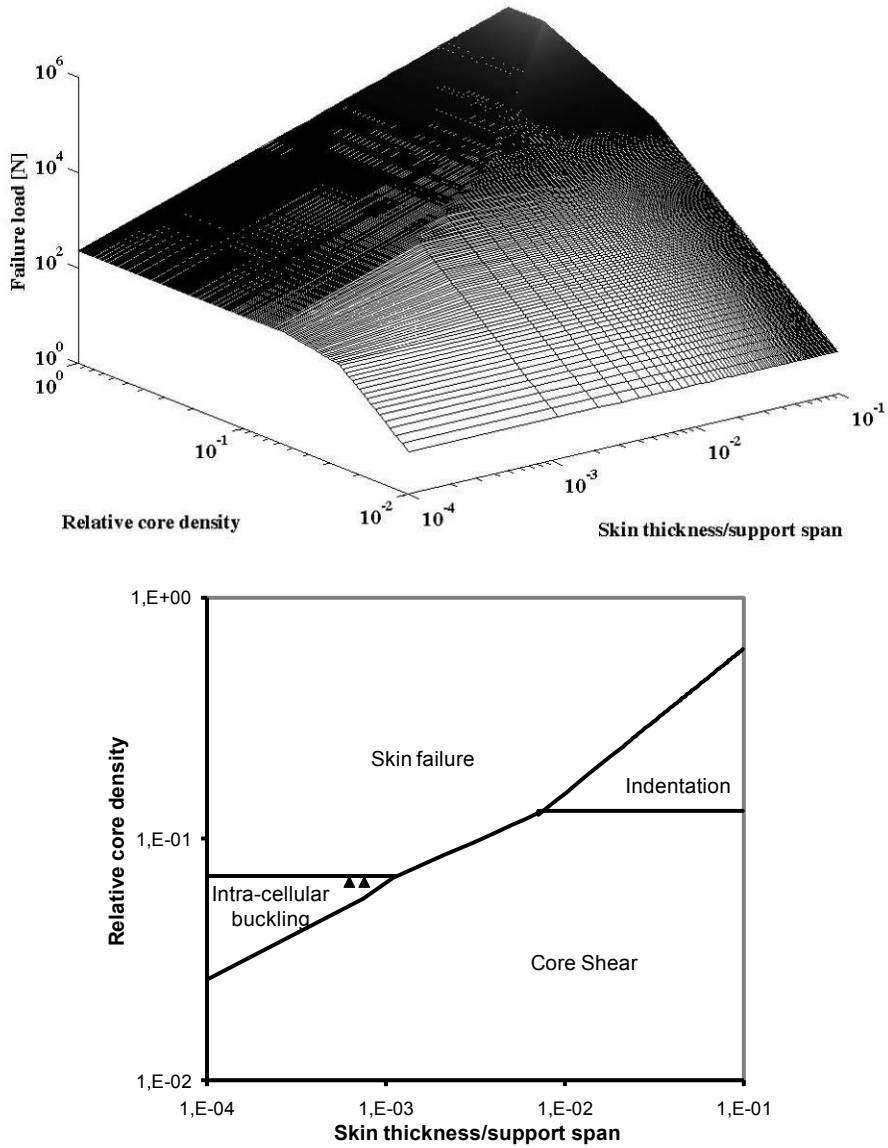
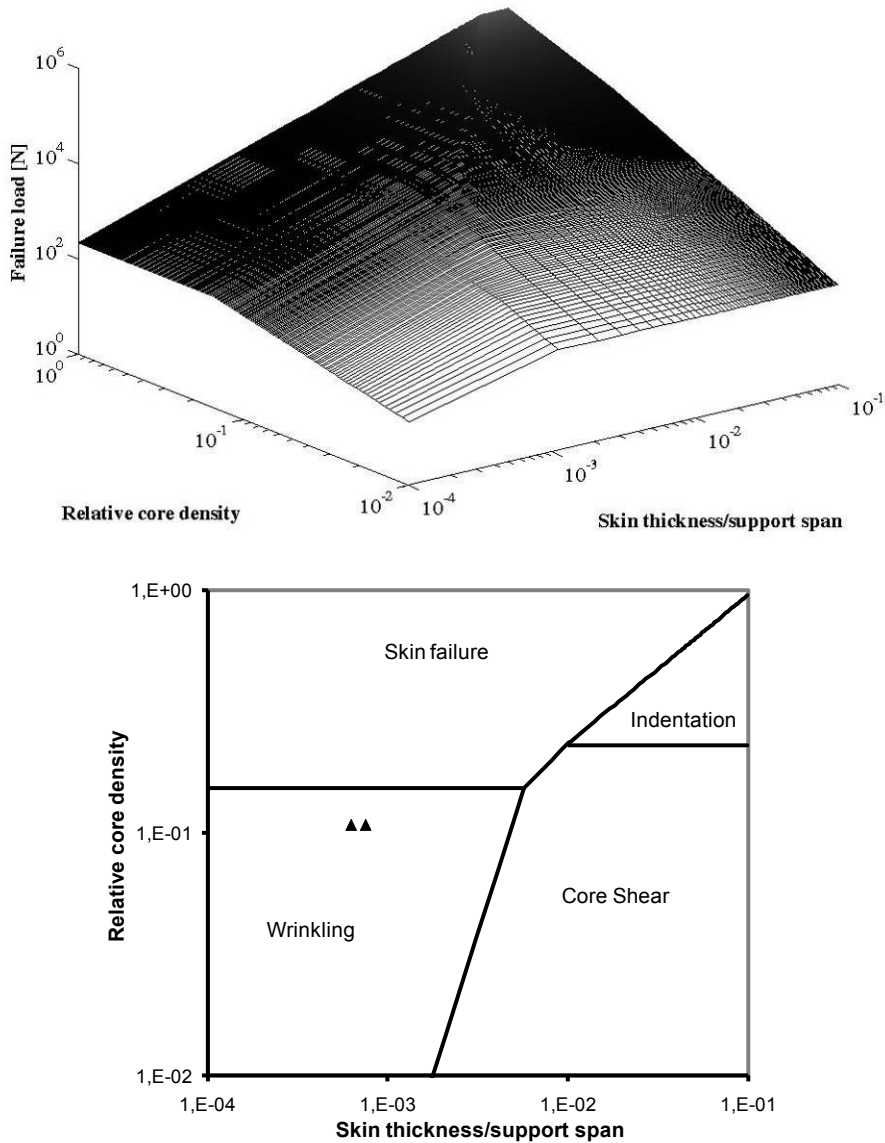


Figure 5.19. Failure mode map of CN sandwich specimens under three point bending tests. The ▲ symbols identify experimental measurements.



**Figure 5.20.** Failure mode map of *Cf* sandwich specimens under three point bending tests. The  $\blacktriangle$  symbols identify experimental measurements.

The HOSBT approach describe in the third chapter has been implemented using the Matlab programming language to calculate the beam response in term of load-displacement curves. Moreover finite element modeling has been developed to perform reliable simulations of structural behavior of sandwich beams to be compared with the experimental data. The analysis

was performed on 3D-models using Nastran<sup>®</sup> finite element codes (Fig. 5.21). The skins were meshed using 4-node shell elements, while the core was meshed using 8-node chexa solid elements. A 2D-orthotropic material was used to define the composite fabric prepreg, and the composite function was used to create the stacking sequence of the face sheets. Isotropic and 3D-orthotropic materials were used for foam and honeycomb core respectively. Skins and core material properties were defined only in the linear elastic range.

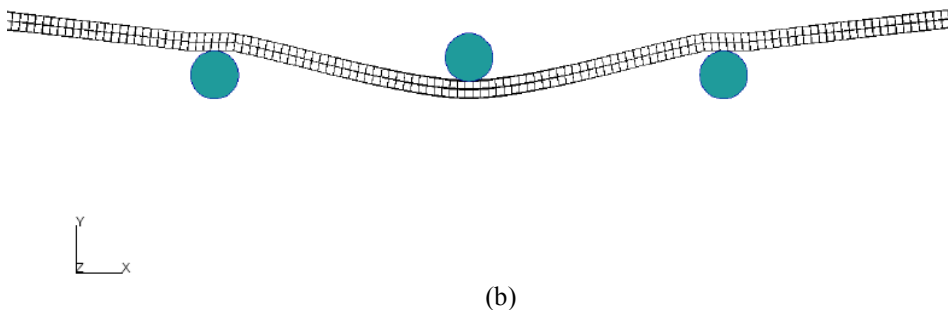
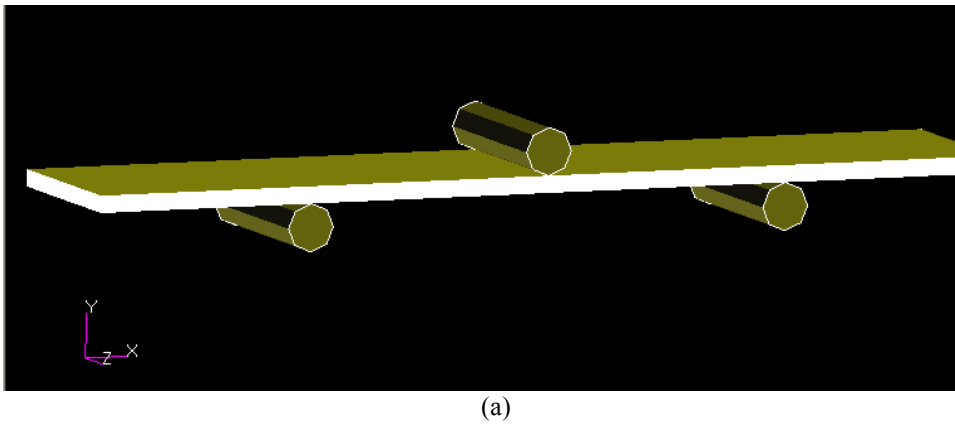
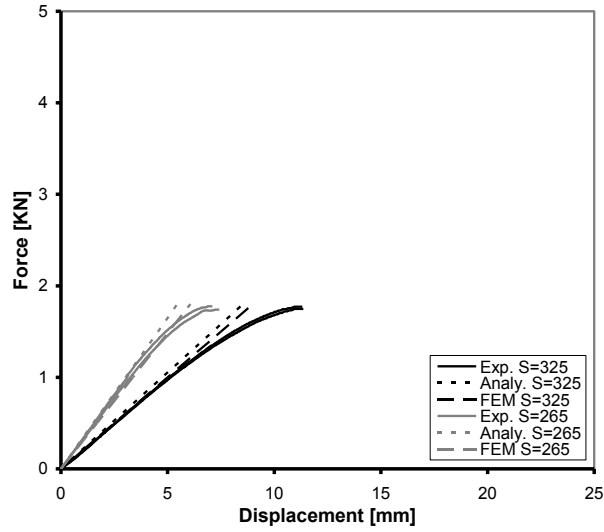
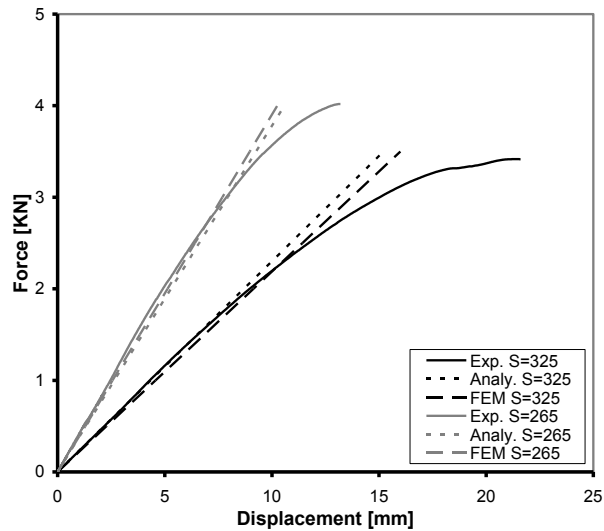


**Figure 5.21: FE model of sandwich specimens: (a) three-point bending loading configuration; (b) deformed shape.**

Figures 5.22 and 5.23 shows that the numerical and analytical behaviors are perfectly matched with the experiments.



(a)



(b)

Figure 5.22: Experimental, analytical, and numerical force-displacement behavior: (a) *GN\_4* specimens; (b) *GF\_1* specimens.

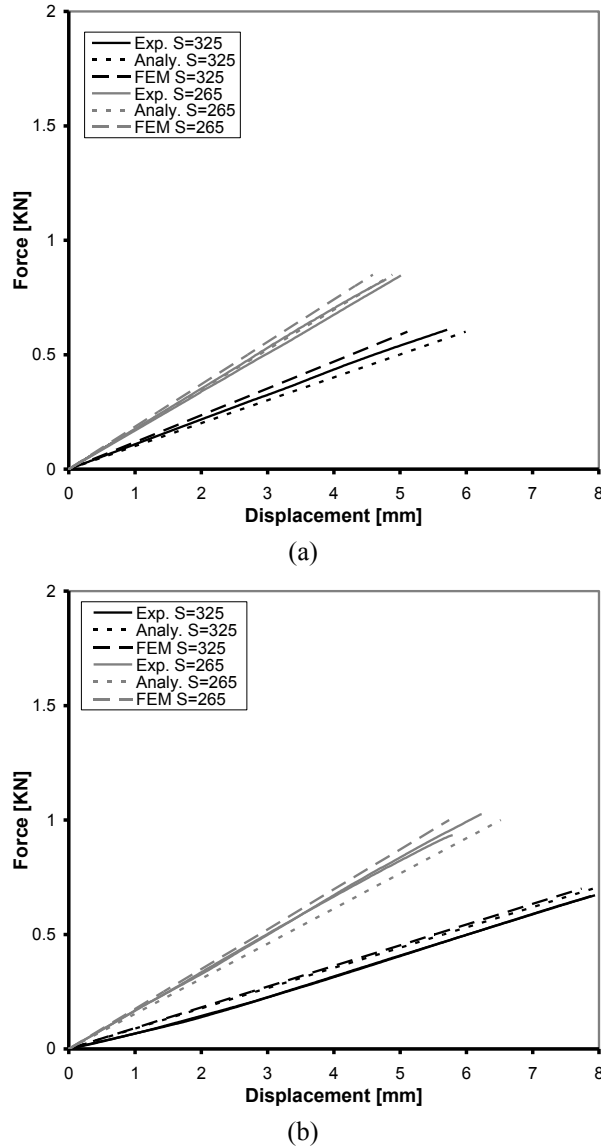


Figure 5.23: Experimental, analytical, and numerical force-displacement behavior: (a) *CN\_1* specimens; (b) *CF\_1* specimens.

## 5.6. Final remarks

The experimental activity presented in this Chapter allows to determinate the basic laminae properties of the selected phenolic impregnated composite

skins and to assess the flexural behavior of sandwich components involving different core structures.

The preliminary investigation on Nomex and aluminum honeycomb sandwich specimens shows that the aluminum honeycomb core do not allow to achieve sufficient bonding strength at core-skin interface, instead of Nomex honeycomb for which no premature failure occurred during the tests. A good core-skin interface have been shown also when foam core is employed.

The main difference between foam core and honeycomb core sandwich specimens can be found in the failure behavior. In fact, the foam core are more susceptible to local instability than honeycomb core (see. failure surface of failure mode maps). In addition, the Nomex honeycomb core, at fixed mechanical properties, allows to achieve a lightweight sandwich components.

As consequence of the above consideration, the following steps of the proposed multiscale procedure have been carried out involving only the selected Nomex honeycomb core combined with glass/phenolic skins. The phenolic/glass, in fact, are expect to guarantee the strength and stiffness requirements for the selected application.

## References

Belingardi G., Cavarota M.P., Duella R., “Material characterization of a composite-foam sandwich for the front structure of high speed train”.

*Composite Structures*, 61, pp 13-25, 2003.

Shin K.B., Lee J.Y., Cho S.H., “An experimental study of low-velocity impact responses of sandwich panels for Korean low floor bus”.

*Composite Structures*, 84, pp 228-240, 2008.

[12] Kim J. S., Lee S.J., Shin K.B., “Manufacturing and structural safety

evaluation of a composite train carbody”. *Composite Structures*, 78, pp 468-476, 2007.

[13] Kim J. S., Chung S.K., “A study on the low-velocity impact response of laminates for composite railway bodyshells”. *Composite Structures*, 77, pp 484-492, 2007.

[14] NAFEMS, *Quality system supplement to ISO 9001 relating to Finite element analysis in the design and validation of Engineering products*. National Agency for Finite Element Methods and Standards. Issue 1.3, 1993.

[15] AFNOR NF F16-101, “*Matériel roulant ferroviaire - Comportement au feu - Choix des matériaux*”, October 1988.

ASTM D3039M, “*Standard test method for tensile properties of polymer matrix composite materials*”, 2000.

ASTM D3518M, “*In-plane shear response of polymer matrix composite materials by tensile test of a  $\pm 45^\circ$  laminate*”, 1994.

ASTM D2344M, “*Standard test method for short-beam strength of polymer matrix composite materials and their laminates*”, 2000.

ASTM C365M, “*Flatwise compressive properties of sandwich cores*”, 2005.

ASTM C393M, “*Core shear properties of sandwich constructions by beam flexure*”, 2006.

ASTM D7250M, “*Determining sandwich beam flexural and shear stiffness*”,  
2006.

## **Chapter VI**

# ***ANALYSIS OF JOINING TECHNIQUES***

### **6.1. Introduction to framework activities**

In the present Chapter possible joining techniques that can be employed in the design process have been analyzed and characterized. Joining of composite sandwich components can be achieved connecting basic sandwich elements. The basic configurations are listed in Fig. 6.1. They can be employed to define all possible configurations to connect sandwich components by varying joint parameters (e.g. shape, position, size).

The basic configurations provide the use of: (a) sandwich skins; (b) sandwich core; (c) both skin and core sandwich elements.

Since for common sandwich structures core is weak, the use of mechanically fasteners requires the use of insert in the core in order to increase the stiffness and the strength of the joint. At the same way, the discontinuity in the core may cause a premature cracks that can propagate towards the skin/core interface.

For these reason, in the present work, the joining of sandwich components have been achieved involving only fiber reinforced skins elements.

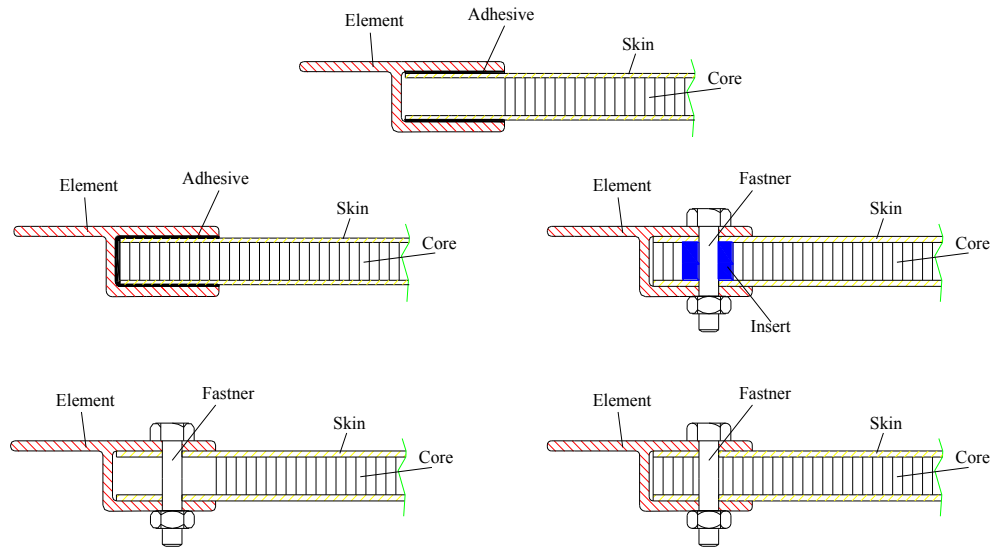


**Fig. 6.1. Basic configuration of sandwich joints.**

## 6.2. Review of joining techniques

Degradation and failure of transportation structures frequently initiate at the joint; therefore, adequacy of joint design exerts strong influence on safety, durability and reliability. The joints are responsible for the majority of vehicle fatigue cracking issues, so the fatigue life of joints both in metallic or composite applications is a topic of primary importance in the structural design.

It is well known that the characterization of the strength and stiffness of composite materials is complicated by the very large number of variables involved. The situation is, of course, considerably worse with regards to the behavior of load-carrying joints in composites since, in addition to the material variables, parameters related to the type of joint and its associated geometry must also be considered. Since it is difficult to reliably predict the influence of all these parameters on joint behavior and life, the designer is often forced to depend on testing to evaluate the performance of various joining techniques.

The use of composite structures presents a significant challenge with respect

to the methods of joining to be used in vehicle assembly. Joining of composite structures can be achieved through the use of mechanical, adhesive bonded or hybrid (mechanical/bonded) joints instead of welding joints that are common used in metal body vehicle.

Mechanically fastened joints are still the dominant fastening solutions used in joining of primary structural parts made of advanced composites. The mechanical joints have several advantages over the adhesively bonded joints, which require careful surface treatment of the adherends, are affected by service environment and are difficult to dismantle for inspection and repair; although adhesive joints allow distributing the load over a larger area than the mechanical joints and thus attaining high structural efficiency, especially with regards to fatigue life.

The relative benefits and limitations of each technique are discussed, in light of demands of transportation industry.

### **6.2.1. Adhesive bonding**

The benefits of adhesive bonding have been extensively demonstrated in literature [1]:

- Adhesive bonding offers improved joint stiffness compared to mechanical fasteners because it produces a continuous bond rather than a localized point contact. This allows attaining high structural efficiency, especially with regards to fatigue life;
- A well designed joint will absorb energy well, and tend to have good noise and vibration damping properties;
- The adhesive is essentially dual purpose in this type of application - as well as providing mechanical strength, the adhesive seals the joint against moisture and debris ingress;
- The smooth joint produced reduces stress concentrations at the joint edges thereby providing good fatigue resistance;
- Adhesive bonds are inherently high strength in shear;
- It is possible to join dissimilar, and otherwise incompatible materials.
- Adhesive bonding has tended to be regarded as a comparatively low cost

process in terms of equipment. However, process automation by robot for example, necessitates such measures as viscosity compensation, either by variable nozzle orifice size or heated supply hoses, to provide consistent application. A control system which allows the robot and adhesive dispenser system to interact is also required [14]. Low cost is therefore arguable and requires further examination of actual cost data to provide an accurate comparison.

The limitations of the process are:

- Current high performance adhesives are epoxy or solvent-based systems, giving rise to considerable environmental concerns. The health and safety hazards involved in the use of these substances implies significant costs in providing adequate fume extraction, protective clothing and adequate provision for fire protection storage. Given current environmental concerns, there is also the possibility that these substances may eventually be banned from use by future legislation;
- Structural adhesives require heat curing;
- There are also foreseeable difficulties with extensive utilization of adhesive joints in volume production. Adhesives have a limited shelf-life and provision must be made for this by materials control. Despite increasingly sophisticated systems designed to counter problems such as increasing viscosity over time, the adhesive dispensers are still likely to require regular cleaning and therefore planned routine maintenance to prevent problems;
- Adhesive joints are inherently weak in peel and vehicle design would need to take account of this, particularly with regard to crashworthiness.

With reference to this final point, in practice a bonded structure often has to sustain a combination of tensile, compressive, shear, cleavage and peel stresses (Fig. 6.2). Therefore in order to minimize the peel stresses experienced by a joint, thereby substantially increasing its robustness, engineers generally use some form of lap shear joint.

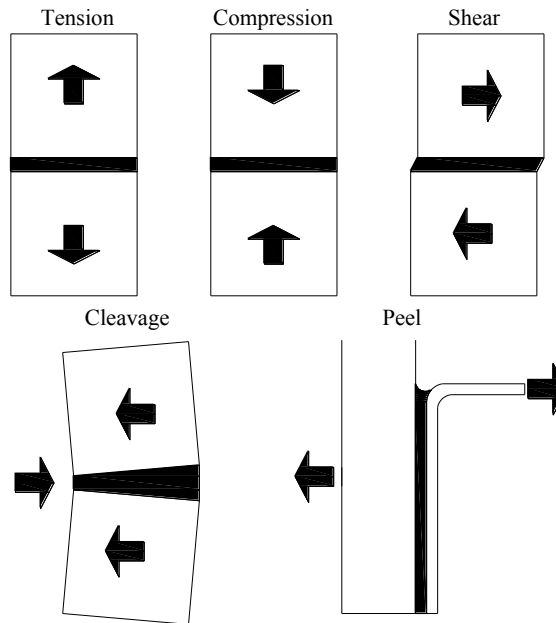


**Fig. 6.2. Five basic loading conditions for adhesive bonded joints**

A simple lap shear joint is not ideal structurally because shear and peel stresses tend to be concentrated at the ends of the joint, thereby weakening it (Fig. 6.3).

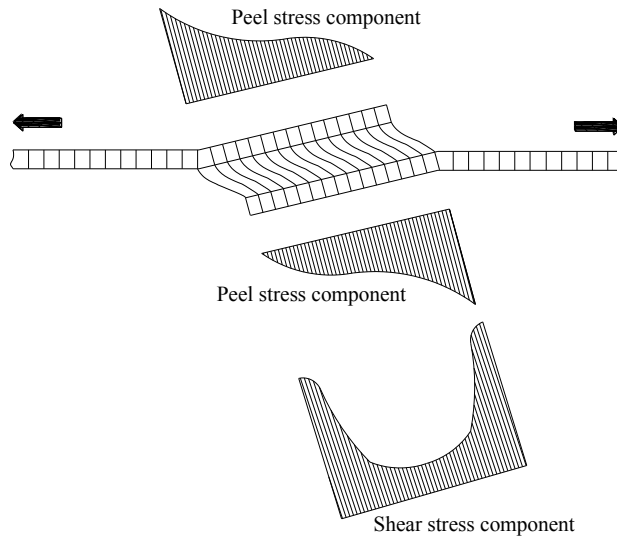


**Fig. 6.2. A simple lap shear joint under load**

Lap shear configurations which minimize these stress concentrations have

therefore been developed (Fig. 6.4) [13].

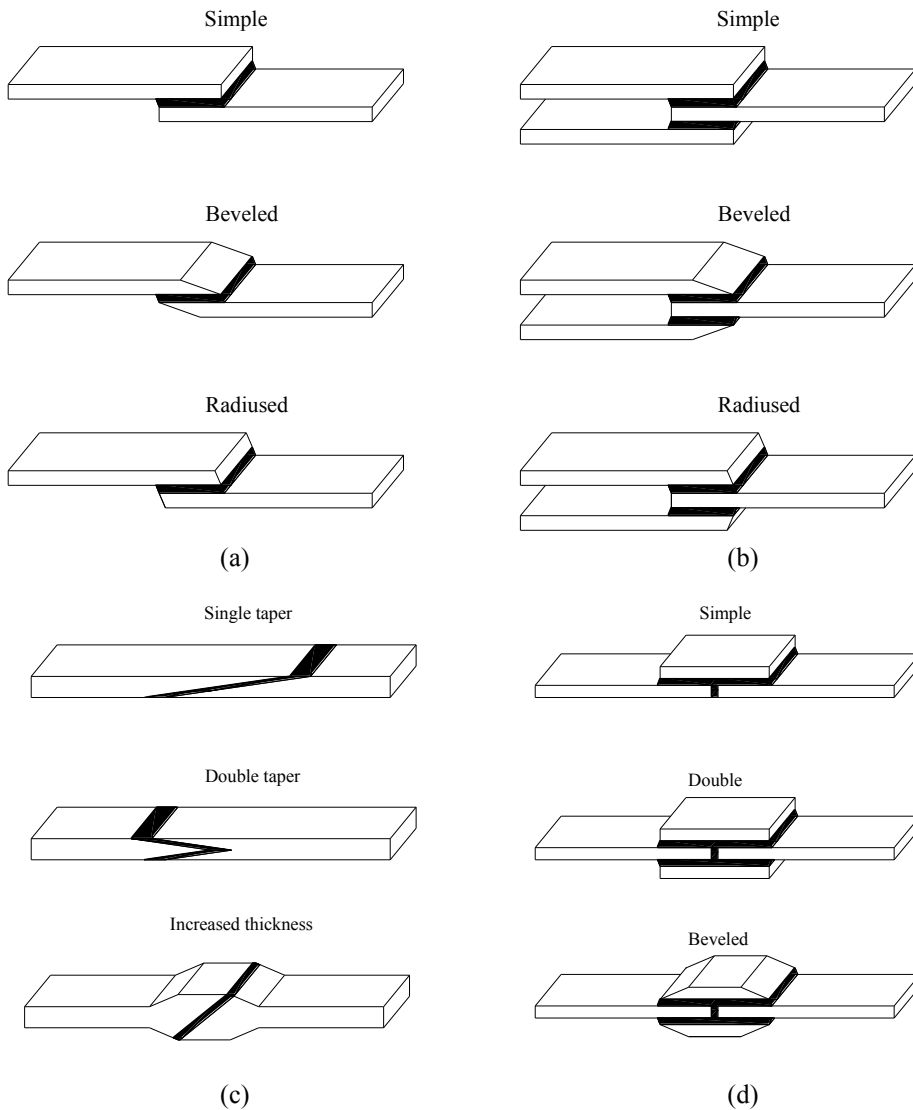


**Fig. 6.4. Bonded joint configurations: (a) single lap; (b) double lap; (c) scarf; (d) strap.**

Such joint designs do however present an additional problem. As yet, such joint designs are unable to prevent displacement of a substantial proportion of the adhesive from the joint area as the surfaces of the joint components slide over each other during assembly.

Aside from the issues outlined above, the need for fixturing to support joints during adhesive curing presents another significant production problem. Such

fixturing has tended to result in a process which is both time-consuming and expensive. The combined use of adhesive and mechanical fasteners provides a solution which obviates the need for much of the fixturing but introduces more consumable items, and weight, into the process. Mechanical fasteners will however, improve the peel strength of joints, an otherwise significant weakness.

Another limitation of adhesive bonding is the sensitivity of joint strength to pre-treatment. Pre-treatment is necessary not only to remove contaminants such as lubricants and oils, but also to provide the intimate contact needed for the adhesive to bond successfully with the adherend surface. The need for pre-treatment inevitably introduces an additional operation to the manufacturing process. Poor adhesive strength, which can result from poor preparation (pre-treatment) of the adherend surfaces during manufacture, may not be immediately evident, and as a result, a poorly prepared joint may satisfy destructive type quality assurance tests. This type of defective joint is however particularly susceptible to environmental degradation. Therefore, over a relatively short period of time the interaction between moisture, temperature and cyclic loading could bring about a substantial reduction in joint durability. It has been shown that the effects of environmental attack can significantly reduce the fatigue life of an adhesively bonded joint.

As consequence of previous considerations, highly conservative safety factors tend to be incorporated into many load-bearing adhesive joints at the design stage.

### **6.2.2. Mechanical fasteners**

The range of mechanical fasteners currently available are numerous. Self-piercing rivets, clinch joints have been identified as two such types of fasteners with considerable potential for use in vehicle bodies. Both processes are essentially cold forming operations in which two or more pieces of material are mechanically fastened together. There is also no requirement, in either case, for the pre-drilling of holes in the components to be joined. As the name suggests, the self-pierce rivet is designed to both

pierce and form a permanent fastening within the materials being joined. Having pierced the upper sheet of material, the rivet expands in the lower sheet, usually without piercing it, to form a mechanical interlock. The actions of piercing and then forming the joint are carried out in a single operation (Fig. 6.5). Such is the nature of the process that quite large setting forces are required (typically 40 kN). For this reason, a C-frame structure is necessary in order to withstand the riveting force. As a result, the process requires access to both sides of the joint.

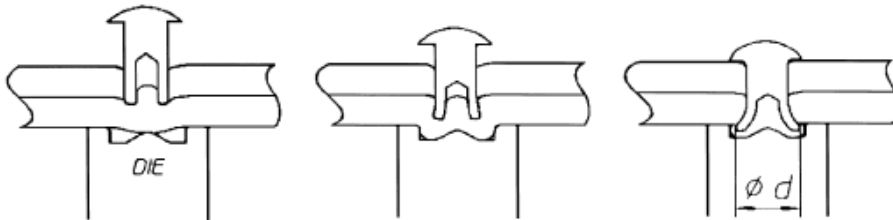


**Fig. 6.5. Schematic of self piercing rivet process.**

The clinch joint is very similar in that, it too involves the deformation of the material being joined to form a mechanical interlock. Clinching does not however use rivets, using instead a punch to force the material into a die (Fig. 6.6). The material is formed between punch and die in such a way that mechanical interlocking of the sheets themselves occurs. For vehicle body applications the sheets of material are generally not pierced, thereby producing a joint which is sealed against moisture ingress [30].

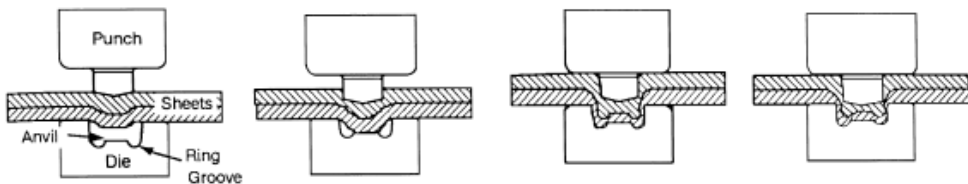


**Fig. 6.6. Schematic of the clinching process.**

The advantages of these fasteners are summarized below:

- Mechanical fasteners are able to be removed without destroying the structure;
- It is possible to join dissimilar, and otherwise incompatible materials;
- Mechanical fasteners are not sensitive to surface preparation, service temperature, or humidity;

- Ease of automation - the equipment can be adapted for use with a robot, and can be easily integrated into fully automated, high-speed assembly lines. Such integration is made particularly easy by the elimination of the need to pre-drill (or punch) holes, and also therefore, the need to align the holes with the rivet setting equipment;
- Little or no part distortion;
- Relatively low capital and operating costs, and equipment has a long service life.

The limitations of the process are:

- Both techniques require access to both sides of the joint;
- The size of the riveting gun restricts access to certain joint areas;
- Bulges and indents associated with both techniques may not be aesthetically desirable;
- Self-piercing rivets introduce additional consumable items, and therefore weight, into the process;

The use of blind rivets (Fig. 6.7) in lightweight structures is not obviated by the considerable benefits offered by self-piercing rivets and clinch joints, not least because blind rivets require access from one side of the joint only. The need for dual access is a significant disadvantage which may preclude the use of self-piercing rivets in some areas of a spaceframe construction. Equally, blind rivets present significant problems by the necessity to pre-drill holes. This introduces an additional operation and requires considerable hole position accuracy and tight assembly tolerances in order to avoid significant assembly problems.

The drilling of holes, by whatever means in blind riveting, will introduce stress concentrations which could be detrimental to fatigue and impact performance.

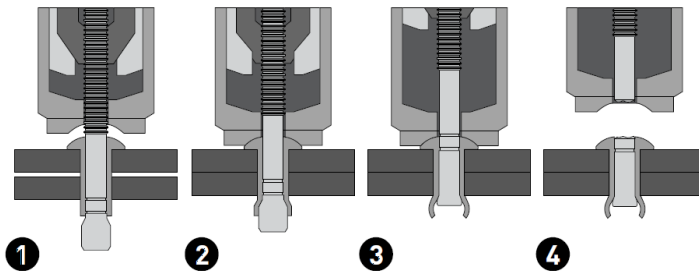


**Fig. 6.7. Schematic of the riveting process.**

### **6.3. Adhesively bonded joint tests**

In the present section static and fatigue behavior of adhesively bonded joints made of composite-composite, composite-aluminum, and aluminum-aluminum adherend combinations have been experimentally investigated to achieve their design allowable properties and to provide and compare the adhesion and compatibility of the adhesive with the selected materials. The adhesive system used for joining the adherends was the SikaFast® 3161; it is a flexible, two component acrylic adhesive designed to efficiently transfer high loads, evenly distribute stresses and improve higher viscosity and longer open time to address the specific requirements of large scale applications. The selected adhesive is suitable for bonding components made of aluminum and fiber reinforced polymers. Since the quality of the bonded joint depends strongly on the surface preparation of the adherends, to ensure good bond strength and durability, a preparation of specimen surfaces was performed as suggested by ASTM D 2093 [40] and ASTM D 3933 [41] for composite and aluminum surfaces respectively.

#### **6.3.1. Static tests**

Static shear strengths of the adhesive have been derived by single lap joint tests as suggested by ASTM D 3165 [42] standard. The tests were performed on thirty-five specimens conform to the form and dimensions shown in Fig. 6.8a. The composite laminate thickness  $t$  of 2 mm was achieved stacking eight prepreg plies all with the warp fibers parallel to the load. Tension loading of single-lap-joint laminated assemblies were performed at room temperature in a servo-hydraulic machine, INSTRON (Model 5566), with a 5 kN universal test frame, controlled by an electronic control unit which allows monitoring the applied load and the stroke of the top cross head. The machine can guarantee an asymmetric tightening of the grips, which allows performing the tests with a perfect alignment between the loading axis and

the layer of the glue (Fig. 6.9a). The tests were conducted in stroke control with a cross head speed of 1.27 mm/min.

Static strength properties of the adhesive in cleavage peel have been derived by tension loading tests as suggested by ASTM D3807 [43] standard. The tests were performed on twenty-two specimens conform to the form and dimensions shown in Fig. 6.8b. The composite laminate thickness  $t$  of 7 mm was achieved stacking twenty-eight prepreg plies all with wrap fibers along the longitudinal direction of the laminate. Tension loading of cleavage/peel configurations (Fig. 6.9b) were performed at room temperature in a servo-hydraulic machine, INSTRON (Model 8005), with a 10 kN universal test frame, controlled by an electronic control unit which allows monitoring the applied load and the stroke of the top cross head. The tests were conducted in stroke control with a cross head speed of 12.7 mm/min.

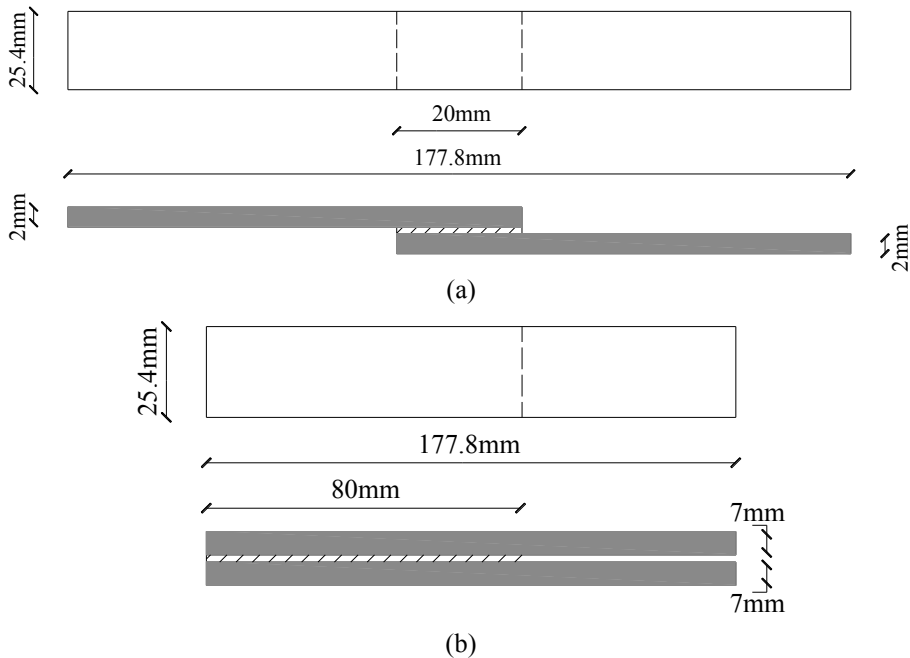


**Figure 6.8. Geometry of coupons: (a) single lap joint test configuration; (b) cleavage/peel test configuration.**

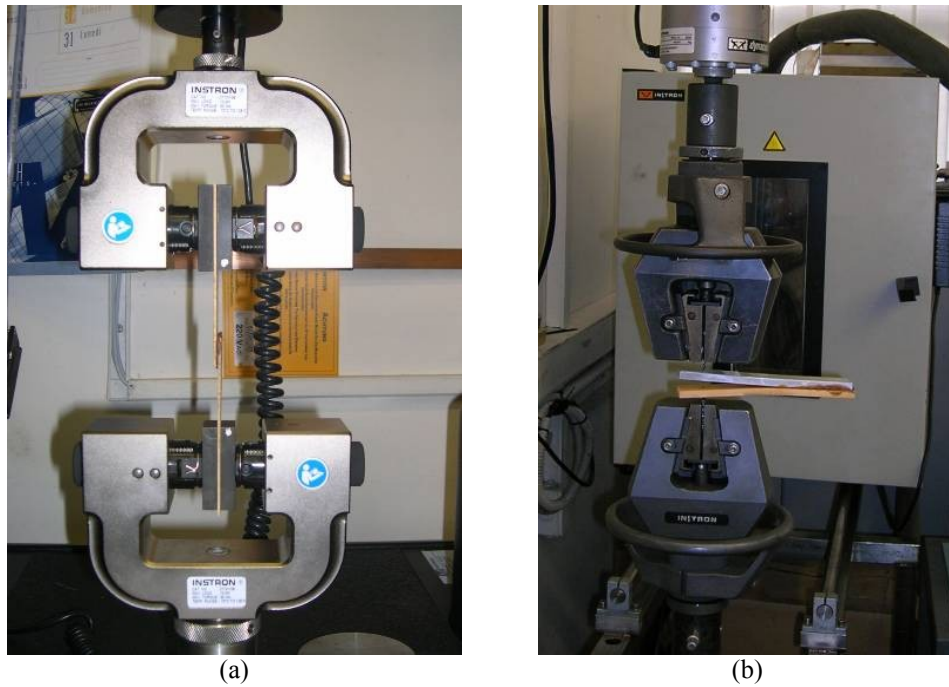


**Figure 6.9. Test set-up: (a) single lap shear configuration; (b) cleavage/peel configuration.**

Figure 6.10a depicts the stress-displacement curves derived by single lap joint tests. Each shown curve represents the mean data of replicate specimens for each adherend combination. As can be seen, the lowest shear strength of the adhesive is achieved when it is used to bond composite laminates, whereas the aluminum-aluminum configuration is the more efficient.

The same argument may be for the performance of adhesive/adherend combinations under cleavage/peel forces. Figure 6.10b shows the load-displacement curves for each adherend combination. The average load has been calculated in kilonewtons per meter width of specimen required to separate the adherends from the autographic curve (Fig. 6.10b) for the first 50 mm of cleavage/peel after the initial peak.

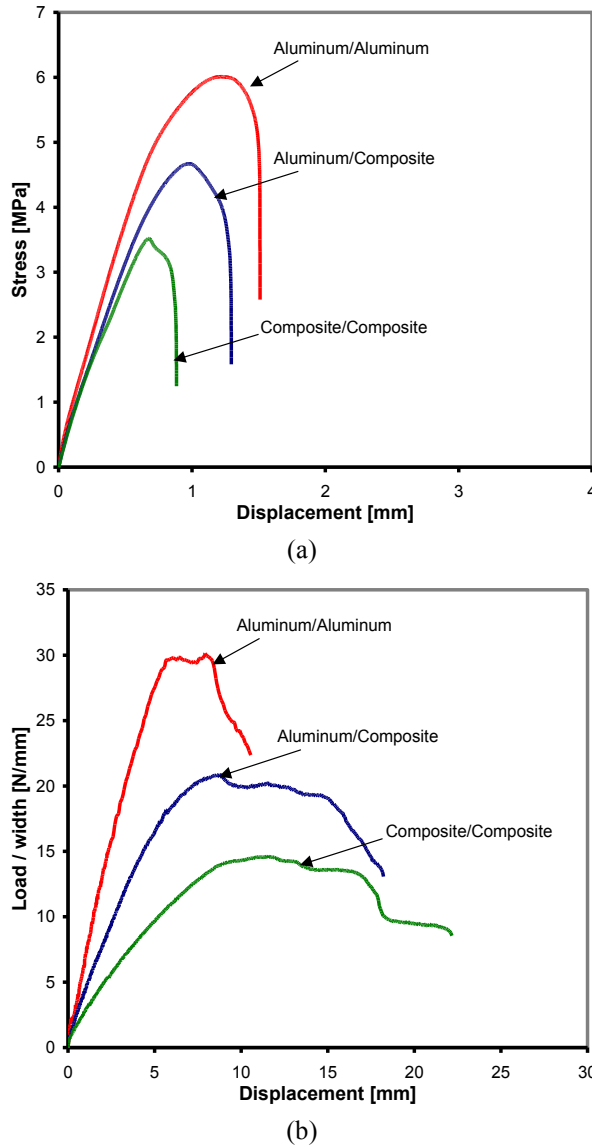


**Figure 6.10. Results of static tests on adhesively bonded joints: (a) single lap shear tests; (b) cleavage/peel tests.**

Adhesive joints can be failed in the following different modes: (I) separation appears to be at the adhesive-adherend interface (interfacial failure IF); (II) separation is within the adhesive (cohesive failure CF); (III) failure appears exclusively within the adherend (adherend failure AF); (IV) the separation is a mixture of different modes (mixed failure MF). Figures 6.11 and 6.12 show

failure modes of the three families of specimens tested in shear and cleavage respectively. As can be seen, the shear tests have been predominantly characterized by interfacial failure, while the main mode in cleavage/peel tests is the mixed mode with regions of IF and CF types for all the adherend-adhesive-adherend combinations. Only for two specimens of the composite-composite configuration adherend failure was observed; in particular the adherend failed by debonding of the first ply.

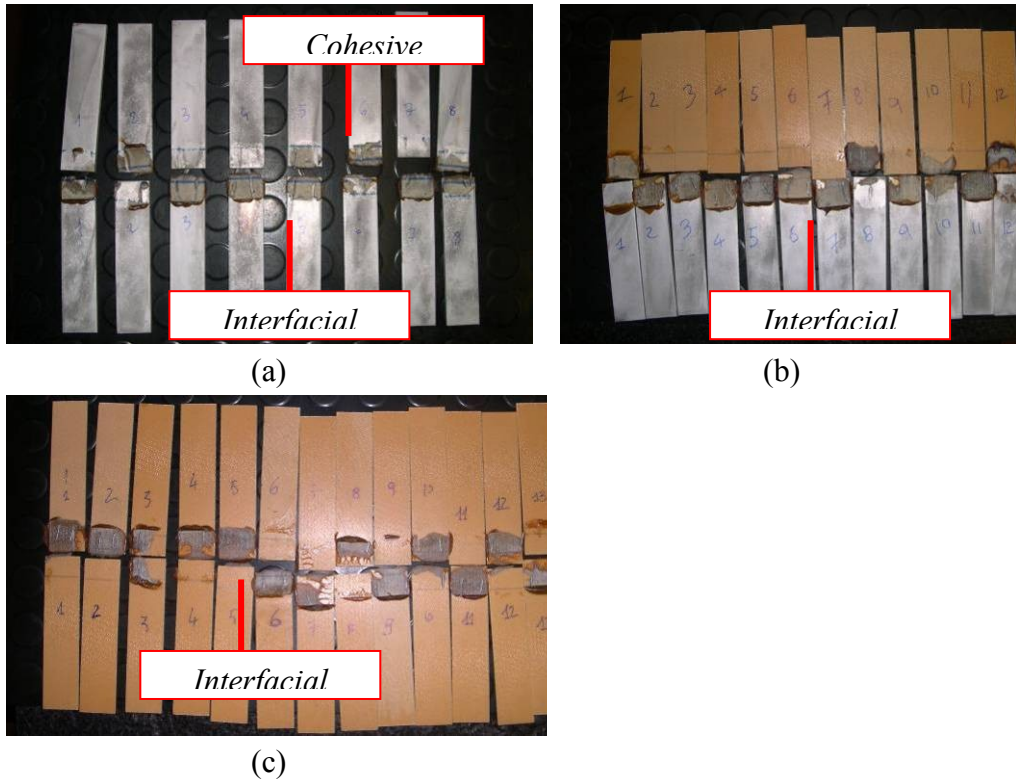


**Figure 6.11. Failure modes of specimens tested in shear: (a) aluminum-aluminum; (b) aluminum-composite; (c) composite-composite.**

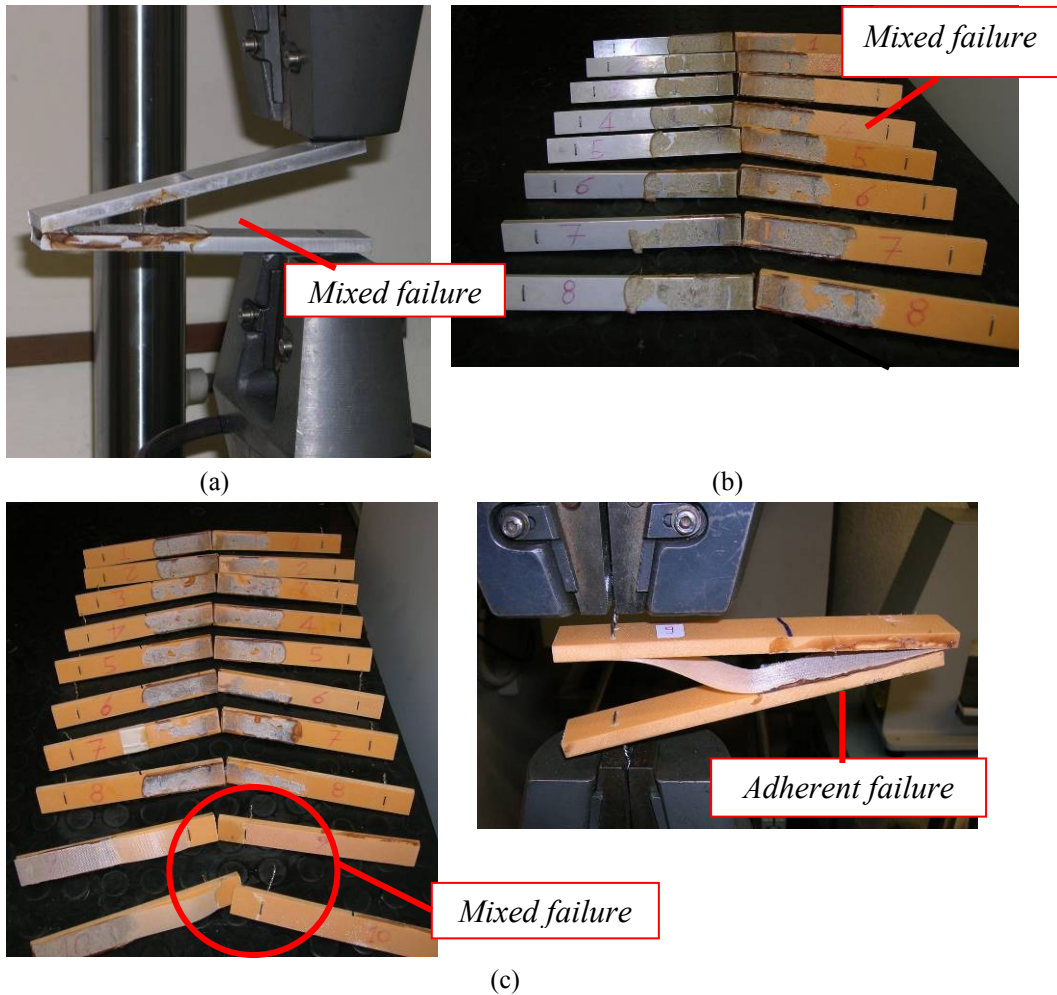


Figure 6.12. Failure modes of specimens tested in cleavage/peel: (a) aluminum-aluminum; (b) aluminum-composite; (c) composite-composite.

### 6.3.2. Fatigue tests

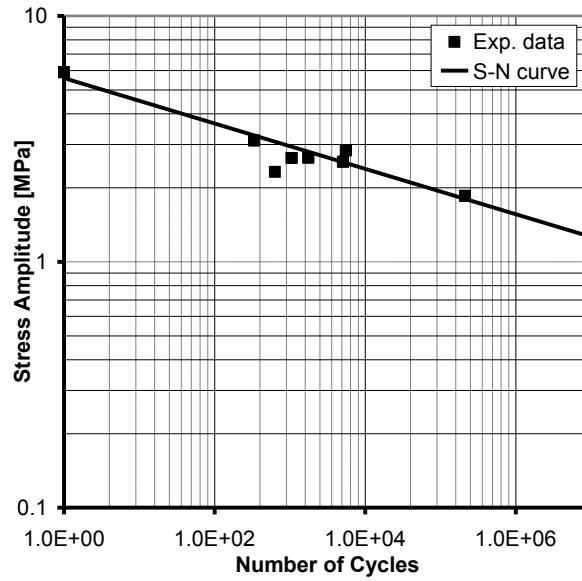
Fatigue properties of adhesive in shear by tension, according to ASTM D3166 [44], have been derived by cyclic tests using S-N approach. The tests were performed on thirty-five specimens conform to the form and dimensions shown in Fig. 6.8a as well as the static configuration. The tests were performed with the same set-up and testing machine with a 1 kN loading cell. Fatigue load was tension-compression type with a stress ratio of -1 and a

frequency of 5 Hz. To obtain statistical analysis of fatigue data, replicate tests were performed with different amplitude as reported in Table 6.1.

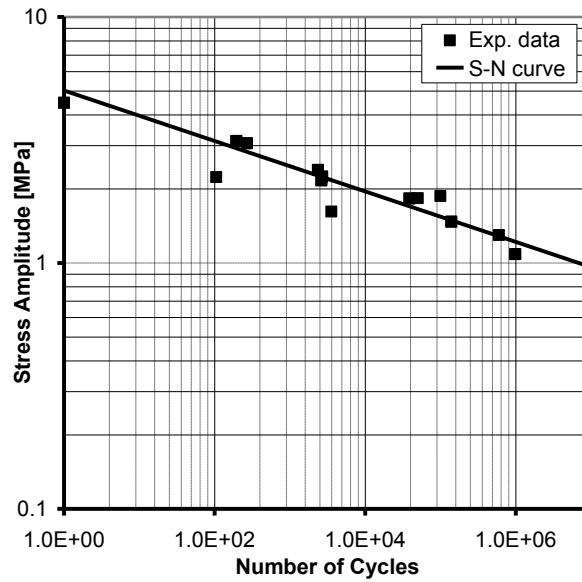
**Table 6.1: Load history of adhesively bonded joints fatigue tests.**

<b>Adherends</b>	<b>N. of specimens</b>	<b>Load Amplitude [kN]</b>
<b>Aluminum-Aluminum</b>	2	0.60
	2	0.80
	2	0.95
	2	1.00
<b>Aluminum-Composite</b>	4	0.45
	2	0.55
	2	0.65
	3	0.70
	2	1.00
<b>Composite-Composite</b>	1	0.30
	2	0.40
	1	0.45
	6	0.50
	4	0.55

Figure 6.13 reports the S-N curves derived by fatigue tests for each adherend combination. The number of cycles to failure and the corresponding loads have been recorded for each specimen and interpolated to provide the S-N relationships. The fatigue properties for each material combination have been obtained as the strength at  $10^7$  cycles. As expected by static tests the maximum value of shear stress at  $10^7$  cycles has been achieved by aluminum-aluminum combination. Whereas at  $10^7$  cycles a low value of strength reduction, which can be observed by the slope of the Wöhler curves, has been achieved by the composite-composite adherend combination.



(a)



(b)

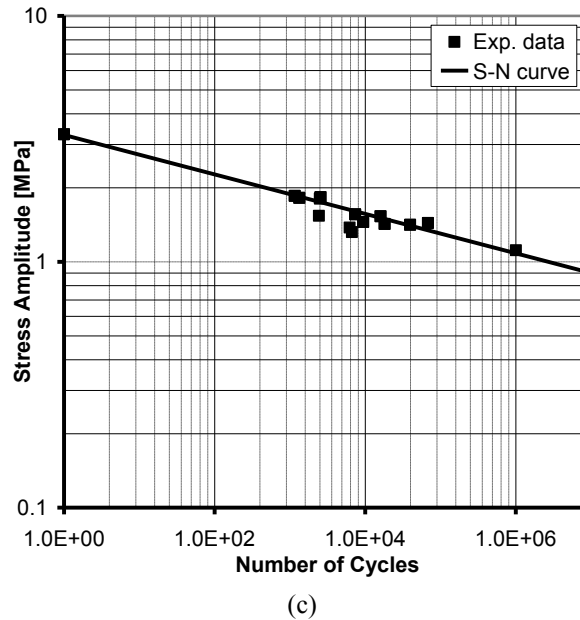


Figure 6.13. *S-N* diagrams for adhesively bonded joints: (a) aluminum-aluminum; (b) aluminum-composite; (c) composite-composite.

Table 6.2 reports static and fatigue mechanical properties derived by experimental activities. Static and fatigue characterization of adhesive and riveted joints to assembly phenolic composite components have been experimentally investigated in order to achieve their design allowable properties, to report the benefits of each joining technique, and to compare the results with regards to aluminum components.

Table 6.2. Tests results on adhesively bonded joints.

Adherents	Static						Fatigue Shear 10 <sup>7</sup> cycle [MPa]
	Shear			Cleavage			
	N. of Specimens	Av. [MPa]	Cv. [%]	N. of Specimens	Av [kN/mm]	Cv. [%]	
Aluminum/ Aluminum	8	5.95	8.37	4	0.3	0.95	1.26
Aluminum/ Composite	14	4.48	10.37	8	0.21	6.35	0.96
Composite/ Composite	14	3.3	19.51	10	0.15	5.53	0.9

## 6.4. Mechanically fastened joint tests

Since the analysis of mechanical fastened joints has not been very satisfactory because of the friction between rivets and holes, the material non-linearity and the presence of three dimensional stresses and strains, in the present section the behaviors of riveted joints have been investigated by experimental methods. In particular the experimental activity counts static and fatigue tests of aluminum blind rivet joining technique able to assembly both aluminum and composite structural component.

Moreover, despite a large number of studies conducted on mechanical joints for composite structures, most of them have focused on bolt or pin joints rather than rivets [32-36]. The range of mechanical rivets currently available is large. Self-piercing, self-drilling and blind rivets have been identified as three types of fasteners with considerable potential for use in automotive bodies. In particular the present study is focused on blind rivet technology which process is less expensive than self-piercing and self-drilling, requires access from one side of the joint only and can be also used for repair. Due to their high structural performances, high-speed assembly and safe process - no fumes or emissions -, the select fasteners typology can be considered belonging to the category of innovative connecting systems.

### 6.4.1. Static tests

Pin-type bearing tests were performed to determine the bearing yield and ultimate strength of the selected aluminum sheets. In particular the result data provide a measure of the load-carrying capacity of a material edge loaded with a close-fitting cylindrical pin through a hole located a specific distance from the edge. The tests, performed in accordance with the ASTM E 238 [45] standard, were run on eight 140x40x3 mm coupons with a circular hole of 6.5 mm in diameter. The bearing load was applied through a (stiffer) steel pin with 6.35 mm of diameter (Fig. 6.14a). Static response of joining technique on the aluminum sheets was also investigated on single-shear single-fastener specimen configuration. The tests were run on four flat, constant rectangular cross-section specimens consist of two like 140x40x3 mm halves fastened

together through one 8 mm centerline hole located near one end of each half, as shown in Fig. 6.14b.

Static bearing response of phenolic E-glass composite laminates has been investigated by single-shear double-fastener joining configuration. The tests, performed in accordance with the ASTM D 5961 [46] standard, were run on ten flat, constant rectangular cross-section specimens composed of two like 210x36x4 mm halves, with a  $[0/90/-45/45]_2s$  stacking sequence, which was known as one of the optimum stacking sequence for the mechanical joint, fastened together through two centerline holes, with 6.4 diameter, near one end of each half (Fig. 6.14c). Two different families of composite riveted joints were tested adopting different length of rivets, called for simplicity short and long rivets respectively. All the static tests were run on a universal test machine (MTS 810) controlled by an electronic control unit which allows monitoring the applied load and the stroke of the top cross head. The specimens were loaded until a load maximum has clearly been reached. All the tests were conducted at a constant cross head velocity of 2 mm/min.

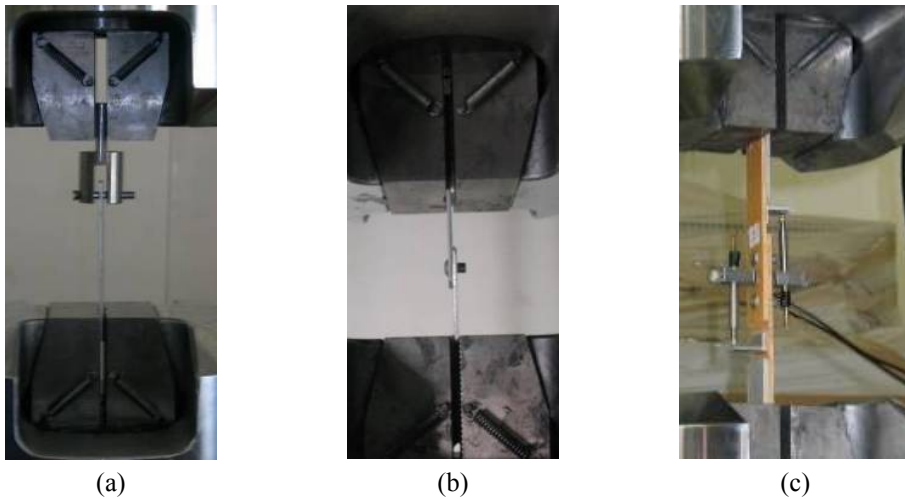


**Figure 6.14. Static test set-up: (a) pin-type configuration; (b) single-shear single-fastener configuration; (c) single-shear double-fasteners configuration.**

Experimental results have been reported in term bearing stress-displacement curves as showed in Fig. 6.15a. Each shown curve represents the mean data of replicate specimens. It is well known that the type of failure mode influences the experimental response of the lap shear tests. In cold-formed

shear connection made of mechanical fasteners, the following types of failure usually occur: (I) shear of fastener; (II) crushing of fastener; (III) tilting and pull-out of fastener; (IV) bearing of sheets; (V) shearing of the sheets; (VI) tearing of the sheets; (VII) cleavage of the sheets; (VIII) lateral (net tension) of the sheets. Obviously, in many cases, a joint can reach a combination of such different types of failures. As far as the current experimental research is concerned, various failure modes were found in accordance with the different specimen typologies. In particular, shear-out failure mode characterized aluminum specimens tested by pin-type bearing configuration (Fig. 6.15b), while mixed failure modes combining types III and IV were achieved by single-shear specimens, as showed in Fig. 6.15c and 6.15d, for both the aluminum and composite (long rivets) configurations respectively. Whereas when short rivets were adopted to provide structural assembly of the selected phenolic composite components, the failure initiated at interface between the rivets and the laminates (bearing mode) then the failure propagated in the lamina and delamination mechanism was observed at the free edge of the composite sheets (Fig. 6.15e).

As results stress-displacement curves of aluminum specimens show the same bearing stiffness but different yield stress; in particular the yield stress due to mixed failure modes is lower than the value achieved by pin-type test where specimens failed by shear-out of a material edge. A comparison between stress-displacement curves obtained by single shear tests on composite joints shows as high value of nominal bearing stress can be achieved joining composite laminates with long rivets in despite of a lower stiffness than both aluminum and short rivet composite configurations. The curve derived for the composite riveted joints is linear up to  $\sim 180$  MPa and  $\sim 145$  MPa for long and short rivets respectively. Beyond these stresses, the joints show non-linear behavior; the nonlinearity is attributed to the friction between rivets and holes.

#### **6.4.2. Fatigue tests**

Bearing fatigue response, according to ASTM D 6873 [47], of riveted joint in single-shear configurations has been investigated subjecting both aluminum

and long rivets composite specimens to repetitive constant amplitude force cycles with a completely reversed load history with a frequency of 5 Hz. It has been demonstrated [48] that the adopted fully reversed (tension-compression with  $R=-1$ ) force ratios are the most critical for bearing fatigue. Instead to obtained statistical analysis of fatigue data replicate tests have been conducted with different amplitude as reported in Table 6.3.

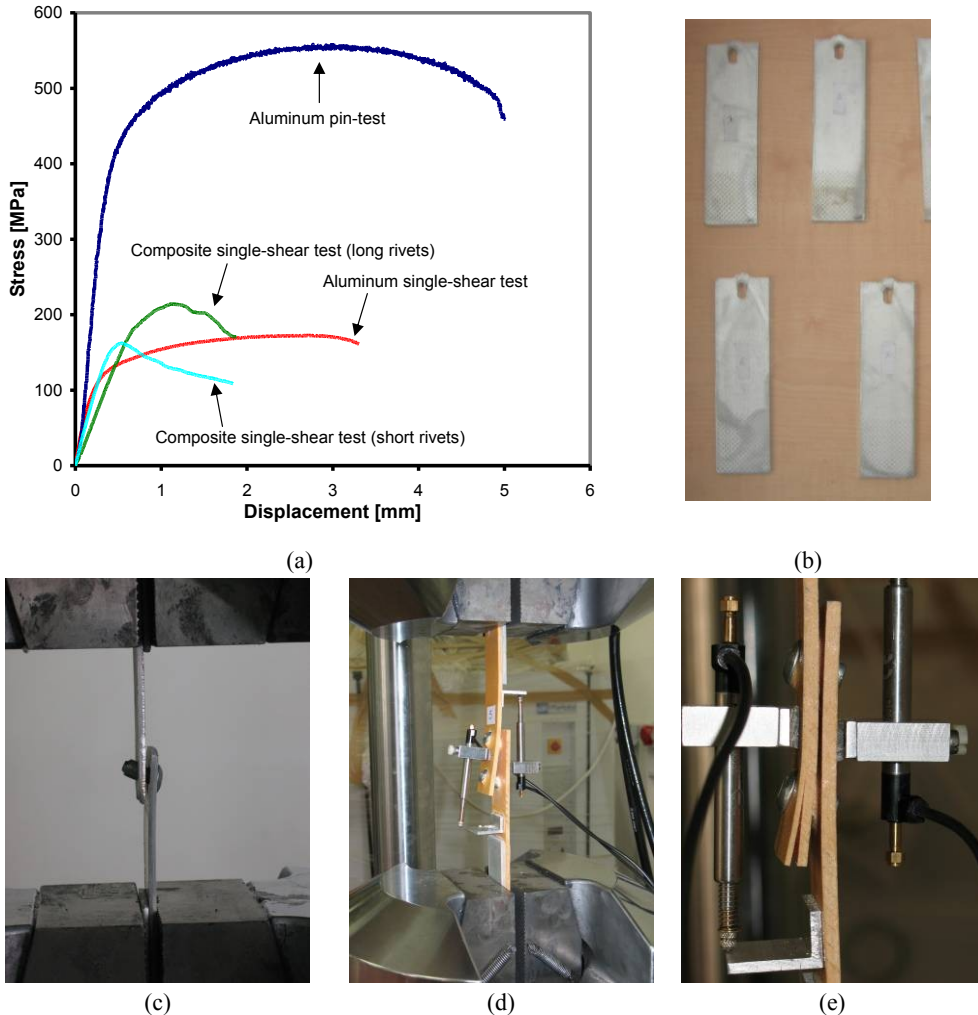


**Figure 6.15. Static tests of riveted joints: (a) bearing stress-displacement curves; (b) failure mode of pin-type specimen configuration; (c) failure mode of aluminum single-shear specimen configuration; (d) failure mode of composite single-shear specimen configuration with long rivets; (e) failure mode of composite single-shear specimen configuration with short rivets.**

The fatigue tests were performed at room temperature in a servo-hydraulic machine, INSTRON (Model 8005), with a 10 kN universal test frame, controlled by an electronic control unit which allows monitoring the applied load and the stroke of the top cross head.

**Table 6.3. Load history of mechanical joints fatigue tests.**

Specimens	N. of specimens	Load Amplitude [kN]
<b>Aluminum-Aluminum</b>	9	5.00
	4	4.00
	8	3.00
	3	2.00
	1	6.00
<b>Composite-Composite</b>	4	4.00
	5	3.50
	4	3.00
	2	2.00

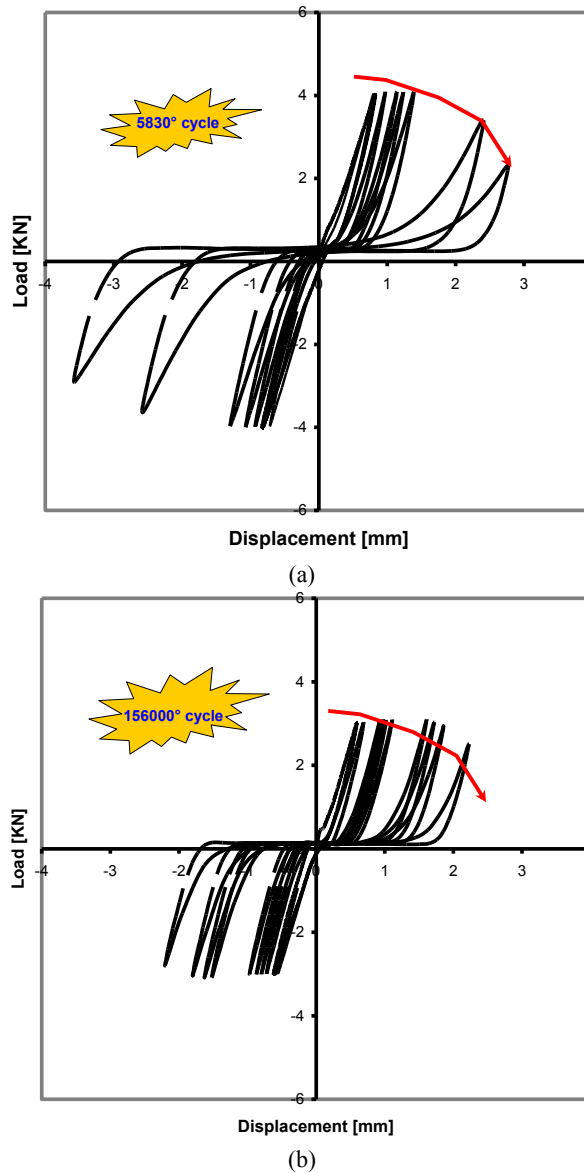
Figure 6.16 shows the load displacement curves of historically bearing fatigue tests at two different fixed load conditions for the phenolic/composite laminates. In particular Fig. 6.16a depicts the shape of hysteresis curves when the fatigue testing has ceased after the load level has reached the 90 % of the initial load level, while Fig. 6.16b depicts the shape of hysteresis curves when the fatigue testing has ceased after the hole elongation level has reached the 25 % of the initial hole diameter. In any case, the composite specimen break at the same mixed failure modes occurred in the static tests.

Figure 6.17 shows the load displacement curves of historically bearing fatigue tests at two different fixed load conditions for the aluminum sheets. In particular the Fig. 6.17a depicts the shape of hysteresis curves when the specimen failure was due to lateral net tension of the sheets, while Fig. 6.17b plots the shape of hysteresis curves when the specimen failure was due to shear of rivet. Net tension of the sheets and shear of the rivets are the only failure modes occurred at fatigue tests of aluminum specimens for the selected joining technique.

The S-N curves derived by fatigue tests of riveted joints of aluminum and composite specimens have been shown Fig 6.18a and 6.18b respectively. As

can be observed the maximum value of bearing stress, like so the low value of strength reduction, have been achieved by aluminum specimens at  $10^7$  cycles.

Table 6.4 reports the static and fatigue mechanical properties derived by experimental activity.



**Figure 6.16. Load-displacement curves of bearing fatigue tests on composite laminates: (a) failure due to load reduction; (b) failure due to hole elongation.**

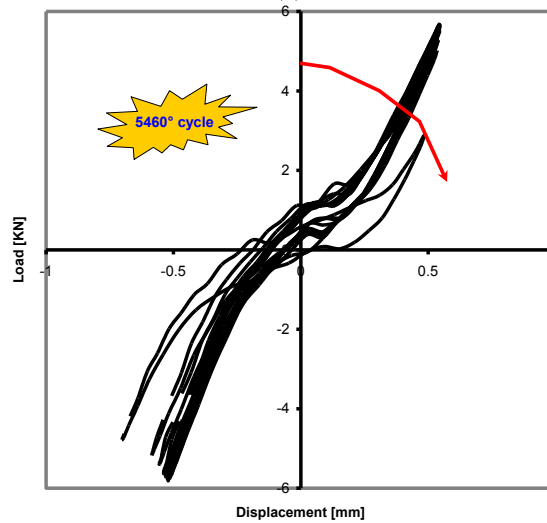
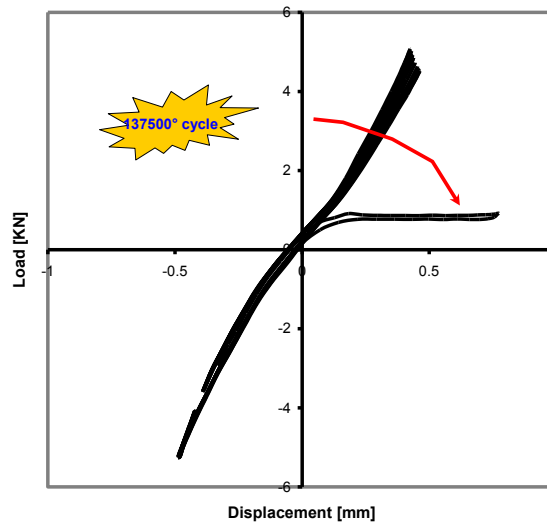
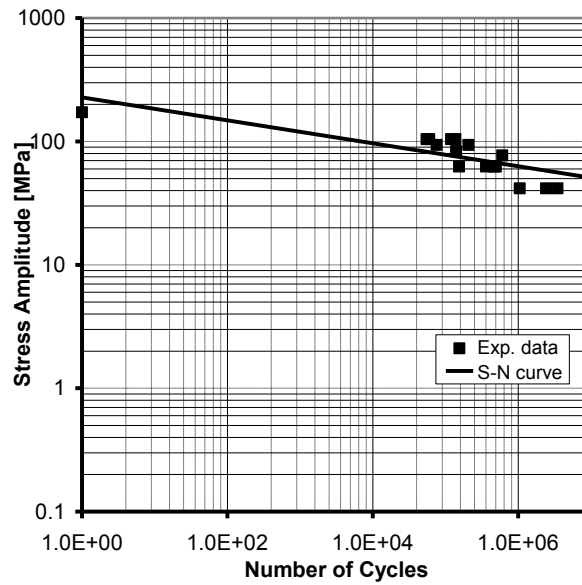
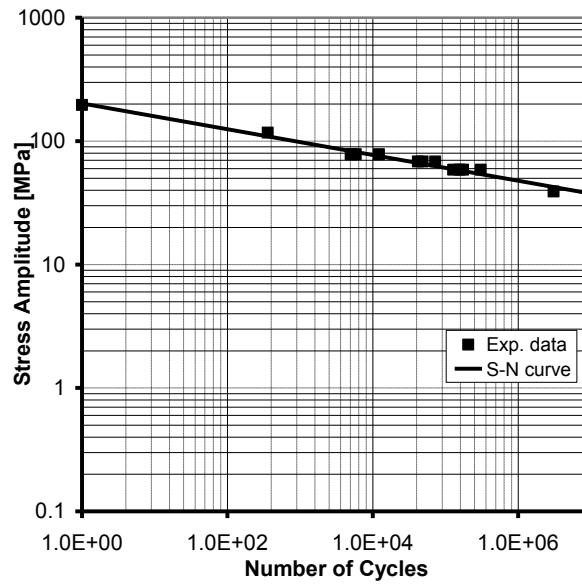


Figure 6.17. Load-displacement curves of bearing fatigue tests on aluminum sheets: (a) failure due to net tension of lamina; (b) failure due to shear of rivet.



(a)



(b)

Figure 6.18. *S-N* diagrams for mechanical joints: (a) single shear single fastener aluminum configuration; (b) single shear double fastener composite configuration.

Table 6.4: Tests results on riveted joints.

Specimens	Static bearing strength			Fatigue bearing strength
	N. of Specimens	Av. [MPa]	Cv. [%]	at $10^7$ cycle [MPa]
Aluminum-Aluminum	4	172.07	0.31	50.89
Composite-Composite (Short rivets)	5	159.94	14.35	-
Composite-Composite (long rivets)	5	206.92	3.68	37.50

## 6.5. Final remarks

About the *adhesively bonded joints*, the following remarks can be made based on the detailed test results:

- ✓ Improved shear and cleavage properties are observed when aluminum adherends are employed: the composite-composite and aluminum-composite adherend combinations achieve the 55% and 75% of the shear strength and the 50% and 70% of the cleavage strength respectively of the aluminum-aluminum adherends configuration.
- ✓ Adherend materials have significant effect on the failure modes of both single lap adhesive joints under tensile loading, which failures are predominantly characterized by interfacial failure and cleavage tests, which failures are predominantly characterized by mixed failure mode involving interfacial and cohesive mechanisms.
- ✓ Adherend failure (first-ply delamination) has occurred on two composite-composite specimens loaded under cleavage/peel; in any way, the cleavage strength value at which first-ply delamination occurred is higher than the average value provided by cleavage tests characterized by mixed failure mode.
- ✓ The fatigue data, reported in terms of S-N curves, show improved fatigue properties when composite adherends are employed providing a lower

reduction of the shear strength at 107 cycles. However the maximum fatigue strength at 107 cycles is achieved, as in the static case, for the aluminum-aluminum adherend configuration.

About the *mechanical fastened joints*, the following remarks can be made based on the detailed static test results:

- ✓ The experimental results have highlighted the influence of the rivet length on the mechanical performance and failure modes of the composite joints. The long rivets composite joints show improved value of nominal bearing stress, ~ 17% and ~ 22% greater than aluminum and short rivets configurations respectively, in despite of a lower stiffness.
- ✓ Mixed failure mode involving pull-out of fastener and bearing of the sheets have characterized both aluminum and long rivets composite joint configurations, whereas edge delamination mechanism has also involved in the mixed failure mode when short rivet are employed.
- ✓ The fatigue data, reported in terms of S-N curves, show improved high value of the bearing strength and high efficiency at 107 cycles when aluminum laminates are employed.

## References

Godwin EW, Matthews FL, “A review of the strength of joints in fibre-reinforced plastics – Part 1. Mechanically fastened joints”, *Composites* (1980), 155-160.

Camanho PP, Matthews FL, “Stress analysis and strength prediction of mechanically fastened joints in FRP: a review”, *Composites Part A* (1997), 28 A, 529-547.

Thoppul SD, Finegan J, Gibson RF, “Mechanic of mechanically fastened joints in polymer-matrix composite structures – a review”, *Composites Science and Technology* (2009), 69, 301-329.

Arnold WS, Marshall IH, Wood J, “Optimum design considerations for mechanically fastened composite joints”, *Composite Structures* (1990), 16, 85-101.

Ireman T, “Three dimensional stress analysis of bolted single-lap composite joints”, *Composite Structures* (1998), 43, 195-216.

Vangrimde B, Boukhili R, “Bearing stiffness of glass fibre-reinforced polyester: influence of coupon geometry and laminate properties”, *Composite Structures* (2002), 58, 57-73.

Okutan B, “The effects of geometric parameters on the failure strength for pin-loaded multi-directional fiber-glass reinforced epoxy laminate”, *Composites Part B* (2002), 33, 567-578.

Khashaba UA, Sallam HEM, Al-Shorbagy AE, Seif MA, “Effect of washer size and tightening torque on the performance of bolted joints in composite structures”, *Composite Structures* (2006), 73, 310-317.

Park HJ, “Effect of staking sequence and clamping force on the bearing strengths of mechanically fastened joints in composite laminates”, *Composite Structures* (2001), 53, 213-221.

Kelly G, Hallstrom S, “Bearing strength of carbon fibre/epoxy laminates: effects of bolt-hole clearance”, *Composites Part B* (2004), 35, 331-343.

Ascione F, Feo L, Maceri F, “An experimental investigation on the bearing failure load of glass fibre/epoxy laminates”, *Composites Part B* (2009), 40, 197-205.

Ascione F, Feo L, Maceri F, “On the pin-bearing failure load of GFRP bolted laminates: An experimental analysis on the influence of bolt diameter”, *Composites Part B* (2010), 41, 482-490.

Chen HS, “The static and fatigue strength of bolted joints in composites with hygrothermal cycling”, *Composite Structures* (2001), 52, 295-306.

Matthews FL, Kilty PF, Godwin EW, “A review of the strength of joints in fibre-reinforced plastics – Part 2. Adhesively bonded joints”, *Composites* (1982), 29-37.

Tsai MY, Oplinger DW, Morton J, “Improved theoretical solutions for adhesive lap joints”. *Int J Solids Structures* (1998), 35, 1163-1185.

Mortensen F, Thomsen OT, “Analysis of adhesive bonded joints: a unified approach”, *Composites Science and Technology* (2002), 62, 1011-1031.

Ascione F, “Mechanical behaviour of FRP adhesive joints: A theoretical model”, *Composites Part B* (2009), 40, 116-124.

Ascione F, “Ultimate behaviour of adhesively bonded FRP lap joints”, *Composites Part B* (2009), 40, 107-115.

da Silva LFM, Carbas RJC, Critchlow GW, Figueiredo MAV, Brown K, “Effect of material, geometry, surface treatment and environment on shear strength of single lap joints”, *Int J Adhesion Adhesives* (2009), 29, 621-632.

da Silva LFM, Adams RD, “Adhesive joints at high and low temperatures using similar and dissimilar adherends and dual adhesives”, *Int J Adhesion Adhesives* (2007), 27, 216-226.

Vallée T, Keller T, “Adhesively bonded lap joints from pultruded GFRP profiles. Part III: Effects of chamfers”, *Composites Part B* (2006), 37, 328-336.

Khalili SMR, Shojuhfar A, Hoseini SD, Bidkhorji, Kahalili S, Mittal RK, “Experimental study of the influence of adhesive reinforcement in lap joints for composite structures subjected to mechanical loads”, *Int J Adhesion Adhesives* (2008), 28, 436-444.

Ferreira JAM, Reis PN, Costa JDM, Richardson MOW, “Fatigue behavior of composite adhesive lap joints”, *Composites Science and Technology* (2002), 62, 1073-1379.

Quaresimin M, Ricotta M, “Life prediction of bonded joints in composite materials”, *Int J Fatigue* (2006), 28, 1166-1176.

de Rijck JJM, Homan JJ, Schijve J, Benedictus R, “The driven rivet head dimensions as an indication of the fatigue performance of aircraft lap joints”, *Int J Fatigue* (2007), 29, 2208-2218.

Cao Z, Cardew-Hall M, “Interference-fit riveting technique in fiber composite laminates”, *Aerospace Science and Technology* (2006), 10, 327-330.

Li QM, Mines RAW, Birch RS, “Static and dynamic behaviour of composite riveted joints in tension”, *Int J Mechanical Sciences* (2001), 43, 1591-1610.

Postec M, Deletombe E, Delsart D, Coutellier D, “Study of the influence of the number of inter-ply interfaces on the bearing rupture of riveted composite assemblies”, *Composite Structures* (2008), 84, pp. 99-113.

Song MH, Kweon JH, Kim SK, Kim C, Lee TJ, Choi Sm, Seong MS, “An experimental study on the failure of carbon/epoxy single lap riveted joints after thermal exposure”, *Composite Structures* (2008), 86, pp. 125-134.

ASTM D3039M, “Standard test method for tensile properties of polymer matrix composite materials”, American Soc. for Testing and Materials, West Conshohocken, PA.

ASTM D3518M, “In-plane shear response of polymer matrix composite materials by tensile test of a  $\pm 45^\circ$  laminate”, American Soc. for Testing and Materials, West Conshohocken, PA.

ASTM D2344M, “Standard test method for short-beam strength of polymer matrix composite materials and their laminates”, American Soc. for Testing and Materials, West Conshohocken, PA.

ASTM D2093, “Practice for preparation of surfaces of plastics prior to adhesive bonding”, American Soc. for Testing and Materials, West Conshohocken, PA.

ASTM D3933, “Guide for preparation of aluminum surfaces for structural adhesives bonding”, American Soc. for Testing and Materials, West Conshohocken, PA.

ASTM D3165, “Standard test method for strength properties of adhesives in shear by tension loading of single-lap-joint laminated assemblies”, American Soc. for Testing and Materials, West Conshohocken, PA.

ASTM D3807, “Standard test method for strength properties of adhesives in cleavage peel by tension loading”, American Soc. for Testing and Materials, West Conshohocken, PA.

ASTM D3166, “Standard test method for fatigue properties of adhesives in shear by tension loading”, American Soc. for Testing and Materials, West Conshohocken, PA.

ASTM E238, “Standard test method for pin-type bearing test of metallic materials”, American Soc. for Testing and Materials, West Conshohocken, PA.

[46] ASTM D5961, “Standard test method for bearing response of polymer matrix composite laminates”, American Soc. for Testing and Materials, West Conshohocken, PA.

[47] ASTM D6873, “Standard test method for bearing fatigue response of polymer matrix composite laminates”, American Soc. for Testing and Materials, West Conshohocken, PA.

[48] 90 Military Handbook - MIL-HDBK-17-3F: Composite Materials Handbook. Vol. 3. Polymer-Matrix Composite Materials Usage, Design, and Analysis US. Department of Defense.

## **Chapter VII**

# **DEGRADATION ISSUES: ENVIRONMENTAL CONDITIONING**

### **7.1. Introduction of framework activity**

In the present Chapter, effects on different environmental condition on phenolic impregnated sandwich components have been preliminary investigated. In particular different experimental techniques have been involved in the present step of the proposed multiscale procedure in order to analyze the effects of single parameters and their specific combinations. In these way, it can be possible find the most critical condition for the selected materials and allows to design specific modification of the system by introducing coating techniques or thin layers that allow to satisfy the durability requirements.

### **7.2. Review of degradation factors**

The durability of composites, in addition to being dependent on loading conditions, is strongly dependent on the environmental conditions, in terms of the specific combinations of temperature, relative humidity, exposure to electro-magnetic radiation, to solvents, acid and alkaline conditions and of their (cyclic) evolution during time. These effects are, in general, peculiar to the polymeric matrix as well as the polymer-fiber interaction and are linked

to a wide variety of phenomena that can ultimately lead, for example, to swelling or even to the dissolution of the polymeric matrix. In the case of sandwich structures, moreover, attention should be focused on environmental degradation of the interface between core and facesheets.

Since the degradation process of a composite sandwich structure depends on the environmental conditions, type of skins and core material, and production process, it is therefore necessary to evaluate the mechanical properties through accelerated ageing tests in order to predict long-term performances of sandwich composites.

Analysis of durability allows, through accelerated conditioning, determining the correlation between mechanical damage and aging due to different environmental factors. It is not possible to carry out tests on each material or structure for periods of time of tens of years, such as to cover the useful life and, for this reason, the use of accelerated methods allows the prediction of the evolution of the stiffness and resistance of composite materials to ensure the integrity and safety of structural components. Furthermore, the accelerated methods of analysis of the conventional metallic materials cannot be directly applied to composite materials, as these types of tests cannot adapt to viscoelastic materials such as polymeric composites, which exhibit strong dependency of the properties on time and temperature.

In practical applications of composites, temperature, ultra-violet radiation, and chemical environments are likely to be the major source of trouble to designers. The effects of these environments are reviewed below.

### **7.2.1. Thermal degradation**

The strengthening achieved through the operation of conventional solid-state mechanisms in metals and plastics is easily destroyed by thermal activation as the temperature is raised and there are few alloy or polymer systems that can continue to give satisfactory service when atomic or molecular mobility is enhanced by heating. But since many of the strong solids used for reinforcement are inherently resistant to this form of instability, up to relatively high temperatures, an important advantage of fiber composites is that they may be expected to retain their strengths to much higher

temperatures than would normally be possible. This would be true for composites reinforced with inorganic synthetic fibers, although metallic fibers are naturally subject to the same limitations as metallic matrices and glassy fibers lose their strengths at the glass-transition temperature when molecular networks become freely mobile.

In reinforced plastics there are few matrix materials that can withstand temperatures above 300°C, and the limiting factor for the most stable of matrices is likely to be chemical degradation. On exposure to air at elevated temperatures, thermosetting materials gradually become degraded through chemical changes which result in loss of material accompanied by loss of mechanical integrity.

Time/temperature superposition is used in the study of polymers to produce master curves of creep compliance or relaxation modulus over a wide range of times on a logarithmic scale.

The time-dependent and frequency-dependent behavior of polymers are closely linked, via the theory of linear visco-elasticity (Ferry, 1980), and are frequently studied by the experimental method known as dynamic mechanical and thermal analysis (DMTA).

Because of its visco-elastic nature, energy is dissipated when a polymer undergoes load cycling and this dissipation, characterized by the hysteresis or energy loss per cycle, reaches a maximum whenever the frequency of molecular motion is close to the cycling frequency. The energy loss is usually measured as the ratio of the loss modulus to the storage modulus, which is approximately equal to the phase angle,  $\tan\delta$ . Thus, measurements of  $\tan\delta$  as a function of temperature will identify the occurrence of specific mechanisms of molecular activity. DMTA is thus a sensitive means of detecting changes in the mobility of molecules and for investigating phase structure and morphology. For polymeric materials, it is able to identify a range of relaxations and transitions, and is thus a potentially powerful tool for assessing the effects of such features of composite materials as matrix polymer modification, matrix crystallinity, transcrystallinity at a fiber/thermoplastic-matrix interface, and interphase behavior or other effects of fiber surface treatments.

### 7.2.2. Hygrothermal degradation

The effects of hygrothermal conditioning on fiber reinforced composites are well documented in the scientific literature. In general, the diffusion of water molecules in a polymer structure causes an expansion or swelling. This increase in distance between the macromolecular chains involves a weakening of the secondary intermolecular forces so that material becomes soft and more ductile. This phenomenon is known as "plasticization": kinetics of water sorption is regulated by diffusion coefficients, as thermal by Chin et al [19]. The plasticization causes a reduction in glass transition temperature of the material; the presence of water molecules, in fact, tends to move the rubbery interval towards lower temperatures by decreasing the resistance of the polymer. In particular, if the glass transition temperature goes below room temperature the transition from a rigid material to a rubbery and flexible one can happen.

The glass reinforcement fibers do not absorb moisture while the resin-fibers interface may become the preferred route for the entry of moisture. As a consequence, fiber reinforced composite materials properties strongly linked to the presence of fiber – i.e. the tensile strength - are not significantly influenced by the presence of moisture, while those linked closely to the polymer matrix, such as the shape and shear strength, are subjected to a significant degradation. Interlaminar shear and flexural properties are generally more susceptible to moisture than the tensile properties; in the literature, several examples of reduction of these characteristics as the hygrothermal aging increases are presented [20, 21].

Shen and Springer [2] studied the effect of moisture and temperature on the tensile strength of composite materials. They measured the degradation of the ultimate tensile strengths of carbon/epoxy composites with material temperatures ranging from  $\sim -73$  to  $+150$  °C and moisture contents from 0% (dry) to 1.5% (fully saturated). All measurements were performed using  $0^\circ$ ,  $90^\circ$  and  $\pi/45$  laminates. They showed that the changes in temperature in the range  $\sim -73$  to  $+100$  °C appeared to have negligible effects on the ultimate

tensile strength of  $0^\circ$  and  $\pi/45$  laminates, regardless of the moisture content of the material. However, for  $90^\circ$  laminates the moisture content and the temperature of the materials affects significantly the ultimate tensile strength. The natural process of absorption of moisture in many composite materials is usually very slow. For this reason it is very difficult to obtain realistic saturation levels of absorption of moisture during a period of time typical of a laboratory test. To speed up the effect of moisture the temperature is increased. Through these methods it is possible to evaluate the relationship between the degree of degradation, for example in terms of "strength retention" as a function of the degrading agent level (% RH) and the exposure time, eventually determining synergistic effects.

In addition, fiber reinforced composite materials when exposed to the freeze-thaw cycles, are subjected to important changes in mechanical properties. During the freeze-thaw cycles micro damage or voids in the polymer matrix may occur mainly due to the difference of coefficients of thermal expansion of fiber and resin [22].

### **7.2.3. Photodegradation**

Photodegradation is an ordinary degradation condition for polymer materials. The polymer materials are irradiated by UV not only at outdoor by exposure to sun light but also indoor by exposure to fluorescent light. In addition, most of the polymer materials possess a chromophoric group in its structure; therefore, various chemical reactions inside of the polymer materials were induced by UV irradiation.

The UV photons of solar radiation may degrade fiber composite structures causing reactions of photo-oxidation which alter the macromolecular polymer chains leading even to micro fracture.

The ultraviolet radiation has sufficient energy to penetrate inside the polymer matrix and interact with constituent atoms or with their electrons (ionization reactions); this may be able to cause the rupture of covalent bond leading to local redistributions of atoms or groups of atoms.

Larsson [4] evaluated the influence on the mechanical properties of unidirectional Kevlar/epoxy laminates of varying thickness due to

degradation by ultraviolet light exposure. He showed that an exposure for 1000 h with a xenon burner was supposed to correspond to 3–4 years of outdoor sun exposure in Florida, USA.

#### **7.2.4. Chemical degradation**

The polymer product used in outdoor circumstances has a great concern about the chemical degradation; because the product for outdoor use is exposed to rain, sunlight, temperature, and environmental bacteria. These factors have sufficient effects in proceeding with the oxidation and the hydrolysis of the polymer materials; moreover, acidic and/or basic conditions have effect in promoting the reaction. The polymer material used in the railway field is affected by respective factors.

There are no standard procedures for measuring the strength of polymer composites against attack by chemical agents. This is obviously linked to the huge number of polymeric materials and existing chemicals, which often have very different characteristics.

One of the most important processes of chemical degradation of polymer matrix composites is the cleavage of the chains caused and accelerated by chemical reactions with oxygen, ozone and other substances.

Glass fibers corrode in acidic as well as alkali environments and lose a significant percentage of their tensile strength when exposed to high temperature [26]. Hartman et al. [27] observed that E-Glass fibers lose more strength than S<sub>2</sub> Glass fibers when exposed at 96°C to acidic environment (H<sub>2</sub>SO<sub>4</sub> and HCl), alkali environment (Na<sub>2</sub>SO<sub>4</sub>) and water for a period of 24 hrs. and 168 hrs. Tannous and Saadatmanesh [28] studied the durability of AR glass FRP bars when exposed to aggressive environment. They observed that bars (vinyl ester matrix) when exposed to Ca (OH)<sub>2</sub> with a pH of 12 and maintained at 25°C and 60°C, experienced strength loss of 13% and 23% respectively. According to Fuji et al. [29] there was a reduction of tensile strength to about 28% when E-Glass fibers were exposed to 5% HNO<sub>3</sub> after 100 hrs.

In general, the polymer matrices deteriorate with non-corrosive process, but degrade (swelling or dissolving) due to the exposure to some fluids. The

swelling occurs when the solute molecules sneak into the molecular structure occupying positions between macromolecules and determining, therefore, a partial solution. The dissolution, however, occurs when the polymer is completely soluble in the liquid with which it comes into contact and can be considered as the continuation of the process of swelling.

The phenomena of swelling and dissolution are strongly influenced by the characteristics of the molecular structure of the polymer. Usually an increase of molecular weight, a high degree of cross linking and crystalline lead to a reduction in these processes of alteration.

The temperature, the state of mechanical stress and time are other important parameters that contribute to the resistance of a resin to chemical agents.

The transitions that the polymer resin may undergo - i.e. the glass-rubber - significantly alter the ability of the material to resist chemical attack; temperatures should not be too much higher than those typical of the conditions of use. Even in the absence of physical changes in the structure, the polymer molecules are more mobile at elevated temperatures and this allows easier penetration of small molecules within the material.

It is also important to consider the exposure time of the polymer to the chemical agent as a short exposure time can cause not immediately detectable effects, but which may affect the polymer properties over time scales longer than the experimental observation.

### **7.3. Thermo-mechanical tests**

#### **7.3.1. Tensile tests**

Influence of temperature on failure properties of the selected phenolic laminate have been investigated under tensile tests both in warp and fill direction. The tests have been performed with the same geometry, procedure and instrumentation as described in Chapter V. Three different temperature (-15°C, 50°C and 80°C) have been investigated. This temperature are in the range on the possible application in ground transportation industry.

A minimum of three replicate tests have been performed per each geometry and environmental configuration. The test apparatus are shown in Fig. 7.1. It

consists of two climatic chamber, one mounted on the frame of the MTS universal testing machine, and one that allows to control the environmental condition.



Figure 7.1. Testing apparatus: climatic chamber mounted on MTS universal testing machine.

Elastic modulus, ultimate stress and stress have been derived by each tests, Figure 7.2. shows the average stress-strain curves obtained for each temperature.

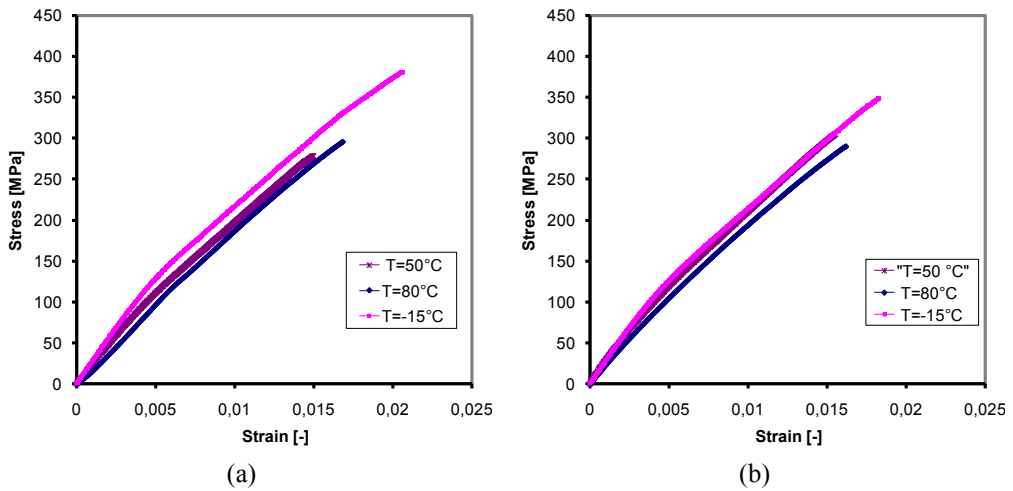
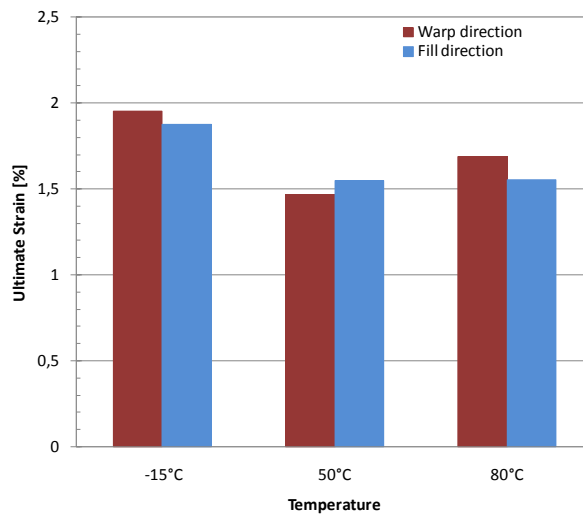


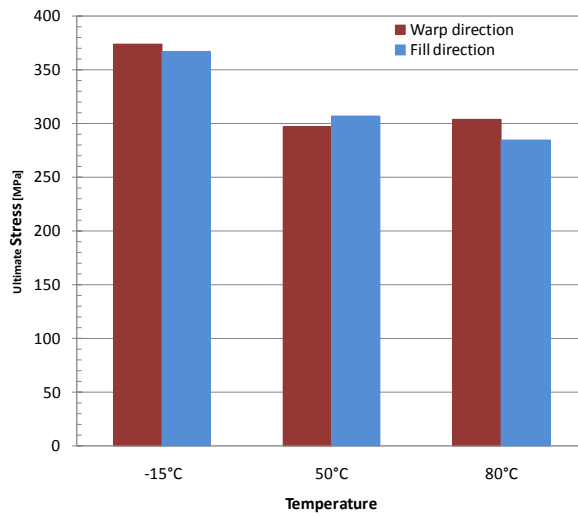
**Figure 7.2. Stress-strain curves of tensile tests under different temperature: (a) warp direction; (b) fill direction.**

The results shows as there are no evident difference in the ultimate strain and stress in the range of 50°C to 80°C compared to the values derived by room-temperature tests, whereas the elastic modulus seems to be the characteristic more susceptible to temperature conditioning. At the opposite an increment of both elastic modulus, ultimate stress and strain have been observed for low temperature.

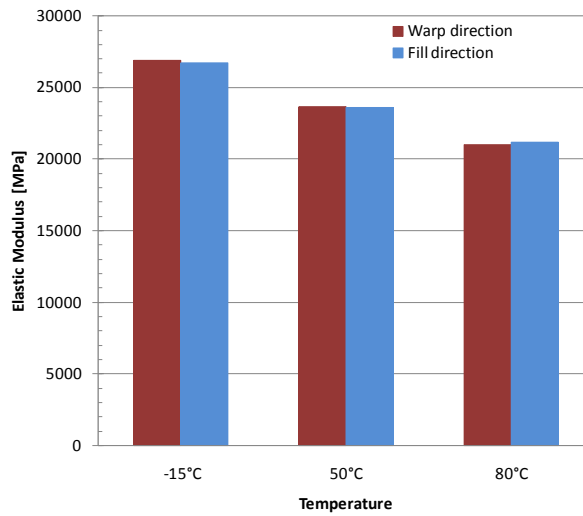
Figure 7.3 allows to compare the variation of the tensile properties of the selected glass/phenolic composite in the temperature range.



(a)



(b)



(c)

**Figure 7.3. Tensile properties of glass/phenolic composite in fill and warp direction at different temperature.**

No evident difference can be found in tensile properties along the warp and fill direction of the fabric composite, where the same trend have been observed by varying the temperature.

### 7.3.2. DMA tests

The glass transition temperatures of cured samples were determined by dynamic mechanical analyzer (DMA). Analysis by DMA is a well-known method for determining viscoelastic properties by applying a controlled sinusoidal strain to a sample and measuring the resulting stress. DMA gives both storage modulus and loss modulus characteristics as a function of temperature. In the present work, DMA has been used for measuring the temperature-dependant elastic moduli of the selected phenolic/glass laminates both in warp and fill directions. Three samples were tested for both warp and fill direction.

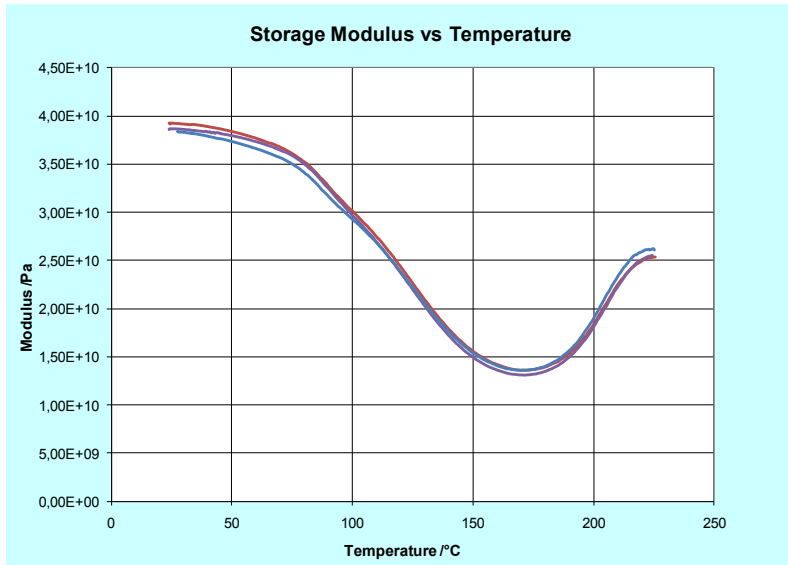
The tested samples, made of four layered plain glass fabric, for a total thickness of 1mm, have been cut into small pieces (9mm wide and 15mm). Tests were conducted in a single bending cantilever configurations under a temperature range of about 20°C to 250°C (Fig. 7.4). Temperature scanning from low to high has been performed with a heating rate of 4°C/min at an oscillation frequency of 1 Hz. The oscillation amplitude of displacement has been kept at 0.05 mm. The test has been carried out according to ASTM D4065-01 [28].



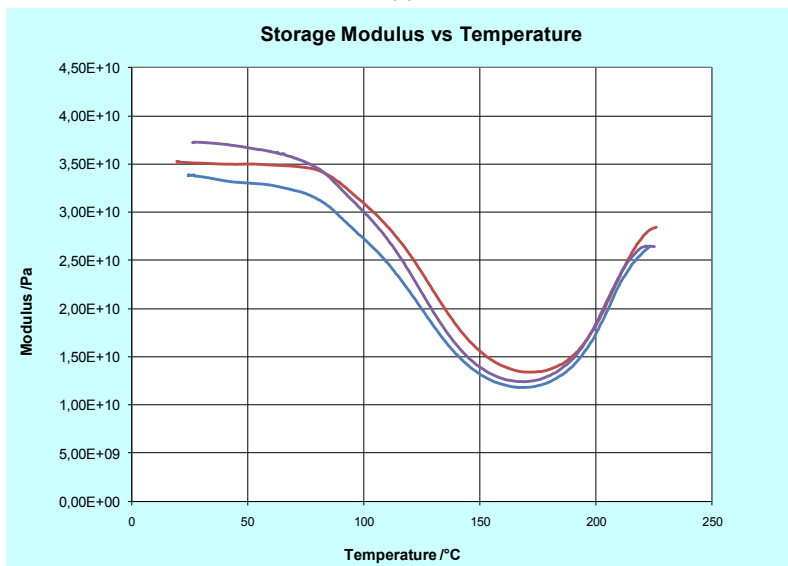
**Figure 7.3. DMA testing apparatus and specimen prepared in a single bending cantilever configurations.**

From the test data, storage modulus, which gives the dynamic elastic response of the samples; loss modulus, which gives the dynamic plastic response of samples and  $\tan \delta$ , which is the ratio of loss modulus/storage modulus were determined. The variations of the storage modulus with

temperature are shown in Fig. 7.4 for both warp and fill direction. the sharp drop in the storage modulus indicates glass transition temperature,  $T_g$ . This sharp drop in storage modulus divides the entire temperature range into two segments—the below  $T_g$  zone and the above  $T_g$  zone. The below  $T_g$  zone is also referred as the operating region while the above  $T_g$  zone is referred as the rubbery plateau.



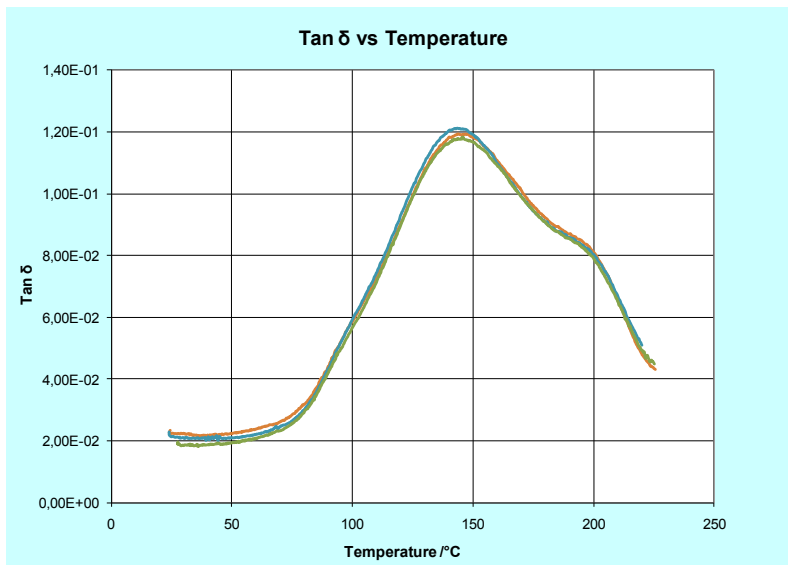
(a)



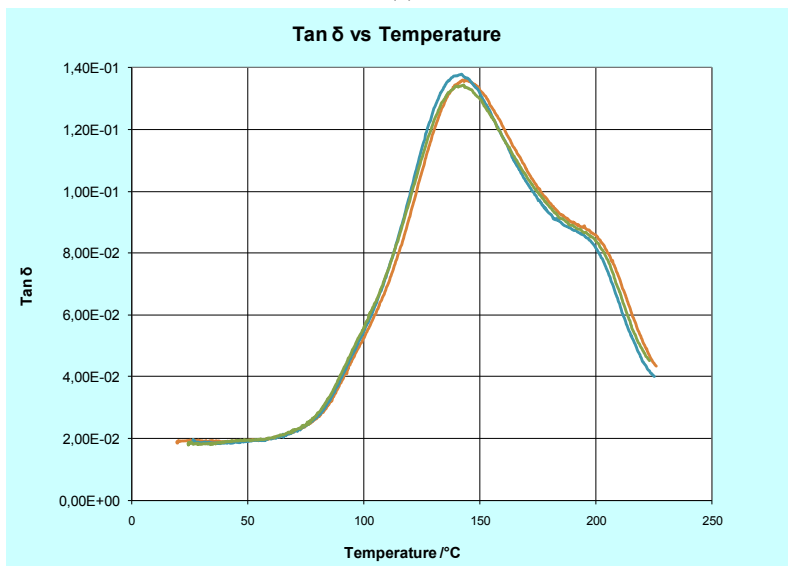
(b)

Figure 7.4. Storage modulus vs temperature: (a) warp direction; (b) fill direction.

The variations of the  $\tan \delta$  with temperature for both sample configuration are shown in Fig. 7.5.



(a)



(b)

Figure 7.5.  $\tan \delta$  vs temperature: (a) warp direction; (b) fill direction.

The test results show a similar thermo-mechanical properties of selected composite laminate in both the main fiber directions. In particular the obtained results are reported in Tables 7.1 and 7.2.

**Table 7.1. Summary of fill data points for DMA test**

	T <sub>g</sub> (°C)	Low Point (°C)	Storage Modulus [MPa]		
			50°C	80°C	T <sub>g</sub>
<b>Fill 1</b>	142.7	171.7	35010	34400	17380
<b>Fill 2</b>	142.1	169.0	36660	34540	15650
<b>Fill 3</b>	143.2	168.4	33020	31360	14480
<b>Average</b>	<b>142.7</b>	<b>169.7</b>	<b>34896.7</b>	<b>33433.3</b>	<b>15836.7</b>
<b>Sn-1</b>	0.55	1.8	1822.6	1796.9	1459.0
<b>Cv [%]</b>	0.39	1.04	5.22	5.37	9.21

**Table 7.2. Summary of warp data points for DMA test**

	T <sub>g</sub> (°C)	Low Point (°C)	Storage Modulus [MPa]		
			50°C	80°C	T <sub>g</sub>
<b>Warp 1</b>	143.9	170.2	38420	35270	16870
<b>Warp 2</b>	143.3	171.5	37930	35010	16390
<b>Warp 3</b>	145.9	170.5	37310	34140	16220
<b>Average</b>	<b>144.4</b>	<b>170.7</b>	<b>37887</b>	<b>34807</b>	<b>16493</b>
<b>Sn-1</b>	1.36	0.7	556.3	591.8	337.1
<b>Cv [%]</b>	0.94	0.40	1.47	1.70	2.04

In particular, the glass transition temperature  $T_g$  is found about 140°C, and the storage modulus shows the same trend of the elastic modulus observed in tensile tests for both warp and fill direction.

How is expected the glass transition temperature of the glass/phenolic composite results higher than value generally observed for epoxy based composite (~70-100°C []).

#### 7.4. Accelerated ageing tests

In the present section, accelerated ageing tests have been presented to analyze long-term performances of both laminate material and sandwich elements exposed to outdoor environmental conditions. The expected service life of

the composite materials used in transportation fields is approximately between 20-30 years—a long period of exposure for polymer materials. Generally, damage by aging or weathering—environmental degradation of structural components of vehicle—can be due to a combination of processes. The main factors that can affect long term properties in the railway field, and consequently considered in accelerated ageing tests, are:

- Hygrothermal conditioning;
- Thermal cycles;
- Ultraviolet Radiation;
- Chemical attacks.

Shin and Hahn evaluated the ageing effects of the carbon/epoxy skins involved in the sandwich body panels of the Korean Tilting Train. They performed accelerated ageing test combining the different environmental factors. In particular, ageing conditions involve the following cycles: dark and water spray of 60 min, light of 40 min, light and water spray of 20 min, and light of 60 min with light cycle of 60°C, dark cycle of 10°C, and setting humidity of 85% RH, and irradiance level of 0.37 W/m<sup>2</sup>. The program was set up to test specimens periodically.

In the present study environmental conditioning have been analyzed individually in order to assess the influence of each factor and design some modification or additional layers.

The natural process of absorption of moisture in many composite materials is usually very slow. To accelerate the effect of moisture, specimens have been conditioned at 80°C and 85% RH (hot-wet conditioning), and 80°C and 0% RH (hot-dry conditioning) for 60 days. To assess the influence of freeze-thaw cycles specimens have been subjected to an alternately decreasing temperature from 4 to -18°C and raising it from -18 to 4°C in not less than 2 hours and not more than 5 hours. All the specimens have been subjected to 250 cycles. The UV environment was reproduced by subjecting the specimens to Cycle C, continuous UV with uninsulated black panel temperature at 50°C, as described in the standard ASTM D 5208 [46]. For the analysis of the degradation due to alkali and acid attack, specimens were submerged, respectively, in alkaline solution (NaOH 1M sodium hydroxide

solution) and acid (HCl 1M Hydrochloric acid) for 20 and 40 days at a temperature of 60°C.

As can be observed employing phenolic resins allows to use high temperature to accelerate the degradation process.

After environmental conditioning, the specimens were tested in order to evaluate in-plane tensile properties of the skin, core shear properties and flexural behavior of the entire sandwich configuration.

The test matrix of accelerated ageing tests is summarized in Table 7.3.

**Table 7.3. Specimen characteristics for accelerated ageing tests.**

Environmental conditioning	Specimen code	n. of specimens	
		Tensile test	Flexural test
Ultraviolet: Cycles C at 50°C	UV	3	4
Freeze/Thaw: 250 cycles from -18 to+ 4°C	FT	3	4
Acid solution: 1 M of HCl for 20 day at 60°C	HC_20d	3	4
Acid solution: 1M of HCl for 40 day at 60°C	HC_40d	3	4
Hot-wet 80°C and 85% RH for 60 day	HW	3	4
Hot-dry 80°C and 0% RH for 60 day	HD	3	4

#### 7.4.1. Laminate tests

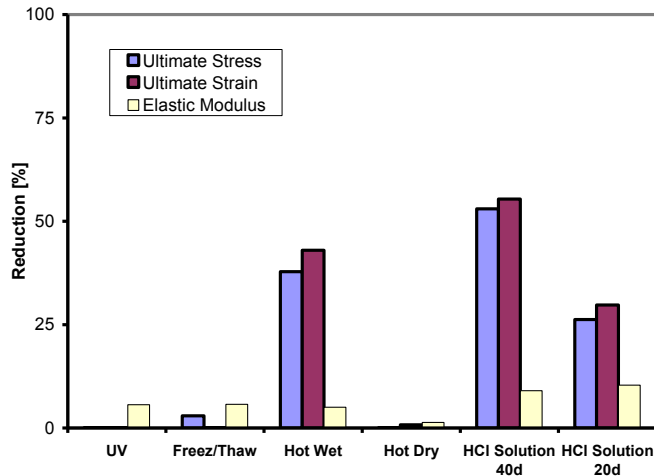
Static tensile tests were run on 1x15x250 mm conditioned coupons with the warp fibers parallel to the load. These tests were performed as described in the static section. Elastic modulus, ultimate strain and stress have been determined by tensile tests for each specimen. It is underlined that coupons dipped into the alkaline solution were completely deteriorated (Fig. 7.6a) and could therefore not be tested. Experimental results are presented in Fig. 7.6b in term of degree of degradation of tensile properties for each environmental conditioning. The obtained values show a considerable reduction in term of ultimate strain and stress for the hot-wet and acid conditionings.

The degradation due to hygrothermal conditioning is related to the diffusion of water molecules in a polymer structure that causes an expansion and swelling of the structure: the increasing in distance between the macromolecular chains involves a weakening of the secondary intermolecular forces so that material becomes soft and more ductile. The chemical environment influences both the glass fibers and the polymeric resin. In

particular, the acid conditioning causes the cleavage of the macromolecular chains, while the effects of the alkaline conditioning include both the disintegration of the matrix and the corrosion of the fibers.



(a)



(b)

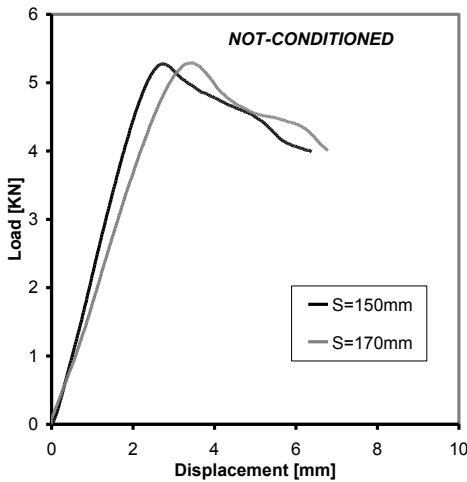
Figure 7.6: Experimental results of conditioned phenolic/composite specimens.

#### 7.4.2. Sandwich tests

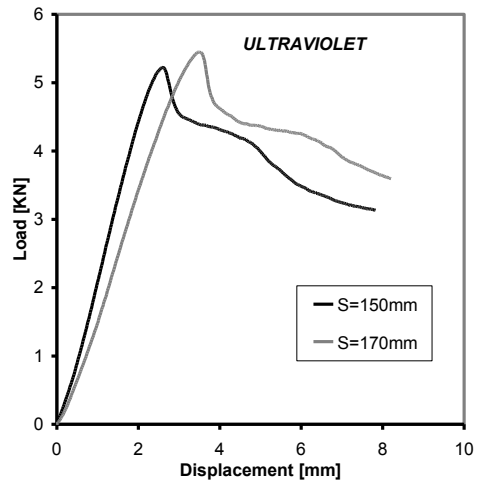
Three point bending tests were run on 16.5x100x235 sandwich panels with equal laminated E-glass/phenolic composite face sheets, each consisting of eight 0/90 woven plies (2 mm total thickness) stacked in the  $[0/90]_{2s}$  arrangements, bonded to 10.5 mm honeycomb Nomex core. Each type of sandwich structure was tested with two different support spans:  $S=170$  mm and  $S=150$  mm. The test procedure is the same as that described previously for unconditioned specimens. Two replicate specimens have been tested per

each geometric and loading configuration.

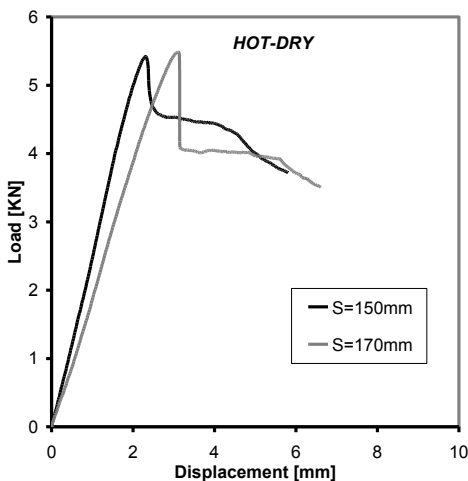
Figures 7.7 and 7.8 shows the average load-displacement curves measured for each conditioned specimen families loaded in flexure. No premature failures (i.e., debonding) occurred during these tests. All specimens failed due to shear into the core (7.8d), so the core shear ultimate strength has been obtained as a function of maximum load. The experimental results show a reduction less than 15% both for the core shear stress and for the sandwich flexural stiffness, while there are no reductions in terms of core shear modulus and sandwich transverse rigidity. As expected the flexural stiffness reduction is due to that one of facesheets elastic modulus per each environmental conditioning.



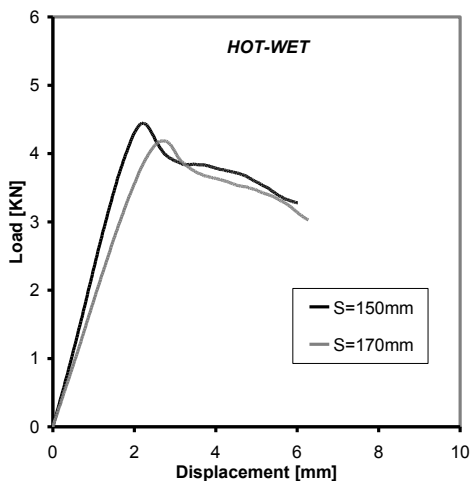
(a)



(b)

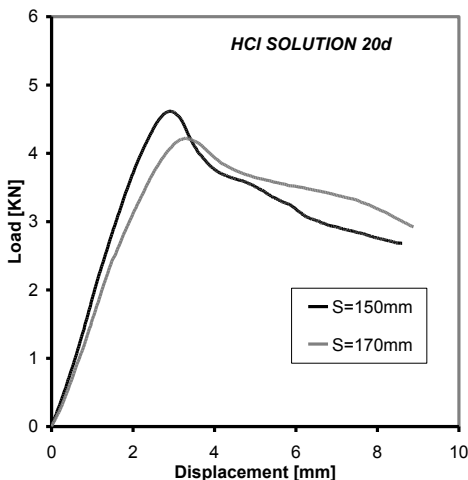


(c)

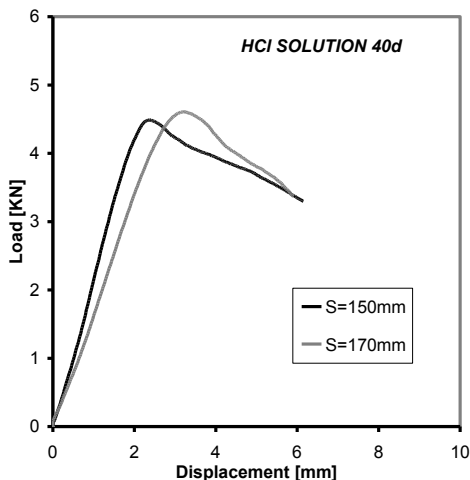


(d)

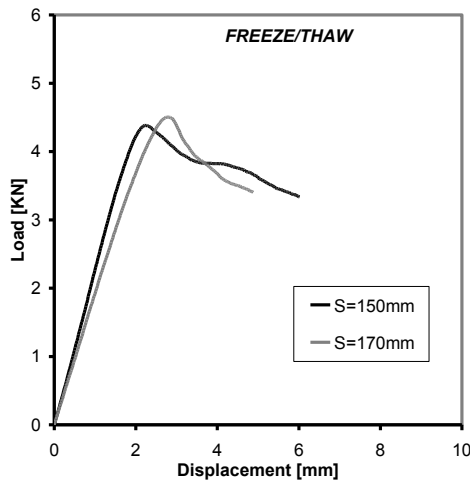
Figure 7.7: Load-Displacement curves derived by bending tests for conditioned specimens: (a) Not-conditioned; (b) Ultraviolet; (c) Hot-Dry; (d) Hot-Wet.



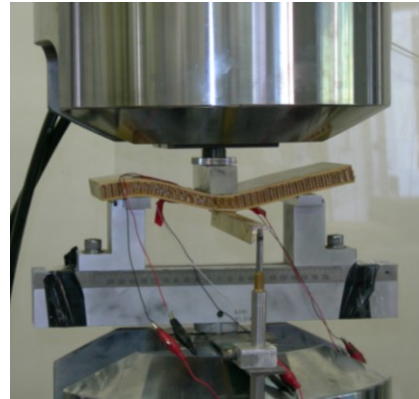
(a)



(b)



(c)



(d)

Figure 7.8. Load-Displacement curves derived by bending tests for conditioned specimens: (a) HCl solution at 20 day; (b) HCl solution at 40 day; (c) Freeze/thaw; (d) core shear failure mode.

## 7.5. Final remarks

In the evaluation of the degradation of the sandwich materials and behavior, no significant reduction was observed in the elastic modulus of the skin, shear strength and modulus of the core, and shear and flexural stiffness of the sandwich configuration, while appreciable reduction of the facesheet strength was observed when exposed to moisture and/or chemical agents.

As consequence, a coating techniques will be introduced to minimize the influences of these environmental factors and a more exhaustive experimental activity will be performed to achieve the influence of the selected factors on all the basic material properties (e.g. interlaminar shear, compressive)

## References

- P. Purnell, J. Beddows “Durability and simulated ageing of new matrix glass fiber reinforced concrete” *Cement and Concrete Composites* 27 (2005) 875-884.
- Rui Miranda Guedes, J.L. Morais, A.T. Marques, A.H. Cardon “Prediction of long-term behaviour of composite materials” *Computers and Structures* 76 (2000) 183-194
- R.D. Bradshaw, L.C. Brinson “Physical aging in polymers and polymer composites: an analysis and method for time-aging time superposition” *Polymer Engineering and science*, January 1997, vol.37, N.1.
- Y. Miyano, M. Nakada, N. Sekine “Accelerated testing for long-term durability of GFRP laminates for marine use”, *Composites Part B* 2004;35 pp 497–502.
- R.M. Guedes “Durability of polymer matrix composites: Viscoelastic effect on static and fatigue loading” *Composites Science and Technology* 67 (2007) pp2754-2583.
- T.A. Collings, R.J. Harvey, A.W. Dalziel "The Use of Elevated Temperature in the Structural Testing of FRP Components for Simulating the Effects of Hot and Wet Environmental Exposure", *Composites*, 24(8), 1993, pp 625-634.
- Jayamaran, K., Reifsnider, K. L., and Swain, R. E., “Elastic and Thermal Effects on the Interface: Part I. Comments on Characterization Methods,” *Journal of Composites Technology and Research*, Vol. 15, No. 1, 1993, pp. 3-13.
- Allred, R. E., “The Effect of Temperature and Moisture Content on the Flexural Response of Kevlar/Epoxy Laminates: Part I [0/90] Filament Orientation,” *Journal of Composite Materials*, Vol. 15, 1981, pp. 100-116.
- Sen, R., Mariscal, D., and Shahawy, M., “Durability of Fiberglass Pretensioned Beams,” *ACI Structural Journal*, Vol. 90, No. 5, 1993, pp. 525-533
- [Zhaohui H, Ian W, Roger J. Fire resistance of composite floors subject to compartment fires. *J Construct Steel Res* (2004) ;60:339–60.

ASTM, Accelerated aging of materials and structures, “The Effects of Long-Term Elevated-Temperature Exposure” - Committee on evaluation of long term aging of materials and structures using accelerated test methods.

M. Ito, K. Nagai, “Degradation issues of polymer materials used in railway field”, *Polymer Degradation and Stability*, 93, 1723-1735, (2008)

Karbhari V. M et al. , “Durability Gap Analysis for Fiber-Reinforced Polymer Composites in Civil Infrastructure”, *Journal of Composite for Construction*, 7(3), 238-247, (2003)

Chin JW, Nguyen T, Aouadi K. “Sorption and diffusion of water. Salt water and concrete pore solution in composite materials.” *J Appl Polym Sci* 1999;71:483–92.

Rivera J, Karbhari V.M, “Cold-temperature and simultaneous aqueous environment related degradation of carbon/vinylester composites”, *Composite Part B:33* (2002) 17-24

T.C. Radtke, A. Charon and R.Vodicka, “Hot/Wet Environmental Degradation of Honeycomb Sandwich Structure Representative of F/A-18: Flatwise Tension Strength “Airframes and Engines Division Aeronautical and Maritime Research Laboratory

V. M. Karbhari, “Response of FRP confined concrete to freeze and freeze-thaw regimes. *ASCE J Compos Constr* 2002 “

ASTM C666M , “Standard Test Method for Resistance of Concrete to Rapid Freezing and Thawing”, 2003.

L.Monney, C.Dubois, D.Perreux, A.Burtheret, A.Chambaudet, “Mechanical behavior of an epoxy-glass composite under photo-oxidation” *Polymer Degradation and Stability* 63 (1999) 219±224

ASTM D5208, “Standard Test Method for Fluorescent Ultraviolet (UV) Exposure of Photodegradable Plastics”, 2001

Vikrant S. Bhise ,”Strength Degradation of GFRP bars”, Thesis submitted to the Faculty of the Virginia Polytechnic and State University

Hartman, D.R., Greenwood, M.E., Miller, D.M. (1994).“ High Strength Glass Fibers,” Technical Paper - Owens Corning.

Tannous, F. and Saadatmanesh, H. (1999). “ Durability of AR Glass Fiber Reinforced Plastic Bars,” ASCE Journal of Composites for Construction, Vol. 3 No.1, pp. 12-19.

Fuji, Y., Murakami, A., Katou, K., Yoshiki, T., Maekawa, Z., Hamada, H. (1993). “Durability of GFRP in Corrosive Environment,” Proceedings of the Third International Offshore and Polar Engineering Conference, pp. 317-320. Combustible materials that can be invested by the flame on one side. Reaction to fire by applying a small flame”.

## **Chapter VIII**

# **DEGRADATION ISSUES: IMPACT ANALYSIS**

### **8.1. Introduction to framework activities**

In the present Chapter, impact response of composite sandwich components for the train roof structure have been analyzed and experimentally evaluated. In particular, indentation problem have been presented for the case of study in order to analyze the crushing behavior of core structures under localized load due to, for example, handling or interaction with attached structures. In addition, impact response and damage have been considered to analyze the impact events induced by trackside debris. The impact response of the selected sandwich configuration have been analyzed involving different parameters, i.e. impact energy/velocity level, skin thickness and impactor diameter.

### **8.2. Review of impact on sandwich structures**

During the life of a structure, impacts by foreign objects can be expected to occur during manufacturing, service, and maintenance operations. An example of in-service impact occurs when stones and other debris from the railway are propelled at high velocities. During the manufacturing process or during maintenance, tools can be dropped on the structures; in this case, impact velocity are small but mass of the projectile is larger.

Laminate composite structures are more susceptible to impact damage than a similar metallic structure. In composite structures, impacts create internal damage that often cannot be detected by visual inspection. This internal damage can cause severe reductions in strength and can grow under load. Therefore the effects of foreign objects impacts on composite structures must be understood, and proper measures should be taken in the design process to account for these expected events.

In the case of composite sandwich structures, a low rigidity of transverse direction results in a low contact stiffness and lower contact force during the impact. Contact laws for sandwich structures are completely different from those of monolithic laminates and are dominated by the deformation of the core.

The indentation of sandwich plates is dominated by the deformation of the core, and it is important to account for the indentation accurately in order to predict the contact force history. As with impacts on monolithic composite structures, the effects of local indentation can be accounted for use a statically determined contact law.

### **8.2.1. Contact between a sandwich beam and a cylindrical indenter**

Experimentally, the contact behavior is determined by conducting tests in which the back face of the specimen is continuously supported by a rigid plate.

Form an analytical point of view, if the back face of a sandwich beam is supported by a rigid plate, the upper facing can be considered as a beam of rigidity  $EI$  supported by a foundation which provide a reaction  $r(x)$  per unit length. The equilibrium of the beam is governed by the equation:

$$EI \frac{d^4 w}{dx^4} + r(x) = 0 \quad (8.1)$$

where  $w$  is the transverse displacement. When the transverse normal stress remain low, the core behaves elastically and the reaction of the foundation is proportional to the transverse displacement ( $r(x)=kw$ ). In that case, the equilibrium of the top facing is governed by the equation for a beam on linear elastic foundation:

$$\frac{d^4 w}{dx^4} + \frac{k}{EI} w = 0 \quad (8.2)$$

The stiffness of the foundation  $k$  is related to modulus of the core in the transverse direction  $E_c$ , the width of the beam  $b$ , and the thickness of the core  $h_c$  by:

$$K = \frac{E_c b}{h_c} \quad (8.3)$$

The general solution of governing equation is

$$w = e^{-\lambda x} (A \sin \lambda x + B \cos \lambda x) + e^{\alpha \lambda} (C \sin \lambda x + D \cos \lambda x) \quad (8.4)$$

Where

$$\lambda = \sqrt[4]{\frac{k}{4EI}} \quad (8.5)$$

The constants  $A$ - $D$  of general solution are determined by requiring the solution remains bounded at infinity and the slope at the origin be zero because of symmetry. In term of  $\alpha$ , the displacement at  $x=0$ , the deflection of the top facing can be written as:

$$w = \alpha e^{-\lambda x} (\sin \lambda x + \cos \lambda x) \quad (8.6)$$

The forced  $P$  required to produce the initial deflection  $\alpha$  is twice the value of the shear force at the origin. That is:

$$P = -2V(o) = 2EI \frac{d^3 w}{dx^3} (0) = 8\lambda^3 EI \alpha \quad (8.7)$$

The contact force increases linearly with the indentation and the initial contact stiffness  $k_l$  is then:

$$k_l = 8\lambda^3 EI = \sqrt{2^3} \left( \frac{E_c b}{h_c} \right)^{\frac{3}{4}} (EI)^{\frac{1}{4}} \quad (8.8)$$

The above equation shows the effects of material and geometric parameters on the initial contact stiffness of the sandwich beam. The radius of curvature at the origin can be calculate from the general solution and put in the form:

$$R = \frac{4\lambda EI}{F} \quad (8.9)$$

The radius of curvature is inversely proportional to the contact force  $F$  so that

as the force increases, the radius of curvature of the top facing decreases. As long as  $R$  remains larger than the radius of the indenter, the top facing will not wrap itself around the indenter and the load can be introduced as a concentrated force.

The foundation behaves elastically as long as the compressive stress in the core does not exceed the value  $\sigma_{max}$ . That is, when the contact force reaches the value:

$$P_1 = \frac{2b\sigma_{max}}{\lambda} \quad (8.10)$$

As the contact force increases, in a region of length  $a$  near the contact zone, the core is assumed to deform under a constant crushing stress  $\sigma_{crush}$  and in that region, the reaction supplied by the foundation is  $r_0 = b\sigma_{crush}$ . In this case the solution of the general integral

$$w = -\frac{r_0}{24EI}x^4 + c_1\frac{x^3}{6} + c_2\frac{x^2}{2} + c_3x + c_4 \quad (8.11)$$

Requiring that the displacements at  $x=0$  be the indentation  $\alpha$ , the slope at origin be zero because of symmetry, and that the shear force at  $x=0$  be equal to  $P/2$ , gives:

$$w = \alpha - \frac{r_0}{24EI}x^4 + \frac{P}{12EI}x^3 + c_2\frac{x^2}{2} \quad (8.12)$$

For problem with core damage there is one solution for the damaged region ( $x < a$ ) and another solution for the undamaged region ( $x > a$ ) given as solution of elastic case of plastic case respectively. In those two expression, there is a total of seven unknowns:  $A, B, C, D, \alpha, c_2$  and  $P$ . The displacement and the slope be bounded at infinity so  $C=D=0$ . For equation are obtained by requiring that two solutions match at  $x=a$ . That is the displacements, slopes, bending moment, and shear forces for the two solutions must be equal at that point. A fifth equation is obtained by requiring that, at  $x=a$ , the transverse normal strain be equal to the maximum core strain before crushing. For a given value of  $a$ , these five linear algebraic equations can be solved for the remaining five unknowns.

### 8.2.2. Contact between a sandwich plate and a spherical indenter

The present case can be studied by modeling the top facing as a plate on elastic foundation and subjected to a concentrated force. The deflection of an infinite isotropic plate on an elastic foundation under a concentrated force  $P$  is given by Timoshenko and Woinowsky-Krieger:

$$w_{\max} = \frac{P}{8(Dk)^{\frac{1}{2}}} \quad (8.13)$$

where  $D$  is the bending rigidity of the plate and  $k$  is the elastic modulus of the foundation. The local indentation of sandwich can be modeled by a linear spring with the stiffness given by:

$$K = 8(Dk)^{\frac{1}{2}} \quad (8.14)$$

This equation can be used to estimate the initial contact stiffness of sandwich plates with quasi-isotropic laminate facings. However, laminated composite facings are not always quasi-isotropic but can be modeled as orthotropic plates if layup is symmetric and consists of more than six plies. According to the classical plate theory, the equation of motion for symmetrical laminated plate on elastic foundation is:

$$D_{11} \frac{\partial^4 w}{\partial x^4} + 2(D_{12} + 2D_{66}) \frac{\partial^4 w}{\partial x^2 \partial y^2} + D_{22} \frac{\partial^4 w}{\partial y^4} + kw = p(x, y) \quad (8.15)$$

where  $w$  is the transverse displacement, the  $D_{ij}$  are the bending rigidities and  $p$  is the distributed loading which can be written as:

$$p = P\delta(x - \eta)\delta(y - \xi) \quad (8.16)$$

when a concentrated force  $P$  is applied at  $x = \eta$  and  $y = \xi$ . As in the case of beams on elastic foundations, the indentation of the top facing is expected to be localized. Therefore, for indentations away from the plate boundaries, the problem can be studied by considering a rectangular plate with simple supports along the edges.

### 8.2.3. Impact Dynamics

To predict the contact force history, the dynamics of both the projectile and the target must be modeled accurately, and local indentation effects must also

be accounted for. Various approaches for studying the impact dynamics can be used to study impact on sandwich structures.

Prediction of structure's dynamic response can be made using mathematical models that appropriately accounts for the motion of the projectile, the overall motion of the target, and the local deformations in the area surrounding the impact point. A particular beam, plate, or shell theory can be selected, and the local deformation in the through-the-thickness direction, which is not accounted for in such theories, can be included through the use of an appropriate contact law, which relate the contact force to the indentation. The choice of a particular structural theory must be based on careful consideration of the effect of complicating factors such as transverse shear deformation and rotary inertia. In particular for large wavelengths, sandwich plates can be modeled using first-order shear deformation theory and sandwich beams can be modeled using Timoshenko beam theory.

With most low-velocity impacts, small amounts of damage are introduced in a small zone surrounding the impact point, and the dynamic properties of the structures usually are not affected by the presence of damage. Therefore, impact dynamic analysis generally do not attempt to model damage as it develops during the impact event.

#### **8.2.4. Impact Damage**

Impacts on sandwich structures can induce damage to the facings, the core material, and the core-facing interface. The type of damage usually found in composite sandwich skins is similar to that observed after impacts on monolithic composites. Damage initiation thresholds and damage size depend on experimental testing conditions, geometric parameters, the properties of the core material and the relationship between the properties of the core and those of the composite facings.

Low-velocity impact damage on sandwich beam and plate with carbon-epoxy skins and honeycomb cores is confined to the top facing, the core-top facing interface, and core. The lower facing generally is left undamaged. Five different failure modes have been identified: (1) core buckling; (2) delamination in the impacted face sheet; (3) core cracking; (4) matrix

cracking, and (5) fiber breakage in the skins. In the upper facing, damage is similar to that observed in laminated composites and consists primarily of delamination with matrix cracks and some fiber failures. In monolithic laminates, the damage area increases almost linearly with the kinetic energy of the projectile. With sandwich structures, skin damage also increases almost linearly with impact energy until a maximum value is reached. At that point, visible damage is noticed and the delamination size remains constant. In honeycomb cores, damage consists of crushing or “buckling” of cell walls in a region surrounding the impact point.

Higher-energy impacts result in partial or complete penetration of sandwich structure. The penetration resistance is governed by the overall rigidity of the target and the resistance of the facing to perforation.

Both experimental and numerical studies [27-30] have been presented on low-velocity impact on Nomex honeycomb sandwich structures, but only a small amount of literature concerns impact tests where complete penetration occurs [31].

### **8.2.5. Strain rate effects**

To design sandwich panels for short-term dynamic loads, it is necessary to have information about the influence of loading rate on the material properties. It is well known that in case of high loading rate an increase in material stiffness and strength compared to the static behavior may occur, which is referred to as the strain rate effect. When this effect is neglected, dynamic finite element (FE) simulations and theoretical derivations based on static material data often do not agree with experimental behavior. Consequently, design approaches using static data can be too conservative, which inhibits potential weight savings.

The strain rate effect on axial behavior of both aluminium [21-24] and Nomex [25, 26] honeycomb structures have been experimentally investigated through dynamic compressive tests performed with different techniques (i.e. drop weight, gas gun, and split Hopkinson bar). The results have been focused on the influence of strain rate on the crush strength of the honeycomb structures, while there are no considerations of the influence on

the compressive strength that cannot be precisely analyzed due to data filtering as result of oscillations.

### **8.2.6. Experimental techniques**

Experimental techniques may be employed to detect impact damage in sandwich structures. The initial kinetic energy of projectile is an important parameter to be considered, but several other factors also affect the response of structure. Several variant of impact test have been generally implemented by most investigators through gas gun, dropweight, pendulum testing, and hydropneumatic (Hopkinson bar) machines.

In *gas gun apparatus*, high pressure compressed air is drawn into an accumulator to give pressure controlled by regulator. The pressure is released by a solenoid valve, the breakage of a thin diaphragm, or other mechanisms. The projectile then travels through the gun barrel and passes a speed-sensing device while still in the barrel of the gun or right at the exit. A simple speed-sensing device consists of a single light-emitting diode (LED) and a photodetector. The projectile, which has a known length, interrupts the light beam, and the duration of that interruption in signal produced by the sensor is used to calculate the projectile velocity. Most experimental setups utilize two LED-photodetector pairs. The travel time between the two sensor is determined using a digital counter and is used to calculate the projectile velocity.

*Dropweight testers* are used extensively and can be of differing designs. Heavy impactors are usually guided by a rail during their free fall from a given height. Usually, a sensor activates a mechanical device designed to prevent multiple impacts after the impactor bounces back up.

*Pendulum-type systems* are also used to generate low-velocity impacts. Pendulum-type testers consist of a steel ball hanging from a string, or a heavier projectile equipped with force transducers or velocity sensor.

### **8.3. Quasi-Static tests**

#### **8.3.1. Uniaxial Compressive tests**

Out-of-plane crushing behavior of Nomex honeycomb has been investigated by flat-wise stabilized compressive tests according to ASTM C365M [35] standard. The tests were run on five 60x60x32.2 mm coupons bonded between two 1-mm-thick phenolic skins with a constant cross head velocity of 0.5 mm/min. The specimens were laminated with external skins in order to prevent local crushing at the edges of the honeycomb cores. Compressive modulus, stabilized compressive strength and strain, crush strength and strain values at which densification occurs have been derived by these tests. The stress-strain relationship (Fig. 8.1a), that is the mean data of five replicate specimens, consists of three stages: the elastic regime up to the stabilized compressive strength, the crushing regime at nearly constant plateau stress (crush strength), and finally the densification regime, where the cellular structure is fully compacted resulting in a steep stress increase. Figure 8.2b shows the three deformation stages of the honeycomb core during a flat-wise compression test.

#### **8.3.2. Indentation tests**

In order to investigate the crushing behavior of sandwich structures subjected to localized point loading, indentation tests were performed on 50x250mm sandwich specimens manufactured by laminating 32.2-mm-thick Nomex core between two 1-mm-thick glass/phenolic skins. The sandwich beams were supported by a steel substrate, thus the overall bending on the specimen was avoided. The tests were carried out under displacement control at a loading rate of 2 mm/min. The indentation load was applied through a steel cylinder (20 mm in diameter) across the whole width of the beam cross-section (Fig. 8.2). The test was conducted on three replicate specimens for each of four different displacement levels. Afterwards the load was released at a cross-head speed of 20 mm/min. During the unloading the face sheet flexed back but did not recover completely its undeformed shape: thus, a residual facesheet dent remained. The load-indentation curve was recorded for both

loading and unloading steps.

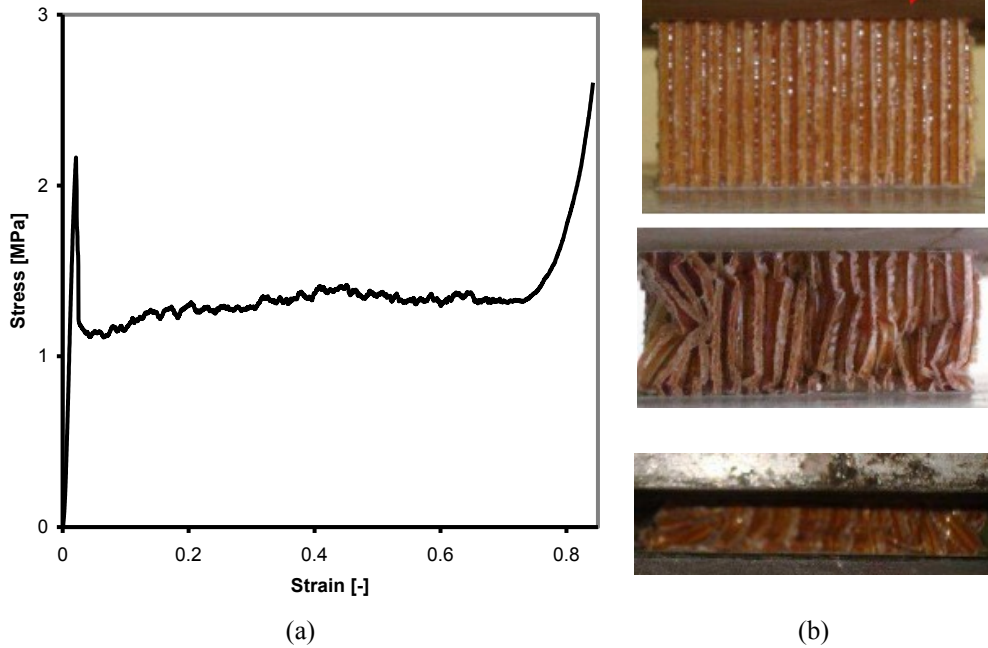


**Figure 8.1.** Experimental results of static flat-wise stabilized compression tests: (a) mean stress-strain curve; (b) deformation stages — initial (top), crushing regime (middle), densification (bottom).

A typical load-indentation curve for a Nomex honeycomb sandwich specimen is shown in Fig. 8.3a. The curve showed a linear behavior up the peak load. It is believed that the emission of a noise (cracking sound) at the end of the linear domain is associated with the onset of core crushing. The maximum contact force prior to plastic deformation can be analytically determined employing a simple indentation model that assumes an elastic Winkler foundation for the elastic core (exp. 1.54 kN [C.v.=8.16%] vs. 1.51 kN).

After the peak indentation force, the force-displacement curve became nonlinear with a decrease in the stiffness. The nonlinear behavior was due to the progressive honeycomb crushing in the area under the indenter. Figure 8.3b shows the residual dent magnitude and the length of damaged area as function of the imposed indentation. Each data point reported in Fig. 8.3b is the average of three tests.

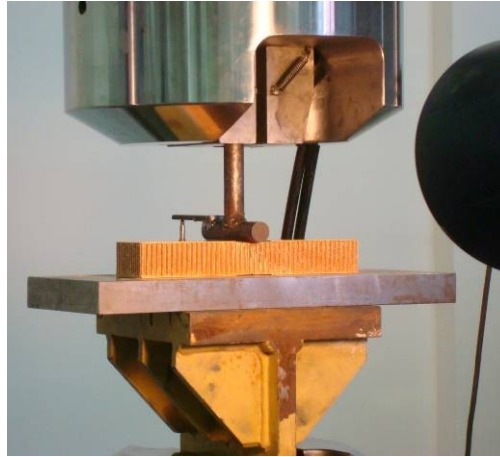


Figure 8.2. Quasi static indentation test: set-up.

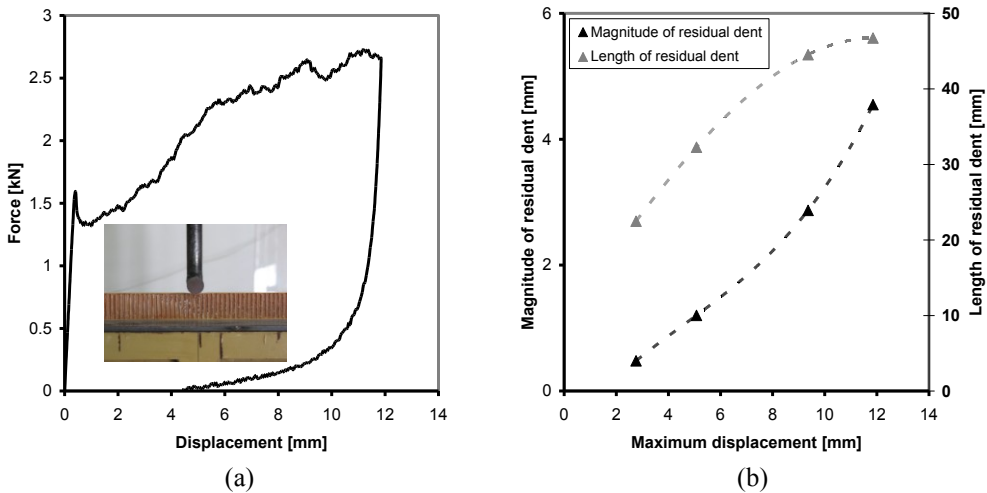


Figure 8.3. Experimental results of indentation test: (a) force-displacement curves; (b) residual dent depth at different imposed displacement values.

The results of the residual dent measurements are very sensitive to the time passed after indentation test. In this study, the measurement of the residual dent, equal to the displacement when the load dropped to zero, were performed directly in the test machine and immediately after unloading to the zero load level, thus, measuring the instantaneous residual dent magnitude. The residual dent magnitude and length can be theoretically found applying the principle of minimum total energy. Energy methods based on assumed displacement functions, such as that used in the analysis of unloading,

provide powerful tools for solving complex problems but do not in general lead to exact solutions as the conditions of equilibrium are only approximately satisfied [44]. For this reason, in Fig. 5b the residual dent magnitude and length have been interpolated by a third order polynomial as function of maximum indentation displacement.

## **8.4. Dynamic tests**

In the present section, the main outcomes of an experimental dynamic characterization of phenolic impregnated Nomex sandwich structures are presented. The experimental investigations addressed the dynamic compression behavior and the impact response of the sandwich panels. Dynamic tests at different loading were conducted using a drop weight tower apparatus, controlled by an electronic control unit which allows monitoring displacement measurements with a laser measurement system. In particular, the compression tests were designed to provide the strain rate effect of the core behavior, whereas the impact tests assess the damage mechanisms occurring in the phenolic skins.

### **8.4.1. Uniaxial Compressive tests**

Out-of-plane compressive tests were conducted on the drop tower facility at three different strain rates (60 s<sup>-1</sup>, 120 s<sup>-1</sup> and 200 s<sup>-1</sup>) on cylindrical specimens of 45 mm diameter and either 32.2 mm or 10.5 mm thickness. The smaller thickness was considered to achieve higher strain rates. In order to prevent local crushing at the edge of the honeycomb structure, the core was bonded to 1 mm glass/phenolic skins. A fourth order butterworth low-pass filter was used in order to filter out superposed high frequency oscillations associated with dynamic loads (Fig. 8.4a). In this way, comparability of dynamic and static test data have been achieved. Figure 8.4b shows the stress-strain-diagrams at the investigated strain rates. Each shown curve represents the mean data of five replicate specimens for each specimen family.

It can be seen that dynamic loading leads to a significant increase of both

compressive and crush strength; in particular the compressive strength presents a DIF (Dynamic Increase Factor, ratio of the dynamic value over the static one) of 1.20 (at 200 s<sup>-1</sup>), whereas the crush strength presents a DIF of 1.10 (at 200 s<sup>-1</sup>). The influence of dynamic loading on the densification point has been also observed: the dynamic strain value is about 10% lower than the quasi-static one. On the contrary, no influence on the initial stiffness has been observed. For aluminum honeycomb structures the DIF for crush strength was observed to be about 33% (gas gun test, 100 s<sup>-1</sup>) [21], 40% (split Hopkinson pressure bar, 800 s<sup>-1</sup>) [22] and 50% (gas gun test, 2000 s<sup>-1</sup>) [23] above the quasi-static value. For Nomex honeycomb structures the increase of plateau stress is about 10-30% in the strain rate domain from 50 s<sup>-1</sup> to 300 s<sup>-1</sup> [26].

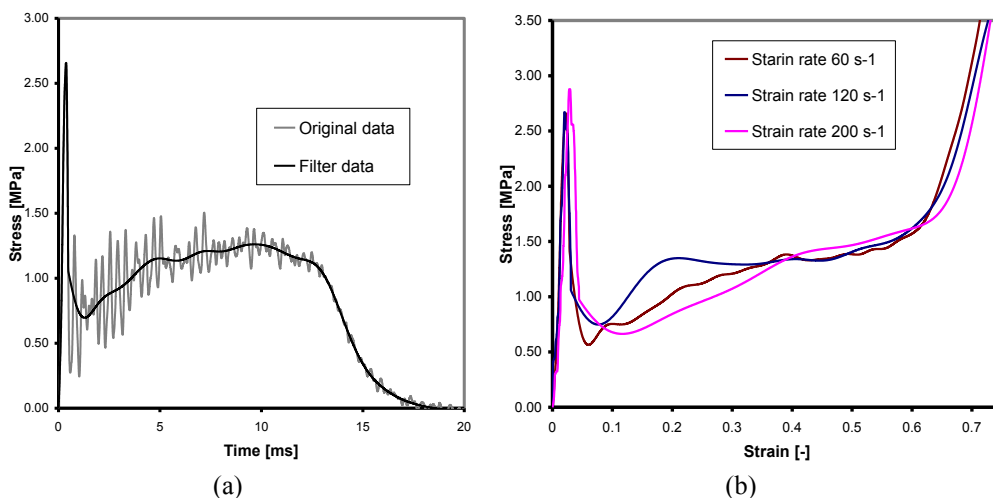


**Figure 8.4. Dynamic compression tests on honeycomb structures: (a) filtering data; (b) stress-strain curves at different strain rates.**

### 8.4.2. Impact tests

Impact tests were performed on specimens prepared with 11-mm-thick Nomex honeycomb sandwiched between either 1-mm or 2-mm glass/phenolic skins consisting four or eight fabric plies, respectively. The specimens were clamped using cylindrical rings and impacted with a 16.8-kg mass at three different energy levels, achieved with three different velocities ( $v=1$  m/s,  $v=4$  m/s and  $v=8$  m/s). Tests at different impact velocities were

performed to provide top skin damage ( $v=1$  m/s) and complete penetration ( $v=4$  m/s and  $v=8$  m/s). Two different hemispherical tips (12.7 mm and 20 mm) were adopted to provide their influences on the impact response. The main objective was to assess the influence of skin thickness, impactor diameter, impact energy and impact velocity on the main outcomes of the impact tests—i.e. the impact damage (damaged area and through-thickness damage), the force history, and the energy absorption.

Load-displacement and energy-displacement curves are plotted in Figs. 8.5-8.7 for impact events which produce respectively visible damage of the top skin ( $v=1$  m/s) and complete penetration ( $v=4$  m/s and  $v=8$  m/s) of the sandwich specimens. All the results in terms of energy absorption and peak force have been summarized in Table 8.1.

**Table 8.1. Impact test results. The reported values are the mean of the three replicate specimens**

	1 mm skin thickness 12.7 mm impactor diameter			2 mm skin thickness 12.7 mm impactor diameter			1 mm skin thickness 20 mm impactor diameter		
	$v=1$ m/s	$v=4$ m/s	$v=8$ m/s	$v=1$ m/s	$v=4$ m/s	$v=8$ m/s	$v=1$ m/s	$v=4$ m/s	$v=8$ m/s
	<b>Absorbed Energy [J]</b>	8.51	21.70	21.73	7.94	59.56	63.23	9.23	43.06
<b>Top skin peak force [kN]</b>	2.16	2.13	2.19	3.79	3.92	4.47	2.70	3.32	3.11
<b>Bottom skin peak force [kN]</b>	-	2.16	2.42	-	5.44	6.09	-	3.36	3.15

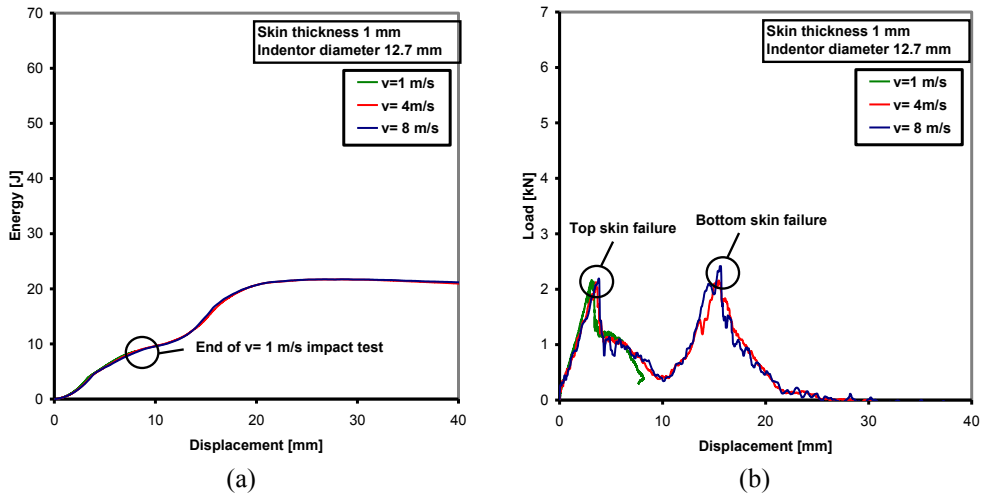


**Figure 8.5.** Experimental results of 1mm skin specimens impacted by 12.7 mm indenter: (a) energy-displacement curves; (b) load-displacement curves.

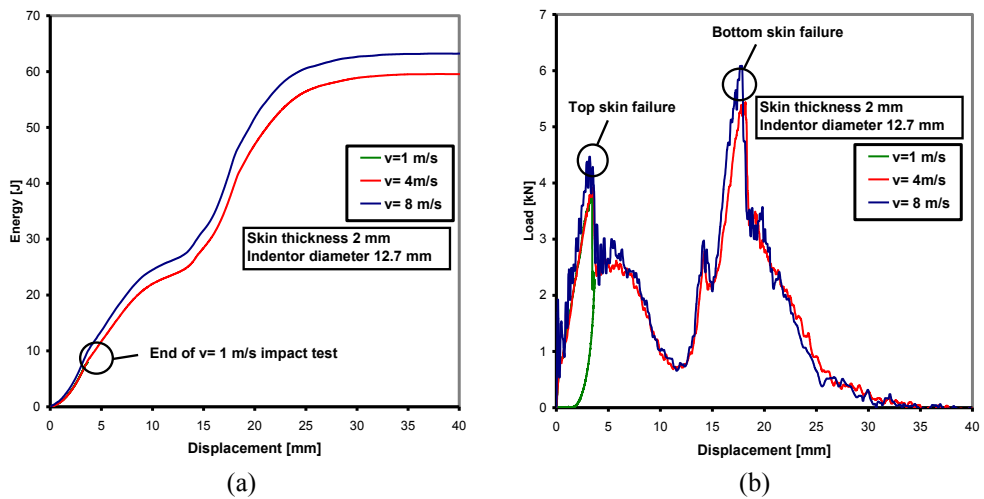


**Figure 8.6.** Experimental results of 2-mm skin specimens impacted by 12.7-mm indenter: (a) energy-displacement curves; (b) load-displacement curves.

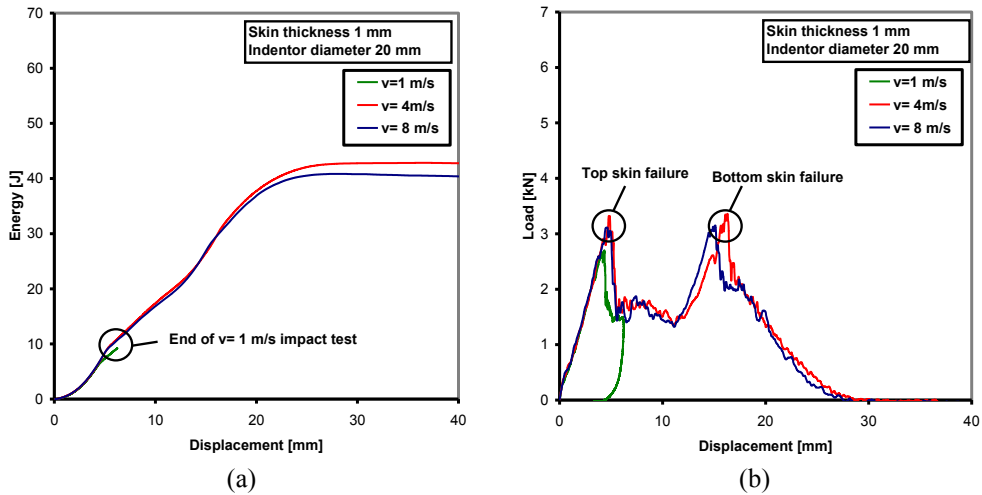


**Figure 8.7.** Experimental results of 1-mm skin specimens impacted by 20-mm indenter: (a) energy-displacement curves; (b) load-displacement curves.

At low level of energy ( $v=1$  m/s), the load curves grow up to a peak level which is due to the penetration of the impactor through the top skin. Furthermore, it can be observed that, before the penetration occurs, the curves present a change of slope due to the crushing of the Nomex honeycomb structures that happens when the Nomex attains the compressive strength. At higher level of energy ( $v=4$  m/s and  $v=8$  m/s), after the first peak the load curves present a low-loading plateau, characterizing the penetration of the honeycomb core, and a second sharp peak level due to the failure of the bottom skin.

The absorbed impact energy displays a constant initial slope up till a penetration of the top skin is achieved. The gradient of the curve reduces when the core is penetrated and increases again when the weight impacts on the bottom skin. In cases of complete penetration, the absorbed energy of the honeycomb, related to the plastic strain of the walls, is very low. However the skins are the main factor responsible for the energy absorption and the energy absorbed by each skin is almost constant. Moreover, increasing the skin thickness increases the energy proportionally.

In case of 1-mm skin thickness, no significant strain rate effects are observed for the peak forces and absorbed energies, whereas in case of 2-mm skin thickness a slight increase of the peak forces is observed (18% for top skin

from 1 to 8 m/s, 12% for bottom skin from 4 to 8 m/s). In any case, the energy absorbed by the facesheets and honeycomb increase with impactor diameter.

In order to further understand the damage mechanism involved in impact events, the influence of skin thickness and impactor size on the failure modes are presented in Figs. 8.8-8.10. The main failure mode in the composite skins is fibre breakage, which represents the basic energy absorption mechanism. However, increasing the skin thickness, delamination mechanisms become relevant on the bottom skin.

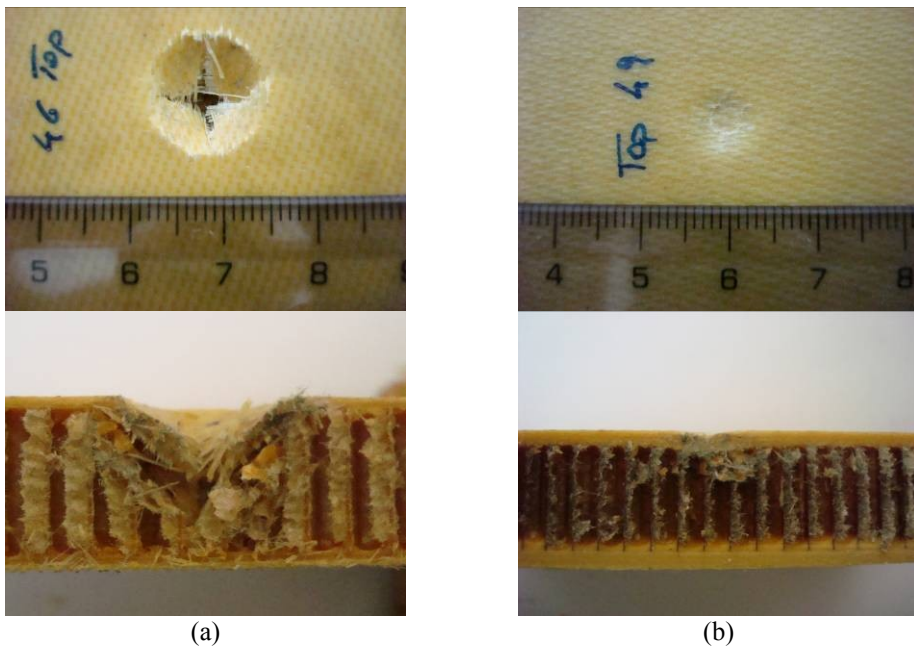
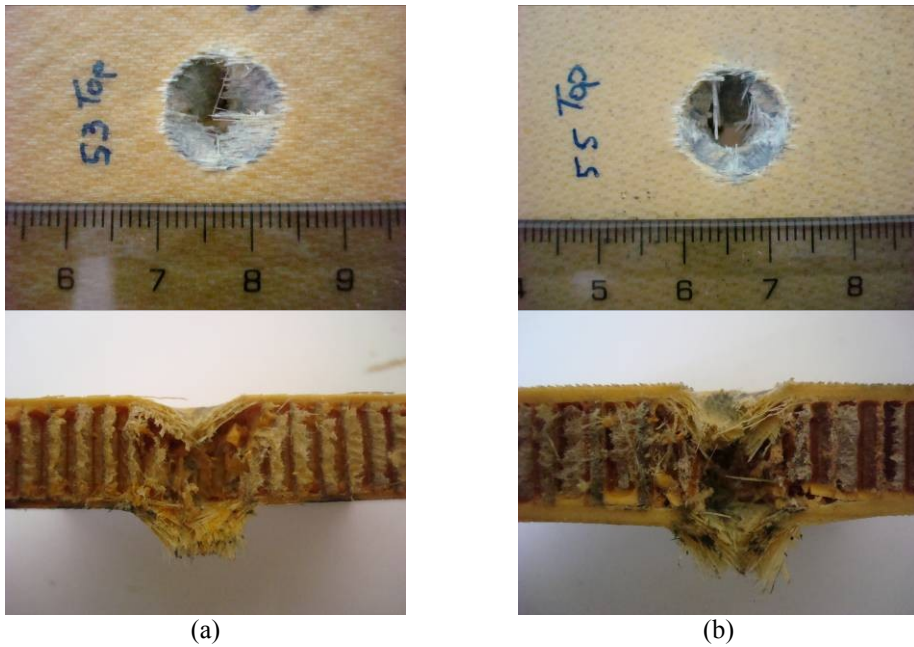


**Figure 8.8.** Pictures of the impact face and cross-sectional view of sandwich specimens: (a) 1 m/s velocity, 1 mm skin thickness and 12.7 mm impactor; (b) 1 m/s velocity, 2 mm skin thickness and 12.7 mm impactor.



(a) (b)  
**Figure 8.9. Pictures of the impact face and cross-sectional view of sandwich specimens: (a) 4 m/s velocity, 1 mm skin thickness and 12.7 mm impactor; (b) 4 m/s velocity, 2 mm skin thickness and 12.7 mm impactor.**

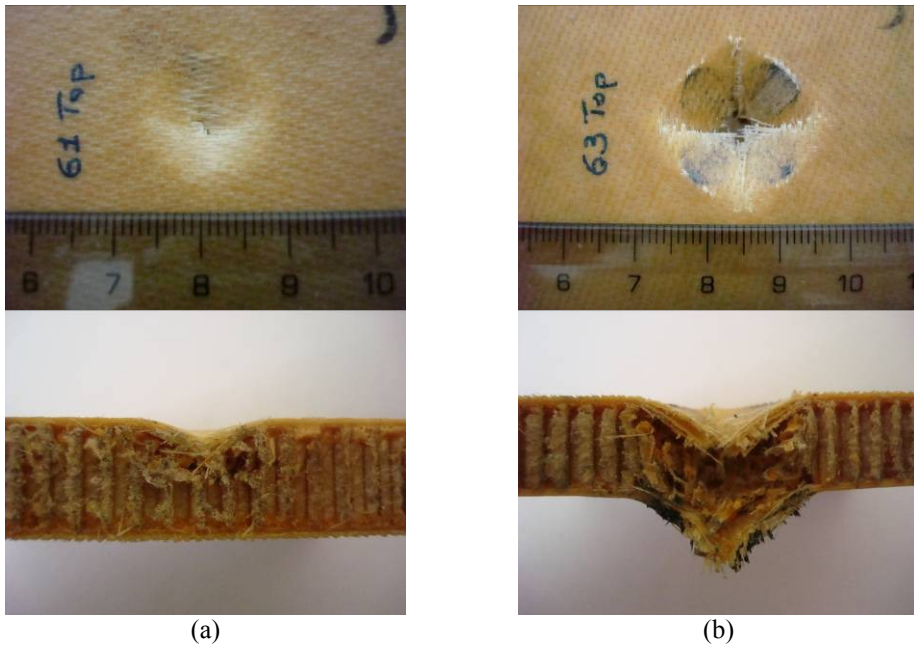


**Figure 8.10.** Pictures of the impact face and cross-sectional view of sandwich specimens: (a) 1 m/s velocity, 1 mm skin thickness and 20 mm impactor; (b) 4 m/s velocity, 1 mm skin thickness and 20 mm impactor.

## 8.5. Final remarks

Quasi-static tests allow to characterize the crushing and indentation behavior of honeycomb Nomex sandwich structures. The dynamic investigation provides the influence of the skin thickness, the material strain rate, the diameter of the impacting projectile and the impact velocity on the dynamic behavior of the sandwich composite material.

Experimentally evidence allows to understand the response of the sandwich material and the damage mechanisms involved in an indentation and impact event on a sandwich structures.

The following main outcomes have been obtained: (i) the Nomex honeycomb structure presents a strain rate sensitive compressive behavior; in particular, at a strain rate of about  $300 \text{ s}^{-1}$ , the compressive strength presented a DIF of 1.20, whereas the crush strength presented a DIF of 1.10; (ii) in case of 1-mm skin thickness, no significant strain rate effects are observed for the peak

forces and absorbed energies, whereas in case of 2-mm skin thickness a slight increase of the peak forces is observed (18% for top skin from 1 to 8 m/s, 12% for bottom skin from 4 to 8 m/s). In any case, the energy absorbed by the facesheets and honeycomb increase with impactor diameter; (iii) in case of thicker skins delamination may occur at the bottom skin.

In addition, Based on the experimental results, dynamic constitutive laws will be calibrated in order to conduct reliable finite element simulations and investigate the main mechanisms and parameters involved in the dynamic behavior. The long-range objective is to obtain a reliable numerical model to be employed in more complex dynamic virtual tests.

## References

- S. Abrate, *Impact on composite structures*, Cambridge University Press, (1998).
- L. Aktay, A. F. Johnson and M. Holzapfel, “Prediction of impact damage on sandwich composites”, *Comp. Mater. Sci.*, 32, 252-260 (2005).
- L. J. Gibson and M. F. Ashby, *Cellular solids: structure and properties*, Cambridge University Press, (1997).
- C. C. Foo, G. B. Chai and L. K. Seah, “Mechanical properties of Nomex material and Nomex honeycomb structures”, *Comp. Struct.*, 80, 588-594 (2007).
- E. Wu and W. S. Jiang, “Axial crush of metallic honeycombs”, *Int. J. Impact Eng.*, 19(5-6), 439-456 (1997).
- H. Zhao and G. Gary, “Crushing behavior of aluminum honeycombs under impact loading”, *Int. J. Impact Eng.*, 21(10), 827-836 (1998).
- W. E. Baker, T. C. Togami and J. C. Weydert, “Static and dynamic properties of high-density metal honeycombs”, *Int. J. Impact Eng.*, 21(3)c, 146-163 (1998).
- M. Yamashita and M. Gotoh, “Impact behavior of honeycomb structures with various cell specifications – numerical simulations and experiment”, *Int. J. Impact Eng.*, 32(1-4)c, 618-630 (2005).
- W. Goldsmith and J. L. Sackman, “An experimental study of energy absorption in impact on sandwich plates”, *Int. J. Impact Eng.*, 12(2), 241-262 (1992).
- S. Heimbs, S. Schmeer, P. Middendorf and M. Maier, “Strain rate effects in phenolic composites and phenolic-impregnated honeycomb structures”,

- Comp. Sci. Tech.*, 67, 2827-2837 (2007).
- M. Meo, R. Vignjevic and G. Marengo, “The response of honeycomb sandwich panels under low-velocity impact loading”, *Int- J. Mech. Sci.*, 67, 2827-2837 (2007).
- E. J. Herup and A. Palazzotto, “Low-velocity impact damage initiation in graphite/epoxy/Nomex honeycomb-sandwich plates”, *Comp. Sci. Tech.*, 57, 1581-1598 (1997).
- J. H. Park, S. K. Ha, K. W. Kang, C. W. Kim and H. S. Kim, “Impact damage resistance of sandwich structure subjected to low velocity impact”, *J. Mat. Process. Tech.*, 201, 425-430 (2008).
- T. Anderson and E. Madenci, “Experimental investigation of low-velocity impact characteristics of sandwich composites”, *Comp. Struct.*, 50, 239-247 (2000).
- R. A. W. Mines, C. M. Worrall and A. G. Gibson, “Low velocity perforation behavior of polymer composite sandwich panels”, *Int. J. Impact Eng.*, 21, 855-879 (1998).
- Hexcel, Mechanical properties of Hexcel honeycomb materials, Publication ATU 123b (2007).

## **Chapter IX**

# ***SUBCOMPONENT OPTIMIZATION AND VALIDATION***

### **9.1. Introduction to framework activities**

In the present Chapter the last step of the proposed procedure have been carried out for the case of study. In particular the presented activities provide to define an optimum configuration of sandwich structure involving glass/phenolic composite skins and Nomex honeycomb core.

The design procedure have been developed for only one panel of the A module as defined in the Chapter IV. After the validation activity the design parameters can be extended also to the other modules of the roof structure.

In the present case, the structural performance of the designed sandwich configuration have been assessed by means of finite element tools. However few benchmark tests can also be employed in the final step of the presented procedure.

### **9.2. Literature review**

The characteristics of a sandwich structure offer a wide range of optimization alternatives. The structure can be optimized for thermal insulation, acoustic damping, energy absorption from impact, weight minimization, stress, strain and stiffness optimization, or other structural characteristic that may be of

interest.

Many studies [ ] show that a failure mode map can be used to optimize the design minimizing the weight (or cost) of the sandwich element for some given structural requirement. In sandwich optimization, generally, The weight of the element is the objective function to be minimized and the design parameters are the face thickness and the core thickness and density.

The studies on composite structural designs using knowledge-based expert systems have recently become available, providing more rapid and direct use of results to the design and manufacturing of composite structures for various purposes. The optimization procedures are extensively automated whereby iterative finite element solutions are executed under the control of a software suite containing information on the optimization parameters, objective functions and constraints.

A range of different algorithms has been developed to carry out the optimization. The selection of an efficient algorithm is of paramount importance particularly in the case of large structures in order to reduce the numbers of iterations to convergence.

In railway field, Harte et al. [ ] investigated the optimization of design parameters associated with composite sandwich bodyshell walls of light rail vehicle. The research provide a multilevel computation procedure that leads to optimum wall ply thickness and geometric shapes for areas such as door and window openings. In the case of the shape optimization, the design variable is the radius of the fillet at the corners of the window opening and the objective function is the structural weight. For the thickness optimization, the design variables are the thicknesses of the plies, which form the facesheets and again the objective function is the structural weight. In each case, the design constraint is that the Tsai–Hill safety margin in each ply must be at least 0.05.

Kim et al. [ ] developed an expert system for the stiffness optimization of the composite train carbody under some classified design rules. In order to optimize the stiffness of a composite laminate, the stacking sequence and the total number of plies were simultaneously optimized. The optimization procedure was performed by the enumeration method, the expert system shell

and the classical laminate theory. In order to optimize simultaneously the stacking sequence and the total number of plies, discrete ply angles were considered and the ply thickness was treated as a constant. The design rules for the stacking sequence of composite laminates was collected and systematically classified for the composite design that can realistically be applied to various purposes. Design rules were stored as knowledge in the expert system and were imposed as heuristic constraints in the enumeration scheme. To optimize the stiffness of composite laminates, the laminate strain induced by the applied loading should be minimized. The optimal stiffness design of composite laminates is performed under the strain constraint and the design rules (maximum strain failure theory).

In addition, Kim. et al. developed a patchwise optimal layup design method for the tapered composite laminates. In the patchwise layup design method, the optimal solution is obtained by integration of an expert system shell, genetic algorithm and finite element method. In this approach, the weight of composite laminates with ply drop (termination of plies at different locations) under strength constraint is minimized and for this purpose, stacking sequences and the number of plies are optimized. The design variables are the discrete ply angles and the number of plies in each patch. Tsai-Hill failure index is investigated to ensure a satisfactory design.

The application of ply drop in composite laminates is common in wing and fin skin structures, helicopter rotor blades, etc. In all these applications, the use of ply drop results in significant saving in material and is therefore, cost effective. However, the ply drop introduces structural difficulties like stress concentration at the drop location. Hence, the potential benefits may be compromised through a substantial reduction in the strength of the laminate. The design variables are the discrete ply angles and the number of plies in each patch. Tsai-Hill failure index is investigated to ensure a satisfactory design.

### **9.3. Optimization procedure**

Due to the size of the problem, optimization of the vehicle body parameters

can be carried out on a panel by panel basis in order to avoid a large number of design variables at a given time. An initial finite element analysis can be carried out in order to identify the critical panel and loading condition (highest levels of Von Mises stress). When the critical panel has been identified, the model will be refined and sandwich panel configuration data are assigned to these elements. This allows parameterization of the critical panel so that shape, lay-up and stacking sequence parameters are made available to the optimization procedure.

The optimization is achieved by changing the values of certain design variables in order to minimize the objective function while at the same time satisfying certain behavioral constraints. This may be expressed mathematically as:

$$\text{Min } f(x_i)$$

$$c_j(x_i) \leq c_j^{\max}, j = 1, m$$

$$x_i^{\min} \leq x_i \leq x_i^{\max}, i = 1, n$$

Where the  $n$  variables  $x_i$  are the design variables and the objective function  $f(x_i)$  is to be minimized subject to the  $m$  constraints  $c_j$ . In addition, side constraints, denoted by  $x_i^{\min}$  and  $x_i^{\max}$ , are placed on the design variables themselves.

In the optimal design of laminated composite structures, individual ply thicknesses, number, and orientations are often selected as design quantities and Tsai-Hill failure theory will be used to ensure a satisfactory design requirements, where a failure index (or safety margin) value will be used to indicate failure.

Collection and classification of design rule for optimum stacking sequence of composite laminates can be found in literature []

To avoid or reduce the stresses coupling effect are:

- A laminate stacking sequence should be symmetric about the mid-plane to avoid the extension–bending coupling.
- A laminate stacking sequence should be balanced to avoid the shear-extension coupling.
- $\pm\theta$  plies should be grouped to reduce the bending-twisting coupling.

To improve the stiffness are:

- A minimum 10% of fibers should be oriented in each  $0^\circ$ ,  $\pm 45^\circ$ , and  $90^\circ$  direction to minimize matrix and stiffness degradation.

To improve the strength are

- Minimize groupings of plies with the same orientation to create a more homogeneous laminate and to minimize inter-laminar stress and matrix cracking during the service period. If plies must be grouped, avoid grouping more than 4 plies of the same orientation together.
- Avoid grouping  $90^\circ$  plies and separate  $90^\circ$  plies by a  $0^\circ$  or  $45^\circ$  ply to minimize inter-laminar shear and normal stress.
- Separate  $\pm\theta$  plies to reduce inter-laminar shear stress.
- Shield primary load carrying plies by locating inside of laminate to increase tensile strength and buckling resistance.
- To avoid large-scale matrix cracking and delamination, the ply angle difference between the adjacent plies must not exceed  $45^\circ$ .
- Avoid locating tape plies with fibers oriented perpendicular to a free edge at the laminate mid-plane to lessen high inter-laminar stress at free edges.

### 9.3.1. Preliminary finite element analysis

The initial finite element model consists of a planar symmetric model of the railcar and is shown in Fig. 9.1. The Firema railcar is all composed by extruded aluminum components. They are modeled by four-noded shell elements.

Boundary conditions are applied to the model to account for the planar symmetry. These consist of horizontal restraints acting along the line of symmetry of the structure. Further boundary conditions consist of vertical restraints at the wheel positions to represent the vehicle being supported on the ground and of longitudinal restraints at the buffer area.

The five static load conditions, provided by European guideline for the vehicle object of the present study as summarized in the Chapter IV, have been applied at the vehicle body in order to identify the critical area of the central module of the roof panel and to assess the critical stress and displacement field.

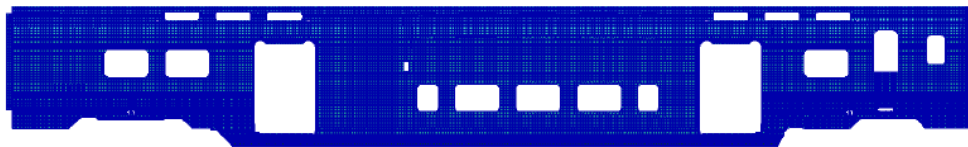


**Figure 9.1.** FE model of the Firema vehicle body.

Figure 9.2 shows a Von Mises stress field due to the second static load combination (Vertical load + compressive force) for the entire vehicle body.

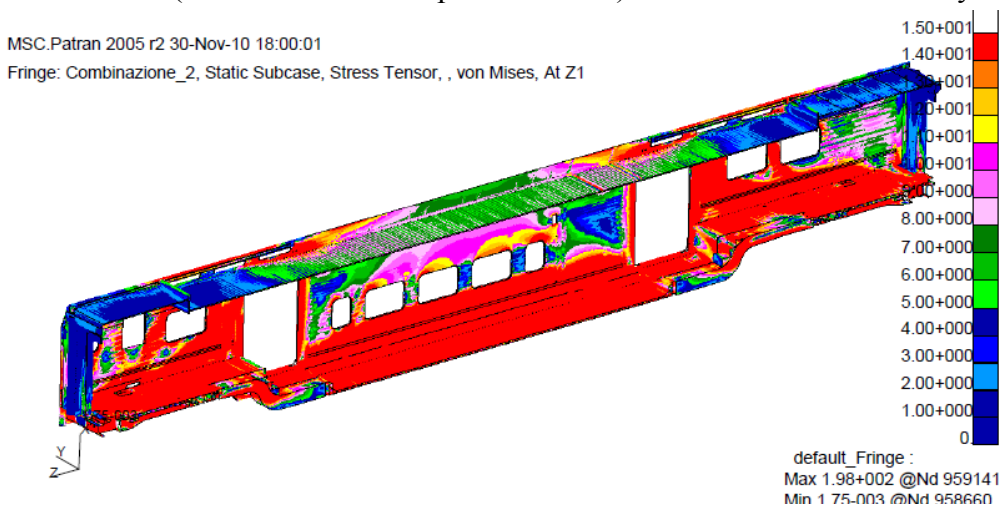


**Figure 9.2.** Von Mises contour plot for the second static load combination.

As can be observed the stress field on composite roof is lower than the other body structures. The stress field shows, in addition, a presence of concentrated stress in the area around the windows. In particular, the maximum value attained by Von Mises stress in the roof panels is estimated  $\approx 10\text{MPa}$ .

The maximum vertical displacements are derived in roof panel for the first and fourth load conditioning, i.e maximum vertical load and vertical load + tensile force. In both the case the maximum vertical displacements are  $\approx 10\text{mm}$ .

However, the main factors that can be led the structural integrity of the roof structures are the stresses at interface between the roof panel and the longitudinal side rails and the concentrated load derived by attached equipments.

A 2450x2674 mm central panel, as presented in the Chapter IV, have been herein considered to the optimization procedure and validation of design activities.

The design of sandwich configuration have been carried out minimizing the weight of the sandwich configuration using ordinary sandwich beam theory for a given stiffness. In this case, the panels is supposed loaded in three-point bending configurations and the stiffness equation (Length/50) is the constraint equation. Fig. 9.3 plot the weight and stiffness function in term of skin and core thickness.

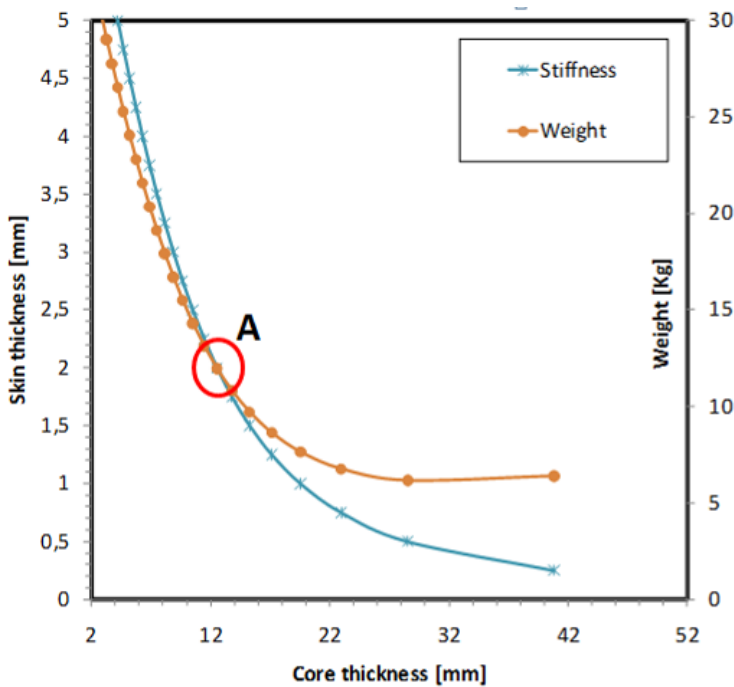


**Figure 9.3. Stiffness-strength-weight optimisation for the selected sandwich panel**

As can be seen, the combination of geometric parameters that allow to optimize the weight function for the selected materials are: 2 mm skin thickness, and 12.5 mm core thickness. The involved thickness are obtained on the basis of closer commercial value matching the empirical value.

In order to ensures that the sandwich panel configuration remains both symmetric and balanced,  $[0,-45,90,+45]_s$  stacking sequence is considered for the composite sandwich skins.

### 9.3.2. Refined FE model

At this point, selected the basic sandwich panel and designed the sandwich configuration, a refined FE model of the roof panel have been developed. The basic module consists of the two aluminum side rail that welded to two aluminum beams define an aluminum frame on which the sandwich panel can be installed. For simplicity a quarter of model have been developed (Fig. 9.4)

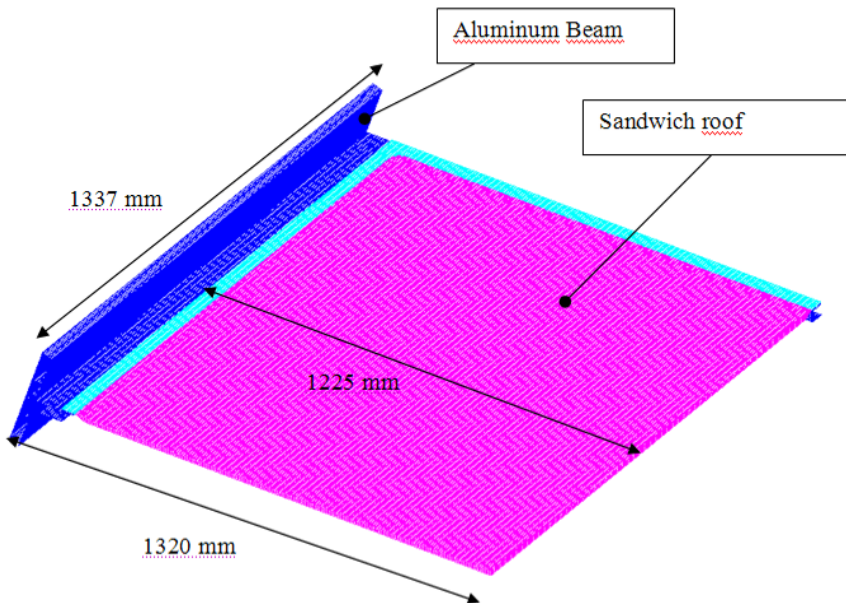


**Figure 9.3. FE model of basic sandwich roof panel.**

Adhesive joint techniques have been involved in order to obtain an hybrid joints between aluminum lamina and composite skins. In particular, a simple lap joint configuration have been considered as shown in Fig. 9.4.

In order to achieve stiff composite laminate in the joints area, a ply-drop techniques have been designed at the end of the sandwich panels (Fig. 9.5)

The model has been performed using MSC Nastran code®. The sandwich panel (Fig. 9.6a) has been modeled using the same elements (solid element for the core and shell elements for the skins) and materials described in Chapter V, whereas shell elements have been employed the aluminum frame using (Fig. 9.6b). The adhesive joint has been modeled using the method

proposed by NASA counting three different springs (one for the axial and two for the shear stiffness of the glue) and two rigid elements to connect the spring to the nodes (Fig. 9.6c).

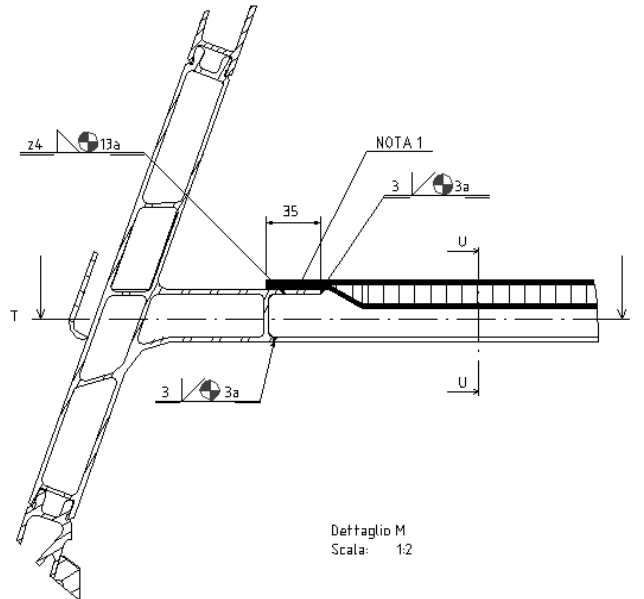


**Figure 9.4. Single lap adhesive joints between the sandwich panel and the aluminum frame.**

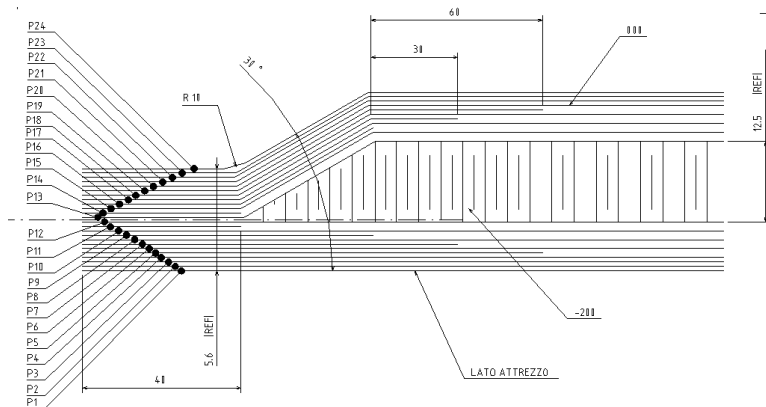


**Figure 9.5. Ply-drop configuration at the end of the panel.**

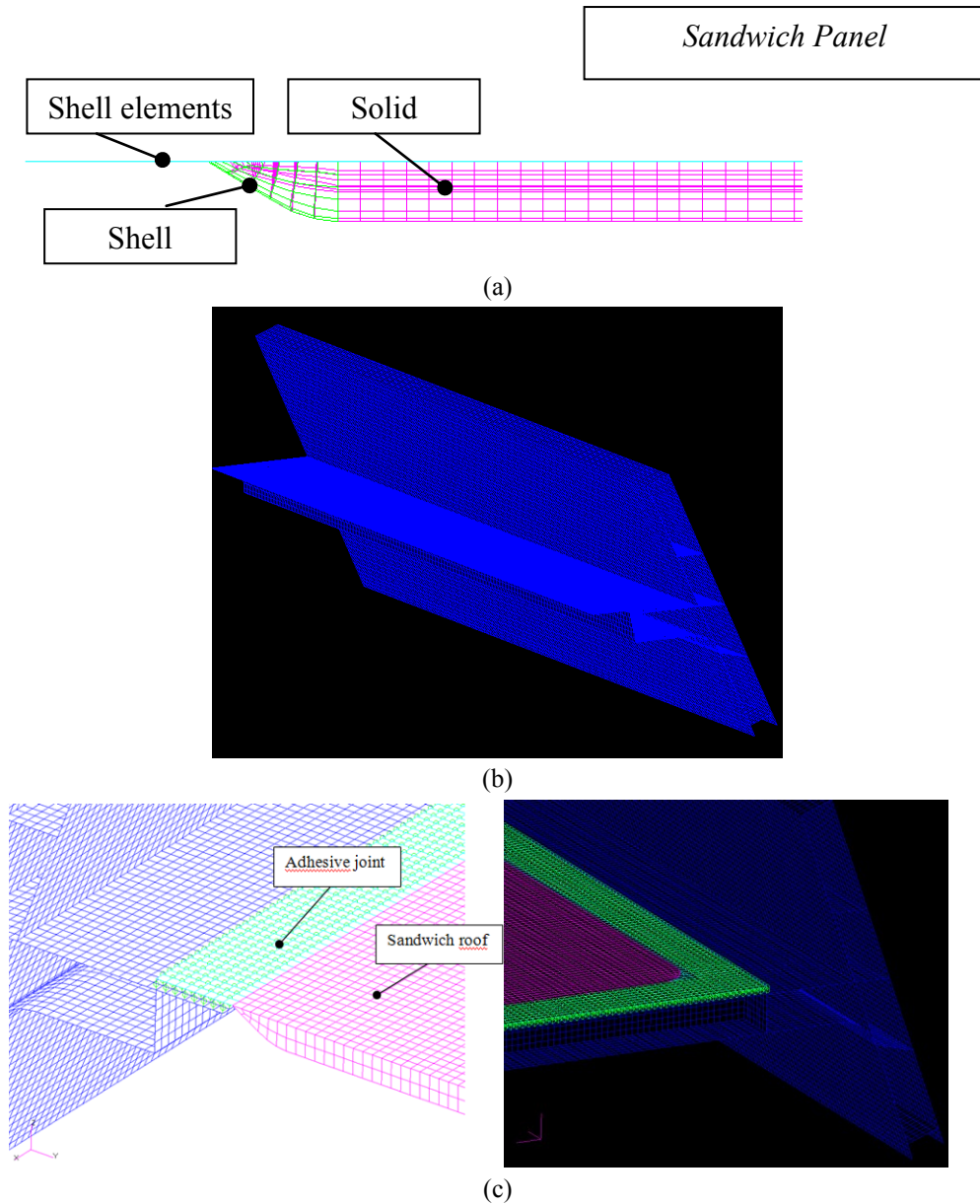


**Figure 9.6.** FE model techniques: (a) sandwich elements; (b) aluminum elements; (c) adhesive joints.

The introduction of ply-drop at the end of the panels need a careful analysis of the stress at this location. At this aim the composite the panel is divided in three domains (Fig. 9.7). The yellow one identifies the card defined into the

model to simulate the sandwich skins, whereas the other two have been defined to characterize the ply-drop configuration.

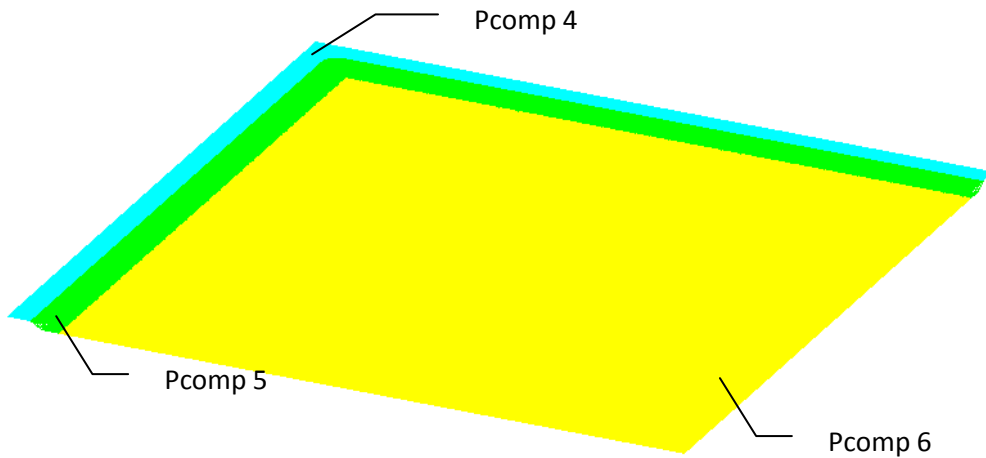


**Figure 9.7. Selection of domains in the panel**

The structural analysis have been carried out considering the maximum load due to heavier attached components (650 Kg). These is the more critical condition for the selected panels (Fig. 9.8).

A concentrated load was applied to simulate the maximum load due to the heavier gear can be placed on the roof.

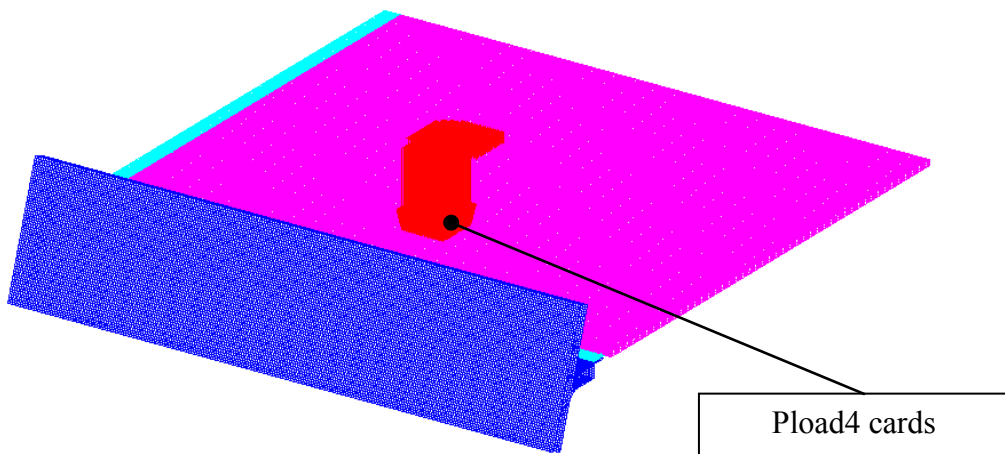


**Figure 9.8. Loading configuration.**

### 9.3.3. Stacking sequence optimization

The ply thickness optimisation is applied to the two domains of the panel substructure using the optimization module of Nastran program. For each domain the stacking sequence of eight ply thicknesses are to be optimized. The  $0^\circ$ ,  $\pm 45^\circ$  and  $90^\circ$  ply orientation have been fixed as discrete variables in the composite laminates that count a total of twenty-four ply thicknesses.

In this case the stacking sequence that allow to achieve the minimum failure index estimated by Tsai-Hill theory have been considered. In the present case the condition is satisfied adopting  $[0,-45,90,0,90,0,90,45,45-45,90,0]_s$  staking sequence.

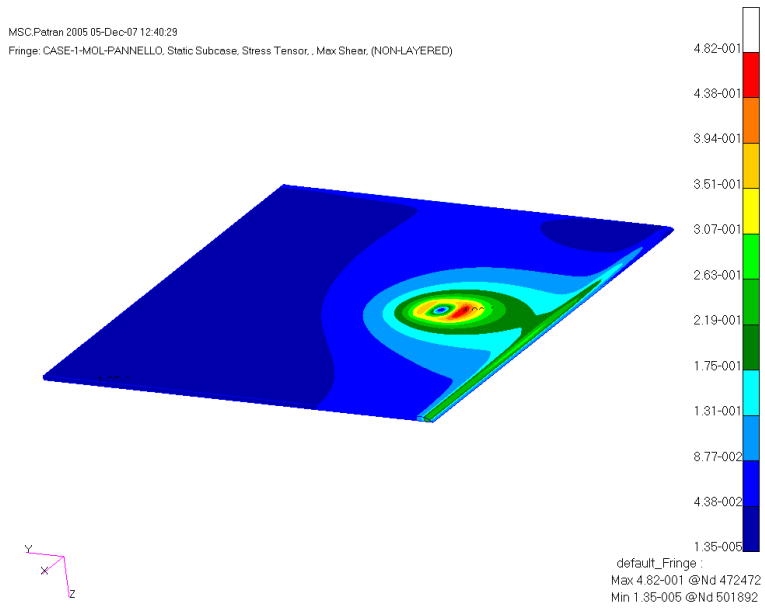
## 9.4. Final Validation

On the described static load condition (Fig. 9.8), static simulation have been carried out in order to validate the design configuration.

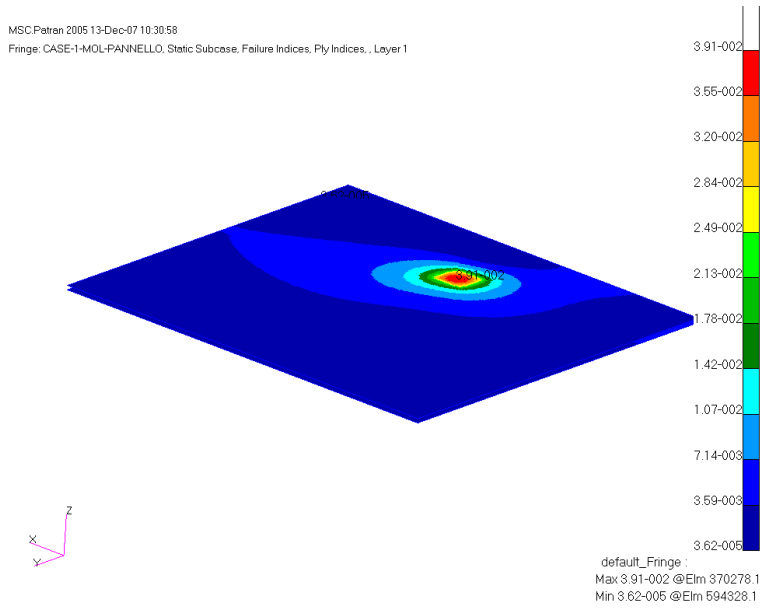
The stress field in the sandwich, derived by the static simulation, has been verified using Hill and maximum stress criteria for skins and core respectively. Figs. 9.9-9.10 shows the contour plot for the critical ply of each domain defined in the model.

Fatigue simulations have been also performed to validate the adhesive joint comparing the data derived by the output of the spring with the experimental values. The two fatigue loading condition described in the Chapter IV have been performed. The derived output are compared with the allowable fatigue properties experimentally derived in the Chapter VI.

Moreover both free and constrained modal analyses on the test article have been performed (Figs. 9.11 9.12). In particular the free analysis verify that the first six modes are rigid, while the seven is different to zero as suggested by the EN 12663 code, which define also the frequency range of the first ten vibration modes that have been satisfied by the constrained analysis. Infact the first vibration mode is very close to the suggest value of 10 Hz, while all the other modes have a high frequency. Table 9.1 reports the derived modal results.

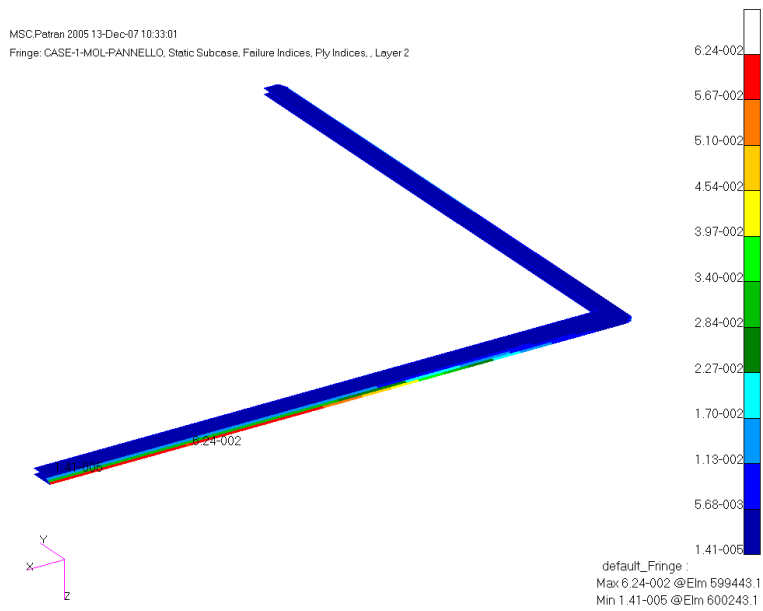


(a)

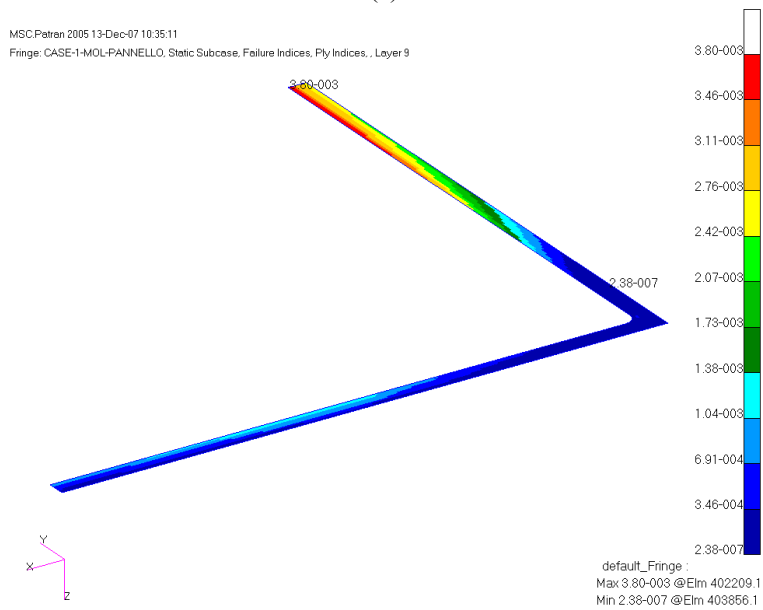


(b)

**Figure 9.8. Failure index of sandwich layer: (a) maximum core shear; (b) Hill failure index**



(a)



(b)

**Figure 9.9. Failure index of sandwich layer: (a) pcom5 domain; (b) pcom6 domain**

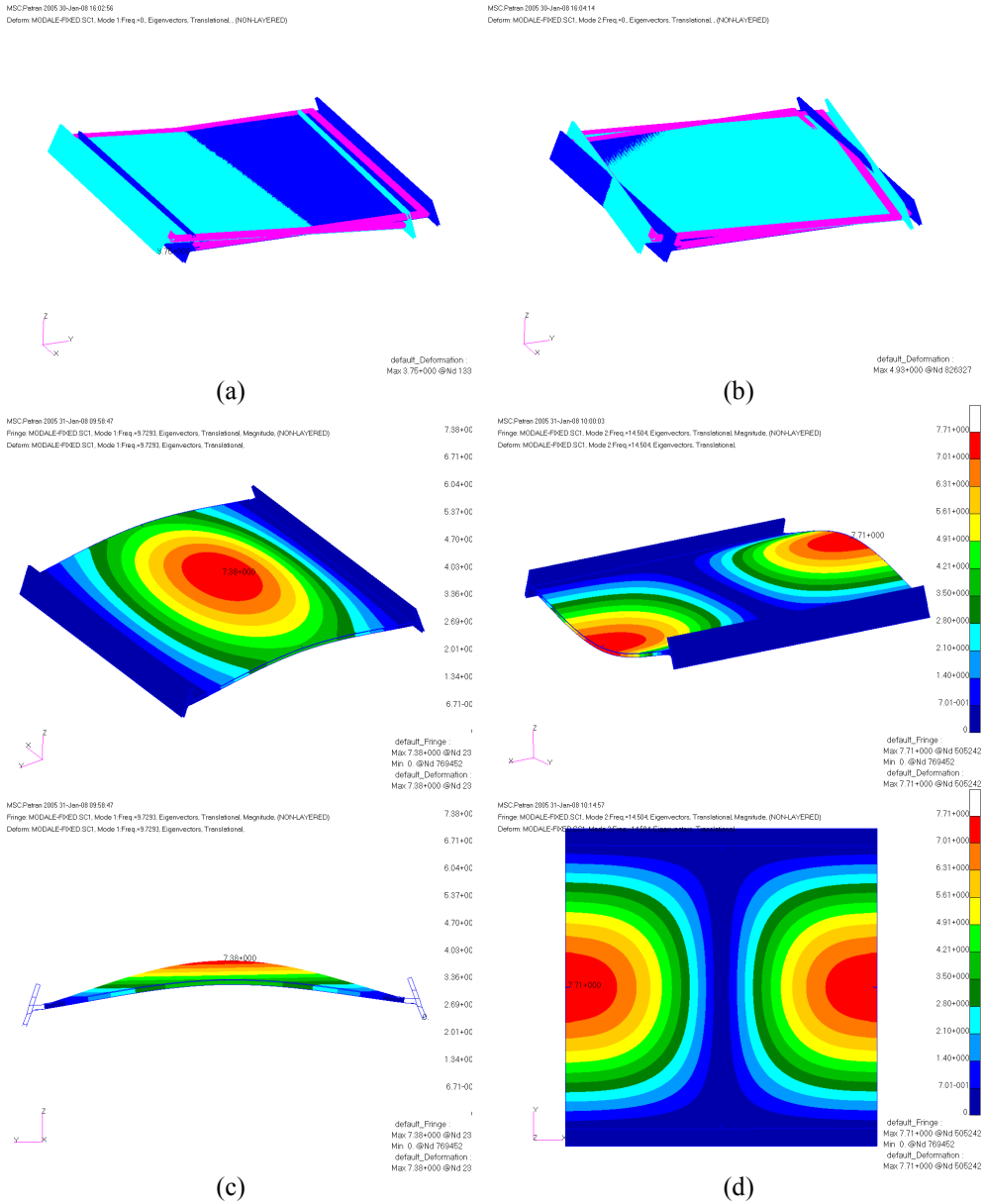


**Figure 9.9. Modal analysis: (a) first model of free analysis; (b) second mode of free analysis; (c) first mode of fixed analysis; (d) second mode of fixed analysis.**

**Table 9.1. Frequency of free and fixed modal analysis**

<b>MODE N°</b>	<b>Modal Free FREQ. [Hz]</b>	<b>Modal Fixed FREQ. [Hz]</b>
<b>1</b>	7.13E-04	9.73E+00
<b>2</b>	6.15E-04	1.45E+01
<b>3</b>	1.18E-04	2.22E+01
<b>4</b>	3.35E-04	2.64E+01
<b>5</b>	4.23E-04	3.58E+01
<b>6</b>	6.49E-04	3.62E+01
<b>7</b>	5.07E+00	4.81E+01
<b>8</b>	9.40E+00	5.15E+01
<b>9</b>	1.90E+01	5.72E+01
<b>10</b>	1.92E+01	6.21E+01

## ***CONCLUSION***

A multiscale procedure have been presented as an optimum tools for the design of composite sandwich elements. In the present work, the proposed design methodology have been implemented for the design of sandwich elements as roof of a railway vehicle.

The procedure involves both experimental, analytical and numerical tools in the different step.

The activity herein presented allows to assess the mechanical properties of the phenolic impregnated skins, expressly manufactured for transportation industry, and to validate and calibrate analytical and numerical models for the sandwich construction with regards to the several failure modes that a sandwich construction can explain. At this aim failure mode map is shown to be a good tool to predict the failure loads and modes as functions of the geometry and materials of the sandwich structure.

In addition, particular attention have been focused on the following degradations factors: (i) degradation of joints; (ii) environmental conditioning; (iii) in service impact events.

About the *adhesively bonded joints*, the following remarks can be made based on the detailed test results:

- ✓ Improved shear and cleavage properties are observed when aluminum adherends are employed: the composite-composite and aluminum-composite adherend combinations achieve the 55% and 75% of the shear strength and the 50% and 70% of the cleavage strength respectively of the aluminum-aluminum adherends configuration.

- ✓ Adherend materials have significant effect on the failure modes of both single lap adhesive joints under tensile loading, which failures are predominantly characterized by interfacial failure and cleavage tests, which failures are predominantly characterized by mixed failure mode involving interfacial and cohesive mechanisms.
- ✓ Adherend failure (first-ply delamination) has occurred on two composite-composite specimens loaded under cleavage/peel; in any way, the cleavage strength value at which first-ply delamination occurred is higher than the average value provided by cleavage tests characterized by mixed failure mode.
- ✓ The fatigue data, reported in terms of S-N curves, show improved fatigue properties when composite adherends are employed providing a lower reduction of the shear strength at 107 cycles. However the maximum fatigue strength at 107 cycles is achieved, as in the static case, for the aluminum-aluminum adherend configuration.

About the *mechanical fastened joints*, the following remarks can be made based on the detailed static test results:

- ✓ The experimental results have highlighted the influence of the rivet length on the mechanical performance and failure modes of the composite joints. The long rivets composite joints show improved value of nominal bearing stress, ~ 17% and ~ 22% greater than aluminum and short rivets configurations respectively, in despite of a lower stiffness.
- ✓ Mixed failure mode involving pull-out of fastener and bearing of the sheets have characterized both aluminum and long rivets composite joint configurations, whereas edge delamination mechanism has also involved in the mixed failure mode when short rivet are employed.
- ✓ The fatigue data, reported in terms of S-N curves, show improved high value of the bearing strength and high efficiency at 107 cycles when aluminum laminates are employed.

In the evaluation of the degradation of the sandwich materials and behavior, no significant reduction was observed in the elastic modulus of the skin, shear strength and modulus of the core, and shear and flexural stiffness of the

sandwich configuration, while appreciable reduction of the facesheet strength was observed when exposed to moisture and/or chemical agents.

As consequence, a coating techniques will be introduced to minimize the influences of these environmental factors and a more exhaustive experimental activity will be performed to achieve the influence of the selected factors on all the basic material properties (e.g. interlaminar shear, compressive).

The dynamic investigation provides the influence of the skin thickness, the material strain rate, the diameter of the impacting projectile and the impact velocity on the dynamic behavior of the sandwich composite material.

Experimentally evidence allowed to understand the response of the sandwich material and the damage mechanisms involved in an indentation and impact event on a sandwich structures. The following main outcomes have been obtained: (i) the Nomex honeycomb structure presents a strain rate sensitive compressive behavior; in particular, at a strain rate of about  $300 \text{ s}^{-1}$ , the compressive strength presented a DIF of 1.20, whereas the crush strength presented a DIF of 1.10; (ii) in case of 1-mm skin thickness, no significant strain rate effects are observed for the peak.

Finally optimization and validation activity have been performed by means of finite element analysis. It allows that the designed sandwich configuration achieves both the structural and functional requirements.

In particular static and modal analysis have been used to validate the final configuration with regards to strength and stiffness requirements, while fatigue analysis shows that adhesive joints can be exploited to assembly railway vehicles.